DESIGN AND ADDITIVE MANUFACTURING OF NOVEL CERAMIC MONOLITHIC CATALYSTS FOR LOW EMISSION VEHICLES

By:

NIKOLINA KOVACEV

A thesis submitted to the University of Birmingham for the degree of

DOCTOR OF PHILOSOPHY

Department of Mechanical Engineering

School of Engineering

University of Birmingham

April 2022

ABSTRACT

Environmental concerns and stringent emission standards have underlined the significance of developing more efficient catalytic converters for exhaust gas aftertreatment. Although the state-of-the-art ceramic honeycomb substrate designs provide a high surface area and low backpressure, further emission reduction advantages can be obtained by introducing advanced designs. The research work presented in this thesis addresses the design and fabrication of advanced ceramic monolithic catalysts using Digital Light Processing (DLP) ceramic additive manufacturing technology. By embracing the advantage of unconstrained conceptual design and overcoming the limitations of traditional manufacturing capabilities, DLP shows a potential use as a catalyst substrate fabrication method to improve catalytic efficiency through advanced catalyst designs.

Firstly, monolithic substrates based on diamond-lattice structures were proposed as an attractive replacement for the conventional honeycomb substrate. The comparison of the thermal-hydraulic characteristics of the honeycomb design and the diamond lattice substrate was achieved by pairing numerical simulations and experimental studies. The results show an increase in the axial temperature distribution for diamond lattice structures and a significant decrease in the pressure drop (38–45%) in comparison with the benchmark honeycomb with a similar surface area.

Secondly, ceramic slurry preparation processes and printing parameters were evaluated to manufacture lattice structures. A Design of Experiments (DoE) technique was used to generate an experimental plan based on all the relevant process parameters, followed by an Analysis of Variance (ANOVA) approach which was then used to determine the optimal processing window and assess the manufacturability along with dimensional accuracy of the lattice

structures. The ceramic slurry with the dispersant pre-treated powder showed appropriate rheological and photopolymerisation behaviour for manufacturing lattice structures with feature sizes up to 500 µm. ANOVA revealed the exposure time, the exposure power and the interaction effect of both had significant influence on the dimensional accuracy of lattice strut diameters.

Thirdly, to demonstrate the potential of the additively manufactured lattice-based substrates as catalytic converters, they were manufactured and coated with Pt-Pd catalyst supported on γ-Al_2O_3. Their light-off behaviour was tested in an exhaust gas environment. In addition, the effect of hydrogen presence on their performance was investigated. The light-off experiments showed superior catalytic activity for abatement of carbon monoxide, hydrocarbons, and nitrogen oxides for additively manufactured diamond-lattice catalysts, in comparison with the conventional honeycomb design, with a significant reduction in the light-off temperatures. The intricate lattice structures allowed greater exhaust gas-solid contact and more efficient utilisation of the given surface area. The light-off curves of all studied species in hydrogen-enriched exhaust gas stream shifted to lower temperatures.

Finally, a proof-of-concept was presented, where two individual substrates were integrated into a single, dual-substrate monolith by various interlocking systems. Based on the findings, the sintered parts displayed anisotropic sintering shrinkage of approximately 14% in the X-Y direction and 19% in the Z direction, with a sintered density of 97.88±0.01%. These novel dual-substrate monoliths lay the foundation for a potential reduction of the complexity and expense of the aftertreatment system.

The findings of this thesis are applicable to catalytic converter systems of spark and compression ignition engines and enrich the current research on moving towards low emissions vehicles.

ACKNOWLEDGEMENTS

I would like to give my thanks and sincere gratitude to my supervisor Dr Khamis Essa for the opportunity to conduct a PhD and for his support and guidance throughout the course of this work. Special thanks go to my co-supervisors, Dr Hassan Hemida and Prof. Athanasios Tsolakis for useful discussions and continuous support. I wish to thank the EPSRC, UK for the funding without which this PhD would not have been possible. I would like to thank the staff from the School of Mechanical Engineering and School of Metallurgy and Materials of the University of Birmingham, especially Mr Jack Garrod, Mr Kevan Charlesworth, Mr Simon Cannon and Mr Jacob Gates. Thanks to Dr Omid Doustdar and Dr Soheil Zeraati Rezaei for their valuable advices and help. Special thanks go to Dr Sheng Li for all his help and support through tears and laughter even when thousands of miles away. Dr Amir Bordbar, Dr Prveen Bidare, Marcin and to all the members of our research group, especially to Michele, Abdullah, Mohammed, Weining and Raja- thank you!

Finally, none of this would have been possible without my Mom and Dad which I thank for their continuous support throughout my life and for respecting every decision I ever made, good or bad. I am also very grateful to my boyfriend Alex for always being there for me, going with me through ups and downs, and especially for his support to retain some work-life balance.

TABLE OF CONTENTS

LIST OF FIGURES

LIST OF TABLES

LIST OF ABBREVIATIONS

A	Cross-sectional area of the substrate, m^2
Al_2O_3	Alumina oxide
AM	Additive Manufacturing
ANOVA	Analysis of Variance
ASC	Ammonia Slip Catalyst
B_d	Broadening depth, µm
BET	Brunauer-Emmett-Teller (BET) surface area
BEV	Battery Electric Vehicle
C_d	Cure depth, µm
CeO_2	Cerium (IV) oxide
CFD	Computational Fluid Dynamics
THC	Hydrocarbons
CI	Compression Ignition
CO	Carbon monoxide
CO_2	Carbon dioxide
CPSI	Cells Per Square Inch
C_w	Cure width, µm
D	Diameter of the substrate, mm
D45	Diamond lattice
D_p	Slurry penetration depth, µm
D_w	Width sensitivity, µm
d_p	Lattice pore diameter, mm
d_h	Hydraulic diameter of the honeycomb channel, mm
DLP	Digital Light Processing
DMD	Digital Micromirror Device
DPF	Diesel Particulate Filter
d_s	Lattice strut diameter, mm
DOC	Diesel Oxidation Catalyst
DoE	Design of Experiments
DSC	Differential Scanning Calorimetry
DTG	First derivative of the TGA curve
E	Energy dose, mJ/cm^2
E_c	Critical energy dose, mJ/cm^2
ED	Elongated diamond lattice
EP	Exposure power, mW/cm^2
ET	Exposure time, s
E_w	Critical energy dose in width direction, mJ/cm^2

GDI	Gasoline Direct Injection
GHSV	Gas Hourly Space Velocity through the substrate, ratio between the gas volume flow rate and the substrate volume, h^{-1}
GPF	Gasoline Particulate Filter
GSA	Geometric Surface Area, m^{2}
$\mathbf{H_2}$	Hydrogen
$\mathbf{H_2O}$	Water
h	Heat transfer coefficient, W/m^{2}K
HC	Conventional honeycomb substrate
HEV	Hybrid Electric Vehicle
ICE	Internal Combustion Engine
$\mathbf{k_s}$	Solid thermal conductivity, W/mK
L	Length of the entire substrate, mm
$\mathbf{La_2O_3}$	Lanthanum oxide
$\mathbf{L_c}$	Cell length, mm
$\mathbf{L_s}$	Strut length, mm
LT	Layer thickness, µm
$\dot{m}$	Mass flow rate, kg/h
NO	Nitrogen oxide
$\mathbf{NO_2}$	Nitrogen dioxide
$\mathbf{NO_x}$	Nitrogen oxides
OFA	Open Frontal Area
$\mathbf{\Delta P}$	Pressure drop through the substrate, Pa
PGM	Platinum Group Metals
Pt	Platinum
Pd	Palladium
PM	Particulate Matter
Q	Total heat loss, W
Re	Reynolds number based on strut diameter
Rh	Rhodium
SCR	Selective Catalytic Reduction
SI	Spark Ignition
SLA	Stereolithography
$\mathbf{SnO_2}$	Tin dioxide
$\mathbf{S_v}$	Specific surface area, m^{-1}
TGA	Thermogravimetric analysis
$\mathbf{T_{gas,\ in}}$	Temperature of the gas at the inlet of the substrate, K
$\mathbf{T_{gas,out}}$	Temperature of the gas at the outlet of the substrate, K
$\mathbf{TiO_2}$	Titanium dioxide

$T_{wall,ave}$	Average temperature of the outer walls of the substrate minus the ambient temperature, K
TWC	Three Way Catalyst
V_{bcc}	Volume of the solid substrate, m^3
$V_{cylinder}$	Volume of the entire cylinder substrate, m^3
ZrO_2	Zirconium dioxide
ε	Porosity of the substrate
Φ	Specific length ratio, the ratio of pore diameter and strut thickness

LIST OF PUBLICATIONS AND PRESENTATIONS

The following publications and conference presentations are a result of the research carried out during the thesis.

Journal article publications

- Kovacev N, Li S, Zeraati Rezaei S, Hemida H, Tsolakis A, Essa K. Effects of the internal structures of monolith ceramic substrates on thermal and hydraulic properties: additive manufacturing, numerical modelling and experimental testing. Int J Adv Manuf Technol. 2020; 112:1115–32.

- Kovacev N, Li S, Essa K. Effect of the preparation techniques of photopolymerisable ceramic slurry and printing parameters on the accuracy of 3D printed lattice structures. J Eur Ceram Soc. 2021;41(15):7734–43.

- Kovacev N, Doustdar O, Li S, Tsolakis A, Essa K. The synergy between substrate architecture of 3D printed catalytic converters and hydrogen for low temperature aftertreatment systems. Appl Catal B Environ. 2022. Under review.

- Kovacev N, Li S, Li W, Zeraati Rezaei S, Tsolakis A, Essa K. Additive manufacturing of novel hybrid monolithic ceramic substrates. Aerospace. 2022; 9(5):255.

Conference presentations

- Kovacev N, Essa, K. Additive manufacturing of monolithic catalyst for automotive applications. Presented at Bluebear conference; University of Birmingham; UK; 2019.

- De Lisi M, Kovacev N, Attia U, Essa K. Numerical simulation of sintering of DLP printed alumina ceramics. Presented online at ASTM International Conference on Additive Manufacturing; California; USA; 2021.

CHAPTER 1 INTRODUCTION

As the global community realises the importance of clean air, environmental standards continue to tighten and get more rigorous. Concerns regarding global warming, climate change and human health are driving the industry to seek innovative solutions to reduce air pollution. Internal Combustion Engines (ICEs) account for 99.8% of all transportation, making them one of the most significant sources of pollution in the atmosphere, especially in urban areas [1]. ICE exhaust gas emissions will undoubtedly continue to have a considerable influence on air quality, given that worldwide ICE use is expected to increase to 1.3 billion over the next decade [2]. Therefore, continuing to improve ICE's aftertreatment system is crucial for ensuring transportation sustainability.

1.1 Background

1.1.1 Exhaust emissions formation and their health and environmental implications

Exhaust gas is emitted as a result of the combustion of fuels such as gasoline, diesel, natural gas, and fuel components such as ethanol or biodiesel, depending on the type of the combustion engine. A Spark Ignition engine (SI; gasoline engine) employs a spark plug to ignite a mixture of air and gasoline fuel, whereas a Compression Ignition engine (CI; diesel engine) ignites diesel fuel by compression to high pressure and temperature [3]. The exhaust gas typically contains nitrogen (N_2), water (H_2O), carbon dioxide (CO_2) and emissions. A variety of factors, such as engine type, engine load, and fuel composition, influence the concentration of the chemical species in the exhaust gas [3]. An exemplary exhaust gas composition for the two is shown in Figure 1.1 [4]. Harmful compounds depicted as emissions, form around 0.5% of the total exhaust gas concentration.

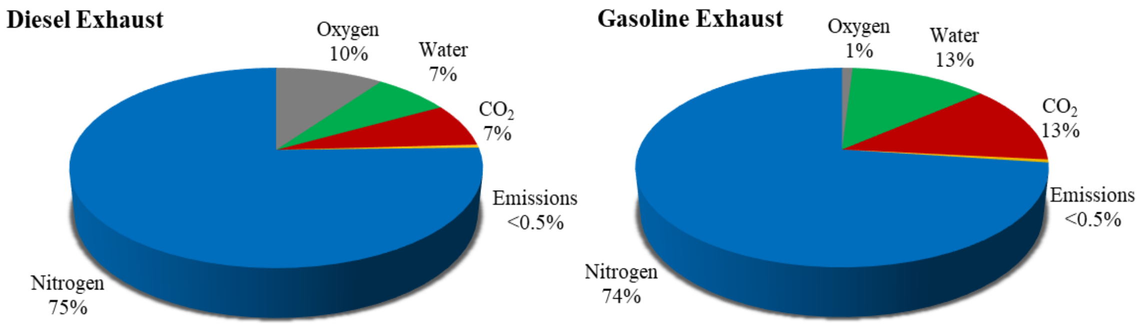

Figure 1.1 Exemplary exhaust gas composition concentration from diesel and gasoline combustion %(v/v) [4]

Regulated emissions include Carbon Monoxide (CO), hydrocarbons (THC), Nitrogen Oxides (NO_x), and Particulate Matter (PM). CO is a product of incomplete combustion due to local lack of oxygen, or excessive oxygen in the combustion chamber, the quantity emitted is determined by the air/fuel mixture. CO is a colourless and tasteless gas that, when inhaled, can bind to haemoglobin in the bloodstream and reduce its ability to carry oxygen [5]. Hydrocarbons are formed due to an incomplete combustion process. Hydrocarbons include alkanes (methane, ethane, pentane, hexane), aromatic hydrocarbons (benzene, toluene, xylene, polycyclic aromatic hydrocarbons) and aldehydes (formaldehyde, acetaldehyde, acrolein). Because of the presence of benzene and aromatic chemicals, they are toxic and can irritate the respiratory system and cause cancer. They also promote ozone formation [5]. NO_x (NO, NO_2, N_2O_2) are a result of the high-temperature reaction between nitrogen and oxygen. NO_x emissions contribute to the formation of ozone and smog [5]. NO_2 itself has the potential to irritate the lungs and reduce resistance to respiratory infections. PM is formed during the combustion process, mostly because of the incomplete combustion of hydrocarbons in fuel and lubricant oil. Diesel engines are particularly notorious for emitting considerable amounts of PM. PM can cause premature death, as well as asthma, lung cancer, and other cardiovascular conditions. Additionally, they contribute to air pollution, decreased visibility, and global warming [5].

To meet stringent emission regulations and reduce the emissions from the ICE exhaust gas, vehicle manufacturers have had to ensure the advancement of combustion technology, engine design, propose novel fuels and develop high-efficiency catalytic exhaust aftertreatment systems [6].

1.1.2 An overview of catalytic exhaust emission control systems

Elimination of the noxious emissions from exhaust gases is accomplished by application of catalytic converters. Catalytic converters, such as a two-way oxidation converter and a three-way oxidation-reduction converter have been employed in the exhaust gas aftertreatment systems of vehicles to reduce tailpipe emissions since the 1970s [5]. The key component of a catalytic converter, shown in Figure 1.2 [7], is an extruded monolith substrate coated with catalytic substances supported on high surface oxides. The structure of the honeycomb consists of an array of parallel millimetre-sized straight flow-through channels that provide a large catalyst surface area. These channels allow exhaust gases to pass through and interact with the active catalyst layer adhered to the channel walls. Exhaust aftertreatment systems can include various catalytic converter technologies such as a catalyst for the Selective Catalytic Reduction of NO_x with ammonia (NH_3-SCR); an Ammonia Slip Catalyst (ASC) to remove the excess NH_3 by selective catalytic oxidation with oxygen to N_2 and H_2O [8]; Diesel Particulate Filter (DPF) to filter out the particulate matter, a two-way catalytic converter, Diesel Oxidation Catalyst (DOC), to simultaneously oxidise CO and hydrocarbons to CO_2 and water [9], or a Three-Way

Catalyst (TWC) to oxidise CO to CO_2, unburnt hydrocarbons to CO_2 and water and reduce NO_x to O_2 and N_2. Gasoline Direct Injection (GDI) vehicles can be equipped with a separate Gasoline Particulate Filter (GPF) to remove particulate matter or an integrated GPF combining filtration and TWC [10].

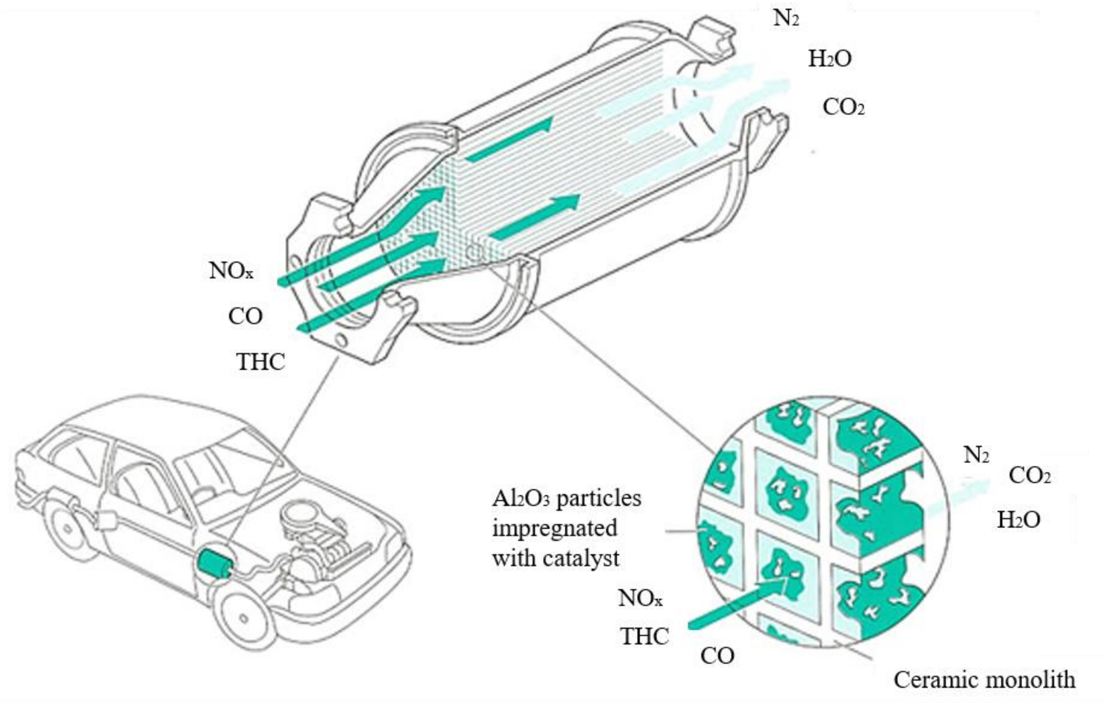

Figure 1.2 Schematic of a typical catalytic converter [7]

1.1.3 Conventional monolith catalyst manufacturing methods

Extrusion is a conventional manufacturing technology for shaping ceramic monolith honeycomb substrates. The material used for the commercial production of the monolithic substrate is cordierite ($2MgO \cdot 2Al_2O_3 \cdot 5SiO_2$), with good resistance to high-temperature changes and a low coefficient of thermal expansion [11]. Cordierite is not the only available construction material for the honeycomb substrates, but it is the most common one. Other types of ceramics, such as silicon carbide, mullite, alumina or zirconia oxide are available as well. The following fundamental phases are involved in the production of cordierite monolith substrates: (i) dry mixing the raw materials (kaolin, raw talc, aluminium, alumina hydroxide, silica and calcined talc) (ii) plasticising with water and other organic additives (wet mixing, kneading); (iii) extrusion of the resulting ceramic paste through suitable dies; (iv) drying to remove moisture; and (v) firing at 1450 °C to transform the raw materials into the cordierite monolithic substrate [11]. The shape, cell density and wall thickness of the honeycomb channels directly affect the pressure drop, mass transfer and heat transfer behaviour of catalysts.

There is not much flexibility regarding the channel design, size and wall thickness since the final geometric shape of the monolith substrate depends on the available extrusion dies. Current manufacturing possibilities through extrusion limit the honeycomb wall thickness to a minimum of 0.05 mm and the cell density to a maximum of 1200 Cells Per Square Inch (CPSI) [12].

1.2 Motivation

Due to the health hazards associated with noxious tailpipe emissions, most countries have enacted progressively stringent emission standards for light-duty and heavy-duty combustion-engine vehicles. These standards include Euro-VI in the European Union (EU), Tier 3 in the United States (US), China-5 and China-6 in China and Bharat III, IV and BS-VI in India. Furthermore, a projected proposal for Euro-VII exhaust gas legislation in 2021 has shifted the importance to even more stringent air pollutant emissions standards for combustion-engine vehicles with particular emphasis on urban settings [13]. The government of the United Kingdom is committed to decarbonising transport by 2035 and transit to transportation governed by Battery Electric Vehicles (BEV) [13]. However, BEVs face considerable barriers to unconstrained and rapid development, and they may not be able to completely replace ICEs for several decades since significant resources are required to provide infrastructure for charging BEVs and CO_2-free electricity production [13]. As previously stated, urban areas can face higher local emissions due to the high traffic density. This causes engines to operate in cold start conditions, low loads, low vehicle speed, frequent stops/starts and acceleration. In the first few minutes of engine operation (cold start), the honeycomb catalyst cannot heat up rapidly enough to reach the operating temperature sufficient for pollutant removal. Up to 80% of pollutant species are released into the atmosphere during this time [14]. Since the conversion of pollutants in catalytic converters is temperature dependent, the time between engine start-up and light-off temperature must be as short as possible, and the catalyst temperature must be kept above the light-off to ensure that emissions from vehicles remain below the air pollutant limits for a wide range of engine conditions [15]. The light-off temperature is defined as the temperature at which the conversion efficiency of pollutants is equal to 50% [14]. Under normal operating conditions, the flow within the honeycomb channels is laminar due to the relatively dense cell structure and small channel diameters, resulting in poor mass transfer coefficients. Furthermore, the honeycomb must have a high internal surface area to reduce emissions efficiently. The conventional manufacturing constraints limit any further developments in the honeycomb design to keep the air pollutant emissions under control in all conditions of use. Compliance with current and upcoming more stringent vehicle emission legislation, as a result, poses significant challenges.

Monolith catalyst designs that incorporate features that interrupt laminar flow pattern and induce turbulence in the flow stream to boost heat and mass transfer are the most attractive ones. Lattice structures, such as Kelvin, cubic, octet and diamond cells have been suggested for various catalytic applications [16,17]. Additive Manufacturing (AM) can offer a solution to manufacturing limitations that have previously decelerated the progress in the advanced design and integration of monolith catalysts. The primary advantage of the AM techniques is that they enable the direct fabrication of components with configurations that would be difficult to achieve using conventional manufacturing methods. Ceramic AM technologies that enable three-dimensional shaping of ceramics using photopolymerisation processes, such as Digital Light Processing (DLP) technology, have been developed throughout the years and offer significant promise of manufacturing components with intricate and fine features. However, there are still significant challenges associated with the use of ceramic photopolymerisable slurries for part manufacturing, therefore the AM's full potential in terms of advanced monolith catalyst fabrication remains unrealised.

1.3 Research aims and objectives

The overall aim of this research is to enhance the design of ceramic monolith catalysts for automotive emissions aftertreatment applications. In particular, the project is focused on overcoming some of the limitations of the conventional honeycomb catalysts to attain higher conversion efficiency and on providing a novel manufacturing route through the use of Digital Light Processing additive manufacturing technology.

To meet the above aim, the following objectives will be fulfilled:

1. Develop and validate Computational Fluid Dynamics (CFD) techniques that predict the fluid flow and thermal performance of the lattices and the honeycomb substrate with the focus on the physical behaviour of the flow within the substrates driven by the geometry change in Chapter 3.
2. Utilise the developed numerical models to predict and evaluate the effect of the design parameters of the lattice structures on geometrical parameters, hydraulic and thermal properties in Chapter 3.

3. Study the effect of the photopolymerisable ceramic slurry preparation techniques on rheology and cure depth and identify the optimal printing parameters for manufacturing tailored lattice structures with fine feature sizes in Chapter 4.
4. Study the effect of DLP additive manufacturing process parameters, for instance, layer thickness, exposure power and exposure time, on the dimensional accuracy of lattice structures in order to manufacture monolithic-type catalysts with lattice architectures in Chapter 4.
5. Develop a catalyst coating to functionalise the sintered ceramic lattices with a catalytic phase in Chapter 5.
6. Compare the light-off performance of the obtained lattice-based catalysts against a conventional honeycomb design under real exhaust engine conditions. Additionally, show potential synergetic effects of the interaction between lattice-based monolithic catalysts and hydrogen in Chapter 5.
7. Propose novel hybrid monolith catalyst concepts featuring various interlocking mechanisms to integrate two substrates into a single one that could offer process intensification and complexity reduction of the aftertreatment system in Chapter 6.

1.4 Thesis organisation

Chapter 1 outlines the motivation behind the work. In this section, the project is introduced along with the aims, objectives, and structure of the thesis.

Chapter 2 reviews the current state-of-the-art in the key research disciplines on which this thesis is based, such as the structure of the traditional monolith catalyst, limitations, state-of-the-art advanced catalyst designs and manufacturing capabilities, ceramic additive manufacturing and photopolymerisable ceramic slurries.

Chapter 3 studies the influence of the lattice design on thermal and hydraulic properties in comparison with the conventional honeycomb. A computational fluid dynamic model is developed, validated for both lattice and honeycomb design, and used to compare the performance between them. The performance of the honeycomb and lattice designs is evaluated in terms of the temperature profile, velocity and pressure drop in a non-reactive environment. Moreover, the impact of the principal design parameters of lattice structures on geometric properties, pressure drop and temperature distribution was studied using numerical simulations.

Chapter 4 evaluates photopolymerisable ceramic slurry preparation strategies to achieve adequate rheology and curing parameters for use in DLP additive manufacturing. The effects of layer thickness, exposure power and exposure time on the dimensional accuracy of lattice strut diameters are studied through statistical methods with a full-factorial Design of Experiment (DoE) and Analysis of Variance (ANOVA). The optimal processing window was found by a systematic study of printing parameters. In addition, the manufacturability and dimensional accuracy of lattice structures with fine features of up to 500 µm were assessed.

Chapter 5 studies the light-off behaviour of additively manufactured diamond-based lattice catalyst structures in comparison with the conventional 400 Cell Per Square Inch (CPSI) honeycomb catalyst design in a real exhaust environment. The substrates were manufactured by DLP technology using the optimised ceramic slurry and printing parameters from Chapter 4. Furthermore, the substrates were catalyst-coated with the in-house developed Pt-Pd/γ-Al_2O_3 catalyst coating. The effectiveness of hydrogen addition in lowering the light-off temperatures for carbon monoxide, hydrocarbons, nitrogen oxide and for the formation of nitrogen dioxide in lattice structures was studied as well.

Chapter 6 provides a proof-of-concept in which hybrid ceramic monolithic substrates are designed and fabricated using the DLP process. The hybrid ceramic substrates contain two separate components that integrate into a single substrate via interlocking system. Several different interlocks were designed to demonstrate the practicality of the manufacturing process.

Chapter 7 provides a general conclusion to the thesis, presenting major findings and concluding remarks from each chapter, followed by future recommendations to the current work.

References

1. Kalghatgi G. Is it really the end of internal combustion engines and petroleum in transport? Appl Energy. 2018;225(4):965–74.

2. Sharma SK, Goyal P, Tyagi RK. Conversion efficiency of catalytic converter. Int J Ambient Energy. 2016;37(5):507–12.

3. Xue H, Jiang S, Liang B. A study on the model of traffic flow and vehicle exhaust emission. Math Probl Eng. 2013;2013:1-6.

4. Aakko-Saksa P, Roslund P, Koponen P. Development and validation of comprehensive emission measurement methods for alternative fuels at VTT. 2017.

5. Resitoglu I., Altinisik K, Keskin A. The Pollutant emissions from diesel-engine vehicles and exhaust aftertreatment systems. Clean Techn Env Policy. 2015;17:15–27.

6. Gao J, Tian G, Sorniotti A, Karci AE, Di Palo R. Review of thermal management of catalytic converters to decrease engine emissions during cold start and warm up. Appl Therm Eng. 2019;147:177–87.

7. Dey S, Dhal GC, Mohan D, Prasad R. Application of hopcalite catalyst for controlling carbon monoxide emission at cold-start emission conditions. J Traffic Transp Eng. 2019;6(5):419–40.

8. Choi J, Ko P. Automotive Emission Control Catalysts. Catalysts. 2016;6(10):155.

9. Ayodhya AS, Narayanappa KG. An overview of after-treatment systems for diesel engines. Environ Sci Pollut Res. 2018;25(35):35034–47.

10. Joshi A. Progress and outlook on gasoline vehicle after treatment systems. Johnson Matthey Technol Rev. 2017;61(4):311–25.

11. Govender S, Friedrich H. Monoliths: A Review of the Basics, Preparation Methods and Their Relevance to Oxidation. Catalysts. 2017;7(2):62.

12. Presti M, Pace L, Mueller W, Witte-Merl O. Vehicle mass lightening by design of light-weight structured substrates for catalytic converters. SAE Int. 2011;1–19.

13. Kalghatgi G. Challenges of energy transition needed to meet decarbonisation targets set up to address climate change. J Automot Saf Energy. 2020;11(3):276–86.

14. Reiter MS, Kockelman KM. The problem of cold starts: A closer look at mobile source emissions levels. Transp Res Part D Transp Environ. 2016;43:123–32.

15. Koltsakis GC, Samaras Z, Karvountzis-Kontakiotis A, Zacharopoulou T, Haralampous O. Implications of Engine Start-Stop on After-Treatment Operation. SAE Int J Engines. 2011;4(1):1571–85.

16. Essa K, Hassanin H, Attallah MM, Adkins NJ, Musker AJ, Roberts GT, et al. Development and testing of an additively manufactured monolithic catalyst bed for HTP thruster applications. Appl Catal A Gen. 2017;542:125–35.

17. Papetti V, Dimopoulos Eggenschwiler P, Della Torre A, Lucci F, Ortona A, Montenegro G. Additive Manufactured open cell polyhedral structures as substrates for automotive catalysts. Int J Heat Mass Transf. 2018;126:1035–47.

CHAPTER 2 LITERATURE REVIEW

This chapter begins with a review of ceramic additive manufacturing techniques and photopolymerisable ceramic slurries. Next, it presents the overview of the structure of the conventional monolith catalysts, key performance characteristics, performance limitations and current strategies to overcome the latter. The evaluation of the current state-of-the-art in design and ceramic additive manufacturing of complex monolith catalysts for automotive aftertreatment applications is given and finally a summary of opened research questions is presented.

2.1 Additive manufacturing of ceramic materials

American Testing and Materials Society defines AM or 3D printing as a technique for depositing, joining and solidifying materials in a layer-by-layer fashion to create three-dimensional objects [1]. The terms 3D printing and AM will be used interchangeably throughout the thesis. According to the Royal Academy of Engineering, the benefits of AM include practical and inexpensive component manufacturing due to the elimination of tooling costs, reduced material waste, production flexibility, and shorter lead time [2]. Plastics and metals dominate the AM industry due to their favourable processing and postprocessing opportunities. AM of ceramic materials has undergone extensive research in recent years, suggesting brand-new possibilities in the creation of complex ceramic components for various industrial applications. The developed technologies generally fall into two categories: (i) direct which generates the geometrical shape and material properties of 3D structures in a single operation and (ii) indirect whereby components are manufactured in two or more operations, the first of which provides the geometrical shape and the second where desired material properties are achieved [3]. The majority of the ceramic AM processes include indirect technologies, due to the challenges of directly processing ceramics. Recently, hybrid ceramic AM technique that combines the application of additive and subtractive manufacturing (3D printing with in-situ machining) has been developed. This approach was shown to be able to produce near-fully dense alumina components with significantly enhanced surface finish when compared to similar components manufactured without in-situ machining. The hybrid technique can eliminate the current restrictions of stand-alone ceramic AM technologies and allow a wide range of processing materials [4,5]. During a typical additive manufacturing process, layers of a material are built up to create a solid object [6]. The desired part is first designed in a computer-aided CAD software and converted into .STL file, which is a standard interface for additive manufacturing systems [1]. The .STL file is then converted to a G-code file via a slicing program where the 3D model is sliced into 2D images.

A brief overview of the available ceramic AM methods is presented in the next section, followed by a more in-depth look at Digital Light Processing Technology, the principal experimental method used in this research.

2.1.1 Brief overview of ceramic AM technologies

According to the terms in the standard (ISO/ASTM 52900), AM processes can be categorised into seven distinct classes, including binder jetting, directed energy deposition, material extrusion, material jetting, powder bed fusion, sheet lamination and vat photopolymerisation [1]. Due to the commercial variations of the AM process methodology, another approach to classify the ceramic AM technologies found in the literature is according to the initial feedstock, which can be powder, slurry, paste, or sheets of material, as shown in Table 2.1 [7].

Table 2.1 Classification of ceramic AM technologies [7]

Ceramic additive manufacturing technologies			
Suspension	**Paste**	**Powder feedstock**	**Sheets**
Slurry-Based 3DP (S-3DP) [8]	Fused Deposition Modeling (FDM) [9]	Selective Laser Melting (P-SLM) [10]	Laminated Object Manufacturing (LOM) [11]
Slurry-Based SLS (S-SLS) [8]	Robocasting [12]	Selective Laser Sintering (P-SLS) [13]	
Vat photopolymerisation (SLA, DLP) [14,15]	Direct Ink Writing (DIW) [16]	Powder-Based 3D Printing (P-3DP) [7]	
Direct Inkjet Printing (DIP) [17]			

In Slurry-Based 3DP (S-3DP) and Slurry-Based SLS (S-SLS) ceramic slurry or slip is used in order to increase the powder packing density in the powder bed [8]. Vat photopolymerisation techniques are based on liquid ceramic photopolymerisable slurries where a UV laser (Stereolithography, SLA) or digital light projector screen (Digital Light Processing, DLP) solidifies thin liquid layers of slurry to fabricate ceramic green objects [14,15]. Vat photopolymerisation techniques can only be used with a limited range of ceramic powders. Due to excessive light scattering, ceramic materials with high refractive index and high coefficients of extinction are difficult to shape. This is especially the case with oxide ceramics that are not white in colour, such as grey or dark colour SiC [18]. Furthermore, processing crack-free parts without excessive porosity is challenging, due to the removal of the organic components through debinding. The process of Direct Inkjet Printing (DIP) entails the deposition of individual drops of ceramic suspension to build up structures. The manufactured parts exhibit a dense microstructure with a high shape accuracy, without any additional machining [17]. However, major challenges are present with DIP to produce ceramics and the ink requires a low viscosity and low solids content. Fused Deposition Modeling (FDM) is extrusion-based layered manufacturing process in which semi-solid thermoplastic polymers gets deposited on a platform through a nozzle [9]. Robocasting and Direct Ink Writing (DIW) involve extrusion of a ceramic paste through a nozzle [12,16]. In Three-Dimensional Printing (P-3DP) an inkjet printing head sets a binding liquid onto a powder bed in the form of the cross section of the object in that layer [7]. In the powder-based Selective Laser Sintering (P-SLS) method the layers of the part are inscribed by a laser beam [13]. Selective Laser Melting (P-SLM) involves a deposited layer of powder on the building platform and the powder bed is sintered or molten selectively by the laser beam [10]. Laminated Object Manufacturing (LOM) involves building 3D components by lamination of sheets at low to medium temperature and pressure. Because the sheets have a limited thickness, the component surface is not very smooth and requires postprocessing [11].

Each of the aforementioned technologies differs in printing resolution and accuracy, final part density and quality, and manufacturing speed [19]. While SLA and DLP both show significant potential for complex structure manufacture, the multi-layer fabrication of ceramic parts via the DLP technology is the one of interest in this work.

2.1.2 Digital Light Processing

Charles Hull, the co-founder of 3D Systems, one of the world's first 3D printing companies, invented and patented SLA in 1986. The basic premise of the SLA technique includes photopolymerisation of a photocurable resin through irradiation with a laser beam, which supplies the energy necessary to trigger a curing reaction. Throughout this process, the liquid resin is transformed into a solid layer, yielding a highly cross-linked polymer [20]. Before 1994, when Griffith et al. [20] proposed extending the SLA technique to ceramic materials, SLA was limited to polymeric materials. They revolutionised the SLA process by extending the resin curing approach to aqueous acrylamide-based alumina and silica ceramic slurries. This was the very first time 3D printed ceramic parts via SLA technology were presented. Digital Light Processing (DLP) technology for ceramic 3D printing was introduced as an updated, more efficient, and faster manufacturing method than SLA. The primary difference between DLP and SLA is the type of light source used, which influences the surface profile, the size of the lowest achievable feature, and the printing time. The DLP uses a projector screen with a Digital Micromirror Device (DMD) to expose the layer to the light source [21]. DMD is an optomechanical device that features an array of microscopic mirrors which can be individually tilted to "on" and "off" positions to create an image. The mirrors represent one pixel of the image, and their size determines the resolution. Upon finalising the green body shaping the part is removed from the building platform, cleaned from any residual slurry and subjected to debinding and sintering process to obtain the final dense part. Even within a specific AM group, sub-category differences exist between specific approaches. For instance, in the DLP technology, in the bottom-up process the light is placed underneath the building platform, and in the top-down, the light is placed on top of the building platform [22]. The main advantages and drawbacks of the two approaches are summarised in Table 2.2. The parts manufactured by the bottom-up technique have more defined details with better precision, in comparison with the top-up approach. The challenges with the bottom-up approach include the periodic introduction of stresses and deformation into the part through the process of part detachment from vat or tape/foil [22].

Table 2.2 Summary of advantages and drawbacks of the DLP approaches [22]

	Top-down	**Bottom-up**
Advantages	No stresses are generated in the part No shape and dimensions limitations	Less material is needed The final surface is smoother Easier to obtain complicated parts
Drawbacks	The vat needs to be filled with resin Polymerisation inhibition due to oxygen The thickness of the cured layer is not precise or constant Components with high accuracy and fine details are hard to obtain	Periodic introduction of stresses and deformations in the component Vacuum is created between the cured layer and fresh layer for which a force is needed to pull the product The objects built are subjected to gravitational force

These deformations could be detrimental for parts with fine structures and could lead to failure during printing or deformations during the thermal treatment so the printing parameters must be strictly controlled. Processing of bulk components via bottom-up technique does not lead to difficulties; the main limitation is related to the length/width ratio of the component. The reliability of the process is reduced when the length is two times the width, increasing the probability of obtaining an incomplete printing job. Regardless of the configuration, during the printing process each image layer is projected onto a layer of photosensitive slurry which hardens when exposed to the light source, and the process is repeated until the green body is formed [23]. The described steps are depicted in Figure 2.1. Upon finalising the green body shaping the part is removed from the building platform, cleaned from any residual slurry and subjected to debinding and sintering process to obtain the final dense part.

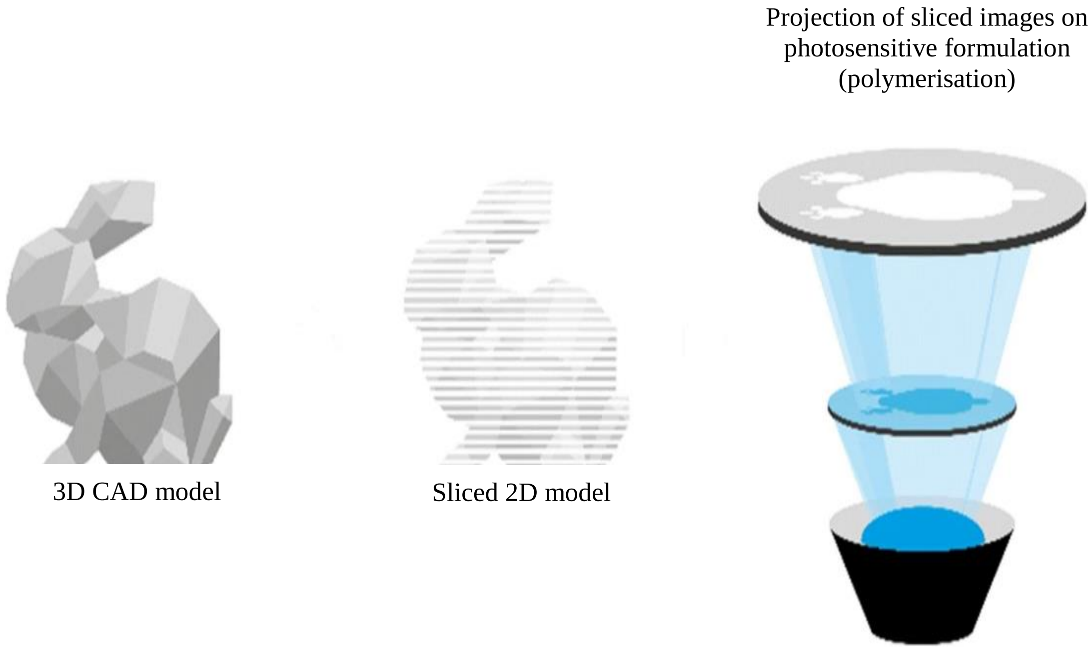

Figure 2.1 Three-dimensional model is sliced into two-dimensional layers. Each of the layers is projected on a photosensitive formulation which polymerises upon the light exposure [23]

2.1.3 Thermal postprocessing

The parts manufactured by DLP require thermal postprocessing to remove the resin components and achieve a dense part. This is the most crucial and challenging step of the manufacturing process, where cracks and defects can arise, compromising the mechanical properties of the final structure. The thermal postprocessing consists of thermal debinding and sintering (Figure 2.2). Organic components that constitute the ceramic slurry are first eliminated through the process of debinding by slowly heating the part to 600 °C. Slow heating rates and appropriate holding temperatures are necessary to avoid delamination, cracks, deformation or collapse caused by thermal stress from the decomposition of the organic components [24]. The process varies depending on the chemical composition of the resin, solid loading of the ceramic powder in the slurry and the geometrical dimensions of the part [25]. Once the part is free of organic components, the ceramic particles are consolidated by heating the debound part to a high temperature through the process of sintering. As a result, the density of the part increases and the part exhibits volumetric shrinkage [26].

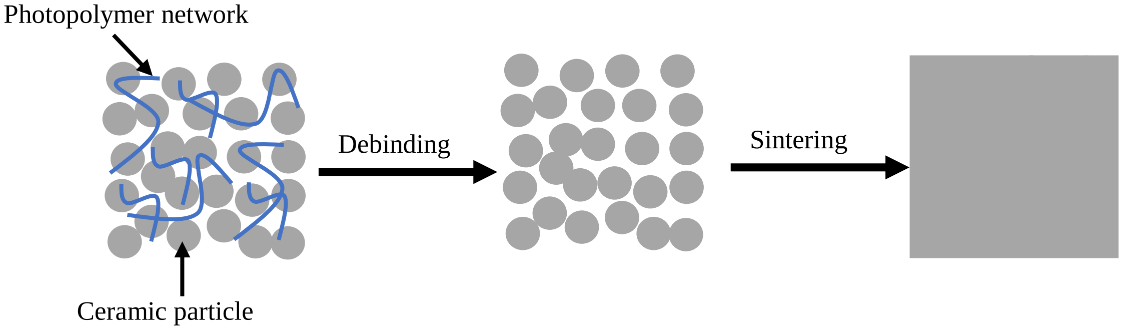

Figure 2.2 Steps of the thermal treatment after green body fabrication: drying, debinding and sintering. Adapted from [26]

2.1.4 Commercial DLP systems

Throughout the years, companies around the world commercialised the ceramic DLP technique. These include Admatec (The Netherlands), Lithoz (Austria), Tethon 3D (The USA), and Prodways (France). Commercial printers along with their main characteristics and price are presented in Table 2.3. There are several configurations available, including vat-based systems in which a tank is filled with photocurable slurry. In a tape casting system, such as the one from Admaflex 130, a doctor blade forms a thin layer of suspension on a tape of slurry which is pulled across the print area in-between the layers. For this research, Admaflex 130 was chosen for efficient feedstock management with virtually zero material waste, and an open platform that allows for the development of custom ceramic slurries. An illustration of the Admaflex 130 DLP printer based on a tape casting process with its main components is shown in Figure 2.3.

Table 2.3 Commercial DLP printers

Company	**Machine**	**Layer thickness, µm**	**X-Y resolution and pixel size**	**Printing area, mm**	**Price, £**	**Configuration**
Admatec	Admaflex 130 Admaflex 300	10-200	1920 x 1080 2560 x 1600 (35 µm-62.5 µm)	up to 260x220x500	90-110k	Tape casting system
Prodways	ProMaker V6000	25-150	1920x1080 (32 µm)	120x500x150	320k	Vat-based system
Lithoz	Cerafab 7500 Cerafab 8500	10-100	1920x1080 (40 µm) 1920x1060 (60 µm)	76x43x200 115x64x200	210-260k	Vat-based system
Tethon 3D	Bison 1000	25-100	1920 x 1080 (57 µm)	110x60x138	13k	Vat-based system

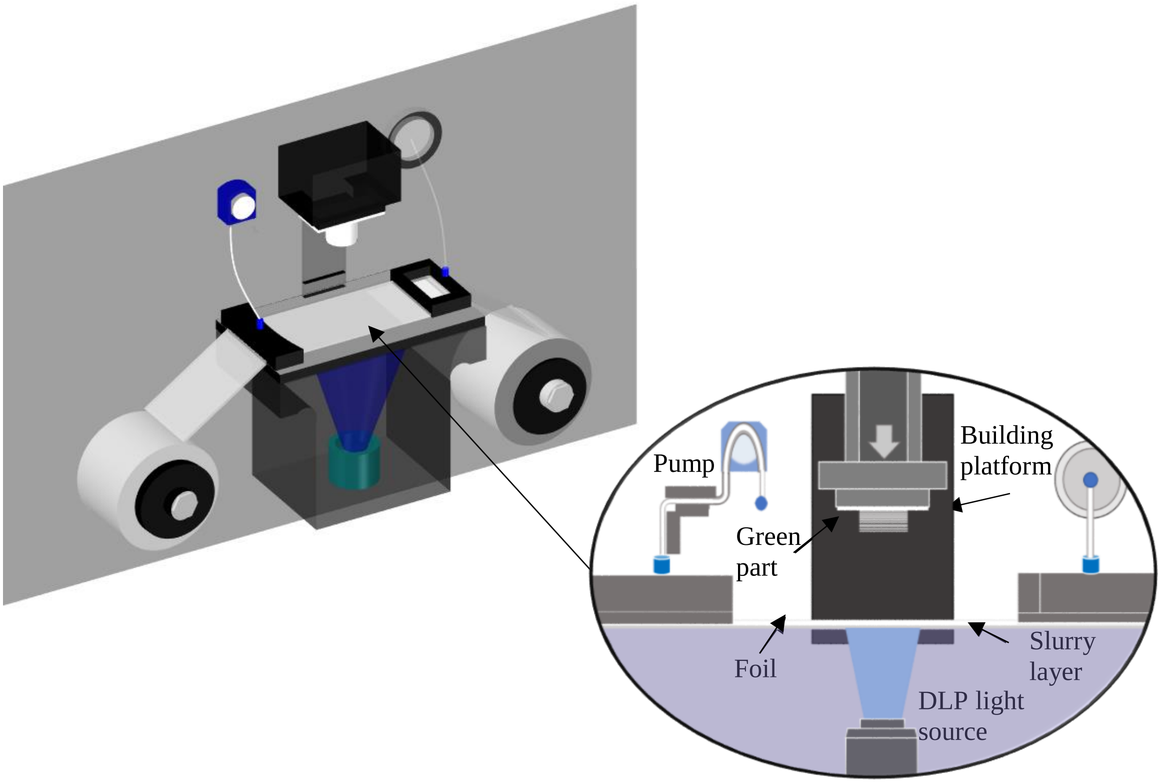

Figure 2.3 Schematic representation of a commercial tape casting DLP printer

2.2 Photopolymerisable ceramic slurries

2.2.1 Fundamental components of the ceramic slurry

Fundamental components of the ceramic slurry include organic resin, ceramic powder, and photoinitiator (Figure 2.4). A typical organic resin is composed of monomers, oligomers, prepolymers, dilutants, and various additives (inhibitors and UV absorbers). Dilutants serve as viscosity and refractive index modifiers. Inhibitors and UV absorbers can be added to control the scattering and cure depth [27]. The number of functional groups (mono-, di-, tri-, tetra-) of the monomer affects the property of the cured structures. Curing of monofunctional monomers results in entangled linear polymers. On the other hand, curing multifunctional monomers generates cross-linked polymer networks resulting in a mechanically tough cured body [14].

Photoinitiator transforms the photolytic energy into reactive species (free radicals, cations or anions) that target the functional groups of monomers and oligomers [28]. Acrylates and methacrylates are used in free-radical photopolymerisation [27]. Commonly employed acrylates include 1,6-hexanediol diacrylate (HDDA) [18,29,30], tripropylene glycol diacrylate (TPGDA) [31] or polyethylene glycol diacrylate (PEGDA) [32].

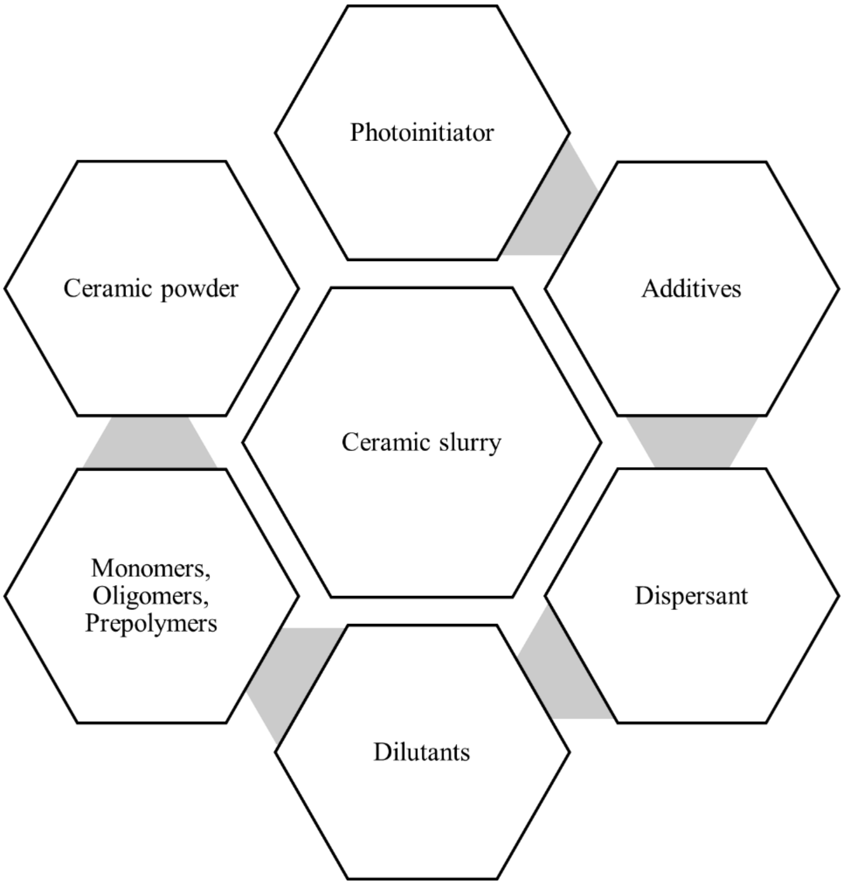

Figure 2.4 Main components of the ceramic slurry

Free-radical polymerisation occurs in three steps: initiation, propagation and termination. In the initial step, the formed radicals (Equation 2.1) attack the monomers/oligomers which form reactive polymer chains (Equation 2.2).

$$I + h\nu \rightarrow 2R \bullet \qquad \text{Equation 2.1}$$

$$R\bullet + M \rightarrow RM\bullet \qquad \text{Equation 2.2}$$

During propagation, the polymer chains start crosslinking (Equation 2.3).

$$RM_n\bullet + M \rightarrow RM_{n+1}\bullet \qquad \text{Equation 2.3}$$

The termination step is the final stage of free-radical polymerisation, where reactive polymer chains combine (Equation 2.4), disproportionate (Equation 2.5) and form a nonreactive polymer molecule (Equation 2.6) [28].

$$RM_n\bullet + RM_p\bullet \rightarrow RM_{n+p}R \qquad \text{Equation 2.4}$$

$$RM_n\bullet + RM_p\bullet \rightarrow RM_n + RM_p \qquad \text{Equation 2.5}$$

$$RM_n\bullet + Z \rightarrow RM_nZ \qquad \text{Equation 2.6}$$

The function of the dispersant is to facilitate the dispersion of hydrophilic ceramic particles in the hydrophobic resin. The type and amount of the dispersant should be carefully selected for each organic resin and powder system, and this is usually done based on the method of trial and error [33]. Li et al. [33] demonstrated that there is an optimum point of dispersant concentration that results in the lowest viscosity; when the dispersant concentration exceeds the optimum dose, the free dispersant molecules between the particles cause bridging flocculation, which ultimately increases the viscosity. The dispersion of the ceramic particles into a photopolymerisable resin can be achieved by either directly incorporating the as-received ceramic powder [34–37], or by pre-treating the surface of the ceramic particles with a dispersant beforehand [32,38]. There is no clear indication of the optimal way of preparation and there is a lack of evidence of how various preparation techniques influence the photopolymerisation behaviour or rheology.

2.2.2 Rheological behaviour of ceramic slurries

For a ceramic slurry to be considered as “printable”, tuning of the rheology is critical. The rheology of the ceramic slurry affects the green part quality and resolution [39]. Achievement of a minimum of 40 vol% of ceramic particles in the slurry is advantageous and desired to enhance the green strength and to decrease the sintering shrinkage of the manufactured parts [29]. For parts with fine geometries, low-viscosity slurries are preferred to avoid high forces during the detachment of the cured layer. Schwarzer et al. [40] printed various lattice geometries with features of 0.50 mm with slurries of various viscosities and solid fractions (42-49 vol%). They reported that a low viscosity slurry was needed to produce final components of high resolution and high-quality. It is possible (although challenging) to obtain parts with ceramic slurries containing a low solid fraction of ceramic powder. Shuai et al. [41] manufactured lattice structures from Al_2O_3 with a strut diameter of 0.17 mm with relatively low solid loading of the ceramic particles (52 wt%). To obtain crack-free parts, they had to ensure strict control of the debinding and sintering processes. Similarly, Guo et al. [42] manufactured lattice structures with a strut diameter of 0.20 mm from TiO_2 slurry with ceramic loading of 30 wt%. Their parts exhibited over 50% shrinkage after debinding and sintering due to the low solid loading of the ceramic material.

The rheological behaviour of the ceramic slurry is strongly affected by the ceramic powder (particle size, particle distribution, particle shape and volumetric loading), dispersant, and the organic components of the resin [39]. To achieve homogeneous recoating and prevent sedimentation of the ceramic particles, the desired behaviour of the ceramic slurries for slurry polymerisation techniques in the range of the recoating system shear rates is non-Newtonian behaviour characterised by shear thinning (Figure 2.5) [39]. In shear thinning slurries, viscosity decreases with increasing shear rate where the particles are rearranged from the equilibrium and become more organised in the flow.

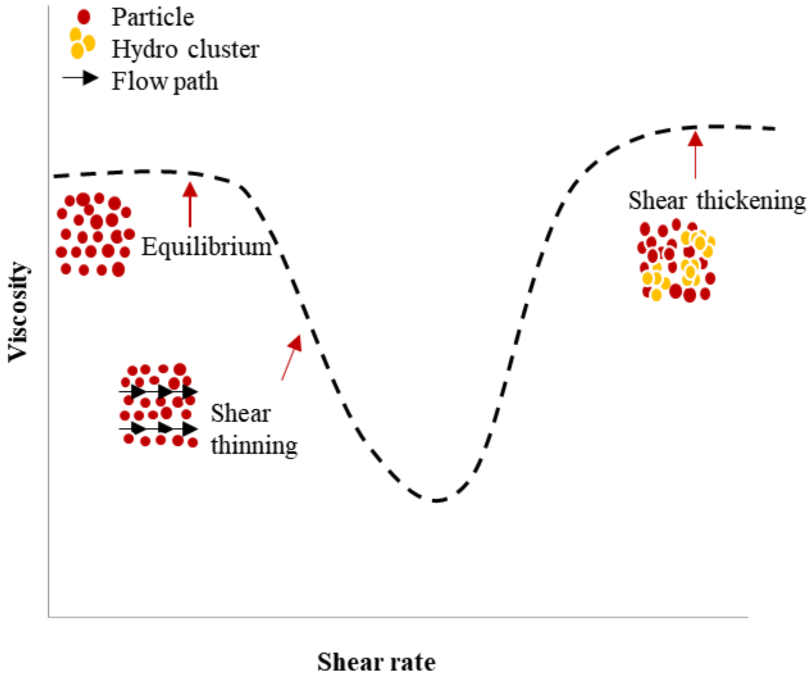

Figure 2.5 Comparison of viscosity curves: shear thinning and shear thickening liquids

The opposite happens when the slurry shear thickens. It is typically observed in suspensions where the ceramic powder is not effectively dispersed in the resin, or when the loading of the particles is very high. In this case, hydro clusters and jamming occur and cause an increase in the viscosity [43]. Shear thickening behaviour characterised by a rise in viscosity with increasing shear rate should be avoided in the working shear rate range of the printer.

It is necessary to adapt the viscosity of the ceramic slurry to the range suitable for the specific photopolymer-based printer. The low viscosity of 3 Pa·s at the shear rate of 10 s^{-1} is commonly considered a rough criterion in tailoring ceramic suspensions for vat-based printers [48]. Nowadays, improvements in coating systems allow ceramic slurries of much higher viscosity. For instance, Admaflex 130 is specifically designed to print slurries with a broad viscosity range, where a tape casting method with rotating foil is used to spread a fresh slurry layer. The recommended rheology of the suspension for Admaflex technology is a shear thinning behaviour with a dynamic viscosity below 10 Pa·s for shear rates from 10 to 300 s^{-1} [43].

2.2.3 Cure depth, scattering and printing accuracy

Cure depth ($\mathrm{C_d}$) defines the maximum thickness of the solidified layer at which polymerisation occurs in the building direction (Figure 2.6). The cure depth can be related to attenuation of light, applied energy dose (E) and critical energy dose ($\mathrm{E_c}$) by Jacobs's equation derived from Beer-Lambert law of absorption (Equation 2.7) [20]:

$$\mathrm{C_d} = \mathrm{D_p} \ln\left(\frac{\mathrm{E}}{\mathrm{E_c}}\right) \qquad \text{Equation 2.7}$$

$\mathrm{D_p}$ is the slurry penetration depth, essentially describing how sensitive the suspension is to light. Higher $\mathrm{D_p}$ results in a more sensitive suspension and a greater cure depth. The constants $\mathrm{D_p}$ and $\mathrm{E_c}$ are dependent on the slurry composition, initiator concentration, and inhibitor concentration.

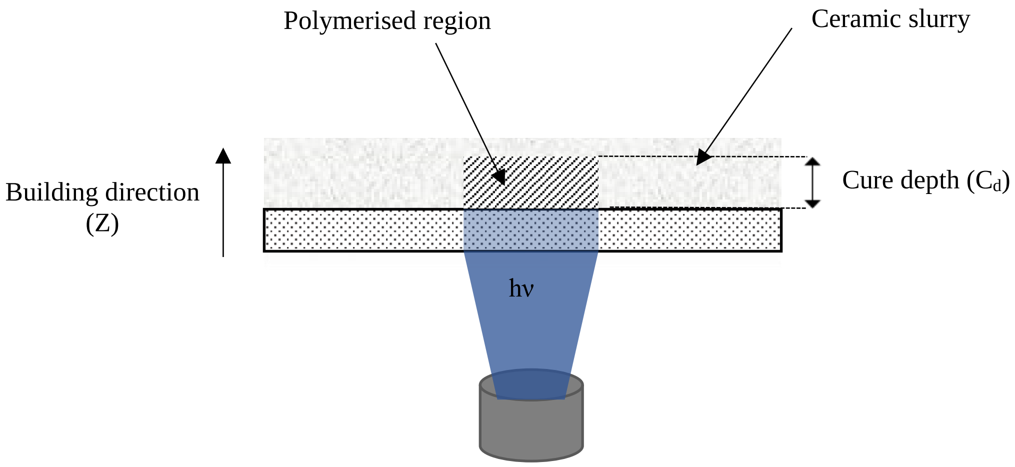

Figure 2.6 Schematic illustration of cure depth

The transition from a liquid to a solid phase occurs only when the light exposure exceeds the critical value. The cure depth is associated with the ceramic particle size, volume fraction, light exposure power, and the materials' refraction index [20]. The working curve of a specific slurry can be determined by plotting the effect of E on C_d as shown in Figure 2.7. The calculation of the constants D_p and E_c are then accomplished by finding the best fit of a logarithmic function to the data, where the gradient of the function is equivalent to D_p and the point at which the function is equal to zero is E_c.

The scattering effect is another factor to consider in the photopolymerisation of ceramic suspensions. When the ceramic powder is combined with resin, it causes light scattering, which reduces light penetration in the Z direction (cure depth) and initiates reactions in the X and Y directions, resulting in a broadening of part dimensions [36]. This effect is related to the disparity in refractive indices, Δn, of the suspending monomer resin solution and the ceramic particles. The higher the value of Δn, the more light is dispersed to the sides and less energy is propagated into the building direction [44].

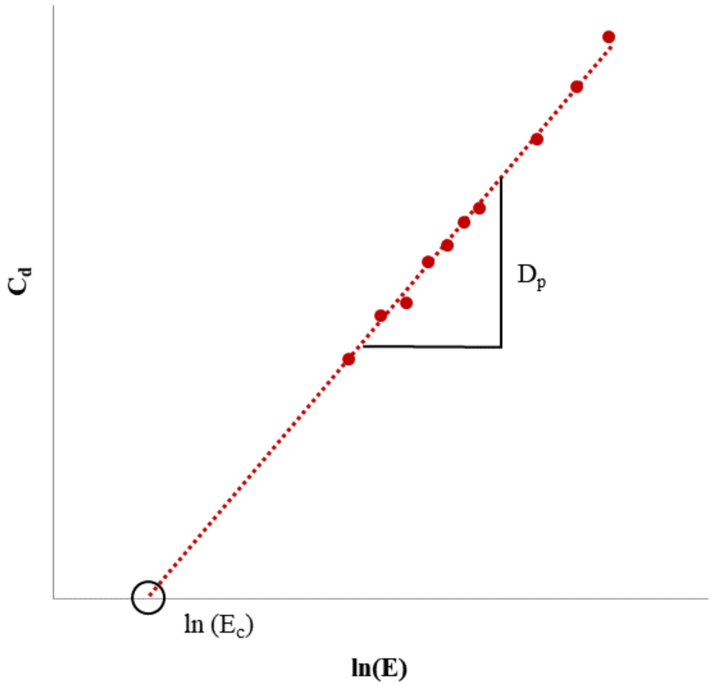

Figure 2.7 Example of a working curve of a ceramic slurry

Higher cure depth can be achieved by using a photocurable resin with a refractive index as close to that of the ceramic powder as possible. The broadening behaviour may be approximated with a quasi-Beer-Lambert relationship between the excess cure width (C_w) and the energy dose:

$$C_w = D_w \ln\left(\frac{E}{E_w}\right) \qquad \text{Equation 2.8}$$

Broadening parameters D_w (width sensitivity) and E_w (critical energy dose) are affected by the scattering of the light, the absorption and the critical energy dose of the resin [45].

Broadening depth (B_d) can then be calculated by:

$$B_d = D_p \ln\left(\frac{E_w}{E_c}\right) \qquad \text{Equation 2.9}$$

Broadening depth is the maximum cure depth that may be obtained before curing in width in X and Y directions starts. To achieve components with high accuracy, the composition should ideally be tuned for maximum broadening depth [46]. Investigation of the accuracy in manufacturing processes generally includes bulk constructions, walls, holes or two-dimensional (2D) squares [47,48]. Rudraraju [46] studied the accuracy of 2D squares when exposed to DLP irradiation. The accuracy of 2D squares smaller than 0.80 mm was found to increase with the increase of the feature size. Similarly, Mitteramskogler et al. [36] evaluated the influence of exposed area of 2D squares when varying exposure time with constant light intensity. Their results showed a decrease in accuracy with the increase of exposure time and exposed area. Conti et al. [48] investigated energy dose and layer height-related accuracy for simple 3D parts, such as holes, gaps, and walls. They reported divergence from the designed dimensions for holes up to 0.50 mm. No trend was found for deviation of gap width and wall thickness.

Since the DLP technology for manufacturing ceramic materials is relatively new, tailoring the rheology and the photopolymerisation behaviour of ceramic suspensions and a systematic study on the influence of the printing parameters on the broadening behaviour and printing accuracy are necessary to understand how to achieve innovative monolith catalysts with fine features.

2.3 The structure of the monolith catalyst

Monolith catalyst is the key part of the catalytic converter, with its inert monolith substrate that can be ceramic or metallic, secondary support (washcoat) and catalytically active component(s) (Figure 2.8). The physical design and chemical features of the catalyst can have an impact on its low-temperature activity [49]. Modification of the physical design includes varying the dimensions, channel design, channel diameter, wall thickness or material. On the other hand, chemical properties include washcoat composition variation, changing the active component concentration in the washcoat along the catalyst length (axial gradients/zone coating), or depositing numerous washcoats sequentially on the monolith forming layers (radial gradients/layers) [50]. In this thesis, the emphasis is placed on the physical design of the monolith catalyst. For an easier understanding of the terms used throughout the thesis, the individual components of the monolith catalyst will be discussed in the next three sections.

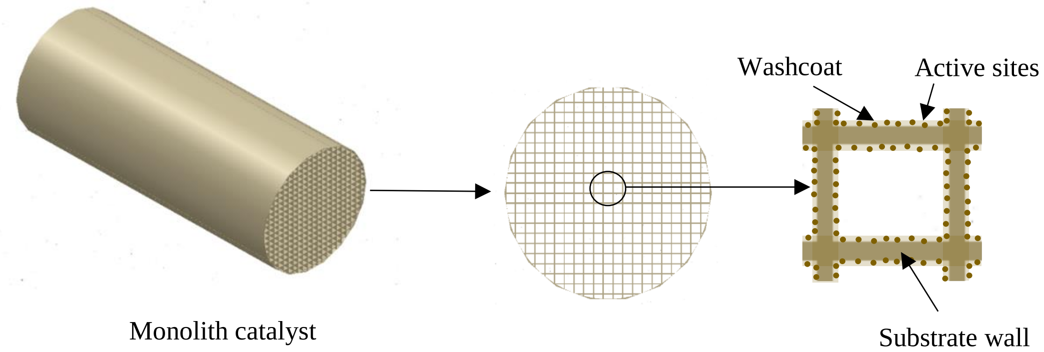

Figure 2.8 Schematic representation of the individual components of a monolith catalyst

2.3.1 Monolith substrate

The primary purpose of the substrate is to provide a large physical surface for the application of a catalytically active washcoat. Perhaps the most attractive application of the monolith is in the automotive industry, where the monolithic reactors (honeycombs) are crucial for emissions abatement in the aftertreatment systems. Early substrates employed in the aftertreatment systems were pellets in a canister or a packed bed arrangement. Honeycomb substrates were designed as an alternative to fixed bed pelleted substrates to overcome their high backpressure and low mechanical strength [51]. They feature a high density of parallel channels divided by thin walls that allow gases to pass through and interact with the active catalyst that is adhered to the channel walls. The shape and size of the channels, cell density and wall thickness should be carefully chosen to suit the requirements of the process and are vastly dependent on the manufacturing abilities of the extrusion process. The available geometric shapes of the extruded honeycomb channels are circular, square, triangular, or hexagonal [52–54]. The square channel extruded honeycomb design is the most common one for the exhaust aftertreatment systems. In the automotive exhaust aftertreatment, the substrate must cope with a wide range of operating conditions, hence the choice of the base material and structure is of high importance [55]. The base material of the substrate must be compatible with the washcoat to prevent detachment of the active material from the channel walls in harsh exhaust gas conditions. More flexibility in the channel design with higher cell density and lower wall thickness can be achieved by employing metallic substrates manufactured by corrugation of thin metal sheets [55]. The common materials used for the production of metallic monoliths include nickel, FeCr alloy containing aluminium, 304 Austenitic stainless steel, and aluminium foams [52]. Although metallic substrates have higher mechanical resistance and thermal conductivity than ceramic ones, adherence of the catalytic coating is more challenging due to the differences in thermal expansions between metallic substrates and washcoat. Furthermore, metallic substrate can melt at temperatures over 1300 °C [56].

Ceramic foams are another class of monolith substrates offering enhanced mass transfer due to improved gas-solid contact. Ceramic foams are mostly manufactured by replication technique where a polymer foam is used as a template, or by direct foaming where gas is dispersed in the form of bubbles into a ceramic slurry resulting in a randomised foam structure [57].

2.3.2 Washcoat

Uncoated monolith substrate is chemically inert and must be functionalised with a catalyst before use in the aftertreatment. Direct application of the catalyst onto the substrate would not result in a highly efficient catalytic converter since the inherent specific surface area of the substrate is low [58]. Washcoat increases the specific surface area, provides a foundation for dispersion of the noble metals and improves the catalyst adhesion [52]. The most common compounds for washcoats are high surface area oxides, such as γ-alumina, silica, zeolites, TiO_2, vanadium, SnO_2. Composite oxide materials (i.e. CeO_2-ZrO_2-La_2O_3- PrO_2-Al_2O_3) [59] or mixed oxides (Al_2O_3/CeO_2/ZrO_2) that improve thermal stability and reduce the light-off temperature can be employed as well [60]. By far the most widely used inorganic carrier of catalysts is high surface area (80-250 m^2g^{-1}) gamma-alumina (γ-Al_2O_3), generated by dehydration of aluminium hydroxides and oxide hydroxides precursors at temperatures from 500 °C to 800 °C [61]. The methods that are regularly employed for the application of high surface area washcoats to the inert substrates are sol-gel, slurry coating or colloidal coating. The coated structural support is then subjected to heat treatments after the washcoat deposition procedure to consolidate the washcoated layer. Care must be taken by controlling the concentration of slurry, calcination time and temperature to achieve a well-adhered washcoat layer with a layer thickness of 1-100 µm [52,61]. For instance, if the substrate is washcoated with γ-Al_2O_3, it is critical to keep the calcination temperature below 750 °C to avoid phase transition to low surface area Al_2O_3 phase and ensure that the washcoat layer has roughly the same specific surface area as the original γ-Al_2O_3 [61].

2.3.3 Catalytic layer

While a washcoat provides a high surface area for chemical reactions, a catalyst is a substance dispersed over the washcoat, that lowers the activation energy of a chemical reaction and thus increases the rate of reaction. For automotive catalysts, Platinum Group Metals (PGMs) have been identified as the most effective class of active components for both oxidation and reduction reactions. Novel PGM-free or reduced PGM coatings have been researched over the years to reduce costs, but are not frequently utilised [62,63]. Platinum (Pt), palladium (Pd) and rhodium (Rh) are the most common PGM coatings for the aftertreatment catalysts. Pt and Pd are used for oxidation reactions in TWC while Rh is necessary for the reduction component of the TWC [64]. For the DOC, Pt, Pd or bimetallic combination of Pt-Pd are suitable for oxidation reactions [65]. The use of a bimetallic Pt-Pd for DOC is attractive as they provide superior activity for CO and hydrocarbon oxidation, and oxidise NO at a lower temperature due to the synergetic effect of the formation of a Pd-Pt alloy [66]. Furthermore, bimetallic catalysts are more resistant to thermal degradation of the catalyst, as well as sulphur and lead poisoning [67]. Catalytic activation of the washcoat support can be performed before washcoating or after washcoating has been applied to the substrate by methods such as incipient wetness impregnation, dry impregnation or selective electrostatic adsorption [61,68]. For this, aqueous solutions of soluble compounds or complexes of the platinum group metals are used, such as palladium nitrate, tetraamine palladium nitrate, platinum chloride, tetraamine platinum acetate, and platinum nitrate among others [69]. Alternatively, for extruded ceramic monolith catalysts, PGM compounds can be combined with the ceramic paste and extruded in a single part. In that case, the active phase is located both on the external wall and within the walls of the monolith [61,70]. Typically, the loading of noble metals for aftertreatment catalysts vary from 30 to 120 g/ft^3 [65,71]. The prepared catalysts are characterised by standard characterisation methods. These include: N_2-physisorption according to the Brunauer-Emmett-Teller (BET) method for evaluating the catalyst specific surface area, X-ray Diffraction (XRD) to determine the structural properties of the catalytic materials before and after the catalyst impregnation, Scanning Electron Microscopy (SEM)/ Energy-Dispersive X-ray Spectroscopy (EDX or EDS) to give information on the morphology of materials and Transmission Electron Microscope (TEM) to determine the size and shape of the catalytic particles [64,72].

Since the available extrusion dies control the final geometric shape of the monolith substrate, there is minimal flexibility in terms of advancement in the channel design to promote the catalytic activity if relying on conventional manufacturing methods. Choice of the washcoat and catalytic formulation is important to promote the desired reactions and allow for high reactivity at low temperatures. Based on the reviewed literature, a bimetallic platinum/palladium catalyst dispersed over high surface gamma-alumina oxide was chosen for the research work presented in this thesis.

2.4 Performance of the conventional monolith catalyst

2.4.1 Thermal performance

Monolithic substrates must be designed in such a way that they can provide a large surface area for catalytic reactions, low backpressure, and rapid light-off. It is crucial to obtain satisfactory catalyst performance as quickly as possible at the lowest feasible temperature to rapidly increase the temperature of the catalyst to effectively reduce emissions [49].

The temperature within the honeycomb catalyst depends on various parameters; convection from the exhaust gas to the solid, radial conduction through channel walls, heat loss to the surroundings and heat generated by the exothermic reactions (only when the reactions occur) [73]. In the first minutes of the engine operation, the exhaust gas passes through the honeycomb channels with a relatively low flow rate and exhaust gas temperature, heating the catalyst relatively slowly. Incomplete combustion during these conditions over the honeycomb catalyst results in significantly high emissions [74]. The key performance criterion of the honeycomb catalyst is the light-off temperature. Only after the light-off temperature is reached can the catalyst be fully operational and successfully convert the pollutants. Variables affecting the light-off temperature include mass flow rate, temperature of the exhaust gas, the rate at which the inlet gas temperature increases, effective conductivity of the monolith, composition of the catalyst, age of the catalyst, flow maldistribution within the monolith and bulk density of the monolith [75]. Besides, it is not uncommon for the temperature in the individual channels to vary considerably [76]. This implies that the light-off might occur in different channels at different times since the contact times between the pollutants and the catalyst could fluctuate from channel to channel. Multiple engine start-and-stops, typical in hybrid vehicles, could produce high emissions, especially if the temperature of the catalyst drops below the light-off temperature [77].

Lefort et al. [78] investigated various wall thicknesses and cell density combinations in square-channelled monolith catalysts to improve the thermal response of the catalyst. The results revealed that a high cell density/thin wall catalyst was the best solution for improving the light-off performance. Unsurprisingly, the proposed catalyst also entailed an increase in pressure losses, which may result in a reduction of peak engine power and reduction in conversion efficiency during the deceleration stages due to rapid cooling.

2.4.2 Pressure loss and flow uniformity

The pressure loss of the substrates is strongly influenced by the channel design, geometry, length, and the channel diameter [54].

Marsh et al. [79] reported that although the catalysts with higher cell densities exhibited higher surface area and better mass transfer, the decrease in the size of the channels increases the backpressure.

Amirnordin et al. [54] numerically studied the influence of the cell shape on hydraulic performance. The results revealed that a hexagonal-shaped cell outperformed a square-shaped cell in terms of lower backpressure. On the other hand, the square-shaped cell had a higher surface area than the hexagonal cell (Figure 2.9).

Furthermore, flow uniformity and flow distribution are critical in the aftertreatment devices since they influence the conversion efficiency and durability of the catalyst.

Jeong et al. [80] observed that the core area of the inlet face of the honeycomb receives more than 50% of the incoming flow with a non-uniform radial velocity profile throughout the honeycomb. Attempts to improve the flow distribution and decrease the pressure drop inside the honeycomb catalysts included shaping the inlet face of the monolith to form a cone or a parabola [81] or introducing monolith substrates with variable cell densities [80].

Innovative ceramic substrates with a larger cell density in the centre and a lower cell density towards the substrate's edge were presented in 2017, bringing the radial variable cell size concept to reality [82].

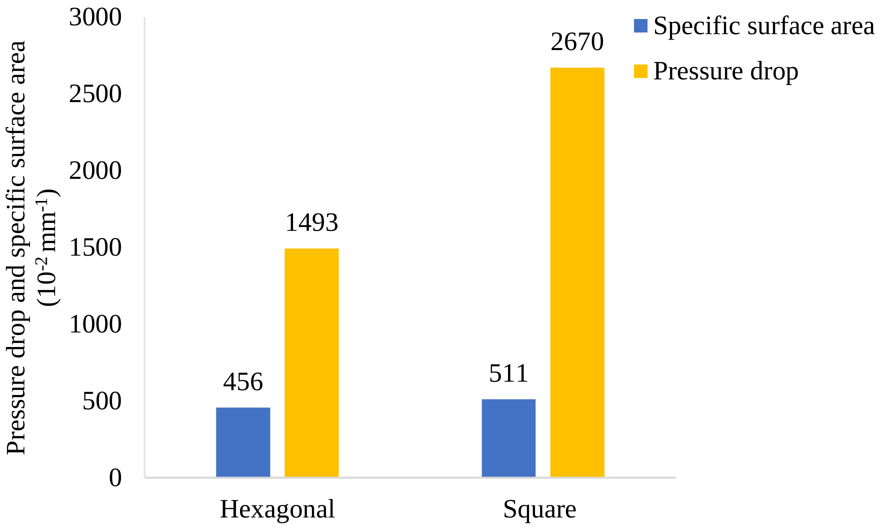

Figure 2.9 Comparison between the hexagonal and the square cells of monolith substrates with 900 CPSI and 0.06 mm wall thickness. Adapted from [54]

2.4.3 Limitations of the conventional honeycomb design

In a typical configuration of a catalytic converter, a monolith catalyst (i.e. honeycomb) is housed in a stainless steel can connected to inlet and outlet pipes with a diverging diffuser and a converging cone (Figure 2.10). The incoming flow from the inlet pipe through the diverging diffuser is turbulent, but once it enters the small honeycomb channels it quickly becomes laminar [83]. The main disadvantage of the honeycomb catalyst is the laminar flow regime within the straight, flow-through channels. In the laminar flow regime, the mass transfer rate of the reactants from the bulk flow to the active sites positioned on the channel walls is slow [84–87]. The pollutants concentrated in the centre of the channel have difficulty reaching the active sites located on the channel walls. Additionally, non-uniform flow distribution inside the honeycomb structure results in a partial utilisation of the catalyst and leads to a shorter catalyst lifetime [76]. Potential improvements in hydraulic and thermal performance imply a change in the monolith catalyst design, flow distribution and the flow regime inside the catalyst.

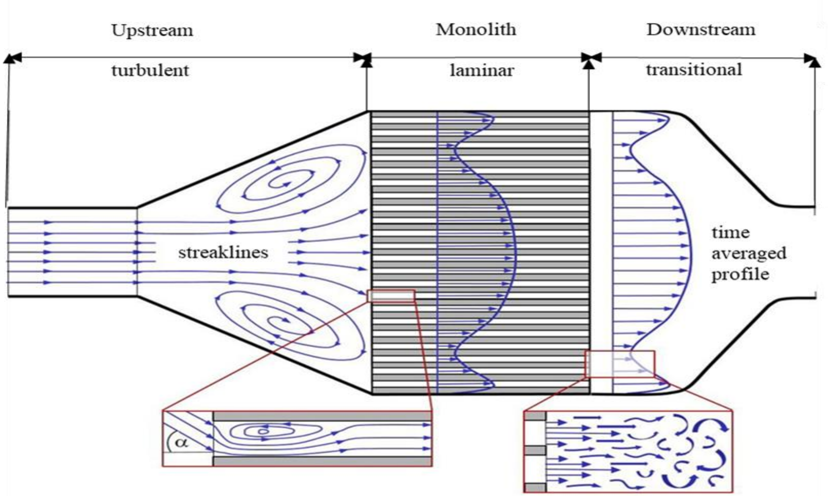

Figure 2.10 Schematic representation of the flow in a typical catalyst assembly. Adapted from [48]

2.4.4 Strategies to enhance the catalytic efficiency and simplify the aftertreatment arrangement

Various strategies to increase the catalytic efficiency and achieve early catalyst light-off have been investigated throughout the years. These include adjustment of the operational engine parameters (retarded ignition timing, variable valve timing, extra combustion devices, higher idle speed and load, air/fuel ratio adjustment) and catalyst heating methods independent of the engine parameters (aftertreatment system layout, modifications of the monolith physical or chemical properties, reformers, burners, thermal insulation methods, electrical heating, phase changing materials) [88]. One of a promising alternative strategies for improving engine performance and enhance emissions conversion efficiencies is addition of hydrogen into the exhaust stream [89,90].

Theinnoi et al. [91] investigated the impact of hydrogen addition on the performance of a commercial 400 CPSI DOC. The hydrogen presence enhanced hydrocarbon and carbon monoxide oxidation at lower temperatures and promoted oxidation of NO to NO_2.

Similarly, Herreros et al. [65] investigated the effect of hydrogen addition on a conventional square channel DOC performance with concentrations ranging from 500 to 8000 ppm. Their results suggest the addition of only 1000 ppm of H_2 has a favourable effect on carbon monoxide, hydrocarbons and nitrogen oxide conversion efficiency.

Prasad et al. [92] studied the performance of methanol fuel in combination with hydrogen for the IC engines. Their findings suggested a substantial improvement in performance and reduction in the overall emissions.

Tsolakis et al. [93] incorporated a reforming reactor into the exhaust system of a diesel engine and demonstrated that 16% of hydrogen was produced with strict parameter control, without the use of externally supplied heat source, air or steam. Hydrogen addition into the exhaust gas, upstream of SCR in the presence of unburnt or injected hydrocarbons improved low-temperature NO_x conversion.

While the benefits of H_2 are apparent for the conventional flow-through honeycomb designs, the effect of the hydrogen-enriched exhaust gas in combination with advanced monolith catalyst designs has not been reported yet.

Regarding modifications of the monolith physical properties, dual-catalyst aftertreatment systems have been proposed to overcome the compromise between surface area, pressure drop and light-off.

Flörchinger et al. [94] suggested incorporation of a dual-catalyst system by placing a low geometric surface area catalyst in front, to keep the heat in the system and allow low pressure drop, followed by a rear higher geometric surface area catalyst to offer high surface area, while still keeping the heat in the system.

Lefort et al. [78] investigated a dual-catalyst configuration composed of one catalyst for quick light-off with low thermal mass and a second one with a higher thermal mass to store heat to allow for higher overall system temperatures to enhance catalyst conversion efficiencies. The dual-catalyst configuration demonstrated only a slight improvement over the reference catalyst, concluding a single catalyst with a cell density of 400 CPSI and wall thickness of 0.10 mm was a better compromise regarding conversion efficiency, pressure drop, manufacturing, and cost of the washcoating material.

Furthermore, as current devices in the aftertreatment systems are dedicated to a single type of emission control, various strategies to reduce the number of individual catalytic systems (e.g. by merging their functions) in the exhaust aftertreatment to provide improved catalytic efficiency have been proposed in the past. Solutions to simplify the aftertreatment arrangement to decrease the volume and weight of the aftertreatment system, have been suggested in the past. For example, an all-in-one Four-Way Catalytic Converter (FWCC) combines oxidation-reduction catalysts to simultaneously remove carbon monoxide, hydrocarbons, particulate matter, and nitrogen oxides. The FWCC is an efficient solution to the limited space capacity in aftertreatment. However, the complex multi-phase reaction processes where the species interact with each other and compete for active sites affect the catalytic efficiency. Modification of the catalyst chemical properties can include, for instance, layering of active washcoats on top of one another, or zoning, where the active component concentration in the washcoat changes along the axial length. For example, Hazlett et al. [16] showed that Pt-Pd bimetallic catalysts can be zoned axially along the monolith in varying ratios to increase NO oxidation selectivity by promoting CO oxidation at the front with a larger quantity of Pd, leaving extra volume for NO oxidation along the length with higher content of Pt. Layering and zoning Fe/ZSM-5 and Cu/zeolite on an SCR catalyst can improve SCR efficiency taking the advantage of the Cu catalyst's better NO_x reduction performance at low temperatures, while the Fe catalyst performs better at high temperatures.

Incorporation of a convoluted flow path to alter the flow regime from laminar to turbulent, or introducing turbulence before the catalyst are auspicious methods to increase the catalytic efficiency. More flexible conventional manufacturing capabilities have enabled innovations in metallic catalyst designs. For instance, an increase of local turbulence is possible by introducing bumps on channel walls (Figure 2.11a) [95], employing a perforated foil (Figure 2.11b) or a longitudinal structure (Figure 2.11c) [86]. The disadvantages of the proposed designs are increased pressure drop, high cost of manufacture and challenging canning process.

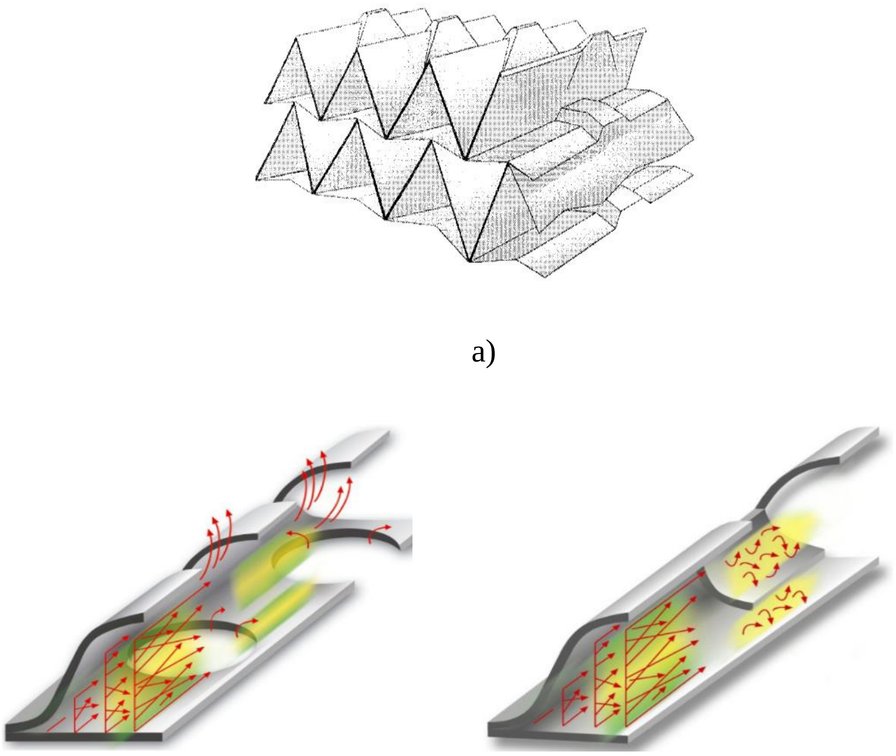

a)

b) c)

Figure 2.11 a) Channel walls with bumps [95] b) Perforated foil structure [86] c) Longitudinal structure [86]

Ceramic foam-based catalysts were found to have enhanced conversion efficiency in comparison with honeycombs due to their high surface area/volume ratio and improved gas-solid contact, but at the expense of an extremely variable pressure drop due to the random structures [96]. This has limited their use in the automotive industry. Properties of foams have been studied in the past using numerical simulations. Sinn et al. [97] investigated heat flow as well as temperature distributions in open-cell ceramic foam in a tubular reactor with constant wall temperature by coupling conjugate heat transfer and heat production. Bracconi et al. [98] coupled numerical and experimental approaches to assess fluid dynamics in virtually-generated foam models and 3D printed replicas. To ease the computational load, the foam structures were also represented with regular cells, such as Kelvin cells [96].

Recently, researchers found regular three-dimensional arrays of Kelvin lattice structures always demonstrated a better trade-off between mass transfer and pressure drop than the counterpart foams with uncontrollable structure [99]. These promising results prompted researchers to investigate the opportunity to employ regular lattice structures as catalyst substrates. Lattice structures are an appealing alternative to foams as their structure can be completely controlled using Computational Aided Design (CAD). Lattice structures, unlike foams, consist of an organised network of struts connected by nodes in a three-dimensional space. Nodally-connected diamond lattice structures have found their use in biomedical applications [100], oil sensing [101], optical applications [102] and heterogeneous catalysis [99,103] and show great potential for automotive catalyst supports. Monolithic catalyst substrates incorporating diamond lattice structures serve as inspiration for the design of advanced monolithic substrates focused on the application of ceramic additive technology in automotive aftertreatment in this research [103]. The innovative lattice supports may be able to overcome some of the limitations of the conventional honeycomb catalyst. Computational Fluid Dynamics (CFD) can be utilised to enhance their design through the study of the fluid dynamics and thermal characteristics in conjunction with additive manufacturing to provide a feasible method of advanced monolithic substrates fabrication. The application of ceramic AM technology for the development of ceramic monolithic catalysts is a relatively new concept and thus far the ceramic AM has seen limited application in the exhaust gas aftertreatment sector.

2.5 Experimental studies on the catalyst light-off

One of the methods to evaluate the catalyst activity is by measuring the conversion of the exhaust gas species as a function of temperature and plotting the conversion values as a function of temperature (light-off curve). For this, a laboratory-scale catalyst is placed in a specially built reactor placed in an electric furnace to regulate the temperature, with continuous mass flow of reactant gases. The inlet gas temperature is steadily increased and the input and output concentrations of the reactants are monitored to calculate the conversion of the reactants as result. The feed exhaust gas could be either fed from the engine as a result of fuel combustion or introduced as a synthetic gas mixture [104].

To assess the catalyst performance through light-off tests, Lefort et al. [104] used a 400 CPSI cordierite honeycomb monolith (Ø25.4 mm×H91.4 mm) with a wall thickness of 0.11 mm coated with 120 g/ft^3 Pt-Pd (weight ratio 1:1) on alumina and zeolite washcoat (2.6 g/in^3 loading) fed with genuine exhaust gas produced by a single-cylinder, direct injection, diesel engine. Their experiment was run in steady state at 1500 rpm and 40% load. The diesel engine was operated with different diesel fuels (diesel, rapeseed methyl ester, gas-to-liquid, propane/ diesel in a dual fuel combustion mode) to study the interaction of the exhaust gas species. The species conversion efficiencies (CO, CH species, and NO_x) were monitored during a heating temperature ramp of around 2 °C/min and an exhaust Gas Hourly Space Velocity (GHSV) of 35 000 h^{-1}. Their study provided methods for qualitatively predicting how effectively CO and various hydrocarbon species will be oxidised in various exhaust gas composition conditions.

Herreros et al. [65] studied the light-off behaviour of DOCs coated with Pt and Pt-Pd (1:1 weight ratio) catalysts with hydrogen addition. They have likewise used lab-scale DOC placed inside a bespoke mini-reactor designed to study the effects of catalyst performance under real diesel exhaust gas. The catalyst loading and the DOC dimensions were the same as in [104] and the catalyst was placed in a tubular furnace with a steady increase of the temperature to 400 °C with a heating temperature ramp of 2 °C/min under GHSV of 35 000 h^{-1}. In their study, the DOCs were thermally aged in a furnace at 500 °C to limit any potential physisorption or chemisorption effects. The engine was fed with ultra-low sulphur diesel fuel.

Concerning the lab-scale AM catalysts, Papetti et al. [99] studied the light-off behaviour of AM catalysts at constant GHSV (60 000 h^{-1}) and increasing furnace temperature with a heating ramp of 10°C/min up to 600 °C using synthetic C_3H_6 8% O_2 balanced with N_2. Hajimirzaee et al. [72] studied methane oxidation using feed that contained 5 vol% CH_4, 10 vol% O_2, 85 vol% He with GHSV of 400, 800 and 1200 h^{-1}. The studies on AM catalysts were performed on bench-top experimental rigs using synthetic gas. The downside of using synthetic feed gas was discussed in detail in work from Lefort et al. [104] highlighting the importance of utilising real exhaust gas to understand the interactions between the chemical species during light-off. This can aid in the design of the aftertreatment system to improve the pollutant removal. Since the subject of AM catalysts is very recent, most advancements on the catalyst functionalisation and performance testing are lab-scale, with structures in the range of only a few centimetres. For this purpose it was decided to use the approach from [104] and [65] to study the light-off behaviour of advanced monolithic catalysts in real exhaust gas conditions.

2.6 State-of-the-art in design and ceramic additive manufacturing of complex monolith catalysts for automotive aftertreatment applications

Two main strategies of design and manufacturing of advanced catalysts for various catalytic applications are found across the literature:

- AM of substrates which includes design of a template that contains a negative copy by 3D printing of a material that can be removed in the high-temperature heat treatment process (Figure 2.12a) [105,106]
- Direct AM of the monolithic substrates via ceramic AM technologies (Figure 2.12b) [12,72,99,107–109]

Parra-Cabrera et al. [110] provide an extensive overview of AM structured catalysts in chemical engineering and various catalytic technologies in their literature review. The most recent 3D printing innovations for catalytic applications are summarised in a review from Zhu et al. [111]. Industrial catalyst manufacturers, such as Johnson Matthey, utilise binder ceramic jetting to manufacture monolith beds that can be useful in filtration systems, adsorption processes or fixed-bed reactors.

Díaz-Marta et al. [109] prepared 3D printed SiO_2 monoliths via AM material extrusion process. The resulting catalysts consisted of cylinder structures with a rod diameter of 0.41 mm and rod spacing of 1 mm as shown in Figure 2.12b). After manufacturing, the samples were debinded, sintered and functionalised by a coating containing immobilized copper and palladium species for application in multicatalytic multicomponent reactions.

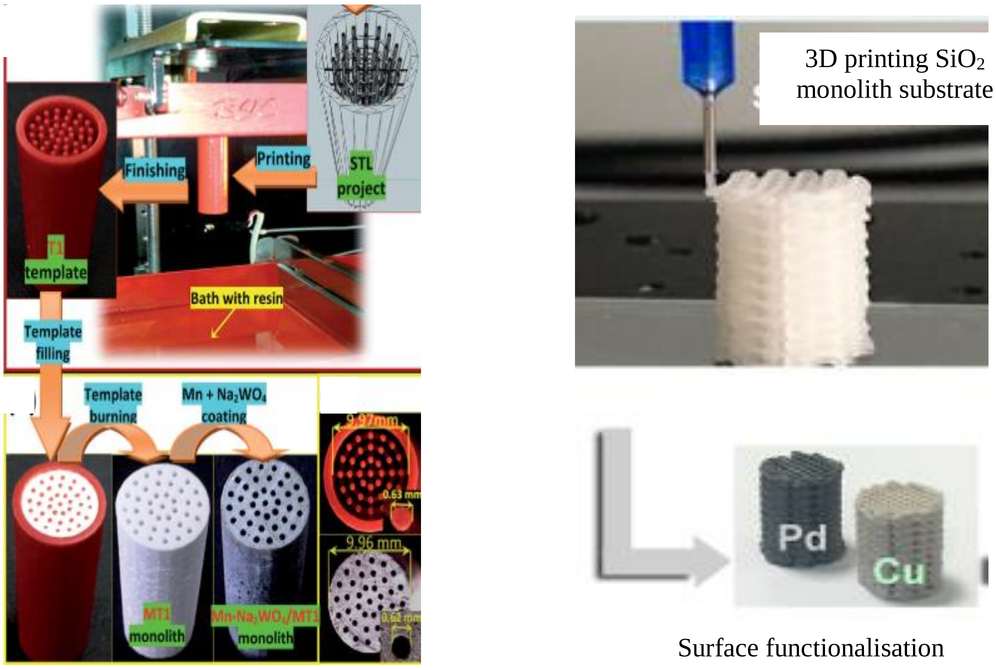

a) b)

Figure 2.12 Examples of a) 3D printing method using a 3D printed polymer template filled with α-Al_2O_3 paste, burning off the template and coating the monolith with active compounds [106] and b) Direct 3D printing method of a ceramic substrate and surface functionalisation with catalytically active materials [109]

Couck et al. [107] manufactured SAPO-34 zeolite cylinders with a diameter of 1 cm and a grid-like filling using material extrusion AM process with a nozzle diameter of 0.33 mm for use in CO_2 adsorption. The measured CO_2/N_2 separation selectivity was evaluated by comparing to the selectivity estimated by the Ideal Adsorbed Solution Theory. Due to very low adsorption, N_2 capacities were close to zero or slightly negative during the trials, implying that absolute selectivity values could not be established.

Ferrizz et al. [12] employed material extrusion AM process to manufacture various Al_2O_3 substrates with interconnected rods that were coated with Pt/γ-Al_2O_3 catalyst for catalytic combustion of natural gas. The 3D printed monoliths exhibited higher mass transfer efficiency, but also had high backpressure with more than an order of magnitude difference in pressure drop between the 3D printed samples and the honeycomb sample.

Papetti et al. [99] utilised vat photopolymerisation technique in 2018 to manufacture Al_2O_3 monolithic substrates (Figure 2.13a)). The design of the substrates was based on a rotated cubic cell. Additively manufactured lattices had a strut diameter of 0.60 mm and unit cell sizes of 3.0 and 4.0 mm. Due to the manufacturing limitations of the stereolithography approach used in their study, structures with strut diameters smaller than 0.50 mm were not possible to build. The AM substrates were coated with platinum dispersed over γ-Al_2O_3 and tested in the abatement of propane. The final surface areas of the samples with a unit cell size of 3.0 and 4.0 mm were 785 and 507 m^2/m^3, respectively. When their light-off was compared to one of the conventional 400 CPSI honeycombs, it was observed that no significant improvement in the conversions was achieved due to the six times smaller surface area. Simulations showed that at the velocity of 10 m/s, a rotated cube lattice with porosity over 95% had four times higher mass transfer than the honeycomb. Although this suggested that a lower amount of the precious metals was required to achieve identical conversion, due to their six times smaller surface area, the volume of the structure of the lattice would have to be 1.5 times the volume of the honeycomb.

Miniature monolithic substrates were manufactured in 2020 by material extrusion AM process (Figure 2.13b)). The designs were based on interconnected rods with repeating angular offset between deposited layers. The results showed improved catalytic activity of the additively manufactured catalysts in methane oxidation, relative to a conventional commercial honeycomb. The authors noted the monoliths were prepared with thick walls (0.60 mm) due to limitations in the extrusion of the material through the nozzle [72].

In a follow-up publication, the authors built a full-size porcelain catalyst substrate in 2021, which they tested in the conversion of CO, methane and non-methane hydrocarbons in a dual-fuel, heavy-duty diesel engine. At low temperatures, where the reaction is governed by kinetic control, there was little difference in the activity between the 3D printed and honeycomb catalyst. For example, when 40% of diesel was substituted by natural gas, CO conversion was 33% on the 3D printed catalyst, while it was 54% for the commercial catalyst. At higher temperatures (200–300 °C), where the reaction rate was governed by internal and external mass transfer, the conversion was higher on the 3D printed catalyst due to the induced internal turbulence in the channels.

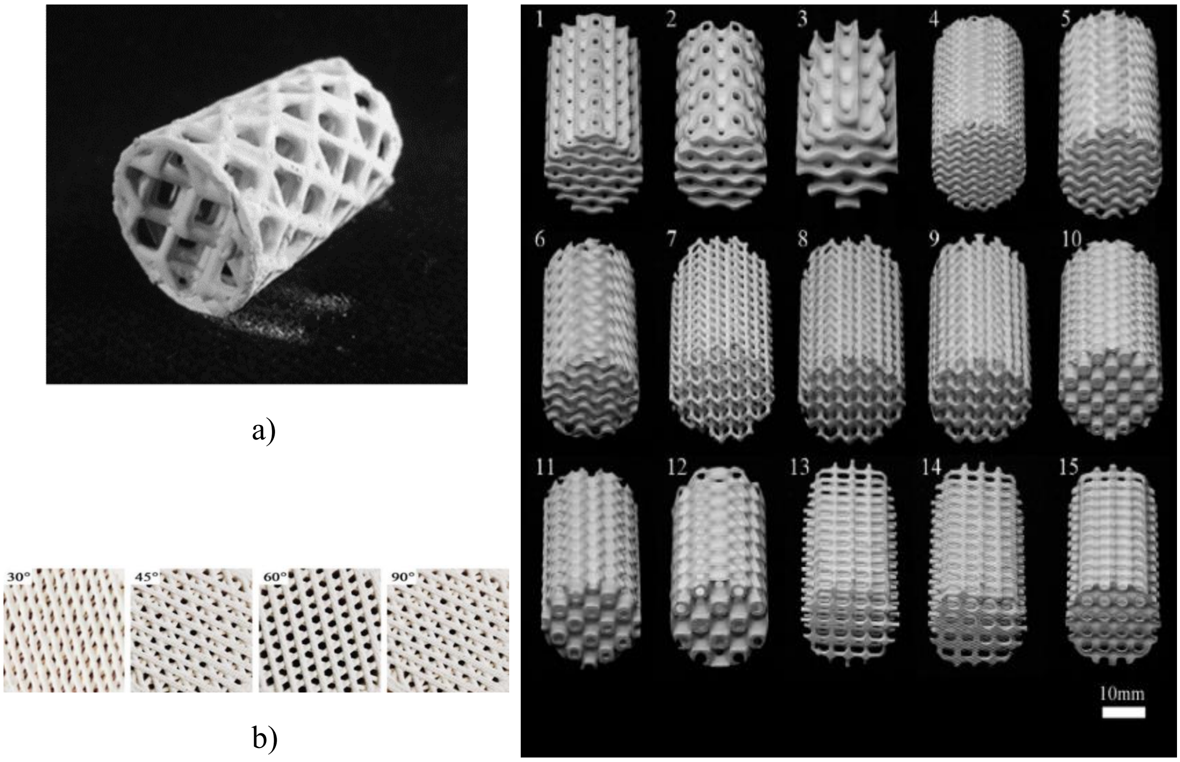

a)

b)

c)

Figure 2.13 a) Coated AM catalyst used for model gas reactor experiments (Ø12 mm × H20 mm) [99] b) AM substrates with different layer orientation offset (Ø20 mm × H20 mm) [72] c) AM substrates with various topologies (Ø20 mm × H35mm) [31]

The findings from their study demonstrated that 3D printing can be utilised to achieve catalytic converter structures with enhanced properties [112].

Al-Ketan et al. [31] manufactured Al_2O_3 substrates in 2019 with architected and controllable topologies based on minimal surface based-topologies via a top-down DLP stereolithography approach (Figure 2.13c)). They did not perform any catalytic testing for their 3D printed samples. The restrictions of the fabrication technique limited the designs to have a minimum of 0.60 mm wall thickness resulting in low surface areas.

A variety of 3D printing materials may be employed to create functional prototypes for catalytic applications. These materials belong to the family of ceramic oxides such as Al_2O_3, CeO_2, ZrO_2, TiO_2 or SiO_2, cordierite or clays, zeolites and SiC [6]. The substrate material is usually selected in conjunction with the respective printing technology. For example, works from Papetti et al. [99] and Al-Ketan et al. [31], as presented above, used vat photopolymerisation processes where the α-Al_2O_3 (corundum) ceramic powder phase was dispersed in a photoreactive resin [31,99]. On the other hand, porcelain and cordierite were used for material extrusion AM [72,112].

There are potential limitations on material choice for AM that depend on the technology. For instance, for technologies that utilise photopolymerisable slurries when selecting solid materials, a balance between viscosity and curing needs to be accounted for as the addition of high refractive index ceramics into the base the resin can affect the accuracy and impede the cure depth.

In summary of the previous research, material extrusion [72,112], and more recently vat phoyopolymerisation processes [15,99] have been utilised for direct AM of the monolithic catalyst for automotive applications. Resulting structures of the monoliths manufactured by material extrusion represent a series of interconnected rods where the geometry is determined by the nozzle geometry, which imposes certain limits on the part's complexity. Additive manufacturing of substrates for catalytic applications still represents a challenge, both in terms of the combined dimensional accuracy and the fine features required in the catalytic substrates to maximise the surface area. The use of vat photopolymerisation techniques for shaping monolith supports is less prevalent. However, the geometrical freedom and resolution are much higher than in material extrusion AM process. Al_2O_3 ceramic material was selected in this study since it is one of the most used structural ceramics and it has been previously used as substrate material for automotive catalysts manufacturing.

In summary, designs for additively manufactured ceramic monolith catalysts have not progressed beyond those based on foam structures and alternating rods structures, despite the valued characteristic of AM-design flexibility. Additive manufacture of complex monolith catalysts has underlined the significance of further research of ceramic additive manufacturing to achieve novel catalyst designs with higher accuracy and finer features to enhance their geometric surface area and gas-solid contact.

2.7 Summary of open research questions

There is still a lot of potential for improvement of the monolithic catalysts for the aftertreatment system applications, especially regarding the improvement of the light-off temperatures. The standard honeycomb catalyst features limitations that impede high heat and mass transfer due to its flow-through channel design and the consequent laminar flow within the channels. Instead, the lattice's network of solid struts is characterised by convoluted routes that promote gas-wall interactions. Despite the design freedom of additive manufacturing, ceramic lattice-based monolith catalysts have not advanced beyond those based on foam structures and alternating rod structures. The manufacturing limitations hinder the widespread implementation of AM for ceramic monolithic catalysts fabrication. To address essential concerns in the development of innovative catalyst designs, the advancement of AM technology requires solving the challenges such as printing accuracy through systematic investigation of printing parameters and preparation techniques of ceramic slurries for the DLP technology. It is vital to grasp thoroughly the ceramic additive process in detail to achieve its full potential. Formulation of a photocurable ceramic slurry with suitable rheological and curing parameters to ensure the success of the shaping process is needed. Furthermore, it is necessary to study advanced catalytic solutions to find a way to minimise the environmental impact of internal combustion engine use. The light-off behaviour of catalytically coated AM advanced catalysts should be studied in a real exhaust gas environment. While the benefits of hydrogen addition for improved catalyst activity are evident for honeycomb catalysts, it is essential to investigate the effect of hydrogen on novel catalysts. Multi-purpose emission control catalytic substrates integrated into a single catalytic substrate brick could be beneficial to reduce the complexity, volume and cost of the aftertreatment system. Therefore, this study aims to overcome the knowledge gaps discussed in the preceding sections, contributing to the endeavour to reduce automotive exhaust emissions.

References

1. ASTM. Additive Manufacturing - General Principles Terminology (ASTM52900). Rapid Manufacturing Association. 2013. p. 10–2.
2. Royal Academy of Engineering. Additive Manufacturing: Opportunities and Constraints. A summary of a roundtable forum held on 23 May 2013. 2013.
3. Moritz T, Maleksaeedi S. Ceramic Components. Additive Manufacturing: Materials, Processes, Quantifications and Applications. Elsevier Inc.; 2018. 105–161 p.
4. Hinton J, Basu D, Mirgkizoudi M, Flynn D, Harris R, Kay R. Hybrid additive manufacturing of precision engineered ceramic components. Rapid Prototyp J. 2019;25(6):1061–8.
5. Hinton J, Mirgkizoudi M, Campos-Zatarain A, Flynn D, Harris RA, Kay RW. Digitally-Driven Hybrid Manufacture of Ceramic Thick-Film Substrates. 2018 7th Electron Syst Technol Conf ESTC 2018 - Proc. 2018;
6. Laguna OH, Lietor PF, Godino FJI, Corpas-Iglesias FA. A review on additive manufacturing and materials for catalytic applications: Milestones, key concepts, advances and perspectives. Mater Des. 2021;208:109927.
7. Zocca A, Colombo P, Gomes CM, Günster J. Additive manufacturing of ceramics: Issues, potentialities, and opportunities. J Am Ceram Soc. 2015;98(7):1983–2001.
8. Cima, M J, Oilvera M, Wang H., Sachs E, Holman R. Slurry-Based 3DP and Fine Ceramic Components. In: 2001 International Solid Freeform Fabrication Symposium. 2001. p. 216–23.
9. Onagoruwa S, Bose S, Bandyopadhyay A. Fused deposition of ceramics (FDC) and composites. Proc Solid Free Fabr Symp. 2001;224–31.
10. Sing SL, Yeong WY, Wiria FE, Tay BY, Zhao Z, Zhao L, et al. Direct selective laser sintering and melting of ceramics: A review. Rapid Prototyp J. 2017;23(3):611–23.
11. Zhang Y, He X, Du S, Zhang J. Al2O3 ceramics preparation by LOM (laminated object manufacturing). Int J Adv Manuf Technol. 2001;17(7):531–4.
12. Ferrizz RM, Stuecker JN, Cesarano J, Miller JE. Monolithic supports with unique geometries and enhanced mass transfer. Ind Eng Chem Res. 2005;44(2):302–8.
13. Shirazi SFS, Gharehkhani S, Mehrali M, Yarmand H, Metselaar HSC, Adib Kadri N, et al. A review on powder-based additive manufacturing for tissue engineering: Selective laser sintering and inkjet 3D printing. Sci Technol Adv Mater. 2015;16(3):1–20.
14. Bae CJ, Ramachandran A, Chung K, Park S. Ceramic stereolithography: Additive manufacturing for 3D complex ceramic structures. J Korean Ceram Soc. 2017;54(6):470–7.
15. Santoliquido O, Bianchi G, Dimopoulos Eggenschwiler P, Ortona A. Additive manufacturing of periodic ceramic substrates for automotive catalyst supports. Int J Appl Ceram Technol. 2017;14(6):1164–73.
16. Lewis JA. Direct ink writing of 3D functional materials. Adv Funct Mater. 2006;16(17):2193–204.
17. Wätjen AM, Gingter P, Kramer M, Telle R. Novel prospects and possibilities in additive manufacturing of ceramics by means of direct inkjet printing. Adv Mech Eng. 2014;2014.
18. Badev A, Abouliatim Y, Chartier T, Lecamp L, Lebaudy P, Chaput C, et al. Photopolymerization kinetics of a polyether acrylate in the presence of ceramic fillers used in stereolithography. J Photochem Photobiol A Chem. 2011;222(1):117–22.

19. Thompson MK, Moroni G, Vaneker T, Fadel G, Campbell RI, Gibson I, et al. Design for Additive Manufacturing: Trends, opportunities, considerations, and constraints. CIRP Ann - Manuf Technol. 2016;65(2):737–60.
20. Griffith ML, Halloran J. Ultraviolet Curing of Highly Loaded Ceramic Suspensions for Stereolithography of Ceramics. Solid Free Fabr Symp. 1994;396–403.
21. Hafkamp T, van Baars G, de Jager B, Etman P. A feasibility study on process monitoring and control in vat photopolymerization of ceramics. Mechatronics. 2018;56:220–41.
22. Santoliquido O, Colombo P, Ortona A. Additive Manufacturing of ceramic components by Digital Light Processing: A comparison between the "bottom-up" and the "top-down" approaches. J Eur Ceram Soc. 2019;39(6):2140–8.
23. Schweiger J, Bomze D, Schwentenwein M. 3D Printing of Zirconia–What is the Future? Curr Oral Heal Reports. 2019;6(4):339–43.
24. Johansson E, Lidström O, Johansson J, Lyckfeldt O, Adolfsson E. Influence of resin composition on the defect formation in alumina manufactured by stereolithography. Materials (Basel). 2017;10(2).
25. Pfaffinger M, Mitteramskogler G, Gmeiner R, Stampfl J. Thermal debinding of ceramic-filled photopolymers. Mater Sci Forum. 2015;825–826:75–81.
26. Altun AA, Prochaska T, Konegger T, Schwentenwein M. Dense, strong, and precise silicon nitride-based ceramic parts by lithography-based ceramic manufacturing. Appl Sci. 2020;10(3).
27. Zakeri S, Vippola M, Levänen E. A comprehensive review of the photopolymerization of ceramic resins used in stereolithography. Addit Manuf. 2020;35:101177.
28. Kowsari K, Zhang B, Panjwani S, Chen Z, Hingorani H, Akbari S, et al. Photopolymer formulation to minimize feature size, surface roughness, and stair-stepping in digital light processing-based three-dimensional printing. Addit Manuf. 2018;24:627–38.
29. Komissarenko DA, Sokolov PS, Evstigneeva AD, Shmeleva IA, Dosovitsky AE. Rheological and curing behavior of acrylate-based suspensions for the DLP 3D printing of complex zirconia parts. Materials (Basel). 2018;11(12).
30. Borlaf M, Serra-Capdevila A, Colominas C, Graule T. Development of UV-curable ZrO2 slurries for additive manufacturing (LCM-DLP) technology. J Eur Ceram Soc. 2019;39(13):3797–803.
31. Al-Ketan O, Pelanconi M, Ortona A, Abu Al-Rub RK. Additive manufacturing of architected catalytic ceramic substrates based on triply periodic minimal surfaces. J Am Ceram Soc. 2019;1–18.
32. Sun J, Binner J, Bai J. Effect of surface treatment on the dispersion of nano zirconia particles in non-aqueous suspensions for stereolithography. J Eur Ceram Soc. 2019;39(4):1660–7.
33. Li X, Zhong H, Zhang J, Duan Y, Bai H, Li J, et al. Dispersion and properties of zirconia suspensions for stereolithography. Int J Appl Ceram Technol. 2020;17(1):239–47.
34. Varghese G, Moral M, Castro-García M, López-López JJ, Marín-Rueda JR, Yagüe-Alcaraz V, et al. Fabrication and characterisation of ceramics via low-cost DLP 3D printing. Bol la Soc Esp Ceram y Vidr. 2018;57(1):9–18.
35. Sokolov PS, Komissarenko DA, Shmeleva IA, Slyusar I V., Dosovitskiy GA, Evdokimov P V., et al. Suspensions on the basis of stabilised zirconium oxide for three-dimensional printing. IOP Conf Ser Mater Sci Eng. 2018;347(1).
36. Mitteramskogler G, Gmeiner R, Felzmann R, Gruber S, Hofstetter C, Stampfl J, et al. Light curing strategies for lithography-based additive manufacturing of customized ceramics. Addit Manuf. 2014;1:110–8.

37. Zhang K, Xie C, Wang G, He R, Ding G, Wang M, et al. High solid loading, low viscosity photosensitive Al 2 O 3 slurry for stereolithography based additive manufacturing. Ceram Int. 2019;45(1):203–8.
38. Wang JC, Dommati H. Fabrication of zirconia ceramic parts by using solvent-based slurry stereolithography and sintering. Int J Adv Manuf Technol. 2018;98(5–8):1537–46.
39. Camargo IL de, Morais MM, Fortulan CA, Branciforti MC. A review on the rheological behavior and formulations of ceramic suspensions for vat photopolymerization. Ceram Int. 2021;47(9):11906–21.
40. Schwarzer E, Götz M, Markova D, Stafford D, Scheithauer U, Moritz T. Lithography-based ceramic manufacturing (LCM) – Viscosity and cleaning as two quality influencing steps in the process chain of printing green parts. J Eur Ceram Soc. 2017;37(16):5329–38.
41. Shuai X, Zeng Y, Li P, Chen J. Fabrication of fine and complex lattice structure Al2O3 ceramic by digital light processing 3D printing technology. J Mater Sci. 2020;55(16):6771–82.
42. Guo J, Zeng Y, Li P, Chen J. Fine lattice structural titanium dioxide ceramic produced by DLP 3D printing. Ceram Int. 2019;45(17):23007–12.
43. Gonzalez P, Schwarzer E, Scheithauer U, Kooijmans N, Moritz T. Additive manufacturing of functionally graded ceramic materials by stereolithography. J Vis Exp. 2019;2019(143):1–8.
44. Liao H. Stereolithography Using Compositions Containing Ceramic Powders. University of Toronto, Canada; 1997.
45. Gentry SP, Halloran JW. Depth and width of cured lines in photopolymerizable ceramic suspensions. J Eur Ceram Soc. 2013;33(10):1981–8.
46. Rudraraju A V. Digital Data Processing and Computational Design for Large Area Maskless. Georgia Institute of Technology; 2013.
47. Schhauer U, Schwarzer E, Moritz T, Michaelis A. Additive Manufacturing of Ceramic Heat Exchanger: Opportunities and Limits of the Lithography-Based Ceramic Manufacturing (LCM). J Mater Eng Perform. 2018;27(1):14–20.
48. Conti L, Bienenstein D, Borlaf M, Graule T. Effects of the layer height and exposure energy on the lateral resolution of zirconia parts printed by lithography-based additive manufacturing. Materials (Basel). 2020;13(6).
49. Lefort I. Thermally efficient advanced diesel exhaust aftertreatment for cleaner vehicles. University of Birmingham; 2015.
50. Hazlett MJ, Epling WS. Heterogeneous catalyst design: Zoned and layered catalysts in diesel vehicle aftertreatment monolith reactors. Can J Chem Eng. 2019;97(1):188–206.
51. Russell A, Epling WS. Diesel oxidation catalysts. Catal Rev - Sci Eng. 2011;53(4):337–423.
52. Govender S, Friedrich H. Monoliths: A Review of the Basics, Preparation Methods and Their Relevance to Oxidation. Catalysts. 2017;7(12):62.
53. Miyairi Y, Aoki T, Hirose S, Yamamoto Y, Makino M, Miwa S, et al. Effect of Cell Shape on Mass Transfer and Pressure Loss. In: SAE World Congress. Detroit, Michigan; 2003.
54. Amirnordin SH, Seri SM, Salim WS-IW, Rahman HA, Hasnan K. Pressure Drop Analysis of Square and Hexagonal Cells and its Effects on the Performance of Catalytic Converters. Int J Environ Sci Dev. 2011;2(3):239–47.
55. Williams JL. Monolith structures, materials, properties and uses. Catal Today.

2001;69:3–9.

56. Tomašić V, Jović F. State-of-the-art in the monolithic catalysts/reactors. Appl Catal A Gen. 2006;311(1–2):112–21.
57. Capasso I, Liguori B, Verdolotti L, Caputo D, Lavorgna M, Tervoort E. Process strategy to fabricate a hierarchical porosity gradient in diatomite-based foams by 3D printing. Sci Rep. 2020;10(1):1–9.
58. Nijhuis TA, Beers AEW, Vergunst T, Hoek I, F. K, Moulijn JA. Preparation of monolithic catalysts. Stud Surf Sci Catal. 2001;43:345–80.
59. Wang S, Cui Y, Lan L, Shi Z, Zhao M, Gong M, et al. A new monolithic Pt-Pd-Rh motorcycle exhaust catalyst to meet future emission standards. Chinese J Catal. 2014;35(9):1482–91.
60. Chen HY, Chang HLR. Development of low temperature three-way catalysts for future fuel efficient vehicles. Johnson Matthey Technol Rev. 2015;59(1):64–7.
61. Visconti CG. Alumina: A key-component of structured catalysts for process intensification. Trans Indian Ceram Soc. 2012;71(3):123–36.
62. Joshi A. Progress and outlook on gasoline vehicle after treatment systems. Johnson Matthey Technol Rev. 2017;61(4):311–25.
63. Hoang S, Lu X, Tang W, Wang S, Du S, Nam CY, et al. High performance diesel oxidation catalysts using ultra-low Pt loading on titania nanowire array integrated cordierite honeycombs. Catal Today. 2019;320:2–10.
64. Gremminger A, Pihl J, Casapu M, Grunwaldt JD, Toops TJ, Deutschmann O. PGM based catalysts for exhaust-gas after-treatment under typical diesel, gasoline and gas engine conditions with focus on methane and formaldehyde oxidation. Appl Catal B Environ. 2020;265:118571.
65. Herreros JM, Gill SS, Lefort I, Tsolakis A, Millington P, Moss E. Enhancing the low temperature oxidation performance over a Pt and a Pt-Pd diesel oxidation catalyst. Appl Catal B Environ. 2014;147:835–41.
66. Ho PH, Woo JW, Ilmasani RF, Han J, Olsson L. The role of Pd-Pt interactions in the oxidation and sulfur resistance of bimetallic Pd-Pt/γ-Al2O3diesel oxidation catalysts. Ind Eng Chem Res. 2021;60(18):6596–612.
67. Daneshvar K, Krishna Dadi R, Luss D, Balakotaiah V, Kang SB, Kalamaras CM, et al. Experimental and modeling study of CO and hydrocarbons light-off on various Pt-Pd/Γ-Al2O3 diesel oxidation catalysts. Chem Eng J. 2017;323:347–60.
68. Adamowska M, Da Costa P. Structured Pd/ γ -Al 2 O 3 Prepared by Washcoated Deposition on a Ceramic Honeycomb for Compressed Natural Gas Applications . J Nanoparticles. 2015;2015:1–9.
69. Mogalicherla AK, Kunzru D. Effect of method of preparation on activity of pd/al2o3 monolith catalysts. Can J Chem Eng. 2010;88(3):367–75.
70. Avila P, Montes M, Miró EE. Monolithic reactors for environmental applications: A review on preparation technologies. Chem Eng J. 2005;109(1):11–36.
71. Kulkarni SP, B MS, Kulkarni AK, Joshi VM, Deore H. Modification of catalytic converters thereby bettering their performance and reducing the cost. Int J Sci Adv Res Technol. 2018;4(2).
72. Hajimirzaee S, Doyle AM. 3D printed catalytic converters with enhanced activity for low-temperature methane oxidation in dual-fuel engines. Fuel. 2020;274:117848.
73. Schweich D, Leclerc JP. Flow, heat, and mass transfer in a monolithic catalytic converter. Stud Surf Sci Catal. 1991;71(C):437–63.
74. Reiter MS, Kockelman KM. The problem of cold starts: A closer look at mobile source

emissions levels. Transp Res Part D Transp Environ. 2016;43:123–32.

75. Hayes RE, Kolaczkowski ST. Mass and heat transfer effects in catalytic monolith reactors. Chem Eng Sci. 1994;49(21):3587–99.
76. Agrawal G, Kaisare NS, Pushpavanam S, Ramanathan K. Modeling the effect of flow mal-distribution on the performance of a catalytic converter. Chem Eng Sci. 2012;71:310–20.
77. Koltsakis GC, Samaras Z, Karvountzis-Kontakiotis A, Zacharopoulou T, Haralampous O. Implications of Engine Start-Stop on After-Treatment Operation. SAE Int J Engines. 2011;4(1):1571–85.
78. Lefort I, Tsolakis A. A thermally efficient DOC configuration to improve CO and THC conversion efficiency. SAE Tech Pap. 2013;2.
79. Marsh P, Acke F, Konieczny R, Brück R. Application guideline to define a catalyst layout for maximum catalytic efficiency. Soc Automot Eng. 2001;(724).
80. Jeong SJ, Kim WS. A study on the optimal monolith combination for improving flow uniformity and warm-up performance of an auto-catalyst. Chem Eng Process Process Intensif. 2003;42(11):879–95.
81. Holmgren A, Gronstedt T, Andersson B. Improved flow distribution in automotive monolithic converters. React Kinet Catal Lett. 1997;60(2):363–71.
82. Yoshida T, Suzuki H, Aoki Y, Hayashi N, Ito K. Development of a New Ceramic Substrate with Gas Flow Control Functionality. SAE Int J Engines. 2017;10(4):1588–94.
83. Litto R, Mmbaga JP, Hayes RE, Plati S, Blagojevic V, Subject P. Exhaust emissions and fuel economy improvements through thermal performance control in a novel three-way catalytic converter. Can J Chem Eng. 2016;94(5):905–12.
84. Boger T, Heibel AK, Sorensen CM. Monolithic catalysts for the chemical industry. Ind Eng Chem Res. 2004;43(16):4602–11.
85. Laguna OH, Domínguez MI, Centeno MA, Odriozola JA. and Microreactors. New materials for catalytic applications. Elsevier B.V.; 2016. 81–120 p.
86. Presti M, Pace L, Mueller W, Witte-Merl O. Vehicle mass lightening by design of light-weight structured substrates for catalytic converters. SAE Int. 2011;1–19.
87. Hettel M, Daymo E, Schmidt T, Deutschmann O. CFD-Modeling of fluid domains with embedded monoliths with emphasis on automotive converters. Chem Eng Process - Process Intensif. 2020;147:107728.
88. Gao J, Tian G, Sorniotti A, Karci AE, Di Palo R. Review of thermal management of catalytic converters to decrease engine emissions during cold start and warm up. Appl Therm Eng. 2019;147:177–87.
89. Golunski S. What is the point of on-board fuel reforming? Energy Environ Sci. 2010;3(12):1918–23.
90. Sitshebo S, Tsolakis A, Theinnoi K. Promoting hydrocarbon-SCR of NOx in diesel engine exhaust by hydrogen and fuel reforming. Int J Hydrogen Energy. 2009;34(18):7842–50.
91. Theinnoi K, Tsolakis A, Sawatmongkhon B, Chuepeng S. A Study of Hydrogen Addition on Diesel Oxidation Catalyst Activities under the Real Diesel Engine. J Res Appl meachanical Eng. 2013;1(3):1–4.
92. Prasad BSN, Pandey JK, Kumar GN. Effect of hydrogen enrichment on performance, combustion, and emission of a methanol fueled SI engine. Int J Hydrogen Energy. 2021;46(49):25294–307.
93. Tsolakis A, Megaritis A, Wyszynski ML. Low temperature exhaust gas fuel reforming

of diesel fuel. Fuel. 2004;83(13):1837–45.

94. Flörchinger P, Day JP. Principles for the design of diesel oxidation catalysts. SAE Tech Pap. 2002;(724).
95. Holmgren AM. Enhanced mass transfer in monolith catalysts with bumps on the channel walls. Ind Eng Chem Res. 1999;38(5):2091–7.
96. Lucci F, Della Torre A, von Rickenbach J, Montenegro G, Poulikakos D, Dimopoulos Eggenschwiler P. Performance of randomized Kelvin cell structures as catalytic substrates: Mass-transfer based analysis. Chem Eng Sci. 2014;112:143–51.
97. Sinn C, Pesch GR, Thöming J, Kiewidt L. Coupled conjugate heat transfer and heat production in open-cell ceramic foams investigated using CFD. Int J Heat Mass Transf. 2019 Aug 1;139:600–12.
98. Bracconi M, Ambrosetti M, Okafor O, Sans V, Zhang X, Ou X, et al. Investigation of pressure drop in 3D replicated open-cell foams: Coupling CFD with experimental data on additively manufactured foams. Chem Eng J. 2019;377:120123.
99. Papetti V, Dimopoulos Eggenschwiler P, Della Torre A, Lucci F, Ortona A, Montenegro G. Additive Manufactured open cell polyhedral structures as substrates for automotive catalysts. Int J Heat Mass Transf. 2018;126:1035–47.
100. El-Sayed MA, Essa K, Ghazy M, Hassanin H. Design optimization of additively manufactured titanium lattice structures for biomedical implants. Int J Adv Manuf Technol. 2020;110(9–10):2257–68.
101. Sabouri A, Yetisen AK, Sadigzade R, Hassanin H, Essa K, Butt H. Three-Dimensional Microstructured Lattices for Oil Sensing. Energy and Fuels. 2017;31(3):2524–9.
102. Essa K, Sabouri A, Butt H, Basuny FH, Ghazy M, El-Sayed MA. Laser additive manufacturing of 3D meshes for optical applications. PLoS One. 2018;13(2):4–11.
103. Essa K, Hassanin H, Attallah MM, Adkins NJ, Musker AJ, Roberts GT, et al. Development and testing of an additively manufactured monolithic catalyst bed for HTP thruster applications. Appl Catal A Gen. 2017;542:125–35.
104. Lefort I, Herreros JM, Tsolakis A. Reduction of low temperature engine pollutants by understanding the exhaust species interactions in a diesel oxidation catalyst. Environ Sci Technol. 2014;48(4):2361–7.
105. Bogdan E, Michorczyk P. 3D Printing in Heterogeneous Catalysis—the State of the Art. Materials (Basel). 2020;13(20):1–23.
106. Michorczyk P, Hędrzak E, Węgrzyniak A. Preparation of monolithic catalysts using 3D printed templates for oxidative coupling of methane. J Mater Chem A. 2016;4(48):18753–6.
107. Couck S, Cousin-Saint-Remi J, Van der Perre S, Baron G V., Minas C, Ruch P, et al. 3D-printed SAPO-34 monoliths for gas separation. Microporous Mesoporous Mater. 2018;255:185–91.
108. Lefevere J, Mullens S, Meynen V. The impact of formulation and 3D-printing on the catalytic properties of ZSM-5 zeolite. Chem Eng J. 2018;349(April):260–8.
109. Díaz-Marta AS, Tubío CR, Carbajales C, Fernández C, Escalante L, Sotelo E, et al. Three-Dimensional Printing in Catalysis: Combining 3D Heterogeneous Copper and Palladium Catalysts for Multicatalytic Multicomponent Reactions. ACS Catal. 2018;8(1):392–404.
110. Parra-Cabrera C, Achille C, Kuhn S, Ameloot R. 3D printing in chemical engineering and catalytic technology: Structured catalysts, mixers and reactors. Chem Soc Rev. 2018;47(1):209–30.
111. Zhu J, Wu P, Chao Y, Yu J, Zhu W, Liu Z, et al. Recent advances in 3D printing for

catalytic applications. Chem Eng J. 2022;433(P1):134341.

112. Hajimirzaee S, Shaw D, Howard P, Doyle AM. Industrial scale 3D printed catalytic converter for emissions control in a dual-fuel heavy-duty engine. Chem Eng Sci. 2021;231.

CHAPTER 3

EFFECTS OF THE INTERNAL STRUCTURES OF MONOLITH CERAMIC SUBSTRATES ON THERMAL AND HYDRAULIC PROPERTIES: ADDITIVE MANUFACTURING, NUMERICAL MODELLING AND EXPERIMENTAL TESTING

Authors Contributions:

This chapter of the alternative thesis format is published in the International Journal of Advanced Manufacturing Technology (2020). I am the first author of this publication. The paper's details and co-authors' contributions are outlined below.

Kovacev N[1]*, Li S*[2]*, Zeraati Rezaei S*[3]*, Hemida H***, Tsolakis A**, Essa K***. Effects of the internal structures of monolith ceramic substrates on thermal and hydraulic properties: additive manufacturing, numerical modelling and experimental testing. Int J Adv Manuf Technol.2020; 112:1115–32.*

[1] **Nikolina Kovacev:** The main author, designed and executed experiments, designed the equipment for experimental rig, numerical simulations, additive manufacturing, performed all necessary characterisation and data analysis and wrote the manuscript

[2] **Dr Sheng Li:** Assisted with setting up of the experiment

[3] **Dr Soheil Zeraati-Rezaei:** Assisted with setting up of the experiment

*** Dr Hassan Hemida**: Supervision and proofreading

****Prof. Athanasios Tsolakis:** Supervision and proofreading

*****Dr Khamis Essa:** Supervision and proofreading

CHAPTER 3:

EFFECTS OF THE INTERNAL STRUCTURES OF MONOLITH CERAMIC SUBSTRATES ON THERMAL AND HYDRAULIC PROPERTIES: ADDITIVE MANUFACTURING, NUMERICAL MODELLING AND EXPERIMENTAL TESTING

Abstract

Rigorous emission regulations call for more efficient exhaust emission control aftertreatment catalysts without affecting the internal combustion process and CO_2 emissions. Although the state-of-art ceramic honeycomb substrate designs provide high surface area and a degree of flexibility for heat and mass transfer adaptations, additional emissions reduction benefits can be achieved when more flexible designs to provide effective thermal management are introduced. The conventional cordierite honeycomb substrates are manufactured by extrusion, therefore only substrates with straight channels can be fabricated. This study aims to highlight any design limitations of conventional substrates by employing additive manufacturing as the main method of manufacturing diamond lattice structures using DLP (Digital Light Processing) technology. Both conventional substrates and diamond lattice structures are studied numerically and experimentally for flow-through resistance and temperature distribution. Numerical predictions and experimental results showed good agreement. The results show the increase of the axial temperature distribution for diamond lattice structures and a significant decrease of the pressure drop (38-45%) in comparison with the benchmark honeycomb with a similar surface area.

Keywords: additive manufacturing; monolith; ceramic substrate; CFD; honeycomb

3.1 Introduction

Environmental concern and ever-changing emissions regulations have raised the significance of improving the performance of the exhaust gas aftertreatment system for stationary and mobile applications [1,2]. In the 1970s, initial trials of exhaust gas purification incorporated placing a catalytic converter in all petrol vehicles [3]. The key part of the converter, honeycomb monolith, typically manufactured by extrusion, consists of thousands of straight, parallel, flow-through channels coated with noble metals accountable for catalytic reactions [4–6]. Due to the restrictions of the extrusion process, the channel design is of a simple shape with thin walls separating the individual channels [7,8]. Only limited geometric shapes of the channels can be manufactured, such as square, hexagonal or triangular [9,10]. Research shows that hexagonal and square channels show similar performance and pressure drop under the same experimenting conditions. Contrarily, triangular channels show the poorest performance [11]. Hotspots and non-isothermal temperature profiles in axial and radial directions present additional issues associated with the substrate design [12,13]. The laminar flow inside of the honeycomb channels decreases the heat and mass transfer [14]. The awareness of the inefficient use of the catalyst full volume led to research of new possible designs of the substrate following the improvement of the manufacturing opportunities.

One way of achieving the necessary requirements to increase the catalyst performance is to cautiously direct the parameters of the substrate structure to achieve the desired pressure drop and improved heat transfer. An interesting approach to enhanced monolith designs is non-stochastic structures (periodic) structures that include repeating 3D lattice structures of strut-and-node arrangement and custom unit cells. Non-stochastic lattice structures consist of unit cells periodically arranged in all three dimensions with the most common, octet, cube, hexagon and tetrakaidekahedron, all inspired by foam designs [14,15]. Topology optimised lattice structures have been utilised in the automotive industry for weight reduction and improvement of the strength of bulk parts [16]. For catalytic applications, modified regular structures manufactured by material extrusion AM provided improved mass transfer compared to the honeycomb sample, with a fairly higher pressure drop [17]. The tortuous path in the channels upsurges the transport between the catalyst surface and the bulk of reactant and product [18,19]. Recent research has revealed rotated cubic cells as a replacement for honeycombs [14]. Samples with 3 mm and 4 mm cell size and strut thickness of 0.5 mm were manufactured and experimentally tested [14,15]. Due to the manufacturing limitations, the samples had a low specific surface area which proved to be a disadvantage [14].

Numerical simulations can give detailed insights into specifics that are not possible or are difficult to capture throughout experimental trials to aid the design of the new catalytic supports. The simplest modelling method for honeycombs is a single-channel, where all channels are assumed to behave alike, however, this assumption is not correct. The flow maldistribution and heat losses to the surroundings are discarded in single-channel models [10,20–23]. Multi-channel models, such as the subgrid-scale model with a couple of representative channels have the same drawbacks as the single-channel method [24]. Continuum models, where the pressure drop of the monolith is implemented into the model from calculations, need to have a correct heat flux at boundary assigned [22,25]. The thermal conditions, in reality, cannot be set as isothermal due to the temperature variations along the length and cross-section of the monolith. Likewise, numerical simulations have been utilised, to some extent, to study the fluid dynamics and heat transfer properties of foams and non-stochastic lattice structures. A comprehensive analysis of pressure drops in virtually reconstructed open cell foams, combining numerical and experimental studies, showed the open-cell foams outperform honeycomb monoliths in the range of low Reynolds numbers [28]. Alternatively, foams can be reconstructed by Laguerre-Voronoi tessellations, with the main drawback being the increase of the computational load [26]. Previous studies have indicated that foam-based catalysts demonstrate greater performance in comparison with the honeycomb in terms of conversion, but might exhibit higher pressure drops [3,27,28]. While foams seem to show increased performance, their non-controllable structure makes it challenging to foresee the flow behaviour [15]. To simplify the modelling of the foams in the past, the foam structure had been represented with regular cells, such as Kelvin cells. The regular structures have actually proved to have a superior trade-off between the mass transfer and pressure drop [29]. Moreover, their superior properties led to study the regular structures as potential catalyst substrates [14, 31]. Modelling of complex non-stochastic structures is particularly challenging, thus short domains consisting of only a couple of cells in the flow direction are generally used for numerical simulations [30–32]. However, the short domains could affect the simulation results as the flow might not be fully developed [30].

Advanced Manufacturing Technologies (AMT) are progressively used in many different industries. Precise and complex components can be fabricated by machining processes such as ball end milling [33] and turning [34]. Furthermore, laser hardening offers short processing time and higher performance for 3D complex shapes [35]. Additive manufacturing eases the manufacturing of complex geometrical shapes by layer-by-layer addition of material. The improvements in the AM technologies have allowed direct fabrications of lattice structures. Selective Laser Melting (SLM) is a widely employed additive manufacturing process that can be used for printing of intricate three-dimensional (3D) structures for various applications [30–32]. Ti–6Al–4V alloy-based 3D meshes with diamond unit cells were manufactured with Concept Laser M2 for optical applications [36]. Moreover, the same technology was utilised to manufacture Ti-6Al-4V optical lattice mesh structure that can be used as an oil sensor [37]. In addition, the studies on the effect of SLM process parameters and their optimisation were performed for manufacturing of biomedical implants [38]. Additive manufacturing of ceramic materials has been an ongoing topic of research due to their challenging processing requirements [39]. One of the challenges is the reduced cure depth in ceramic suspensions due to scattering, resulting in a decrease of the bonding between the layers. However, reducing the layer thickness to increase the bonding of the layers as a consequence increases the building time. Correspondingly, the viscosity of the suspension must be optimised to ensure uniform layer recoating during the build [40]. Nevertheless, AM can overcome the traditional ceramic manufacturing methods limitations, such as complex geometry production. Net shape YSZ/Al_2O_3 nanocomposite micro-components were successfully manufactured through a process based on soft lithography and powder dispersion [41]. Techniques involving polymerisation of the photoactive resin can generally be divided into Stereolithography (SLA) based on spot scanning and Digital Light Processing (DLP) based on mask-image-projection [42]. Lattice structures have been manufactured by stereolithography in the past, however the disadvantages of this process include the need of support for manufacturing and the stair-case effect which can be highly detrimental under load [15,43]. Digital Light Processing AM technology generally has faster manufacturing speed and is advantageous for the building small components [42]. Thus, Digital Light Processing (DLP) additive manufacturing technology has been used in this study due to the significant advantages of high-precision and low-cost for advanced ceramic manufacturing [41].

Research conducted so far on improvement of the monolith designs has merely explored unit cells derived from foams, such as Kelvin cell or a simple cubic cell [14,17]. The dimensional limitations of the manufacturing technique used to manufacture the substrates cause the aforementioned to have large strut diameters and inadequate substrate dimensions resulting in low geometrical surface areas [14]. Short domains chosen for the experiments and numerical modelling of lattice structures can cause inaccuracies in pressure drop prediction and overall performance as the flow might not be fully developed [14,30]. Morphological parameters of honeycomb and lattice design need to be investigated in conditions other than isothermal. In this study, hot gas is used as the heat source rather than isothermal conditions on the outside wall. The numerical model contains longer length of the lattice structure with a higher aspect ratio. The effect of geometrical structure between lattice and traditional monolith substrate in terms of heat transfer and flow resistance is investigated by employing a steady-state three-dimensional conjugate heat transfer model.

The aim of this paper is to develop and manufacture a lattice monolithic ceramic substrate. Computation Fluid Dynamic model is developed to aid the design and is validated for both designs and used to compare between them. The performance of the two substrate designs is tested in terms of temperature profile and pressure drop in a non-reactive environment. Finally, the effect of lattice design on the specific surface area, pressure drop and thermal management is investigated.

3.2 Methodology

3.2.1 Design of lattice structures

Lattice can be defined as a structure which consists of a regular network of struts connected by nodes in a three-dimensional space. The unit cell size, type, strut size and cell orientation have a considerable influence on the surface area, thermal properties of the structure and fluid flow behaviour. Diamond lattice cell has been selected as the representative model as it has shown great performance for other applications and it is self-supportive, which is of great importance for successful additive manufacturing [37,44]. The CAD model of the investigated diamond lattice substrate is shown in Figure 3.1a) with the corresponding internal structure in Figure 3.1b) and a diamond unit cell in Figure 3.1c) and Figure 3.1d), illustrating the main properties of the diamond lattice structure.

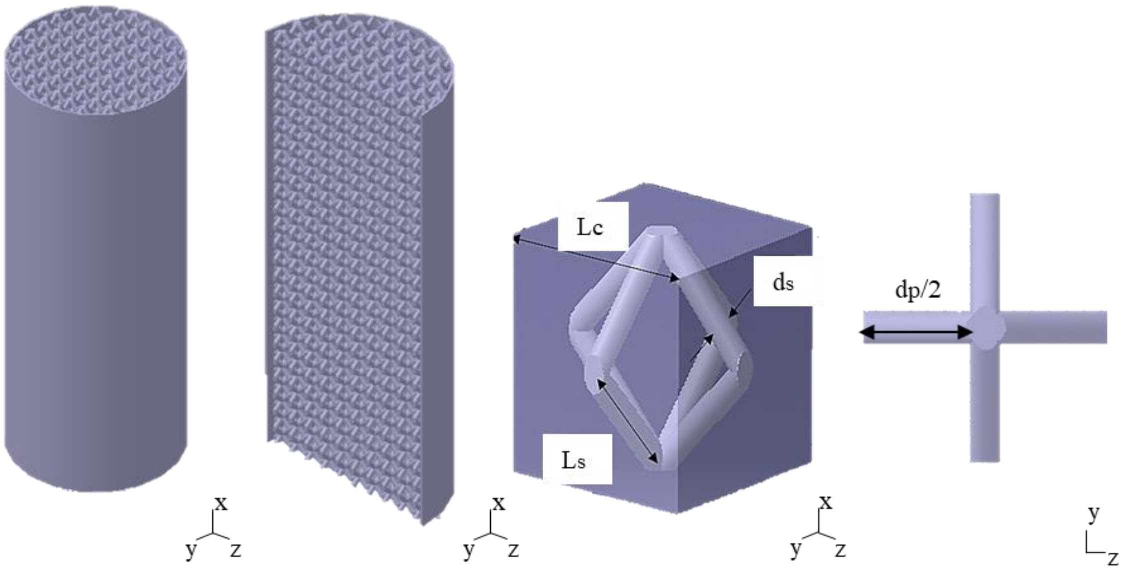

a) b) c) d)

Figure 3.1 CAD representation of a) Full-length lattice model b) Internal structure of the lattice model c) Unit cell diamond lattice with geometrical parameters, L_s strut length, L_c cell length, d_s strut diameter d) Unit cell in flow direction, where d_p/2-half pore

The porosity was calculated from the volume distribution of the solid and total volume of the cylindrical samples as shown in Equation 3.1:

$$\varepsilon = \left(1 - \frac{V_{BCC}}{V_{cylinder}}\right) \qquad \text{Equation 3.1}$$

The specific surface area was calculated as the geometrical surface area of the whole substrate divided by the volume of the cylinder as shown in Equation 3.2:

$$S_v = \frac{GSA}{V_{cylinder}}\ [\mathrm{m}^{-1}] \qquad \text{Equation 3.2}$$

Honeycomb monoliths are available in different cell density and shapes. Nevertheless, the most common commercial honeycomb is a square channelled 400 CPSI [14,28,45,46]. Therefore, a square channelled honeycomb monolith with 400 CPSI and 0.2 mm thick walls is used as the benchmark. The CAD model of the honeycomb substrate is illustrated in Figure 3.2a).

Figure 3.2b) represents the internal structure and Figure 3.2c) the single channel. The main properties of the honeycomb are channel diameter of 1.05 mm, porosity of 0.68 and specific surface area of 2480 m^{-1}.

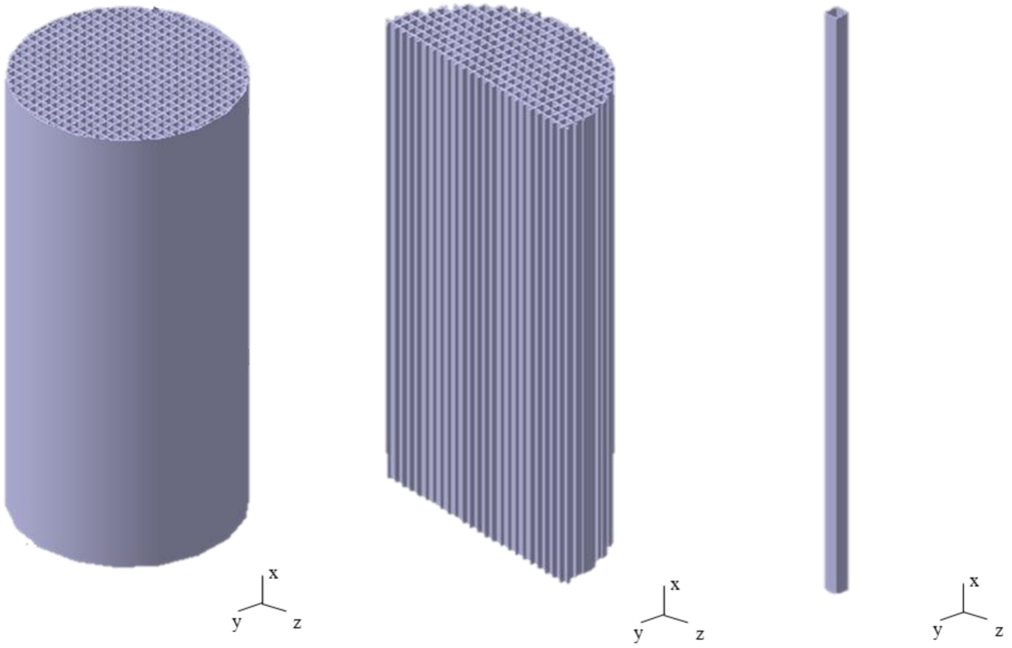

a) b) c)

Figure 3.2 CAD model of a) Full-length honeycomb model b) Internal honeycomb structure, and c) Single channel

3.2.2 Numerical modelling

In order to aid the design of the lattice structures, a numerical approach using Computational Fluid Dynamics (CFD) is used to predict the effect of the internal structure of the substrate on fluid dynamics, pressure drop and temperature distribution. The main focus of the numerical study is on the physical behaviour of the flow within the substrate, therefore the chemical reactions are not taken into the account for simplifications and to place the interest strictly on the flow behaviour driven by geometry change, which is a common practice when investigating fluid flow in substrates [1,31,47]. The main idea is that, with the lattice design, the temperature distribution in radial and axial direction of the substrate will be considerably different than of the traditional honeycomb substrate, concluding that the geometry can influence the temperature distribution. A finite-volume-based commercial code ANSYS CFX enables to solve the conjugate heat transfer problems with two separate domains, where the thermal energy of solid and fluid is exchanged in their interface [48]. The equations required are momentum balances and energy balances for the solid and fluid phases. The transport of enthalpy through the fluid and heat transfer is modelled with thermal energy model. Steady-state Navier-Stokes equations were solved in the laminar model for honeycomb substrate and in Shear Stress Transport k-ω model for the lattice substrate. It is important to note that two CFD models have been developed and validated; one for the lattice structure and one for the honeycomb (this is because the lattice structure has different dimensions due to the manufacturing limitations). Second-order upwind biased discretisation is used to calculate the advection terms in the discrete finite volume equations. Residuals are the most important measure of convergence; hence RMS residuals are set as the convergence criteria with the magnitude of limit 10^{-6}. Pressure drop was monitored as the value of interest, and it was ensured that the steady-state value was reached with the overall imbalance less than 1%. The boundary conditions and the computational domains are shown in Figure 3.3. Table 3.1 summarises in detail the computational domains and the boundary conditions for the numerical models. The boundary conditions are constructed with mass flow rate and temperature at the inlet, zero-gauge pressure at the outlet and constant heat transfer coefficient at the walls. The computational domain is represented as a quarter of the full substrate with lateral boundaries as symmetry for the honeycomb and periodic for the lattice. The dimensions of the honeycomb and lattice domain are matched with the dimensions of the substrates in the experiments.

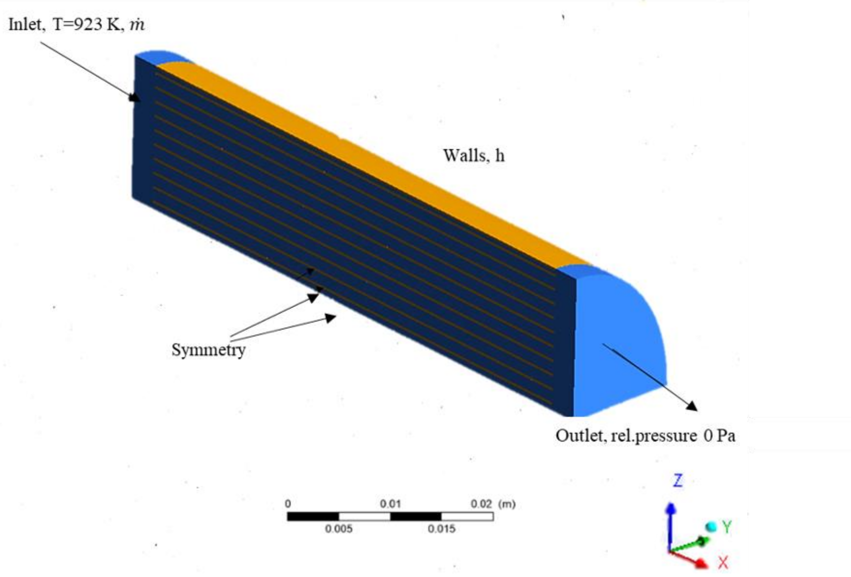

a)

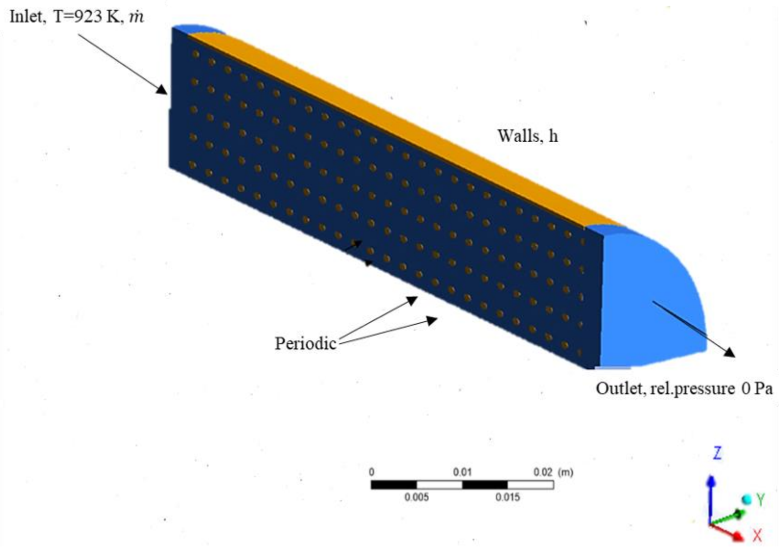

b)

Figure 3.3 Solid (yellow) and fluid (blue) domains with boundary conditions for a) Honeycomb and b) Lattice

Table 3.1 Summary of the computational domains and boundary conditions

DOMAIN	**Section**	**Dimensions Radius x Length (mm)**	**Condition**
Fluid domain	Air	12.5 x 63	Air at 923 K
	Honeycomb	12.7 x 67	k_f- Sutherland formula
	Lattice		ρ- Sutherland formula
Solid domain	Honeycomb	12.5 x 57	Cordierite,k_s=2.5 W/mK
	Lattice	12.7 x 61	ZrO_2, k_s=2.5 W/mK
BOUNDARY CONDITIONS	**Named section**		**Condition**
Mass flow rate inlet	Inlet		$\dot{m}$= 0.4-1.8 kg/h
Pressure outlet	Outlet		$P_{out,gage}$= 0 Pa
Wall with constant h	Wall_fluid		No-slip, h= 16 W/m^2K
Wall with constant h	Wall_solid		No-slip, h= 16 W/m^2K
INTERFACE	**Condition**		
Fluid-solid interface	No-slip, heat transfer, symmetry condition through x-axis (honeycomb), periodic condition through x-axis (lattice)		
Solid-fluid interface	Heat transfer, symmetry condition through x-axis (honeycomb), periodic condition through x-axis (lattice)		

The fluid domain was extended by 3 mm before and after the solid. Thermal conductivity of 2.5 W/mK is used for the cordierite honeycomb in the present model [1,49]. Zirconia has a reported thermal conductivity in the range of 2.2–2.9 W/mK [50]. The value chosen was the same as for the cordierite sample as in this range significant differences in the temperatures were not observed. The fluid is considered as an ideal gas, thus the equation of state $pV = nRT$ is valid. The temperature of the incoming exhaust gas in automotive exhaust systems can be as high as 1173 K [51]. Relatively high air temperature of 923 K was chosen for model validation for higher experimental measurement accuracy. The heat transfer coefficient was calculated from average sample surface temperature and inlet and outlet temperatures obtained from the experiment [52]. Radiation heat transfer was not taken into the account since the outer tube temperatures were low [53]. Total heat losses Q (W) were obtained with Equation 3.3:

$$\dot{\mathrm{Q}} = \dot{\mathrm{m}}\mathrm{c}_{\mathrm{p,air}}(\mathrm{T}_{\mathrm{gas,in}} - \mathrm{T}_{\mathrm{gas,out}}) \qquad \text{Equation 3.3}$$

Total heat transferred from the substrate wall, through the wrapping and the pipe is calculated from Equation 3.4:

$$\dot{Q} = hAT_{wall,ave} \qquad \text{Equation 3.4}$$

Equating Equation 3.3 and Equation 3.4, heat transfer coefficient can be derived as:

$$h = \frac{\dot{m}c_{p,air}(T_{gas,in} - T_{gas,out})}{\pi DLT_{wall,ave}} \qquad \text{Equation 3.5}$$

The laminar flow (Re= 125-1250) in the honeycomb due to the very small channel diameter (1.05 mm) justifies the use of the laminar model. The determination of the flow behaviour in the lattice includes calculation of Reynolds number with appropriate characteristic length. Various definitions of the characteristic length for lattice structures are found in the literature. Strut diameter, mean cell diameter or hydraulic diameter can be used to find the Reynolds number [14,30,54].

In this study, the Reynolds number was calculated with strut diameter as the characteristic length as suggested in [14]. The Reynolds number based on the strut diameter in this study lies in the range of 2-25 suggesting laminar to early transition regime [14]. The simulations for the lattice structure were performed both by laminar and SST- k–ω model. The simulation results were compared to the experimental results resulting in smaller discrepancy when using SST- k–ω model. Consequently, the SST- k–ω model is selected given that it is able to deal with transitional flows and performs well in the proximity of solid walls. The mesh is constructed using Ansys software package built-in mesher.

The fluid domain of the honeycomb channels is meshed with hexahedral elements with the mesh details shown in Figure 3.4a), whereas the inlet and outlet sections are meshed with unstructured mesh. Mesh independence is reached at element count of 8 162 045. The solid channels of the monolith substrate are meshed using adaptive hexahedral mesh with a global size of 0.2 mm. It is assumed that there are no considerable thermal gradients across the structure due to very fine thickness of the channel walls, which is confirmed through a set of additional simulations with only 0.3% error between temperatures at the interface when using mesh with 350 373 (0.2 mm element size) and 6 849 920 elements (element size 0.04 mm).

For the lattice structure, different meshing approach is used. Owing to the complex structure, unstructured mesh is generated for both solid and fluid domain. The details of the mesh for the fluid domain are presented in Figure 3.4b). Curvature-based mesh-refinement with fine mesh around the lattice strut surface is used, with mesh size gradually increasing away from the surface at growth-rate of 1.3 until the maximum value. The mesh independent solution is reached with 7 912 022 elements. Solid domain is meshed with adaptive unstructured mesh with a global size of 0.2 mm.

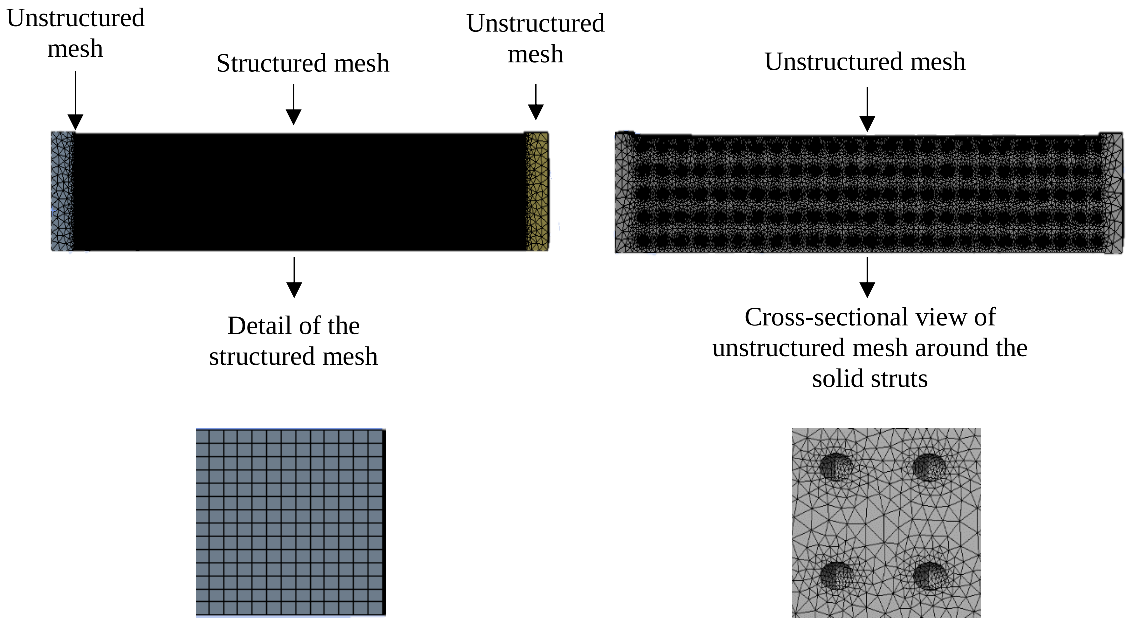

a) b)

Figure 3.4 Example of the CFD mesh used in the present work. a) Honeycomb mesh with channel mesh detail b) Unstructured mesh of the lattice substrate with cross-sectional view of the mesh detail

The main parameter for the mesh dependence test is pressure drop, as higher variations of calculated pressure gradients are noticed with change of the element count, whereas the temperature values only varied slightly. Figure 3.5 represents the variation of pressure drop values with the number of elements for the honeycomb and lattice model.

The highest RMSE % from the experimentally obtained pressure drop is less than 10% for both structures using mesh with around 8 million elements for the fluid domains.

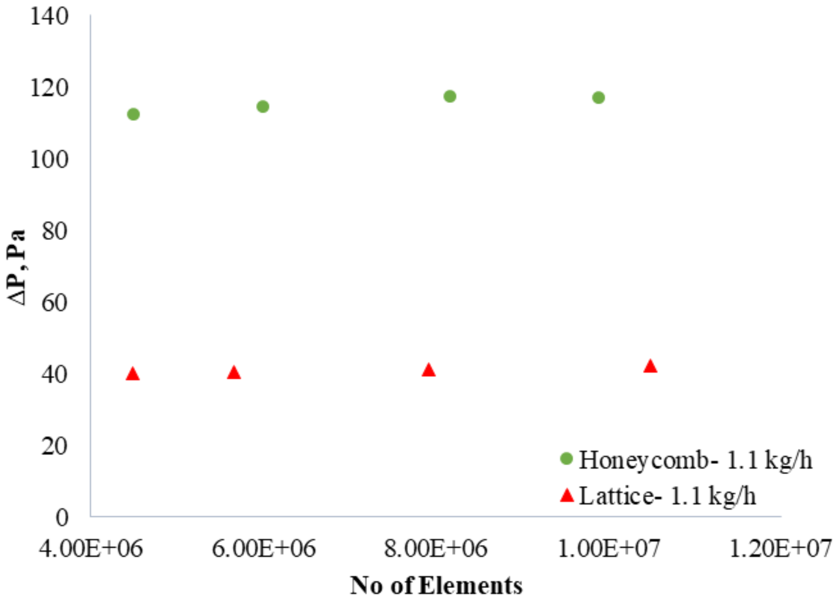

Figure 3.5 Mesh independence study for honeycomb and lattice model

3.2.3 Additive manufacturing

Stereolithography based method with DLP light source is used to polymerise the photocurable resin and form the green bodies in this study. The aforementioned is a promising additive manufacturing technology for complex shape ceramic part production [42]. The DLP technology might overcome the manufacturing limitations observed in previous research, where the resulting substrates had low specific surface area, requiring higher overall catalyst volume [14]. The samples were manufactured on Admaflex 130 (Admatec Europe BV, The Netherlands) with a X-Y resolution of 40 µm. The printing area consists of a transparent glass surface at the bottom and the building platform, which moves vertically up and down, at the top. The light source with DMD chip comprising an array of several thousand microscopic mirrors that rotate according to the pixels in the image is located under the glass. The Admaflex

130 is equipped with a rotating foil system which transports the slurry on the foil from the reservoir to the manufacturing zone and to the pump where the excess slurry is pumped back to the reservoir. Photopolymerisable light sensitive resin is exposed to the UV light (405 nm), which subsequently cures and hardens the resin. The process of curing layer by layer is repeated until the final three-dimensional green body is built [55]. The commercial ceramic suspension (Z-130, Admatec Europe BV, The Netherlands) was used for manufacturing of the representative diamond lattice sample. The Z-130 feedstock contains a mixture of photosensitive resins and a solid loading of zirconia powder. The layer thickness was set as 25 µm and the exposure time was varied between 1.5 to 2 seconds. The remaining slurry on the surface of the sample was cleaned immersing the sample to ultrasonic bath filled with ethanol. Consequent two thermal treatments were performed to achieve a dense ceramic substrate**.** The debinding in a tube furnace (TSH/1S/75/450, Elite Thermal Systems Ltd, United Kingdom) and sintering in a chamber furnace (HTF 17/27, Carbolite Gero, United Kingdom) were performed using cycles recommended by the Admatec company. The final sintered product is shown in Figure 3.6a), with a diameter of 25.4 mm and 61.3 mm length achieved by carefully attaching four shorter substrates with Zirconia Resbond 904 adhesive (Final Advanced Materials, France). The manufactured sample has a pore diameter of 1.85 mm, strut diameter 0.65 mm, specific surface area of 1480 m^{-1} and the porosity of 0.73. The strut thickness was measured on the realised sample with Digital Vernier Caliper (150mm Digital Caliper, RS PRO, United Kingdom) and confirmed with SEM (JCM-6000, JEOL Ltd., Japan) as reflected in Figure 3.6b), similar approach was used by [14,56]. The benchmark cordierite honeycomb used for the experimental validation has square channels with a cell diameter of 1.05 mm, separated by 0.2 mm walls. The diameter of the sample is 25 mm and the length is 57 mm. The geometric specific surface area of the sample is 2870 m^{-1} with the porosity of 0.68.

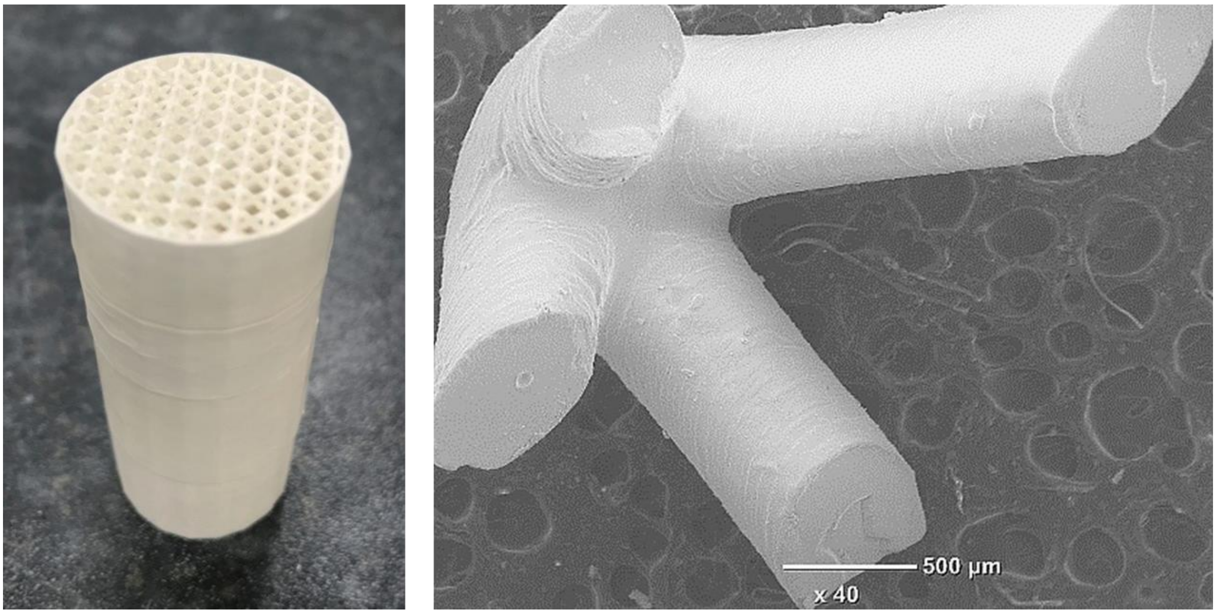

a) b)

Figure 3.6 Image of the a) Final AM lattice with internal diamond structure b) SEM image of one diamond cell of the AM substrate with apparent AM layers

3.2.4 Experimental setup

A bespoke test facility was designed and constructed to allow for heat transfer characterisation and pressure drop measurements of both, the conventional honeycomb support and the novel additive manufactured lattice support. The main functions of the test facility are to measure the inlet and outlet air temperature, surface temperature of the substrate and lastly to measure the pressure drop over the substrate. The schematic of the experimental setup is shown in Figure 3.7a). Compressed air is fed into variable flow meter (Omega, FL-2517, accuracy: ±5% of full-scale reading, Omega Engineering, United Kingdom) with a valve used to control the flow rate. The air flow is lead through a heated line and stainless-steel spiral placed in the furnace to heat the air to a high temperature. The sample is wrapped with insulation mat and placed into the testing section.

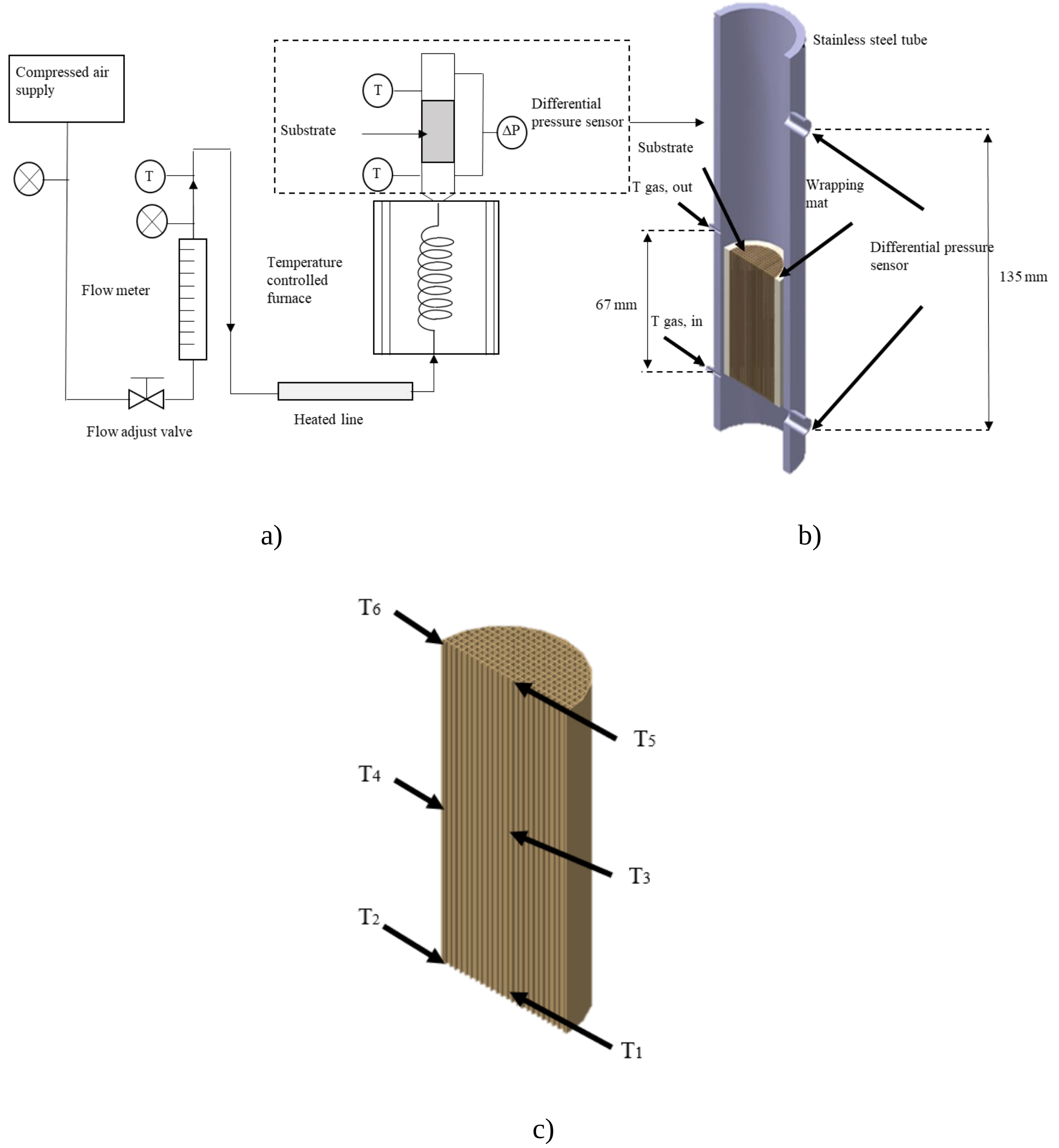

Figure 3.7 a) Schematic of the experimental setup b) CAD model of the cross-section of the testing section with the main segments c) Position of the thermocouples to measure temperature in centre points (T_1, T_3, T_5) and at the surface of the substrate (T_2, T_4, T_6)

Once the air before the substrate ($T_{gas,\ in}$) reaches 923 K and the values of interest do not change over time, the system is being considered in steady-state and the temperatures and differential pressure values are captured. The vertical testing section shown in Figure 3.7b) is equipped with two openings for the differential pressure sensor (NXP MPX5010DP piezoresistive transducers with 5.0% maximum error, range 0 to 10 kPa, RS Components Ltd, United Kingdom) connection and two openings for temperature (K type, TC direct, United Kingdom) measurements before and after the substrate sample. Temperatures across the substrate (T_1, T_2, T_3, T_4, T_5, T_6) were measured to obtain the temperature distribution as depicted in Figure 3.7c). The air volumetric flow rate is controlled to yield mass flow rates of 0.4 kg/h, 0.7 kg/h, 1.1 kg/h and 1.8 kg/h representing the range of gas space hourly velocities (GHSV) of approximately 30 000 to 170 000 h^{-1}.

3.3 Results and discussion

3.3.1 Model validation

The pressure loss of substrates is highly dependent on the channel design, geometry, length and hydraulic diameter of the channels [47]. The substrates must be designed in a way to offer high surface area for catalytic reactions, low backpressure and fast light-off without compromises in mechanical properties. Therefore, our aim is to understand the pressure drop and thermal behaviour of both the conventional honeycomb and diamond lattice structures. The validation of the numerical model consists of comparing the experimental results for pressure drop and temperature (T_1, T_2, T_3, T_4, T_5, T_6) with results obtained by numerical simulations. The validation has been achieved for various mass flow rates. The obtained results for the temperature distribution showed similar trends, hence for simplification purposes only the results for 1.1 kg/h are presented. The lattice sample is 4 mm longer than the 400 CPSI honeycomb substrate due to the manufacturing limitations. However, it is believed the minor difference in the length of the lattice will not have a great impact on the obtained results. The validation of Computation Fluid Dynamic models for both lattice and honeycomb design is presented in this section.

3.3.2 Validation of model for the honeycomb structure

Figure 3.8 shows the experimental results of the pressure drop for honeycomb substrate with varying mass flow rate (0.4-1.1 kg/h) and constant inlet gas temperature of 923 K. Note that the error bars are in the order of graph point size.

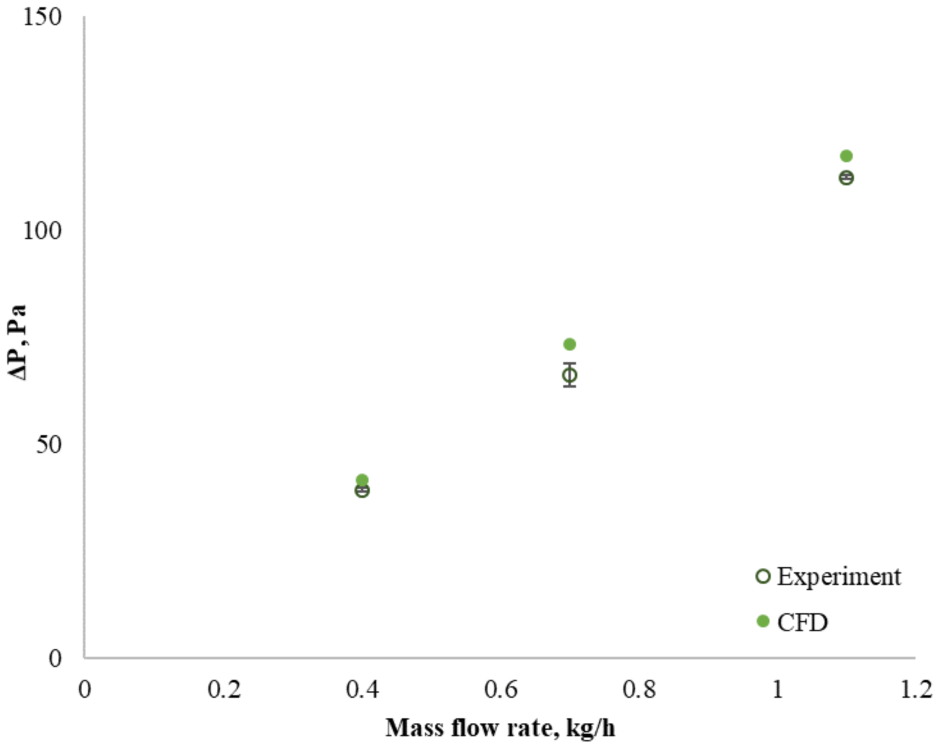

Figure 3.8 Comparison of the experimental and numerical results for pressure drop of the honeycomb monolith at various flow rates

Due to the small channel diameter (1.05 mm) and low Reynolds number (< 2300) the channels exhibit laminar flow behaviour. The model predicts the minimum pressure drop for the lowest flow rate (0.4 kg/h) as 41 Pa with a linear increase of the pressure drop with the increase in the mass flow rate, resulting in pressure drop of 117 Pa at the highest examined flow rate (1.1 kg/h). Similar trend where the pressure drop shows a linear dependency to the mass flow rate is found in the literature [47,57]. It can be concluded that the CFD prediction results for pressure drop agree well with experimentally measured pressure drops.

The second part of the study is to validate the numerical model against experimental data for temperature measurements. Figure 3.9 shows the temperature distribution along the honeycomb substrate, at the surface as well as the centre, with mass flow rate of 1.1 kg/h. Note that the error bars lie within the point. The maximum temperature equal to the inlet gas temperature of 923 K is found at the centre of the inlet of the honeycomb substrate. The temperature gradually decreases as the flow reaches the exit of the substrate and the lowest temperature point is located at the outer surface of the honeycomb substrate with a value of 768 K. The temperature gradient between the centre and the surface of the monolith is expected due to the heat losses to the surroundings. The axial gradient from the inlet centre to the exit centre is around $\Delta T_{T1\text{-}T5}$=82 K for the honeycomb substrate highlighting the non-uniform axial temperature distribution. Very good agreement between the CFD model prediction and experimental results with a maximum of 3.5% error at the mass flow rate of 1.1 kg/h is achieved.

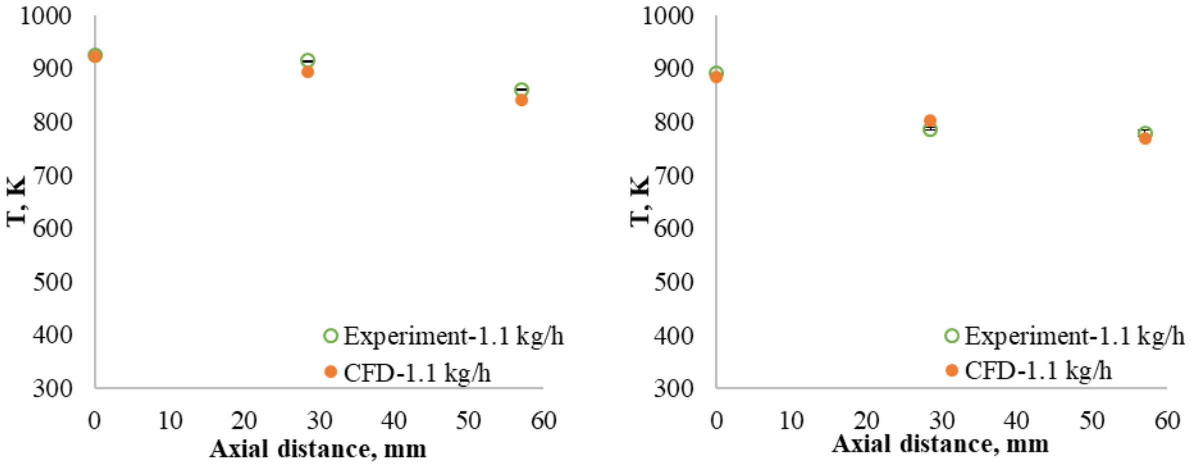

a) b)

Figure 3.9 Comparison of the experimental and numerical results for temperature distribution along the honeycomb monolith a) Centre points (T_1, T_3, T_5) and b) Surface points (T_2, T_4, T_6) at the mass flow rate of 1.1 kg/h

3.3.3 Validation of model for lattice structures

Validation study with respect to the obtained experimental results is performed to determine the accuracy of the model with lattice structures. The lattice substrate has a diameter of 25.4 mm with 61.3 mm length, pore diameter of 1.85 mm, strut diameter of 0.65 mm, specific surface area of 1480 m^{-1} and the porosity of 0.73. Figure 3.10 shows the model validation of the pressure drop for lattice substrate with varying mass flow rate (0.7-1.8 kg/h) and constant inlet gas temperature of 923 K. The pressure drop linearly increases with the flow rate and at the highest flow rate examined (1.8 kg/h) is 78 Pa as seen in Figure 3.10. The linear dependence is expected in the examined mass flow rate range where the maximum inlet velocity at the highest mass flow rate is equal to 1.6 m/s. Exponential trend for lattice structures is observed in literature for higher velocities [14,58,59]. The numerical model over predicts the pressure drop values for 0.7 and 1.1 kg/h, but slightly under predicts the value at the highest flow rate (1.8 kg/h) by 1.6%. The percentage error between the experimental and numerical data is decreasing with the increase of the mass flow rate. Higher percentage error between the lowest flow rate pressure drop obtained by experiment and simulation of 13.7% is explained by possible instrument uncertainty in the given range. Namely, the value of pressure drop in the experiment is 22 Pa while the differential pressure device has a maximum error of 5% in the instrument range. This observation is assumed to be correct owing to the reduction of percentage error with the increase of the mass flow rate. The numerical results for pressure drop agree well with experimentally measured pressure drop.

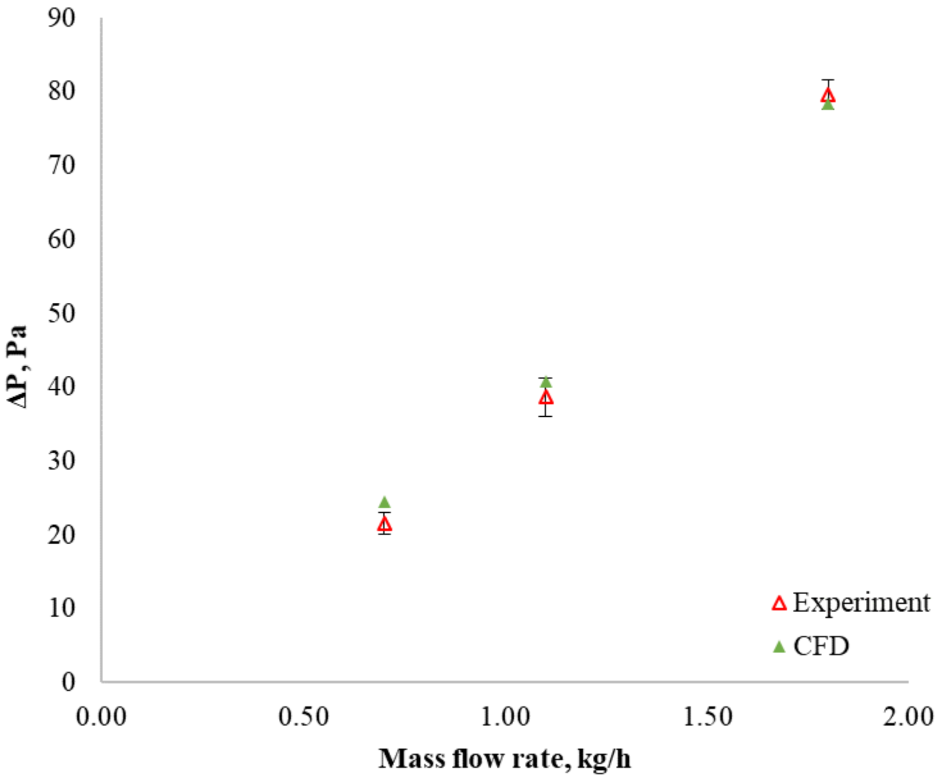

Figure 3.10 Comparison of the experimental and numerical results for pressure drop of the lattice structure for various mass flow rates

The same validation approach as in the honeycomb model has been applied for the temperature distribution. Figure 3.11 shows the temperature distribution along the axial length of the lattice substrate, at the surface as well as the centre, at mass flow rate of 1.1 kg/h. Note that the error bars lie within the point. Maximum temperature is located at the inlet centre of the lattice substrate with a value of 922 K, whereas the lowest temperature is located at the exit outer surface with a value of 694 K. The predicted temperatures calculated with the numerical model follow the same trend as in the experiments. The highest temperature values are located in the inlet centre of the sample, whereas the lowest temperatures are located towards the outer surface of the sample. Heat losses to the surroundings cause the radial temperature gradient in the lattice substrate, the same as for the honeycomb substrate. The axial gradient from the inlet centre to the exit centre is around $\Delta T_{T1\text{-}T5}$=66 K for the lattice substrate, 20% lower than for the honeycomb substrate. Generally, the numerical data is closely matched with the experimental data with the highest discrepancy of 9.6% between the calculated and measured temperatures.

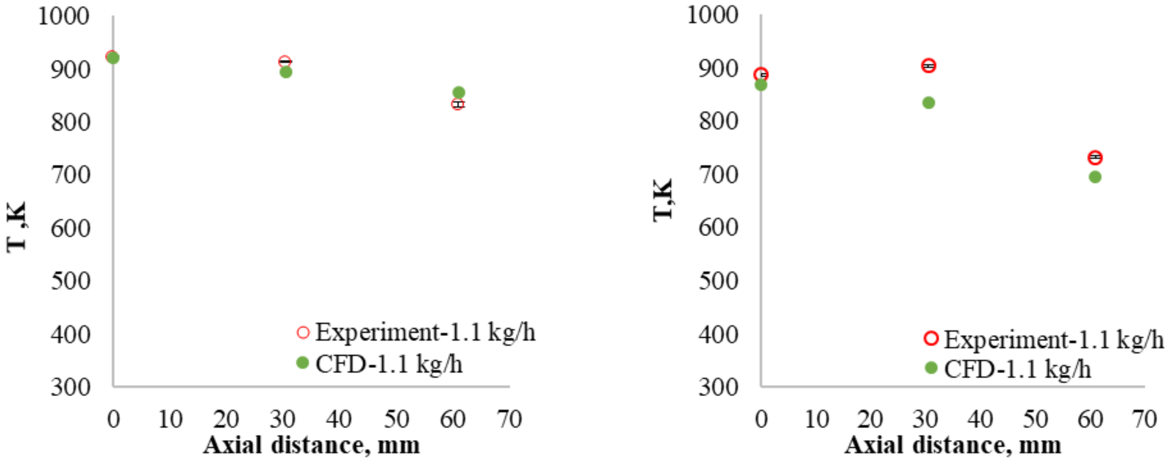

a) b)

Figure 3.11 Temperature in the a) Centre (T_1, T_3, T_5) and b) Surface (T_2, T_4, T_6) of the lattice at the mass flow rate of 1.1 kg/h

Numerical models have been validated for both benchmark honeycomb substrate and a lattice substrate. For the honeycomb model, the pressure drop can be predicted with a maximum error of less than 10% and the predicted temperatures show a deviation of approximately 4% from the experimental results. Lattice model can predict the pressure drops with a maximum error below 14% in the studied range, while the temperatures show a maximum deviation of less than 10% from the experimental results. Both models show good agreement with the experiment.

3.3.4 Comparison between the honeycomb and lattice designs with the same cell density

CFD model has been validated for a lattice with pore diameter (d_p) of 1.85 mm, although the DLP technology is superior to SLA for manufacturing of complex geometries, the ceramic slurry formulation needs to be optimised for a successful print with thinner struts and smaller cell sizes. However, to have a fair comparison between the honeycomb and the lattice design, the same cell density is investigated with the validated numerical model. Square channelled honeycomb monolith with 400 CPSI and 0.2 mm thick walls was chosen as the benchmark. The investigated lattice has identical pore diameter of 1.05 mm as the honeycomb, with strut diameter of 0.2 mm, porosity of 0.87 and specific surface area of 2062 m^{-1}. The diameter and the length of both models were kept the same to rule out any dimensional effects. The corresponding values are 12.5 mm and 57 mm for diameter and length, respectively.

Velocity

In the actual honeycomb channels, the velocity is affected by the flow maldistribution, consequently affecting the residence time and conversion efficiency, therefore resulting in utilisation of only a part of the substrate [10,60]. Research has found that the reactions do not influence the flow distribution as much as the heat loss to the surroundings [10], therefore it is feasible to study the flow distribution in non-reactive conditions. It has similarly been determined that the heat losses cause variations in temperature profile in the monolith [61]. The velocity flow field is likely to present some essential differences between honeycomb monoliths and lattices. Below, we investigate the differences in the air flow velocity field between the honeycomb and the lattice.

Figure 3.12 shows the air velocity contours at mass flow rate of 1.1 kg/h for both honeycomb and lattice substrates. According to the Figure 3.12a) the incoming air flow velocity increases instantly after entering the honeycomb channels due to the reduction in the cross-sectional area. As expected, each channel exhibits parabolic velocity profile with the maximum velocity at the centre of the channel and zero at the walls of the channels [10]. The velocity increases to the highest velocity of 4.02 m/s in the centre of the channel for the flow rate of 1.1 kg/h. As opposed to the single-channel model, generally used to model the monolith flow behaviour, the channels do not show identical velocity profile [10]. Channels close to the periphery of the substrate show higher maximum velocity than the channels in the centre of the sample due to the fluid's physical properties at the periphery. Since the air is treated as compressible fluid, the specific volume decreases along the channel length due to the decrease in temperature causing the decrease in the average velocity in axial direction in the substrates.

Figure 3.12b) presents the velocity field contour for the lattice. The flow distribution can be explained as a combination of external flow around cylinders and internal flow between the lattice cells. Flow path in the lattice becomes tortuous where the velocity of the fluid changes rapidly as the fluid comes in contact with the lattice struts [59]. The struts of the lattice present resistance to the fluid flow with forward stagnation point and wake region behind the strut. Maximum velocity is observed in between the lattice cells with a value of 3.08 m/s. The overall lower velocity values in the lattice can benefit the efficiency of the substrate due to the increase of the residence time of the flow in the substrate and increased flow to solid interaction. Moreover, the reduction of the overall velocity could have influence on the thermal degradation of the substrate brick and pressure drop decrease across the entire substrate [62].

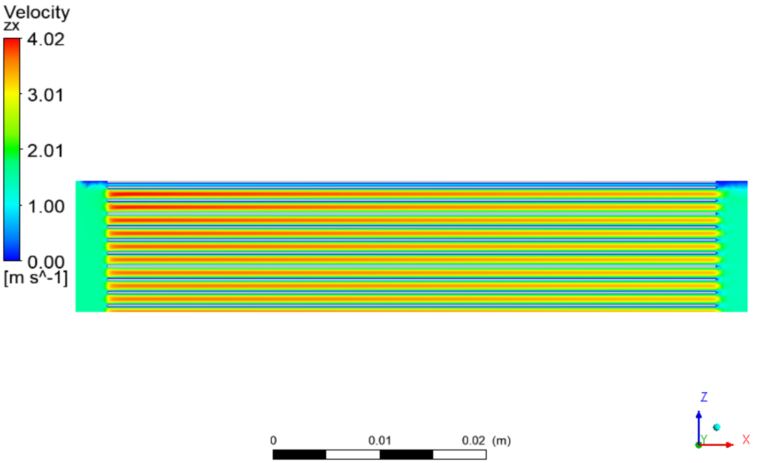

a)

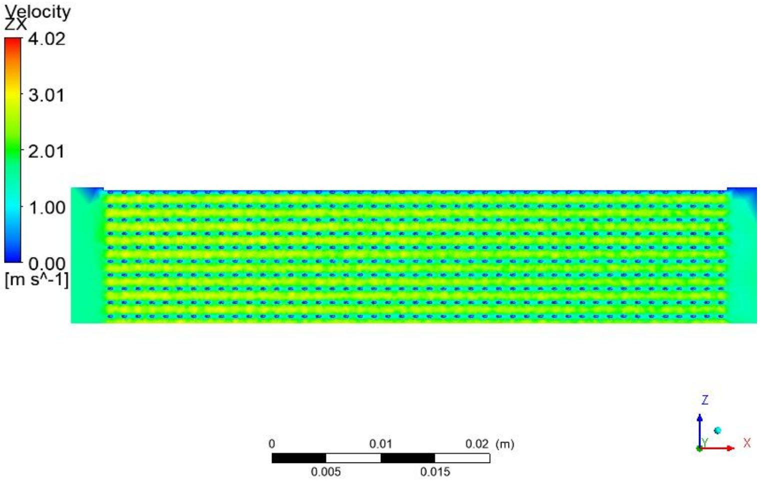

b)

Figure 3.12 Velocity field contour for the a) 400 CPSI honeycomb at the inlet mass flow rate of 1.1 kg/h (ZX plane) b) Velocity field contour for the lattice at the inlet mass flow rate of 1.1 kg/h (ZX plane)

Pressure drop

Reliable comparison of the backpressure between the lattice and honeycomb sample is achieved using the values of normalised pressure drop presented as pressure drop over length of the sample. The comparison of the pressure drop for a lattice with same pore density as the benchmark honeycomb is shown in Figure 3.13. In the mass flow rate range of interest, the pressure drop of the honeycomb varies linearly with the mass flow rate [47, 56, 62]. Considering the flow in the honeycomb channels is fully laminar, the viscous effects are the main contributor to the pressure drop in the studied mass flow rate range [60]. Furthermore, the pressure drop follows the same linear trend in the examined mass flow rate range for the lattice structure.

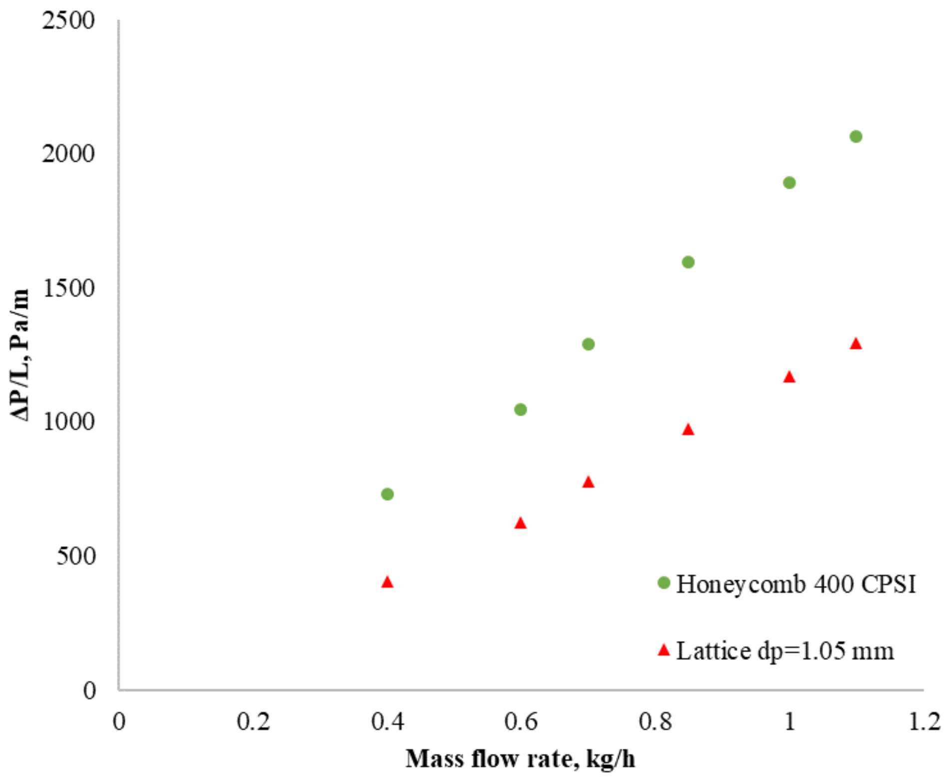

Figure 3.13 Normalised pressure drops versus mass flow rate for 400 CPSI HC and lattice with d_p =1.05 mm

In contrast to the honeycomb substrate, the pressure drop across the d_p=1.05 mm lattice is 38-45% lower. The lower pressure drop is a consequence of the higher porosity of the lattice. Namely, the higher porosity significates that the void fraction, which is available for the fluid flow in the lattice structure, is higher. Similarly, lower pressure drop with respect to the honeycomb, at low mass flow rates has been observed in literature for open cell substrates with a porosity of 0.95 [14].

Thermal properties

It is expected that the tortuous pathway of the lattice substrate can enhance the heat transfer and minimise the manifestation of hot spots that cause catalyst deactivation. Interconnected solid struts in the internal structure of the lattice structure allow cross-mixing of the flow leading to an augment of the heat transfer [63]. The studies demonstrate that flow distribution within the honeycomb has an immense influence on the distribution of temperature and species concentration in the substrate [64]. Therefore, thermal properties of the honeycomb and lattice were investigated. Figure 3.14 shows the temperature distribution contours using 1.1 kg/h mass flow rate for honeycomb and lattice substrate. In case of the honeycomb, as seen in Figure 3.14a), the area with the peak temperature, equal to the temperature of the incoming gas, is located in the central region of the substrate. The contour shown for honeycomb implies that by increasing the axial distance the temperature gradient from the inlet face to the outlet face increases. Decrease of the temperature radially to the direction of the surface of the substrate is a consequence of the heat losses to the ambient [1,10,64]. The shape of the peak temperature region shows a downward slope in axial direction indicating the highest heat transfer in the inlet central region of the honeycomb.

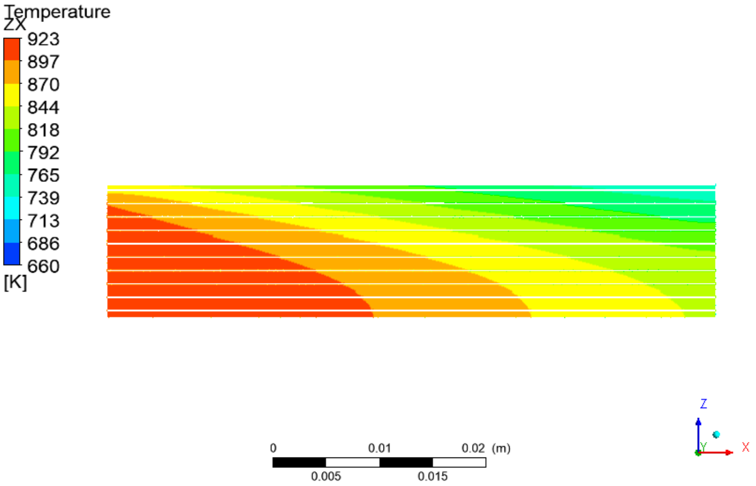

a)

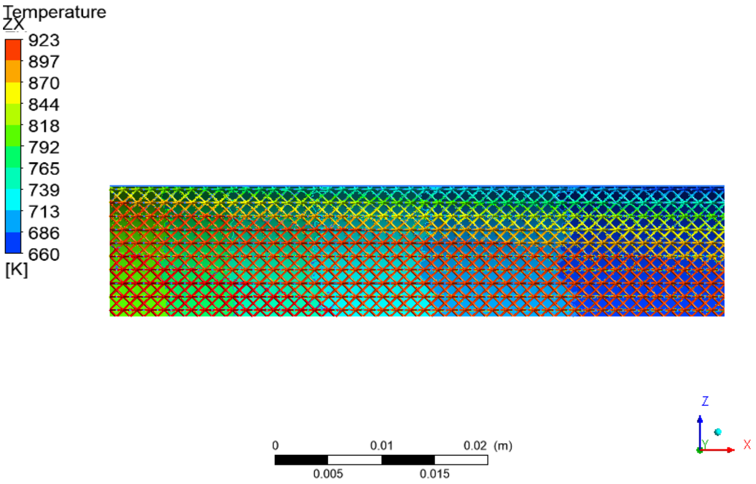

b)

Figure 3.14 Temperature contour of a) Honeycomb with 400 CPSI cell density and 0.2 mm walls and b) Diamond lattice with 1.05 mm pore diameter and 0.2 mm strut diameter at mass flow rate of 1.1 kg/h

On the other hand, the diamond lattice (Figure 3.14b)) has a more uniform temperature distribution at the whole core region in the axial direction indicating the higher heat transfer caused by less thermal mass. The peak temperature region has a downward slope trend from the inlet to the exit region.

The channel flow and the presence of the solid walls in the honeycomb, cause limitations in radial heat transport. In contrast, the solid material of the honeycomb substrate increases thermal resistance and causes higher temperatures towards the substrate's outer surface. The same temperature distribution trend is expected at lower inlet temperatures.

Further optimisation of the lattice design is needed to obtain higher temperatures at the outer surface of the substrate. It can be concluded that the lattice substrate performed better thermally and hydraulically. The predictions of the pressure gradient presented the same trend in which the pressure drop across the lattices is lower regardless of the increase of the mass flow rate as compared to the benchmark honeycomb in the studied range. This pressure drop study indicates that utilising the lattice design is significantly more efficient due to the lower pressure drop and lower average velocity in comparison to the 400 CPSI HC. The d_p=1.05 mm lattice substrate showed improvement in the thermal performance showing lesser axial temperature gradients in the core of the substrate. The lower temperature at the periphery of the lattice is a consequence of the lower amount of solid phase causing higher heat dissipation to the surroundings. Hence, the lattice design should be optimised to achieve higher temperatures at the outer surface.

3.3.5 Effect of the lattice design on the substrate performance

The main parameters of the lattice are the strut diameter (d_s), strut length (L_s), cell length (L_c), pore diameter (d_p), porosity (ε) and the specific surface area (S_v). The strut diameter affects the porosity, the specific surface area of the substrate as well as the mechanical strength. If the volume of the substrate is to be constant, the feasible increase of the lattice porosity is achievable by increasing the pore size. Should the pore size be double, samples with up to 94% porosity are achievable. Doubling the pore size, on the other hand, decreases the surface area by half. The specific surface area (S_v) of the lattice substrate has a large influence on the resulting temperature profile [65]. Current improvements in the ceramic additive manufacturing could allow fabrication of strut diameters as low as 0.2 mm. The strut diameter in this study was varied from 0.2 mm to 0.65 mm, covering a wide range of substrate porosities. Table 3.2 presents the main geometrical properties of the studied lattice structures.

Table 3.2 Main geometrical properties of the lattice structures

ε, -	**d_s, mm**	**d_p, mm**	**L_c, mm**	**L_s, mm**	**S_v, m^{-1}**
0.94	0.2	2	2.2	1.56	950
0.90	0.3	2	2.3	1.63	1090
0.79	0.5	2	2.5	1.77	1290
0.73	0.65	2	2.65	1.87	1333

Figure 3.15 shows the effect of the strut diameter on the specific surface area and the effect of porosity of the diamond lattices on the specific length ratio. Specific surface area increases with the increase of the strut diameter as pictured in Figure 3.15a). As an overall trend, the specific surface increased with increasing the cell size and strut thickness at constant pore diameter. The specific length ratio, Φ, representing the ratio of pore diameter and strut thickness, is plotted against porosity in Figure 3.15b). As the specific length ratio increases, the porosity of the sample increases because the strut diameter becomes smaller compared to the pore diameter [13]. Figure 3.16 shows the effect of the lattice porosity (X-axis) on specific surface area (blue bars) and pressure drop (yellow bars). With the decrease of the porosity, specific surface area and pressure drop values increase. The lowest pressure drop of 269 Pa/m is observed for lattice porosity of 0.94, whereas the highest pressure drop of 579 Pa/m is observed for the lattice porosity of 0.73.

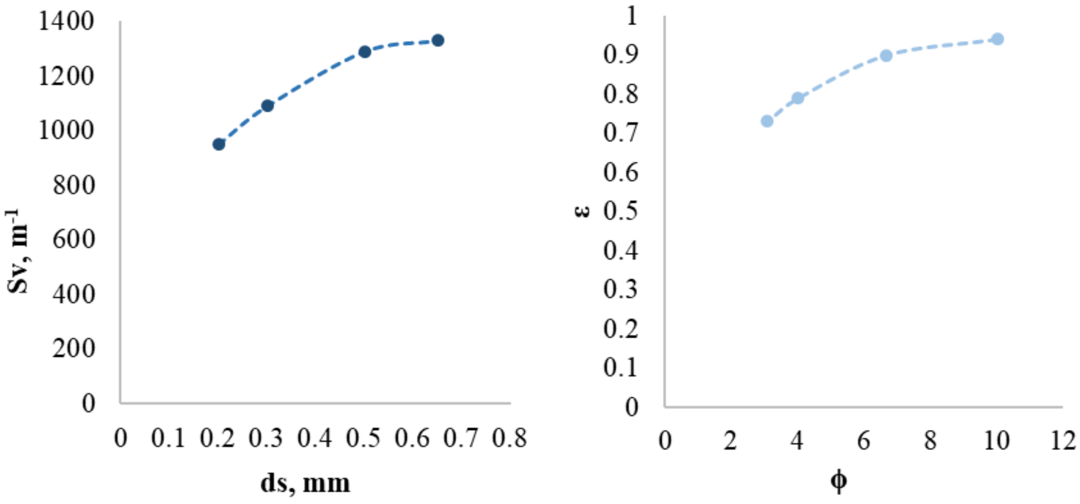

a) b)

Figure 3.15 a) Effect of the strut diameter on the specific surface area b) Effect of the porosity on the specific length ratio

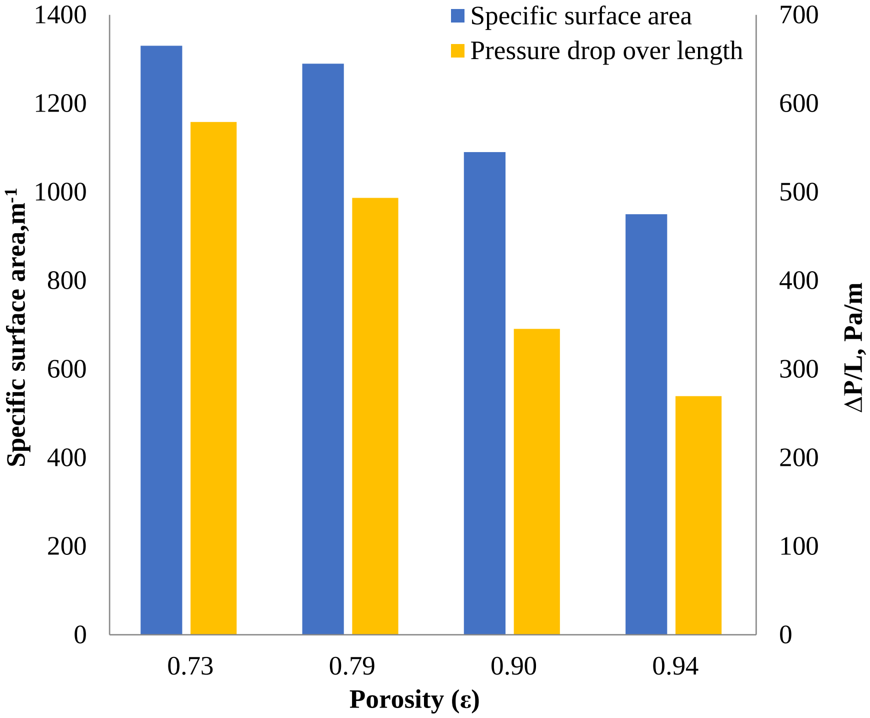

Figure 3.16 Effect of the porosity of the lattice on the pressure drop and specific surface area

The results show the pressure drop is inversely proportional to the porosity, which is in agreement with the literature [26]. On the other hand, the specific surface area of the lattice increases by 29% with the decrease of the porosity from 0.94 to 0.73. The increase of the surface area caused by the increase of the strut diameter at constant pore diameter results in a decrease of the porosity [26]. As a drawback of the increase of the surface area and the decrease of the porosity, the pressure drop increases.

From the results presented in Figure 3.16 it can be concluded that the pressure drop is directly proportional to the specific surface area. Since the increase of the strut diameter increases the amount of the solid phase, the strut diameter increase is expected to have an influence on the heat transfer. Therefore, a study of the strut thickness increase on the temperature distribution is conducted in the following section. The strut diameter was varied from 0.2 mm to 0.65 mm resulting in a decrease of the substrate porosity at constant pore diameter as shown in Table 3.2.

In Figure 3.17 one can see the result of the increasing strut thickness on temperature distribution in lattice substrate at the inlet mass flow rate of 1.1 kg/h. Figure 3.17a) illustrates the temperature contour for the lattice with a strut diameter of 0.2 mm. This design has the least surface area of 950 m^{-1} and the highest porosity of 0.94 among all substrates. The temperature distribution in the solid is uniform throughout the whole core area with steep radial gradients due to the heat loss boundary on the outer surface wall of the lattice. The lowest temperatures are present in the periphery of the substrate as a result of less solid material in the radial direction. Similarly, low axial temperature gradients in the core of the substrate are seen for the lattice with d_s=0.3 mm Figure 3.17b) with sharp radial gradients towards the substrate’s periphery. In comparison, the temperatures are slightly higher at the periphery of the substrate with d_s=0.3 mm than with d_s=0.2 mm due to the thicker outer mat providing more resistance to the external heat loss. Further increase of the strut diameter to 0.5 mm (Figure 3.17c) causes the increase of the axial temperature gradients. On the other hand, the temperature at the periphery of the sample is higher when compared to substrates with d_s= 0.2 mm and d_s= 0.3 mm. The lowest uniformity of temperature in the core of the substrate is apparent when the strut thickness value is 0.65 mm Figure 3.17d). The substrate with d_s=0.65 mm has the lowest porosity of 0.73, hence the highest amount of solid material present in the substrate volume. The increase of the strut diameter results in the decrease of the void to solid ratio. Additionally, the higher the amount of solid, the poorer the heat transfer to the solid resulting in higher temperature gradients.

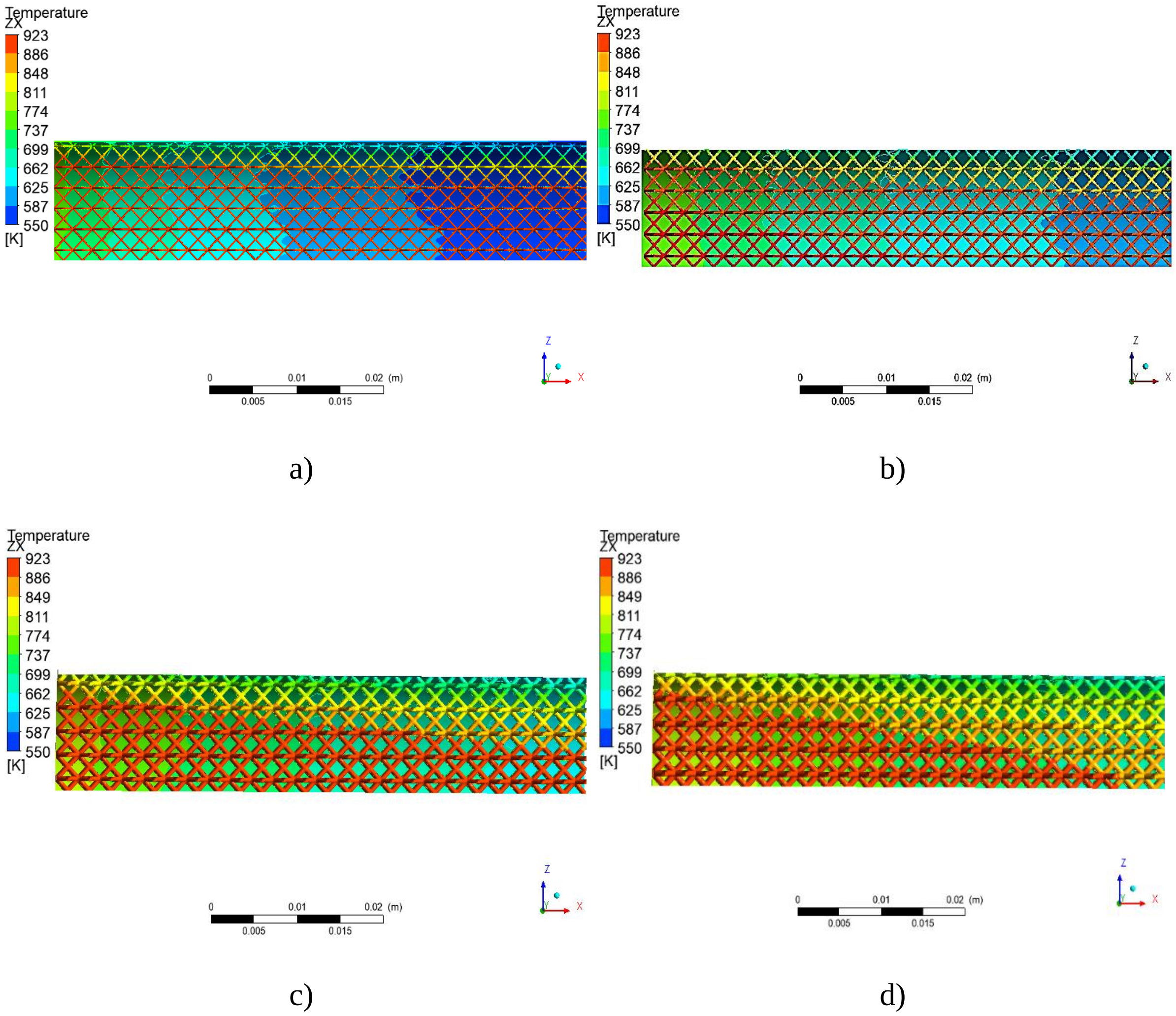

a)

b)

c)

d)

Figure 3.17 Temperature distribution along the lattice substrate at different strut diameters and constant flow rate of 1.1 kg/h a) d_s =0.2 mm b) d_s = 0.3 mm, c) d_s = 0.5 mm, d) d_s =0.65 mm

The highest axial temperature gradients are thereupon observed with the highest strut thickness. The velocity in between the lattice cells for the larger strut diameter is higher, resulting in decrease of the residence time in the lattice following a decrease in total heat transfer.

From the presented contours it can be concluded that the increase of the heat exchange surface formed by the increase of the strut diameter increases the temperature gradient over the core region. Nevertheless, the increase of the solid phase has a positive influence on the temperatures in the substrate periphery. This improvement indicates a possibility of more effective utilisation of the heat within the lattice by tailoring the lattice design and strut thickness where necessary. As described earlier, one of the key design requirements for the monolith substrates is high surface area and low pressure drop. When judging the efficiency of the substrate, priority can be given to higher surface area to increase the conversion efficiency, however with a penalty of increased pressure loss. The increase of the strut diameter results in the increase of the specific surface area due to the additional solid material present in the substrate, however the additional exposed surface slightly increases the pressure drop and increases the temperature gradients. The experimental tests have been performed with the target to make the catalyst more efficient under heating conditions and a similar experiment could have been also performed under cooling conditions. The judgement on the optimal strut thickness must be made considering the environment in which the substrate will be used. The substrate with thicker struts and lower pore density could be retaining more heat during cooling periods because of the higher thermal inertia, whereas the substrate with thinner strut diameter and higher pore density possesses higher surface area and possibility of a quicker warm up.

3.4 Conclusions

In this study, an additively manufactured ceramic diamond lattice substrate has been proposed to overcome the limitations of the conventional honeycomb substrate. DLP additive manufacturing technology has been successfully used to manufacture the diamond lattice substrate. The comparison of the honeycomb design and the diamond lattice has been achieved by pairing numerical simulations and experimental studies with additive manufacturing.
The effect of the cell size and strut diameter on the geometric characteristic as well as pressure drop and temperature distribution were studied through numerical simulations.

The key findings of this study may be summarised as follows:

- DLP additive manufacturing technology enables fabrication of self-supported ceramic diamond lattice substrates.
- As an overall trend, the specific surface area of the lattice increases with increasing the cell size and strut thickness at constant pore diameter. As a consequence, the increase of the surface area results in a decrease of the porosity which results in the increase of the pressure drop.
- The pressure drop across the diamond lattices is lower regardless of the lattice pore size as compared to the honeycomb, with a decrease of up to 80%, but with a penalty of lower surface area.
- The lattice with a pore size of 1.05 mm and strut thickness of 0.2 mm with a similar surface area as the honeycomb substrate, demonstrates a decrease of pressure drop by 38-45% at studied flow rates.
- Diamond lattices exhibit lower axial temperature gradients for all porosities examined. The lattices display homogeneous temperature distribution at the core area relative to a

conventional honeycomb design, indicating the higher heat transfer properties caused by the tortuosity of the flow and the ability of flow exchange in both radial and axial direction. This improvement indicates a possibility of more effective utilisation of the heat within the lattice.

The reduction of the backpressure could have a positive impact on the fuel economy, while the improved core temperature distribution allows to conclude that the lattice structure could have better thermal performance in the exhaust system. The findings have repercussions for prospective improvement of the design of the ceramic catalytic supports by utilisation of DLP additive manufacturing technology. The diamond lattice could be specifically tailored to yield desired temperature distribution and pressure drop by controlling the strut diameter and cell size. Further design improvement of the diamond lattice is needed to obtain higher temperatures at the periphery of the substrate, as well as coating and testing with the actual exhaust gas to get the insights on the conversion efficiency and warm-up/ cool down behaviour of the diamond lattice structures.

Acknowledgements

The research leading to these results has received funding from the Engineering and Physical Sciences Research Council for project FACE - Novel Integrated Fuel Reformer-Aftertreatment System for Clean and Efficient Road Vehicles under grant number EP/P03117X/1. N.K. also thanks the University of Birmingham for award of a PhD scholarship.

References

1. Ibrahim HA, Ahmed WH, Abdou S, Blagojevic V. Experimental and numerical investigations of flow through catalytic converters. Int J Heat Mass Transf. 2018;127:546–60.
2. Shaw BT, Fischer GD, Hedrick JK. A Simplified Coldstart Catalyst Thermal Model To Reduce Hydrocarbon Emissions. 15th Triennial World Congress. Barcelona, Spain: IFAC; 2002. p. 307–12.
3. Boger T, Heibel AK, Sorensen CM. Monolithic catalysts for the chemical industry. Ind Eng Chem Res. 2004;43(16):4602–11.
4. Williams JL. Monolith structures, materials, properties and uses. Catal Today. 2001;69:3–9.
5. Govender S, Friedrich H. Monoliths: A Review of the Basics, Preparation Methods and Their Relevance to Oxidation. Catalysts. 2017;7(2):62.
6. Nijhuis TA, Beers AEW, Vergunst T, Hoek I, F. K, Moulijn JA. Preparation of monolithic catalysts. Stud Surf Sci Catal. 2001;43:345–80.
7. Avila P, Montes M, Miró EE. Monolithic reactors for environmental applications: A review on preparation technologies. Chem Eng J. 2005;109(1):11–36.
8. Lachman IM, Williams JL, Park S. Extruded monolithic catalyst supports. Catal Today. 1992;14:317–29.
9. Chakravarthy VK, Conklin JC, Daw CS, D'Azevedo EF. Multi-dimensional simulations of cold-start transients in a catalytic converter under steady inflow conditions. Appl Catal A Gen. 2003;241(1–2):289–306.
10. Agrawal G, Kaisare NS, Pushpavanam S, Ramanathan K. Modeling the effect of flow mal-distribution on the performance of a catalytic converter. Chem Eng Sci. 2012;71:310–20.
11. Goralski CT, Chanko TB. Modeling the effect of substrate cell shape on conversion in monolith catalysts. SAE Tech Pap Ser. 2010;1(724).
12. Soltani S, Wang-Hansen C, Andersson R, Andersson B. CFD characterization of monolithic reactors for kinetic studies. Can J Chem Eng. 2014;92(9):1570–8.
13. Busse C, Freund H, Schwieger W. Intensification of heat transfer in catalytic reactors by additively manufactured periodic open cellular structures (POCS). Chem Eng Process Process Intensif. 2018;124:199–214.
14. Papetti V, Dimopoulos Eggenschwiler P, Della Torre A, Lucci F, Ortona A, Montenegro G. Additive Manufactured open cell polyhedral structures as substrates for automotive catalysts. Int J Heat Mass Transf. 2018;126:1035–47.
15. Santoliquido O, Bianchi G, Dimopoulos Eggenschwiler P, Ortona A. Additive manufacturing of periodic ceramic substrates for automotive catalyst supports. Int J Appl Ceram Technol. 2017;14(6):1164–73.
16. Aslan B, Yildiz AR. Optimum design of automobile components using lattice structures for additive manufacturing. Mater Test. 2020;62(6):633–9.
17. Ferrizz RM, Stuecker JN, Cesarano J, Miller JE. Monolithic supports with unique geometries and enhanced mass transfer. Ind Eng Chem Res. 2005;44(2):302–8.
18. Li Y, Chen S, Cai X, Hong J, Wu X, Xu Y, et al. Rational design and preparation of hierarchical monoliths through 3D printing for syngas methanation. J Mater Chem A. 2018;6(14):5695–702.
19. Von Rickenbach J, Lucci F, Dimopoulos Eggenschwiler P, Poulikakos D. Pore scale

modeling of cold-start emissions in foam based catalytic reactors. Chem Eng Sci. 2015;138:446–56.

20. Heck RH, Wei J, Katzer JR. The Transient Response of a Monolithic Catalyst Support. In: Chemical Reaction Engineering- II. 1975. p. 34–45.
21. Chen J, Yang H, Wang N, Ring Z, Dabros T. Mathematical modeling of monolith catalysts and reactors for gas phase reactions. Appl Catal A Gen. 2008;345(1):1–11.
22. Pant A, Paramadayalan T. Continuum computational fluid dynamics model of heat transfer in monolith converter. Energy Emiss Control Technol. 2013;1–13.
23. Cornejo I, Nikrityuk P, Hayes RE. The influence of channel geometry on the pressure drop in automotive catalytic converters: Model development and validation. Chem Eng Sci. 2020;212:115317.
24. Amirnordin SH, Seri S, Salim WSW, Rahman HA. Pressure Drop Prediction of Square-cell Honeycomb Monolith Structure. Int Conf Environ Sci Eng (ICESE 2011). 2011;8:281–5.
25. Hayes RE, Fadic A, Mmbaga J, Najafi A. CFD modelling of the automotive catalytic converter. Catal Today. 2012;188(1):94–105.
26. Nie Z, Lin Y, Tong Q. Numerical investigation of pressure drop and heat transfer through open cell foams with 3D Laguerre-Voronoi model. Int J Heat Mass Transf. 2017;113:819–39.
27. Falfari S, Micci G, Bianchi GM, Brusiani F, Montenegro G, Torre A Della, et al. Design of catalytic devices by means of genetic algorithm: Comparison between open-cell foam and honeycomb type substrates. SAE Int J Engines. 2016;9(3).
28. Lucci F, Della Torre A, Montenegro G, Dimopoulos Eggenschwiler P. On the catalytic performance of open cell structures versus honeycombs. Chem Eng J. 2015;264:514–21.
29. Lucci F, Della Torre A, von Rickenbach J, Montenegro G, Poulikakos D, Dimopoulos Eggenschwiler P. Performance of randomized Kelvin cell structures as catalytic substrates: Mass-transfer based analysis. Chem Eng Sci. 2014;112:143–51.
30. Ferrari L, Barbato MC, Ortona A, Angelo CD. Convective Heat Transfer In Cellular Ceramic: A 3D Numerical Solution. In: 10th International Conference on Heat Transfer, Fluid Mechanics and Thermodynamics (HEFAT 2014). Orlando, Florida; 2014. p. 476–81.
31. Pusterla S, Barbato M, Ortona A, D’Angelo C. Numerical study of cell morphology effects on convective heat transfer in reticulated ceramics. Int J Heat Mass Transf. 2012;55(25–26):7902–10.
32. Kumar V, Manogharan G, Cormier D. Design of periodic cellular structures for heat exchanger applications. 20th Annu Int Solid Free Fabr Symp. 2009;738–48.
33. Gök A, Demirci HI, Gök K. Determination of experimental, analytical, and numerical values of tool deflection at ball end milling of inclined surfaces. Proc Inst Mech Eng Part E J Process Mech Eng. 2014;230(2):111–9.
34. Gök A. 2D numeric simulation of serrated-chip formation in orthogonal cutting of AISI316H stainless steel. Mater Tehnol. 2017;51(6):953–6.
35. Martínez S, Lamikiz A, Ukar E, Calleja A, Arrizubieta JA, Lopez de Lacalle LN. Analysis of the regimes in the scanner-based laser hardening process. Opt Lasers Eng. 2017;90:72–80.
36. Essa K, Sabouri A, Butt H, Basuny FH, Ghazy M, El-Sayed MA. Laser additive manufacturing of 3D meshes for optical applications. PLoS One. 2018;13(2):4–11.
37. Sabouri A, Yetisen AK, Sadigzade R, Hassanin H, Essa K, Butt H. Three-Dimensional Microstructured Lattices for Oil Sensing. Energy and Fuels. 2017;31(3):2524–9.

38. Elsayed M, Ghazy M, Youssef Y, Essa K. Optimization of SLM process parameters for Ti6Al4V medical implants. Rapid Prototyp J. 2019;25(3):433–47.
39. Zocca A, Colombo P, Gomes CM, Günster J. Additive manufacturing of ceramics: Issues, potentialities, and opportunities. J Am Ceram Soc. 2015;98(7):1983–2001.
40. Li X, Zhong H, Zhang J, Duan Y, Bai H, Li J, et al. Dispersion and properties of zirconia suspensions for stereolithography. Int J Appl Ceram Technol. 2020;17(1):239–47.
41. Hassanin H, El-Sayed MA, Elshaer A, Essa K, Jiang K. Microfabrication of net shape zirconia/alumina nanocomposite micro parts. Nanomaterials. 2018;8(8).
42. He R, Liu W, Wu Z, An D, Huang M, Wu H, et al. Fabrication of complex-shaped zirconia ceramic parts via a DLP- stereolithography-based 3D printing method. Ceram Int. 2018;44(3):3412–6.
43. Bianchi G, Gianella S, Ortona A. Design and additive manufacturing of periodic ceramic architectures. J Ceram Sci Technol. 2017;8(1):59–66.
44. Essa K, Hassanin H, Attallah MM, Adkins NJ, Musker AJ, Roberts GT, et al. Development and testing of an additively manufactured monolithic catalyst bed for HTP thruster applications. Appl Catal A Gen. 2017;542:125–35.
45. Bach C, Eggenschwiler PD. Ceramic foam catalyst substrates for diesel oxidation catalysts: Pollutant conversion and operational issues. SAE Tech Pap. 2011;20110459.
46. Ibrahim HA, Abdou S, Ahmed WH. Understanding Flow through Catalytic Converters. Proceedings of the 4th International conference of Fluid Flow, Heat and Mass Transfer (FFHMT'17). Toronto. 2017.
47. Amirnordin SH, Seri SM, Salim WS-IW, Rahman HA, Hasnan K. Pressure Drop Analysis of Square and Hexagonal Cells and its Effects on the Performance of Catalytic Converters. Int J Environ Sci Dev. 2011;2(3):239–47.
48. ANSYS,Release 16.2, ANSYS CFX-solver theory guide, ANSYS, 2016, https://www.ansys.com/products/fluids/ansys-cfx. 2015.
49. Lynch CT. CRC Handbook of Material Science, Volume III: Nonmetallic Materials and Applications. In Boca Raton, FL: CRC Press; 1975.
50. Zhao H, Yu F, Bennett TD, Wadley HNG. Morphology and thermal conductivity of yttria-stabilized zirconia coatings. Acta Mater. 2006;54(19):5195–207.
51. Koltsakis GC. Warm-up behavior of monolithic reactors under non-reacting conditions. Chem Eng Sci. 1997;52(17):2891–9.
52. Durat M, Parlak Z, Kapsiz M, Parlak A, Fiçici F. Cfd and Experimental Analysis on Thermal Performance of Exhaust System of a Spark Ignition Engine. J Therm Sci Technol. 2013;33(2):89–99.
53. Fernández-Yáñez P, Armas O, Gómez A, Gil A. Developing computational fluid dynamics (CFD) models to evaluate available energy in exhaust systems of diesel light-duty vehicles. Appl Sci. 2017;7(6).
54. Lage JL, Lemos MJS De, Nield DA. 8 - Modeling Turbulence in Porous Media. In: Transport Phenomena in Porous Media II. Oxford: Pergamon; 2002. p. 198–230.
55. Varghese G, Moral M, Castro-García M, López-López JJ, Marín-Rueda JR, Yagüe-Alcaraz V, et al. Fabrication and characterisation of ceramics via low-cost DLP 3D printing. Bol la Soc Esp Ceram y Vidr. 2018;57(1):9–18.
56. Inayat A, Schwerdtfeger J, Freund H, Körner C, Singer RF, Schwieger W. Periodic open-cell foams: Pressure drop measurements and modeling of an ideal tetrakaidecahedra packing. Chem Eng Sci. 2011;66(12):2758–63.
57. Tsinoglou DN, Koltsakis GC, Missirlis DK, Yakinthos KJ. Transient modelling of flow distribution in automotive catalytic converters. Appl Math Model. 2004;28(9):775–94.

58. Dimopoulos Eggenschwiler P, Tsinoglou DN, Seyfert J, Bach C, Vogt U, Gorbar M. Ceramic foam substrates for automotive catalyst applications: Fluid mechanic analysis. Exp Fluids. 2009;47(2):209–22.
59. Inayat A, Klumpp M, Lämmermann M, Freund H, Schwieger W. Development of a new pressure drop correlation for open-cell foams based completely on theoretical grounds: Taking into account strut shape and geometric tortuosity. Chem Eng J. 2016;287:704–19.
60. Ekström F, Andersson B. Pressure Drop of Monolithic Catalytic Converters Experiments and Modeling. SAE Tech Pap Ser. 2010;1(724).
61. Kumar A, Mazumder S. Toward simulation of full-scale monolithic catalytic converters with complex heterogeneous chemistry. Comput Chem Eng. 2010;34(2):135–45.
62. Kim JY, Son S. Improving flow efficiency of a catalytic converter using the concept of radially variable cell density - Part I. SAE Tech Pap Ser. 1999;(724).
63. Bracconi M, Ambrosetti M, Maestri M, Groppi G, Tronconi E. A fundamental analysis of the influence of the geometrical properties on the effective thermal conductivity of open-cell foams. Chem Eng Process - Process Intensif. 2018;129:181–9.
64. Jeong S-J, Kim W-S, Kim T. An application of CFD to improve warm-up performance of the 3-way auto-catalyst by high surface area and low thermal mass. Int J Veh Des. 2005;29(3):243.
65. Klumpp M, Körner C, Inayat A, Schwerdtfeger J, Freund H, Schwieger W, et al. Periodic open cellular structures with ideal cubic cell geometry: Effect of porosity and cell orientation on pressure drop behavior. Chem Eng J. 2014;242:364–78.

CHAPTER 4

EFFECT OF THE PREPARATION TECHNIQUES OF PHOTOPOLYMERISABLE CERAMIC SLURRY AND PRINTING PARAMETERS ON THE ACCURACY OF 3D PRINTED LATTICE STRUCTURES

Authors Contributions:

This chapter of the alternative thesis format is published in the Journal of the European Ceramic Society (2021). I am the first author of this publication. The paper's details and co-authors' contributions are outlined below.

Kovacev N[1], Li S[2], Essa K[*]. Effect of the preparation techniques of photopolymerisable ceramic slurry and printing parameters on the accuracy of 3D printed lattice structures. J Eur Ceram Soc. 2021;41(15):7734–43.

[1] **Nikolina Kovacev:** Main author, designed the experiments, slurry preparation, executed the printing experiments and performed all necessary characterisation and data analysis and wrote the manuscript

[2] **Dr Sheng Li:** Proofreading

***Dr Khamis Essa:** Supervision and proofreading

CHAPTER 4

EFFECT OF THE PREPARATION TECHNIQUES OF PHOTOPOLYMERISABLE CERAMIC SLURRY AND PRINTING PARAMETERS ON THE ACCURACY OF 3D PRINTED LATTICE STRUCTURES

Abstract

Digital Light Processing (DLP) technology demonstrates the potential for manufacturing parts with complex structures for various engineering applications. The purpose of this study is to evaluate Al_2O_3 ceramic slurry preparation techniques, establish optimal processing window and assess the manufacturability and dimensional accuracy of lattice structures with CAD strut diameters of up to 500 µm. Two preparation techniques of the ceramic slurry were investigated. The slurry with the pre-treated powder showed appropriate rheological and photopolymerisation behaviour. Full factorial Design of Experiments (DoE) was conducted to generate an experimental plan and assess the influence of the printing parameters on the dimensional accuracy. Analysis of Variance (ANOVA) revealed the exposure time, the exposure power, and the interaction effect of both had a significant influence on the dimensional accuracy of lattice strut diameters. The excess cure width was found to be dependent on the feature size, the energy dose and the layer thickness.

Keywords: additive manufacturing; DLP; ceramic slurry; lattice; DoE

4.1 Introduction

There is a rapidly growing demand for lattice structures in the industry for various applications ranging from porous bio ceramics in regenerative medicine, reducing the weight of parts for industrial applications, for optical applications, as well as monolithic supports for catalytic applications [1–8]. However, their manufacturing is impossible via well-established conventional methods. A promising alternative to conventional manufacturing is additive manufacturing. Additive Manufacturing (AM) is a process of three-dimensional object manufacturing via the addition of individual layers according to a sliced Computer-Aided Design (CAD) model. Considering the materials processed, plastics and metal AM are currently leading on the market, whereas ceramic AM has been gaining lots of interest recently [9,10]. Ceramic AM is generally divided into two categories: indirect and direct. The majority of the ceramic AM processes include indirect technologies [11]. These are, to name a few, Laminated Object Manufacturing (LOM), Selective Laser Sintering (SLS) and Stereolithography (SLA). Stereolithography dates to the early 1980s and is one of the widely used forms of ceramic additive manufacturing. Digital Light Processing (DLP) based on mask-image projection and laser-based Stereolithography based on spot scanning both work on the principle of the photopolymerisation of a ceramic slurry. The advantage of DLP technology is a faster realisation of an object as the projected image hardens a layer of slurry at a time [12]. A critical aspect of the AM is to achieve dimensional accuracy and repeatability of the manufactured parts [13]. Detailed studies on the influence of the printing parameters on the part dimensions are generally found for metal AM. Metal lattice structures with fine strut diameters were fabricated in the past by Laser Powder Bed Fusion [14] and Selective Laser Melting [15]. The investigation of the laser power and scanning speed on the dimensional accuracy of the strut diameter of a diamond lattice cell showed the increase of the strut diameter with the increase of the laser power [16]. Similarly, Qiu et al. [17] found that the deviations of the experimental strut diameter from the designed value were increasing with the increase of the laser power. The influence of the printing parameters on the dimensional accuracy for ceramic stereolithography based processes is not widely investigated. Generally, the studies on accuracy include bulk structures, walls, or gaps. Fu et al. [18] studied the influence of the laser power on the dimensional accuracy of SLA of bulk products, concluding that the length and width increased with the increase of the laser power due to the increase of the light scattering. A study of printability and lateral accuracy of holes and walls with lithography-based AM showed holes down to 200 µm could be fabricated, but those smaller than 500 µm would have a large deviation from the CAD design [19]. Similarly, the dimensional accuracy of designed hexahedral cavities in a lattice structure manufactured by lithography-based technology was evaluated. Manufactured cavities were 15 to 30% smaller as compared to theoretical values [20]. Schhauer et al. [21] reported successful manufacturing of a honeycomb structure with a wall thickness of 100 µm. However, the experiments revealed that the holes with diameters of less than 200 µm were clogged. In another study, the printing parameters were experimentally varied in manufacturing of a gear geometry via LCM and it was found the horizontal resolution increased with the decrease of the exposure energy. The diameter of the hole presented higher dimensional difference for all sets of printing parameters [22]. Manufacturing parts that contain small features, such as lattice structure is challenging. Although complex Al_2O_3 and TiO_2 lattice structures with 170 µm and 200 µm strut diameter were manufactured in the past, the debinding and sintering processes needed optimisation and strict control to obtain samples without cracks since low solid loadings caused high shrinkage up to 70% during thermal postprocessing [23,24].

The slurries suitable for ceramic AM contain ceramic filler mixed in with binder, photoinitiator and other additives. For ceramic additive manufacturing ceramic particles such as alumina (Al_2O_3), pure zirconia (ZrO_2), zirconia stabilized with yittria, silicon dioxide (SiO_2), hydroxyapatite, cordierite, and others can be used as the ceramic filler [25–29].

The dimensional inaccuracy in ceramic-based stereolithography is a consequence of scattering caused by the addition of the ceramic particles to the UV resin [7,30]. High refractive index difference between the ceramic particle and photopolymerisable resin results in a reduction of the cure depth and distortion of the resolution [30,31]. The working curve of the ceramic slurry describes the thickness to which a slurry cures as a function of the light dose for a given light source. Polymerisation depth in vertical direction $\mathrm{C_d}$, can be expressed empirically with Jacob's equation:

$$C_d = D_p \ln\left(\frac{E}{E_c}\right) \qquad \text{Equation 4.1}$$

where $\mathrm{D_p}$ is the depth of penetration, E is the exposure energy density on the slurry surface, and $\mathrm{E_c}$ is the critical exposure energy density of the slurry [32]. The critical exposure energy density presents the minimum energy density required for photopolymerisation of the slurry [33]. The depth of penetration presents the distance at which the light intensity is reduced by e^{-1} [34]. $\mathrm{E_c}$ and $\mathrm{D_p}$ are solely parameters of the resin that do not depend on the exposure parameters. Bennet [35] performed experiments with various light intensities and proved that $\mathrm{D_p}$ and $\mathrm{E_c}$ for each power density vary by about 10% and 3%, respectively. This minor variation was attributed to the errors in the measurements of the cure depths and power densities.

Gentry et al. [30] proposed a quasi-Beer-Lambert relationship between the excess cure width (C_w) and the energy dose:

$$C_w = D_w \ln\left(\frac{E}{E_w}\right) \qquad \text{Equation 4.2}$$

where D_w is the width sensitivity and E_w is the width critical energy dose. Broadening parameters D_w and E_w are affected by the scattering of the light, the absorption and the critical energy dose of the resin [30]. In their work, the semilogarithmic dependence of excess line width on energy dose was proven for various ceramic suspension. They introduced broadening depth (B_d) which is the depth of the cure at the onset of broadening:

$$B_d = D_p \ln\left(\frac{E_w}{E_c}\right) \qquad \text{Equation 4.3}$$

Rudraraju [36] demonstrated that with DMD projection the broadening behaviour depends upon the feature size, the energy dose and the cure depth by curing 2D squares with the size of 25-900 pixels. The reported behaviour is studied only for experiments where a single-layer is cured; hence it is necessary to determine whether this is the case when a 3D object is manufactured as subsequent layer curing can affect print-through to the previous layer.

Dissimilar routes of ceramic suspension preparation are present in the literature. The ceramic powder can be either used as-received [32,37–40] or the surface of the ceramic particle can be pre-treated with a dispersant prior to the addition to the photopolymerisable resin [34,41,42]. Clear indication of the best method of preparation and evidence of the photopolymerisation behaviour and rheology is lacking. An important factor in the development of the ceramic slurry is to achieve a solid loading of over 40 vol% [25,28,32]. On the one hand, high solid loading is desirable as it improves the mechanical properties and reduces sintering shrinkage. On the other hand, the introduction of the hydrophilic ceramic particles into the hydrophobic resin drastically increases the viscosity. To achieve a high solid loading and good dispersion of the ceramic particles in the resin, it is required to add a dispersant to provide steric barriers between ceramic particles that compensates van der Waals attractive forces between them and prevents collision of the particles caused by Brownian motion [32]. The recommended rheology of the suspension for Admaflex technology is a Non-Newtonian behaviour with shear thinning and a dynamic viscosity below 10 Pa·s for shear rates of 10 to 300 s^{-1} [43].

In summary, fine-tuning the process parameters is important for precise part manufacturing. Developing ceramic slurry with high solid loading, low viscosity and good resolution is the key issue for ceramic stereolithography based additive manufacturing. The accuracy of parts manufactured by DLP technology is a complex interaction between process parameters, printer resolution and formulation of the photopolymerisable slurry. Although there have been various studies focusing on the effects of printing parameters on the performance of fabricated parts, systematic investigation on the effects of slurry preparation and printing parameters on the dimensional accuracy for DLP additive manufacturing of lattice structures with small features (<500 µm) is required. Broadening of various feature sizes in 3D object at different layer thicknesses and energy doses must be studied to assess the broadening behaviour. The aim of this study is to evaluate ceramic slurry preparation techniques and to establish optimal printing parameters. Two distinct addition procedures of the ceramic powder in the photoreactive resin were considered for the preparation of low viscosity, high reactive alumina slurry. The effect of the pre-treatment of the ceramic particles compared to as-received powder was studied in terms of rheology and photopolymerisation. To address the gaps in the literature, the effort to understand the effect of the layer thickness, exposure power and exposure time on the dimensional accuracy of lattice strut diameters are investigated by adopting statistical approaches by means of a full-factorial Design of Experiment (DoE) and Analysis of Variance (ANOVA). The determination of the optimum process parameters is conducted based on the evaluation of the printing dimensional accuracy compared with CAD models.

4.2 Methodology

4.2.1 Ceramic slurry preparation and characterisation

The resin consisted of a mono-functional, di-functional and tetra-functional monomer and a plasticiser in the appropriate proportions [43]. Phosphoric ester salt of a high molecular weight copolymer with pigment-affinic groups was selected as the dispersant (BYK-Chemie GmbH, Wesel, Germany). Diphenyl (2,4,6-trimethylbenzoyl) phosphine oxide (Sigma Aldrich, Gillingham, UK) was used as the initiator of the polymerisation reaction. Commercially available alumina oxide powder (A16 SG, Almatis GmbH, Ludwigshafen, Germany) was used as the ceramic filler. Table 4.1 contains the particle size distribution of the as-received (AR) and the pre-treated (PT) alumina powder.

Table 4.1 Ceramic powders used in the photopolymerisable ceramic suspensions

Material	**d_{10}, µm**	**d_{50}, µm**	**d_{90}, µm**
Al_2O_3- As-Received (AR)	0.22	0.80	4.90
Al_2O_3- Pre-treated (PT)	0.23	0.80	2.31

The particle size distribution of the ceramic powder was evaluated with Sympatec Helos (Sympatec GmbH, Clausthal-Zellerfeld, Germany) using R1 lens. The morphology of the powder was examined using SEM (Jeol JCM 600, Tokio, Japan). Figure 4.1 shows a) the particle size cumulative distribution curves of the powders and SEM images of b) AR powder and c) PT powder. The AR powder consists of large, spherical, aggregated particles (Figure 4.1b)); after milling the agglomerates appeared less spherical, and some large flaked particles can be observed from Figure 4.1c).

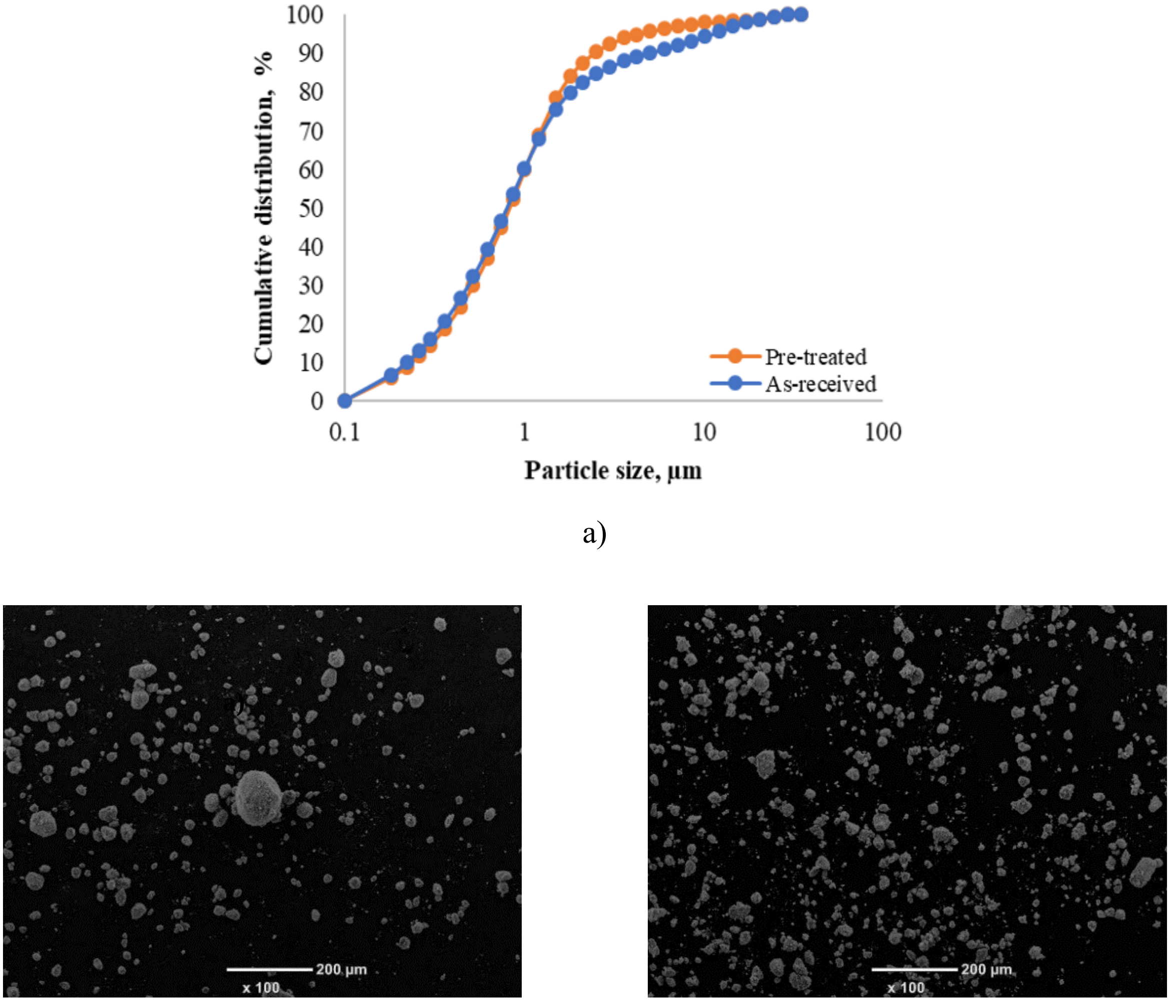

a)

b)

c)

Figure 4.1 a) Cumulative particle size distribution curves b) SEM of the as-received powder and c) SEM of the PT powder

The ceramic slurry preparation procedures were adapted from the literature [43]. The first procedure included combining resin components with an overhead mixer at room temperature for 30 minutes, followed by addition of 2 wt% of dispersant. The mixture was stirred for an additional hour. The AR powder was added in small increments until the solid loading of 57 vol% was reached. Finally, a small amount of photoinitiator was added into the mixture together with zirconia oxide grinding media of the same mass weight as the powder and the slurry was placed on the roller for 24 h. In the second procedure, the AR ceramic powder was combined with ethanol and 2 wt% of the dispersant followed by planetary ball milling with 1 mm zirconia grinding media at 400 rpm for 2 hours. The mixture was first air-dried for 24 h and then dried in the oven for 12 h at 110 °C to allow solvent decomposition. The PT dry powder was sieved through a mesh of 250 µm and added into the resin until the solid loading of 57 vol% was achieved. This was followed by addition of the photoinitiator and zirconia oxide grinding media of the same mass weight as the powder. Lastly, the slurry was placed on the roller for 24 h.

Rheological behaviour of the ceramic suspensions was tested on AR 500 (TA Instruments, New Castle DE, USA) with a 20 mm gold on rhodium plate varying the shear rate from 0.1 to 300 s^{-1} at a constant temperature of 20.0 °C. The refractive index of the resin was measured using a digital pocket refractometer at T=18.5 °C (ATAGO CO., LTD., Tokyo, Japan). A single-layer curing method was used for measurement of the cure depth at various exposure energies to determine the critical exposure energy and depth of penetration. Prior to the measurement, the prepared slurries were treated in a vacuum degasser for 10 minutes to remove the air bubbles and reduce the inhibition polymerisation. An image of a checkboard pattern was projected to a layer of photopolymerisable slurry. Cured layers were peeled off the foil and the thickness of the cured material was determined with a handheld micrometer (Mitutoyo Digimatic

Micrometer, MDC-25PX, Kawasaki, Japan). Three consequent measurements were made, and the average cure depth was recorded.

4.2.2 Design of the lattice structures

The lattice structures designed for this study were based on a unit cell of a diamond lattice elongated in the Z direction. The dimensions of the repeating unit cell were 1.25 mm (X) by 1.25 mm (Y) by 2.5 mm (Z). The strut diameter was varied from 100 µm to 500 µm to study the manufacturability and the effect of the processing parameters on the dimensional accuracy. The generated CAD diagram is shown in Figure 4.2.

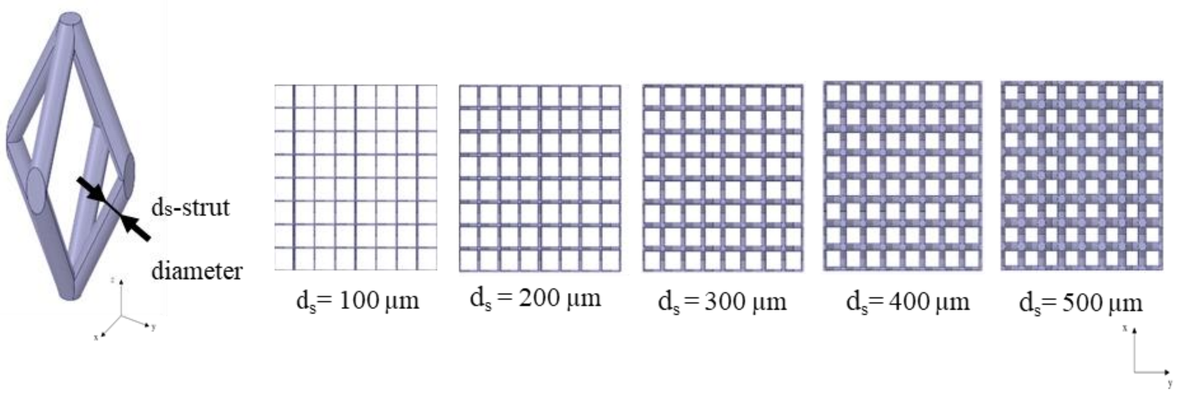

Figure 4.2 CAD design of lattices with varying strut diameter

4.2.3 Experimental design

Full factorial Design of Experiments (DoE) was conducted to generate an experimental plan and assess the influence of the printing parameters on the dimensional accuracy of lattices with various CAD strut diameters. The Analysis of Variance (ANOVA) was used to identify the significant printing parameters and interactions on the process outputs [13]. The factors selected for the experiments were exposure time (ET), exposure power (EP) and sliced layer thickness (LT). Three levels were selected for the exposure time and the exposure power and two levels for layer thickness (Table 4.2).

Table 4.2 Factors, levels, and their corresponding values for the experimental test

Factors	**Levels**		
	L1	**L2**	**L3**
Exposure time (ET), s	1.5	2	3
Exposure power (EP), mW/cm^2	6.72	14	20.79
Sliced layer thickness (LT), µm	10	25	-

The exposure power is expressed as a certain percentage of the maximum light intensity of the DLP light source, yielding irradiance of 6.72 mW/cm^2 for 10%, 14 mW/cm^2 for 20% and 20.79 mW/cm^2 for 30%. Sliced layer thickness is the thickness of each individual slice of the model. The exposure time is the duration where the resin is exposed under a light source for each layer. Layer curing times of only 1.5–3 seconds were required due to the high reactivity of the resin.

Table 4.3 presents the experimental matrix for the full factorial experiment. The total number of conducted experiments was 18 for each lattice sample. To study the statistical significance of factor effects on each response, the Analysis of Variance (ANOVA) using Minitab 19 statistical software was performed. The diameters of the struts of the green parts were determined from images taken by Alicona InfiniteFocusG5 plus (Bruker Alicona, Leicestershire, UK) optical microscope using a 5× objective. The strut diameter measurements were taken at the edges of the samples and an average was calculated from the total of 16 measurements for each of the 18 conditions in Table 4.3.

Table 4.3 Experimental matrix

Run	**ET, s**	**EP, mW/cm^2**	**LT, µm**
1	1.5	6.72	10
2	1.5	14	10
3	1.5	20.79	10
4	2.0	6.72	10
5	2.0	14	10
6	2.0	20.79	10
7	3.0	6.72	10
8	3.0	14	10
9	3.0	20.79	10
10	1.5	6.72	25
11	1.5	14	25
12	1.5	20.79	25
13	2.0	6.72	25
14	2.0	14	25
15	2.0	20.79	25
16	3.0	6.72	25
17	3.0	14	25
18	3.0	20.79	25

The dimensional effectiveness of the printing process was assessed through printing accuracy represented by the calculated linear dimensional change of the strut diameter of as-printed green parts, compared with those of the original CAD model presented by:

$$D(i) = \frac{d_{s,CAD} - d_{si}}{d_{s,CAD}} \times 100\ \% \qquad \text{Equation 4.4}$$

Where D(i) is deviation, $d_{s,CAD}$ is the CAD strut diameter and d_{si} strut diameter of the as-printed green samples.

4.2.4 Additive manufacturing

The printing experiments were conducted on the Admaflex 130 (Admatec Europe BV, Alkmaar, The Netherlands) working with a light source of λ =405 nm and X, Y resolution of 40 µm. The technology is based on Digital Light Processing with a DMD chip that comprises of thousands of mirrors that rotate according to pixels to project the image. The Admaflex 130 is equipped with a rotating foil system that transports the slurry on the foil from the reservoir to the manufacturing zone and to the pump where the excess slurry is pumped back to the reservoir. Photopolymerisable light-sensitive slurry is exposed to light which subsequently cures the whole layer. The process of curing layer by layer is repeated until the final three-dimensional green body is built. The printed parts were cleaned by using dibasic ester (Sigma Aldrich, Gillingham, UK) and compressed air. Figure 4.3 shows the lattice samples produced on Admaflex 130 machine.

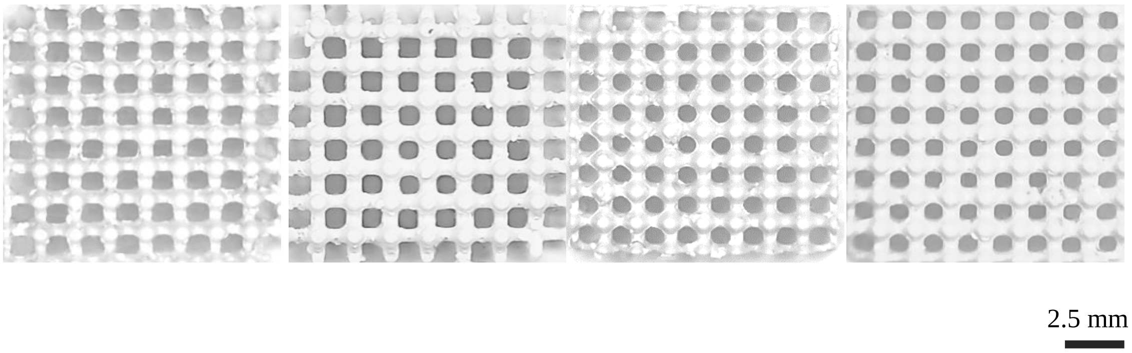

a) $d_{s,CAD}$=200 µm b) $d_{s,CAD}$=300 µm c) $d_{s,CAD}$=400 µm d) $d_{s,CAD}$=500 µm

Figure 4.3 Lattice samples produced on Admaflex 130

4.3 Results and discussion

4.3.1 Rheology of the ceramic slurry

The rheological behaviour of the prepared slurries expressed by viscosity curves as a function of shear rate is presented in Figure 4.4. For comparison purpose, the rheological behaviour of the blank resin was plotted as well. The addition of the powder into the resin mixture highly increased the viscosity. The addition of the AR Al_2O_3 powder causes shear thickening at shear rates higher than 100 s^{-1}. The lower flowability of the AR Al_2O_3 slurry can be attributed to the agglomeration of the fine particles [29,40]. In contrast, decreasing viscosity with increasing shear rate is shown by the suspension with the PT powder. With the pre-treatment of the powder by ball-milling and the dispersant, the level of agglomeration was reduced.

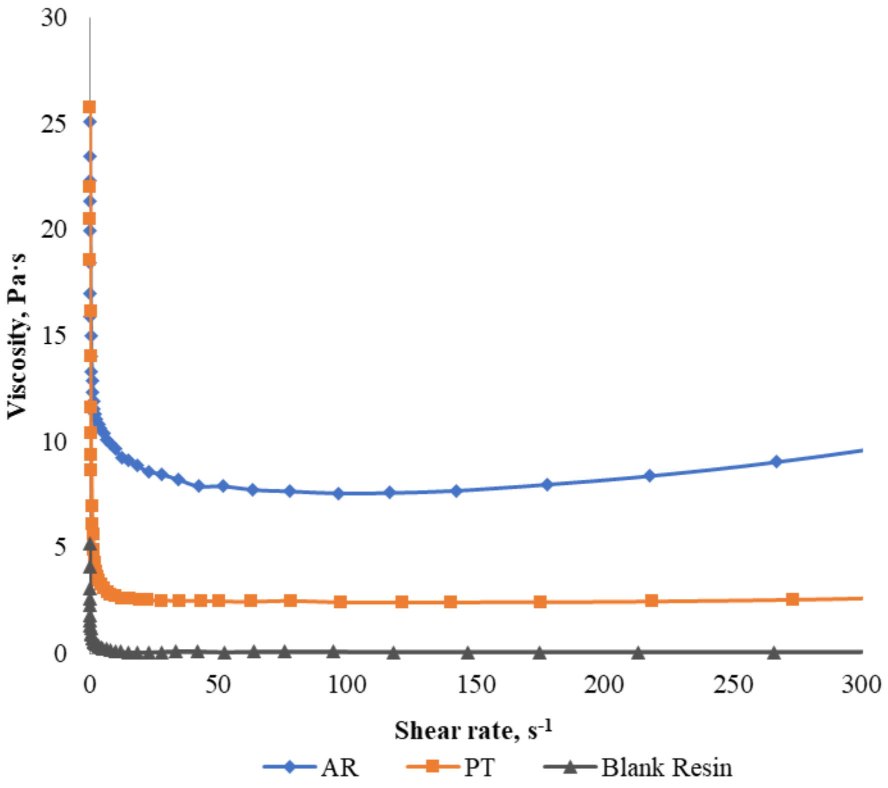

Figure 4.4 Rheology of the ceramic slurries and the blank resin

The pre-treatment of the Al_2O_3 powder causes the adsorption of the dispersant on the particle surface resulting a in more efficient dispersion of the ceramic particles in the resin. The viscosity of the prepared slurry with the pre-treated Al_2O_3 powder was lower than that of limit value for the Admaflex technology and considerably lower than that of the slurry with AR powder.

The critical exposure energy and depth of penetration were determined by performing a linear regression on the experimental C_d values plotted as a function of $\ln(E)$ as seen in Figure 4.5. Both slurries had high cure depths at all energy densities. This can be contributed to the high reactivity of the resin. Equally, it is interesting to note the difference between the cure depths for the AR and PT powders.

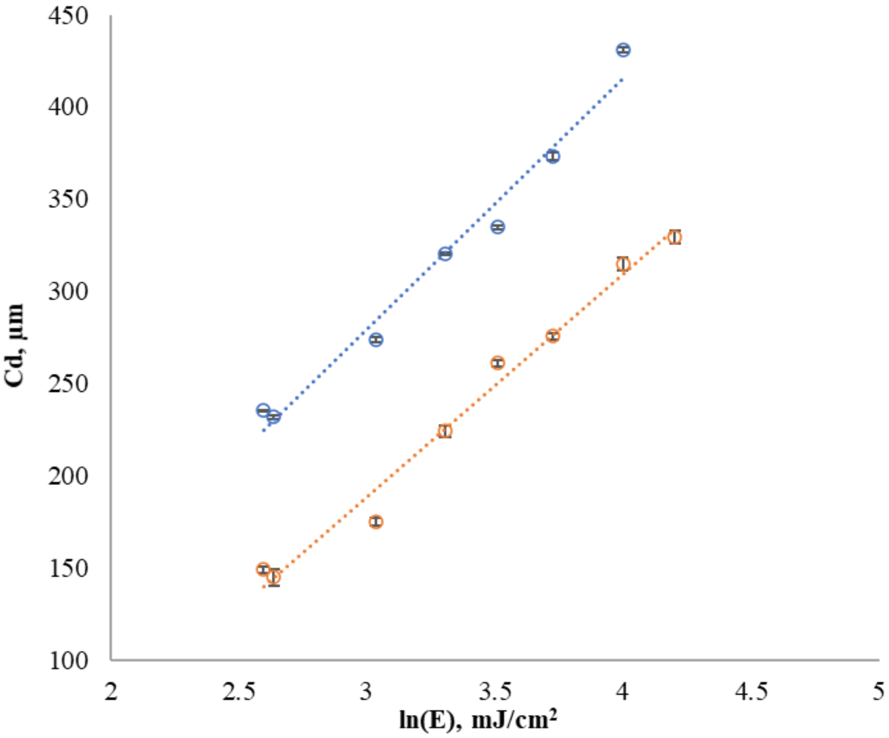

Figure 4.5 The relation of the cure depth and the exposure energy density

The critical energy of the slurry with PT powder increased as seen in Table 4.4. This demonstrates how critical energy is altered by deagglomeration of the powder. The critical energy could similarly be increased by adding the appropriate inhibitors or absorbers into the suspension. However, those decrease the cure depth necessary for a stable part build up [44]. Depth of penetration has a significant impact on the polymerisation width at the surface of a layer of the slurry. By pre-treatment of the powder, the D_p was decreased by 11%. Lower D_p value allows better control of the lateral definition [45]. Suspensions prepared with the AR powder had greater C_d compared with suspensions prepared with PT ceramic particles, owing to the higher degree of scattering. Moreover, it was observed that the strong scattering effect caused by large agglomerates in AR powder resulted in poor spatial resolution. The ceramic slurry with PT powder showed better rheological and curing properties and is selected for further investigation.

Table 4.4 The values of E_c and D_p

Suspension	**E_c, mJ/cm^2**	**D_p, µm**
w/AR Al_2O_3	5.47	136.04
w/PT Al_2O_3	9.03	120.74

.

4.3.2 Effect of the process parameters on the geometrical accuracy

The results of the DoE presented in Table 4.3 are shown graphically in Figure 4.6. Deviation from the CAD strut diameter was calculated based on Equation 4.4 (for layer thickness 10 and 25 µm) and used to represent the printing accuracy. The deviation from the CAD strut diameters is presented for each combination of the exposure time and the exposure power. Note that $d_{s,CAD}$ represents the strut diameter in the designed CAD model. From Figure 4.6 a) and b) it can be seen that at constant exposure power, the increase of the exposure time, i.e. energy density, increases the deviation for each of the conditions. Furthermore, with the increase of the strut diameter, at constant exposure power and exposure time, the deviation is higher for larger strut dimensions. The actual strut diameters of fully dense samples were not measured; hence the fully dense samples represent 100% deviation in Figure 4.6. The deviations for the conditions that resulted in a non-continuous build are not presented in the graph. For instance, lattices with designed CAD strut diameter of 100 µm were not mechanically stable during the manufacturing process and the complete failure of the part was observed in the initial layers; hence the deviations for the aforementioned are not shown in the graph. All successfully manufactured samples showed a positive deviation compared to the designed CAD strut diameter which is a consequence of light scattering effects caused by the different refractive indices of the resin and ceramic powder. The results are in line with the findings in the literature for ceramic stereolithography processes which revealed that dimensions of the fabricated objects were higher than their designed values with the increase of energy density and exposed area [19,39,46].

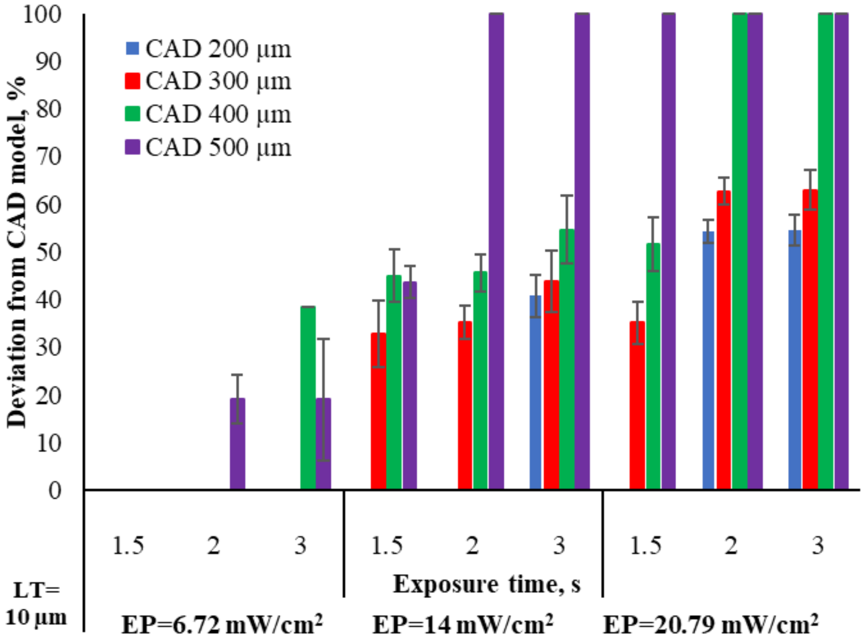

a)

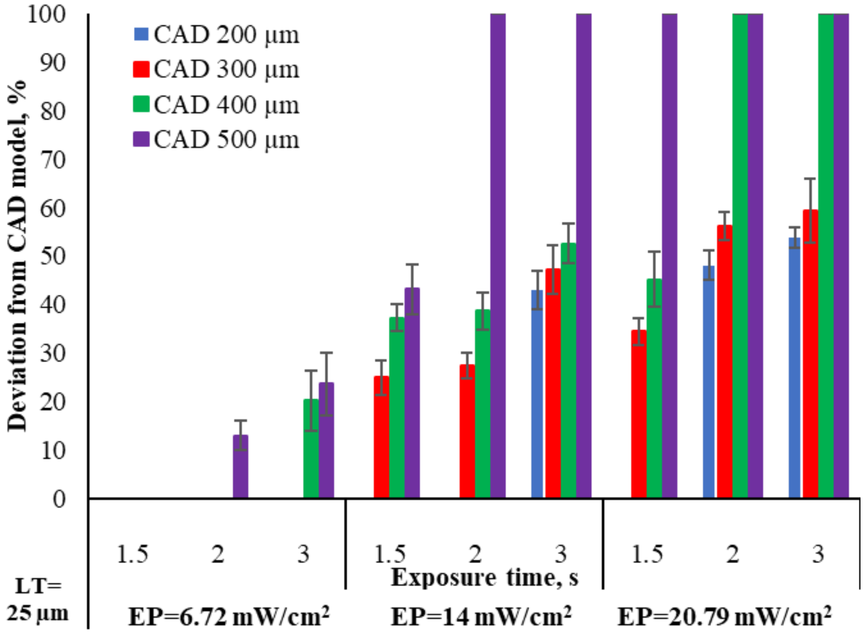

b)

Figure 4.6 Results of the DoE in terms of deviation from the CAD strut diameter model for a) LT=10 µm and b) LT=25 µm

ANOVA has been used to determine which parameters have the most influence on the printing accuracy of lattices with the designed CAD d_s of 200 µm to 500 µm. The layer thickness, the exposure time, the exposure power and their interaction are the source factors. The P-values for factors and their interactions are shown in Table 4.5. Based on a 95% confidence level, factors and interactions with P-value equal to or less than 0.05 are significant process parameters. Therefore, it can be concluded that the exposure time, the exposure power and their interaction are the most significant process parameters. The layer thickness is not considered as a significant parameter which was also observed in the literature [19]. Main effects and interaction plots assist in finding the optimal level of significant factors. Effect of significant process parameters and interactions are illustrated in Figure 4.7 and Figure 4.8 respectively. The main effects demonstrate the trends in the mean percentage deviation data as the significant factors (EP, ET) were varied. These trend lines represent the effect of a single independent variable on the response disregarding the other process variable. According to Figure 4.7a) the exposure time slightly dominates against the exposure power for deviation of $d_{s,CAD}$=200 µm.

Table 4.5 P-values for factors and their interactions

Source	**P-Values**			
	$d_{s,\,CAD}$= 200 µm	**$d_{s,\,CAD}$= 300 µm**	**$d_{s,\,CAD}$= 400 µm**	**$d_{s,\,CAD}$= 500 µm**
LT	0.455	0.131	0.148	0.837
ET	0.000	0.002	0.006	0.004
EP	0.000	0.000	0.001	0.000
LT*ET	0.337	0.444	0.787	0.449
LT*EP	0.252	0.473	0.798	0.981
ET*EP	0.000	0.009	0.001	0.000

The exposure power dominates against the exposure time for the mean of deviation of $d_{s,CAD}$=300 µm, $d_{s,CAD}$=400 µm and $d_{s,CAD}$=500 µm (Figure 4.7b), c) and d)). The lowest point on the graph indicates the factor level that has a minimum deviation in the response.

Clearly, for each condition, different values of factors and levels will yield the least mean of deviation. A similar analysis was performed to interpret the effect of the interactions, where the impact of one factor depends on the level of the other factor.

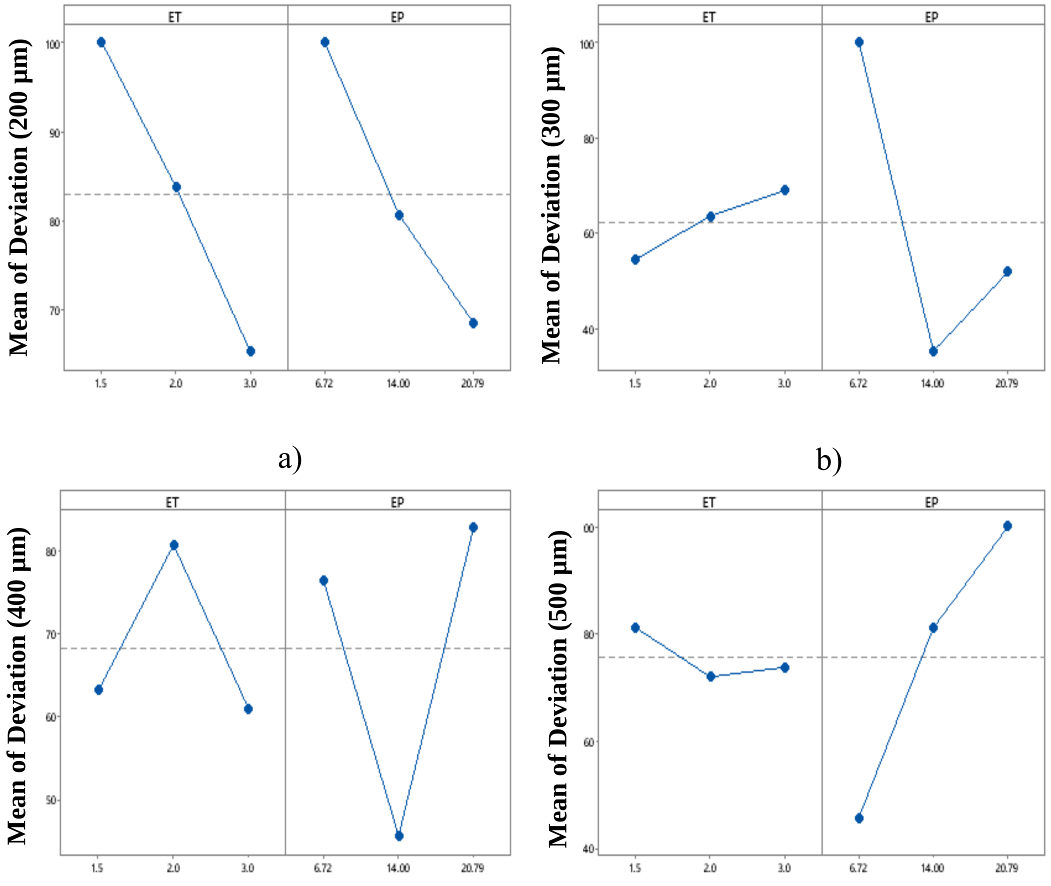

a) b)

c) d)

Figure 4.7 Effect of the significant process parameters on the mean of deviation for a) $d_{s,CAD}$=200 µm b) $d_{s,CAD}$=300 µm c) $d_{s,CAD}$=400 µm d) $d_{s,CAD}$=500 µm

From Figure 4.8 it can be observed that the least deviation for $d_{s,CAD}$=200 µm and $d_{s,CAD}$=300 µm is achieved with the mid-level of EP when ET is at the highest level for $d_{s,CAD}$=200 µm (Figure 4.8a)) and at the lowest level for $d_{s,CAD}$=300 µm (Figure 4.8b)). When EP is at mid-level, lower deviations are seen for $d_{s,CAD}$=400 µm and $d_{s,CAD}$=500 µm at the lowest level of ET. Nonetheless, the least deviation is achieved when EP is at the lowest level and ET at the highest level for d_{sCAD}=400 µm and mid-level for d_{sCAD}=500 µm.

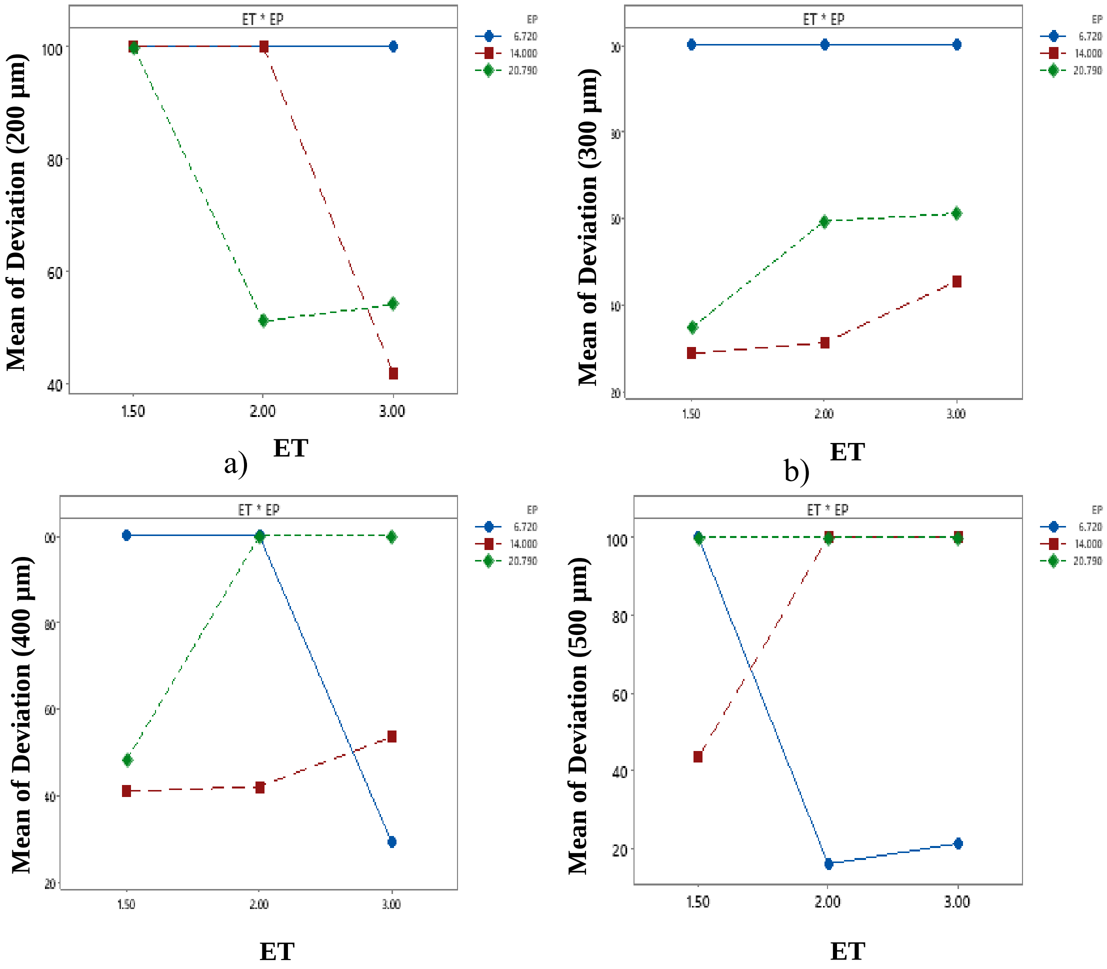

a) b) c) d)

Figure 4.8 Significant interaction effects for a) $d_{s,CAD}$=200 µm b) $d_{s,CAD}$=300 µm c) $d_{s,CAD}$=400 µm d) $d_{s,CAD}$=500 µm

Based on Figure 4.8, in order to generate a minimum percentage deviation (i.e. maximum printing accuracy), the following process parameters can be considered: EP= 14 mW/cm^2, ET=3 s for $d_{s,CAD}$=200 µm, EP= 14 mW/cm^2, ET=1.5 s for $d_{s,CAD}$=300 µm, EP=6.72 mW/cm^2, ET=3 s for $d_{s,CAD}$=400 µm, EP=6.72 mW/cm^2, ET=2 s for $d_{s,CAD}$=500 µm.

Generally, to ensure the adhesion between the layers, the cure depth needs to be a couple of times higher than the applied layer thickness [19,47,48]. The initial layers of the sliced CAD model with $d_{s,CAD}$=100 µm are essentially circles with a diameter of 100 µm and an area of 7853 µm^2. Due to this particularly small exposed area, the attaching force between the layer and the transparent foil is higher than the bonding force of the layer with the previous layer. It is important to mention that the resulting energy density is well above the critical value for the exposure power of 6.72 mW/cm^2 and the exposure time of 1.5 s. Therefore, even though in theory the resolution may allow a construction of parts with resolution as low as 40 µm, the part with $d_{s, CAD}$=100 µm is not strong enough to withstand the manufacturing process. Similarly, findings in the literature indicate that the walls with CAD thickness less than 300 µm could not be manufactured via DLP process, and the thinnest stable walls had the thickness of 300 µm to 400 µm [19]. This suggests that to ensure adequate adhesion between the adjacent layers, the cure depth must be significantly higher than the recommended cure depth. At the lowest exposure power (6.72 mW/cm^2) the only manufacturable lattices were those with designed strut diameter $d_{s,CAD}$=400 µm and 500 µm. Figure 4.9 shows the printed sample of $d_{s,CAD}$=500 µm (left). This implies that the applied exposure energies and resulting cure depths were not sufficient for manufacturing of $d_{s,CAD}$ <400 µm. The minimum cure depth necessary to manufacture the CAD strut diameter of 500 µm at 6.72 mW/cm^2 was 143 µm, yielding the factor of 14.3 for the layer thickness of 10 µm and 5.72 for the layer thickness of 25 µm. For CAD strut diameter of 400 µm, the minimum cure depth necessary to manufacture at the power of 6.72 mW/cm^2 is 192 µm, yielding the factor of 19.2 for the layer thickness of 10 µm and 7.68 for the layer thickness of 25 µm. An increase of the exposure power to 14 mW/cm^2 resulted in the manufacturing of CAD strut diameters of 300 µm and 400 µm at all exposure times but distorted the 500 µm resulting in a fully solidified green part at higher exposure times (Figure 4.9b)).

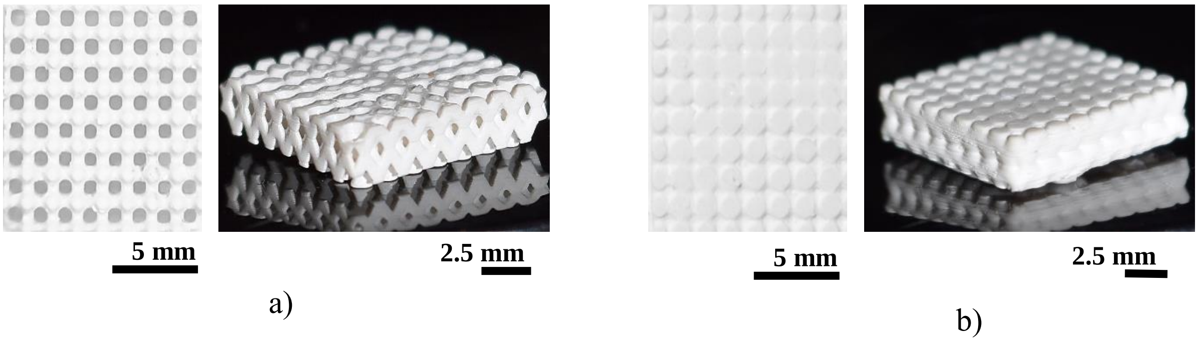

Figure 4.9 a) Cross-section and side view of the green part $d_{s,CAD}$=500 µm (LT=25 µm, EP=6.72 mW/cm^2, ET=2 s) and b) Cross-section and side view of the over- exposed part $d_{s,CAD}$=500 µm (LT=25 µm, EP=20.79 mW/cm^2, ET=2 s).

At the exposure power 14 mW/cm^2 and at both layer thicknesses, the 500 µm sample was possible to manufacture at the lowest exposure time, resulting in the cure depth of 196 µm and yielding the factor of 19.6 for the layer thickness of 10 µm and 7.84 for the layer thickness of 25 µm. The 300 µm samples and 400 µm sample were manufacturable at all combinations of the exposure time, the exposure power and the layer thickness at cure depths of 196 µm, 231 µm, 280 µm. Furthermore, at the highest exposure time (3 s) the lattice structure with CAD strut diameter of 200 µm was possible to manufacture with cure depth of 280 µm, yielding the factor of 28 for the layer thickness of 10 µm and 11.2 for the layer thickness of 25 µm. The highest exposure power (20.79 mW/cm^2) resulted in completely dense $d_{s,CAD}$=500 µm sample, at both layer thicknesses. The samples with 400 µm CAD strut diameter were manufacturable at the lowest exposure time (1.5 s). Higher exposure times were necessary to manufacture the

$d_{s,CAD}$=300 µm and $d_{s,CAD}$=200 µm and the minimum cure depth necessary for manufacturing was 196 µm and 280 µm, respectively. Comparing the $d_{s,CAD}$=500 µm and $d_{s,CAD}$=200 µm as the highest and lowest manufacturable samples, the $d_{s,CAD}$=200 µm requires almost double the cure depth than the $d_{s,CAD}$=500 µm. As the exposure area increases, the necessary cure depth for the part to withstand the manufacturing process decreases. This leads to conclude that, for small exposure areas, higher cure depths are necessary for proper adherence of the adjacent layers. Although the recommended cure depths should be a couple of times higher than the layer thickness to avoid over curing, the results suggest that the manufacturability of lattice structures is a factor of not only the cure depth, but also the size of the sliced layer exposure area and the over curing effects should be considered when designing the starting CAD model.

4.3.3 Broadening behaviour

To evaluate the overgrowth in the horizontal direction, the cure excess width was plotted against the logarithm of the energy dose in Figure 4.10 for $d_{s,CAD}$= 300 µm and $d_{s,CAD}$= 400 µm at two different layer thicknesses (LT= 10 and 25 µm), constant exposure power (14.79 mW/cm^2) and varying exposure time (1.5 s-3 s). Not enough data is present for samples with CAD strut diameter of 200 µm and 500 µm. Therefore, only the excess cure widths for 300 µm and 400 µm were plotted. Gentry et al. [30] reported a linear relationship of the cure width and logarithm of the energy dose. Rudraraju [36] reported that the cure width varies linearly with respect to the energy dose. The relationship between the cure width and the logarithm of the energy dose from our experimental results based on 3D samples is linear following the quasi-Beer Lambert model, similar to work reported by Gentry et al. [30]. Since the Equation 4.2 is derived from Jacob's equation for the working curve of the slurry, it is assumed that the E_w and D_w are constants and solely characteristics of the slurry [36].

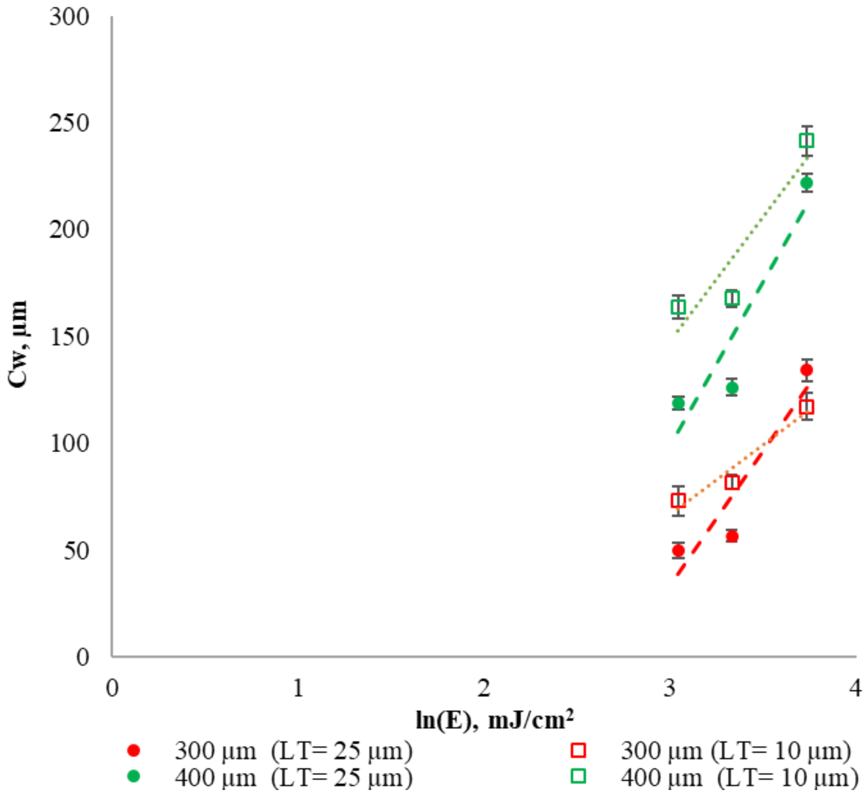

Figure 4.10 Variation of cure width (C_w) with respect to the logarithm of the energy dose

However, for broadening phenomena this is not the case. Table 4.6 contains a summary of the constants E_w and D_w for different layer thicknesses and feature sizes. Depth at the onset of broadening, B_d (Equation 4.3) was calculated to describe the effect of broadening in the suspension [30]. For $d_{s,CAD}$= 300 µm E_w and D_w are lower with respect to $d_{s,CAD}$= 400 µm for both layer thicknesses. With the increase of the layer thickness, the parameters E_w and D_w increase for both $d_{s,CAD}$= 300 µm and $d_{s,CAD}$= 400 µm. It is evident that E_w decreases with the increase of the feature size, whereas D_w increases with the increase of the feature size, in accordance with the literature [36]. Moreover, the broadening increases with the energy dose. To limit the excess broadening, lower width sensitivity is desired [30]. Similar trends of broadening behaviour were reported in the literature, where it was found that the broadening depends upon the feature size and the energy dose for a single-layer curing [30,36,39]. Here, we report that layer thickness has an influence on the broadening parameters. This is the consequence of the decrease of side scattering with the increase of layer thickness where the light propagates more into the vertical direction before it gets scattered to the horizontal direction. Furthermore, B_d is negative for the layer thickness of 10 µm. This is seemingly contrary to practicality, as negative cure depths are not realistic. However, it indicates that at LT= 10 µm for all energy doses (in the experimental range) the broadening will occur at all cure depths. At LT= 25 µm the broadening will start to occur at cure depths of 66.34 µm and higher for $d_{s,CAD}$= 300 µm and 18.04 µm and higher for $d_{s,CAD}$= 400 µm. The results show that the broadening is inevitable with the current ceramic slurry composition.

Table 4.6 Critical width energies and width sensitivities

	LT= 10 µm			**LT= 25 µm**		
$d_{s,CAD}$, µm	**E_w, mJ/cm^2**	**D_w, µm**	**Bd, µm**	**E_w, mJ/cm^2**	**D_w, µm**	**Bd, µm**
300	6.69	65.43	-36.29	15.64	126.42	66.34
400	5.47	116.52	-60.44	10.48	154.73	18.04

The experimental strut dimensions are all found to have a large deviation from the designed values. The larger experimental strut dimensions can be attributed to the following reasons. Firstly, the addition of the ceramic particles into the resin attributes to the scattering of light within the suspension. The scattering phenomena is usually attributed to the difference in the refractive indices of the resin and ceramic particles [39,49]. The blank resin had a RI of 1.49 whereas the alumina powder has RI of 1.77 yielding the RI contrast of 0.28 [50]. The scattering effects could be reduced by modifying the refractive index of the UV curable resin [51]. Secondly, the control of the dimensional overgrowth could be achieved by the addition of UV blockers or absorbers, which could, on the other hand, lead to unfavourable cure depth reduction

[42,52]. Furthermore, as high cure depths were necessary for successful manufacturing, the lateral over curing had the effect on the deviation from the CAD models. For the part with the smallest strut diameter ($d_{s,CAD}$=200 µm), the cure depth necessary was almost double than that of the sample with $d_{s,CAD}$=500 µm. This implies that with the increase of the exposed area, the energy dose and consequently the cure depth should be lower to reach the least deviation. Lastly, the control of the part's dimension could be achieved by using a correction factor to modify the starting CAD model. To manufacture a lattice structure with precisely dimensioned features for a particular application it is vital to select the optimal processing conditions or to account for the geometrical overgrowth of the strut diameters relative to the design diameter.

4.4 Conclusions

In the present study, two preparation methods of Al_2O_3 photopolymerisable slurries for DLP were described. There was a need to control the process parameters and materials for the lattice structures fabrication. The main factors that influence the printing accuracy were investigated. Full factorial design of experiments was used to assess the influence of the exposure power, the exposure time and the layer thickness accordingly.

The conclusions drawn from the study are as follows:

- The slurry prepared with the pre-treated powder showed acceptable viscosity for successful processing on the Admaflex 130.
- The depth of penetration, which is crucial for dimensional accuracy, was lower for the ceramic slurry with the pre-treated powder.
- Lattices with strut diameter of 100 µm were not strong enough to withstand the manufacturing process. However, lattices with CAD designed struts of 200-500 µm

were successfully manufactured. The cure depth necessary for successful manufacturing was found to be inversely proportional to the exposed area.

- The experimental strut diameters were found to be larger than the designed values for all manufactured samples. This is attributed to the light scattering within the ceramic slurry due to the refractive index contrast between the ceramic powder and the resin and the over curing effect necessary for a successful build.
- The most significant parameters that directly influence the dimensional accuracy were the exposure time, the exposure power and the interaction of both.
- The excess cure width was found to linearly increase with the logarithm of the energy dose.
- The broadening parameters were found to be dependent on the layer thickness as well as the energy dose and the feature size.

By careful control of the process parameters and by using appropriate preparation of the photopolymerisable slurry, the dimensional accuracy of the lattice structures can be improved. Further research of the broadening behaviour should be conducted to gain a better understanding of the lateral accuracy in DLP technology. Different orientation and position of the model on the building plate could possibly have an influence the dimensional accuracy. The investigation of different formulations of the resin is necessary to understand how different components influence the broadening behaviour of a 3D printed sample. Nevertheless, the findings from this work can serve as a guideline for photopolymerisable slurry preparation and for adjusting the printing parameters to improve the dimensional characteristics of 3D printed ceramic lattices.

Acknowledgements

The research leading to these results has received funding from the Engineering and Physical Sciences Research Council for project FACE - Novel Integrated Fuel Reformer-Aftertreatment System for Clean and Efficient Road Vehicles under grant number EP/P03117X/1. N.K. also thanks the University of Birmingham for award of a PhD scholarship.

References

1. Lin K, Sheikh R, Romanazzo S, Roohani I. 3D printing of bioceramic scaffolds-barriers to the clinical translation: From promise to reality, and future perspectives. Materials. 2019;12(7).
2. Papetti V, Dimopoulos Eggenschwiler P, Della Torre A, Lucci F, Ortona A, Montenegro G. Additive Manufactured open cell polyhedral structures as substrates for automotive catalysts. Int J Heat Mass Transf. 2018;126:1035–47.
3. Flores I, Kretzschmar N, Azman AH, Chekurov S, Pedersen DB, Chaudhuri A. Implications of lattice structures on economics and productivity of metal powder bed fusion. Addit Manuf. 2020;31:100947.
4. Elsayed M, Ghazy M, Youssef Y, Essa K. Optimization of SLM process parameters for Ti6Al4V medical implants. Rapid Prototyp J. 2019;25(3):433–47.
5. Hassanin H, El-Sayed MA, Elshaer A, Essa K, Jiang K. Microfabrication of net shape zirconia/alumina nanocomposite micro parts. Nanomaterials. 2018;8(8).
6. Sabouri A, Yetisen AK, Sadigzade R, Hassanin H, Essa K, Butt H. Three-Dimensional Microstructured Lattices for Oil Sensing. Energy and Fuels. 2017;31(3):2524–9.
7. Sun C, Zhang X. The influences of the material properties on ceramic micro-stereolithography. Sensors Actuators, A Phys. 2002;101(3):364–70.
8. Kovacev N, Li S, Zeraati-Rezaei S, Hemida H, Tsolakis A, Essa K. Effects of the internal structures of monolith ceramic substrates on thermal and hydraulic properties: additive manufacturing, numerical modelling and experimental testing. Int J Adv Manuf Technol. 2020;112:1115–32.
9. Bikas H, Stavropoulos P, Chryssolouris G. Additive manufacturing methods and modeling approaches: A critical review. Int J Adv Manuf Technol. 2016;83(1–4):389–405.
10. Yang L, Miyanaji H. Ceramic additive manufacturing: A review of current status and challenges. In: Solid Freeform Fabrication 2017: Proceedings of the 28th Annual International Solid Freeform Fabrication Symposium - An Additive Manufacturing Conference, SFF 2017. 2020. p. 652–79.
11. Zocca A, Colombo P, Gomes CM, Günster J. Additive manufacturing of ceramics: Issues, potentialities, and opportunities. J Am Ceram Soc. 2015;98(7):1983–2001.
12. Jasveer S, Jianbin X. Comparison of Different Types of 3D Printing Technologies. Int J Sci Res Publ. 2018;8(4):1–9.

13. Farzadi A, Solati-Hashjin M, Asadi-Eydivand M, Osman NAA. Effect of layer thickness and printing orientation on mechanical properties and dimensional accuracy of 3D printed porous samples for bone tissue engineering. PLoS One. 2014;9(9):1–14.
14. Tan C, Li S, Essa K, Jamshidi P, Zhou K, Ma W, et al. Laser Powder Bed Fusion of Ti-rich TiNi lattice structures: Process optimisation, geometrical integrity, and phase transformations. Int J Mach Tools Manuf. 2019;141:19–29.
15. Essa K, Hassanin H, Attallah MM, Adkins NJ, Musker AJ, Roberts GT, et al. Development and testing of an additively manufactured monolithic catalyst bed for HTP thruster applications. Appl Catal A Gen. 2017;542:125–35.
16. Sing SL, Wiria FE, Yeong WY. Selective laser melting of lattice structures: A statistical approach to manufacturability and mechanical behavior. Robot Comput Integr Manuf. 2018;49:170–80.
17. Qiu C, Yue S, Adkins NJE, Ward M, Hassanin H, Lee PD, et al. Influence of processing conditions on strut structure and compressive properties of cellular lattice structures fabricated by selective laser melting. Mater Sci Eng A. 2015;628:188–97.
18. Fu X, Zou B, Xing H, Li L, Li Y, Wang X. Effect of printing strategies on forming accuracy and mechanical properties of ZrO2 parts fabricated by SLA technology. Ceram Int. 2019;45(14):17630–7.
19. Conti L, Bienenstein D, Borlaf M, Graule T. Effects of the layer height and exposure energy on the lateral resolution of zirconia parts printed by lithography-based additive manufacturing. Materials. 2020;13(6).
20. Schwarzer E, Holtzhausen S, Scheithauer U, Ortmann C, Oberbach T, Moritz T, et al. Process development for additive manufacturing of functionally graded alumina toughened zirconia components intended for medical implant application. J Eur Ceram Soc. 2019;39(2–3):522–30.
21. Schhauer U, Schwarzer E, Moritz T, Michaelis A. Additive Manufacturing of Ceramic Heat Exchanger: Opportunities and Limits of the Lithography-Based Ceramic Manufacturing (LCM). J Mater Eng Perform. 2018;27(1):14–20.
22. Ozog P, Blugan G, Kata D, Graule T. Influence of the Printing Parameters on the Quality of Alumina Ceramics Shaped by UV-LCM Technology. J Ceram Sci Technol. 2019;10:1–10.
23. Shuai X, Zeng Y, Li P, Chen J. Fabrication of fine and complex lattice structure Al2O3 ceramic by digital light processing 3D printing technology. J Mater Sci. 2020;55(16):6771–82.
24. Guo J, Zeng Y, Li P, Chen J. Fine lattice structural titanium dioxide ceramic produced by DLP 3D printing. Ceram Int. 2019;45(17):23007–12.
25. Griffith ML, Halloran J. Ultraviolet Curing of Highly Loaded Ceramic Suspensions for Stereolithography of Ceramics. Solid Free Fabr Symp. 1994;396–403.
26. Johansson E, Lidström O, Johansson J, Lyckfeldt O, Adolfsson E. Influence of resin composition on the defect formation in alumina manufactured by stereolithography. Materials. 2017;10(2).
27. Peñaloza G. Additive manufacturing of Zirconia [master's].Gothenburg: Chalmers University of Technology;2018.
28. Song SY, Park MS, Lee D, Lee JW, Yun JS. Optimization and characterization of high-viscosity ZrO2 ceramic nanocomposite resins for supportless stereolithography. Mater Des. 2019;180:107960.
29. Hwa LC, Rajoo S, Noor AM, Ahmad N, Uday MB. Recent advances in 3D printing of porous ceramics: A review. Curr Opin Solid State Mater Sci. 2017;21(6):323–47.

30. Gentry SP, Halloran JW. Depth and width of cured lines in photopolymerizable ceramic suspensions. J Eur Ceram Soc. 2013;33(10):1981–8.
31. Hu K, Wei Y, Lu Z, Wan L, Li P. Design of a Shaping System for Stereolithography with High Solid Loading Ceramic Suspensions. 3D Print Addit Manuf. 2018;5(4):311–8.
32. Komissarenko DA, Sokolov PS, Evstigneeva AD, Shmeleva IA, Dosovitsky AE. Rheological and curing behavior of acrylate-based suspensions for the DLP 3D printing of complex zirconia parts. Materials. 2018;11(12).
33. Griffith ML, Halloran JW. Scattering of ultraviolet radiation in turbid suspensions. J Appl Phys. 1997;81(6):2538–46.
34. Abouliatim Y, Chartier T, Abelard P, Chaput C, Delage C. Optical characterization of stereolithography alumina suspensions using the Kubelka-Munk model. J Eur Ceram Soc. 2009;29(5):919–24.
35. Bennett J. Measuring UV curing parameters of commercial photopolymers used in additive manufacturing. Addit Manuf. 2017;18:203–12.
36. Rudraraju A V. Digital Data Processing and Computational Design for Large Area Maskless Photopolymerization [dissertation]. Atlanta: Georgia Institute of Technology; 2013.
37. Varghese G, Moral M, Castro-García M, López-López JJ, Marín-Rueda JR, Yagüe-Alcaraz V, et al. Fabrication and characterisation of ceramics via low-cost DLP 3D printing. Bol la Soc Esp Ceram y Vidr. 2018;57(1):9–18.
38. Sokolov PS, Komissarenko DA, Shmeleva IA, Slyusar I V., Dosovitskiy GA, Evdokimov P V., et al. Suspensions on the basis of stabilised zirconium oxide for three-dimensional printing. IOP Conf Ser Mater Sci Eng. 2018;347(1).
39. Mitteramskogler G, Gmeiner R, Felzmann R, Gruber S, Hofstetter C, Stampfl J, et al. Light curing strategies for lithography-based additive manufacturing of customized ceramics. Addit Manuf. 2014;1:110–8.
40. Zhang K, Xie C, Wang G, He R, Ding G, Wang M, et al. High solid loading, low viscosity photosensitive Al 2 O 3 slurry for stereolithography based additive manufacturing. Ceram Int. 2019;45(1):203–8.
41. Sun J, Binner J, Bai J. Effect of surface treatment on the dispersion of nano zirconia particles in non-aqueous suspensions for stereolithography. J Eur Ceram Soc. 2019;39(4):1660–7.
42. Wang JC, Dommati H. Fabrication of zirconia ceramic parts by using solvent-based slurry stereolithography and sintering. Int J Adv Manuf Technol. 2018;98(5–8):1537–46.
43. Gonzalez P, Schwarzer E, Scheithauer U, Kooijmans N, Moritz T. Additive manufacturing of functionally graded ceramic materials by stereolithography. J Vis Exp. 2019;2019(143):1–8.
44. Tomeckova V, Halloran JW. Predictive models for the photopolymerization of ceramic suspensions. J Eur Ceram Soc. 2010;30(14):2833–40.
45. Delhote N, Bila S, Baillargeat D, Chartier T, Verdeyme S. Advanced Design and Fabrication of Microwave Components Based on Shape Optimization and 3D Ceramic Stereolithography Process. Adv Ceram - Synth Charact Process Specif Appl. 2011.
46. Jang KJ, Kang JH, Fisher JG, Park SW. Effect of the volume fraction of zirconia suspensions on the microstructure and physical properties of products produced by additive manufacturing. Dent Mater. 2019;35(5):e97–106.
47. Borlaf M, Serra-Capdevila A, Colominas C, Graule T. Development of UV-curable

ZrO2 slurries for additive manufacturing (LCM-DLP) technology. J Eur Ceram Soc. 2019;39(13):3797–803.

48. Zhang J, Wei L, Meng X, Yu F, Yang N, Liu S. Digital light processing-stereolithography three-dimensional printing of yttria-stabilized zirconia. Ceram Int. 2019;46(7):8745–53.
49. Sun C, Zhang X. Experimental and numerical investigations on microstereolithography of ceramics. J Appl Phys. 2002;92(8):4796–802.
50. Gentry SP, Halloran JW. Light scattering in absorbing ceramic suspensions: Effect on the width and depth of photopolymerized features. J Eur Ceram Soc. 2015;35(6):1895–904.
51. Badev A, Abouliatim Y, Chartier T, Lecamp L, Lebaudy P, Chaput C, et al. Photopolymerization kinetics of a polyether acrylate in the presence of ceramic fillers used in stereolithography. J Photochem Photobiol A Chem. 2011;222(1):117–22.
52. Wang J, Dommati H. Applied Solvent-based slurry stereolithography process to fabricate high- performance ceramic earrings with exquisite details. Solid Free Fabr Symp. 2017;2790–800.

CHAPTER 5

THE SYNERGY BETWEEN SUBSTRATE ARCHITECTURE OF 3D PRINTED CATALYTIC CONVERTERS AND HYDROGEN FOR LOW-TEMPERATURE AFTERTREATMENT SYSTEMS

Authors Contributions:

This chapter of the alternative thesis format is under review in Applied Catalysis B: Environmental. I am the first author of this publication. The paper's details and co-authors' contributions are outlined below.

Kovacev N[1], Doustdar O[2], Li S[3], Tsolakis A[*], Essa K[**]. The synergy between substrate architecture of 3D printed catalytic converters and hydrogen for low-temperature aftertreatment systems. Appl Catal B Environ. 2022. Under review

[1] **Nikolina Kovacev:** The main author, designed and executed experiments, additive manufacturing, catalytic coating, performed all necessary characterisation and data analysis and wrote the manuscript

[2] **Dr Omid Doustdar:** Assistance with the engine operation

[3] **Dr Sheng Li:** Proofreading

***Prof. Athanasios Tsolakis:** Supervision and proofreading

****Dr Khamis Essa:** Supervision and proofreading

CHAPTER 5

THE SYNERGY BETWEEN SUBSTRATE ARCHITECTURE OF 3D PRINTED CATALYTIC CONVERTERS AND HYDROGEN FOR LOW-TEMPERATURE AFTERTREATMENT SYSTEMS

Abstract

In this study, 3D printed diamond-based lattice substrates are proposed as catalytic converters in the automotive aftertreatment system to improve vehicle cold start emissions. The 3D printed diamond-based lattice substrates induce flow mixing that increases interaction of the flow with the washcoated catalyst and allows for efficient use of the available surface area. The study aimed to compare the influence of the 3D printed diamond-based catalyst structures on the light-off behaviour in comparison with the conventional 400 Cell Per Square Inch (CPSI) honeycomb catalyst design. The lattice substrates were manufactured by Digital Light Processing (DLP) technology. Further, they were catalyst coated and their light-off behaviour was studied in a diesel exhaust environment. In addition, the effect of H_2 addition on their performance was investigated. A significant improvement in the light-off temperatures for CO, THC and NO was observed for the 3D printed lattice structures. Furthermore, H_2 presence additionally enhanced the low-temperature activity.

Keywords: aftertreatment system; 3D print; additive manufacturing; honeycombs; automotive catalysts

5.1 Introduction

Stringent legislation to combat the air pollution caused by internal combustion engine exhaust emissions requires the automotive industry to convert into the development of more efficient combustion strategies and advanced catalysts for exhaust gas aftertreatment. EU legislation set mandatory CO_2 emissions targets for new cars and light commercial vehicles to reduce the average fleet CO_2 emissions by 30% in 2030, compared to New European Drive Cycle (NEDC)-based CO_2 limits of 95 g/km for passenger cars and 145 g/km for light commercial vehicles in 2020. Alternatives to Internal Combustion Engines (ICEs), such as Battery Electric Vehicles (BEVs), confront substantial challenges to unrestricted and rapid development, and will not be able to entirely replace ICEs for several decades [1]. The ICEs are anticipated to maintain their dominance in the worldwide maritime, rail, and continental truck industries for years to come. As a result of incomplete combustion in ICEs, carbon monoxide (CO), unburnt hydrocarbons (THCs), nitrogen oxides (NO_x) and particulate matter (PM) are released into the atmosphere. To reduce air pollution, all vehicles are fitted with a catalytic converter designed to purify hazardous gases before they are discharged into the atmosphere. Even though diesel engines have been identified as a viable option to gasoline engines due to their operation at high air/fuel ratios under lean conditions, resulting in high fuel economy, low exhaust gas temperature during cold start and engine stop-start has been brought up as a significant concern in the reduction of THC and CO emissions under a tighter regulatory environment [2]. Various strategies for more effective thermal management of the aftertreatment systems have therefore been researched over the years to achieve early catalyst light-off. These include reducing the weight of the substrate [3], employing electrical heating [4] or the addition of promoters such as hydrogen (H_2) [5,6]. It has previously been observed that hydrogen has a beneficial influence on CO, hydrocarbon oxidation, and NO_2 generation over various diesel oxidation catalysts [6].

In addition, the structure of the monolith substrate can be designed to improve the catalyst light-off performance. Extrusion is without a doubt the most widely used method for manufacturing conventional ceramic honeycomb monolith substrates. Consequently, the honeycomb design depends on the specially designed dies, limiting the design to simple geometric shapes, such as square, hexagonal, circular or triangular [7]. Recognition of the honeycomb's limited performance owing to the laminar flow inside the channels [8], hot spots and non-isothermal temperatures in axial and radial directions [9], has resulted in an extensive research of possible process intensification by direct alteration of the design of the monolith substrate. Randomised foam-like structures have been investigated as potential alternative catalyst supports to achieve a higher catalytic performance [10]. Considering the demand for process intensification, regular periodic open cellular supports provided more design freedom and outperformed the randomised foam structure [11]. However, only limited advanced catalyst architectures, inspired by foams structure cell design, have been proposed due to conventional manufacturing procedures limiting the design flexibility.

Additive Manufacturing (AM) provides a level of design freedom previously unattainable by the extrusion process, providing a remedy to extrusion's limitations. By adding materials layer-by-layer, the creation of complex geometrical shapes in a wide range of materials is facilitated [12]. For the processing of ceramics, vat polymerisation technologies based on liquid ceramic suspensions such as Stereolithography (SLA) and Digital Light Processing (DLP) offer the best printing resolution and surface quality [13]. Bogdan et al. [14] give an informative state-of-art-review on 3D printing technologies used to fabricate a range of heterogeneous catalysts and supports. 3D printing has also enabled fabrication of complex ceramic supports for use in HTP thruster applications [15,16], biomedical applications [17–19], oil sensing [20], and as potential catalytic converters in the automotive sector [21–23]. According to the previous research related to the catalytic converters in the automotive sector, manufacturing constraints limited the amount of design freedom in investigations on 3D printed catalyst substrates, resulting in low surface areas, low cell densities and strut size limited to a minimum of 0.50 mm [22,23]. The substrate designs have not progressed beyond those based on foam structures, not being effective enough for substantial commercial use in the automotive industry. Balzarotti et al. [24] highlight this issue noting that “Technological developments of additive manufacturing techniques able to produce structures with thinner struts would provide increasing advantages.”. In terms of catalyst development, it appears that AM's full potential is yet to be realised.

3D printed ceramic diamond-based lattice structure design was found as a suitable substitute to a traditional channel design in previous research from this group based on numerical simulations of the fluid flow and heat transfer [25].

In the present paper, ceramic diamond-based lattice structures are manufactured via DLP additive manufacturing technology, functionalised with catalytic coating, and tested for their effectiveness in a real exhaust gas environment. Therefore, this study aims to compare the influence of the 3D printed diamond-based catalyst structures on the light-off behaviour with the benchmark 400 CPSI honeycomb catalyst design. Moreover, the benefits of H_2 addition on the performance of lattice structures are examined for the first time, to further increase the low-temperature catalytic efficiency. Findings from this study on 3D printed lattice can be implemented in all catalytic converter systems of all commercial and Hybrid Electric Vehicles (HEV) to meet stringent emissions legislation and enriches the research on moving towards low emissions vehicles.

5.2 Methodology

5.2.1 Substrate design

Diamond unit cell was chosen as the basis for the design of the lattice substrates as it has shown great performance in other catalytic applications [15] and has demonstrated thermal and hydraulic advantages over the 400 CPSI honeycomb (HC) [25]. A diamond lattice has an isotropic geometry that consists of four struts, which are connected nodally with another four struts. Diamond cell with strut orientation angle (θ) of 45°, referred to as D45, is depicted in Figure 5.1a). Elongated diamond unit cell design is shown in Figure 5.1b). This structure results in struts that are more aligned with the incoming flow, as a result of the lower strut orientation angle of 20°, which is expected to reduce the aerodynamic resistance.

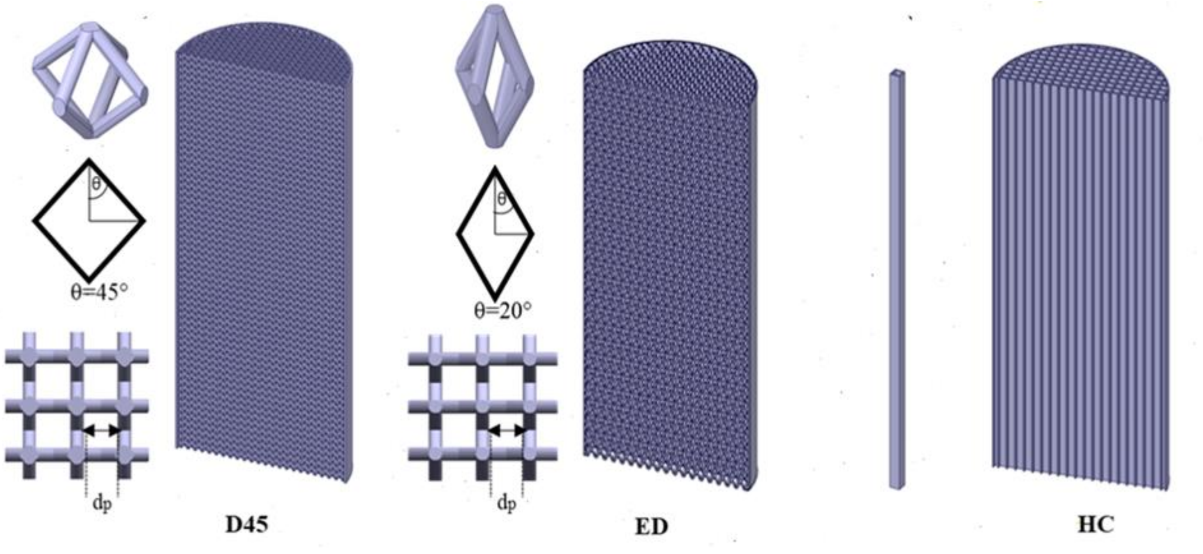

a) b) c)

Figure 5.1 CAD designs of the studied substrates a) Diamond (D45) b) Elongated Diamond (ED) c) Honeycomb (HC)

Based on its wide usage as catalyst support, the 400 CPSI honeycomb monolith design shown in Figure 5.1c) is chosen to provide a baseline case [26,27]. The lattices were designed to have similar CPSI as the benchmark 400 CPSI HC. The geometric surface area of the designed substrates was estimated based on the generated CAD models. Geometrical features of the samples: diameter (D), length (L), geometric surface area (S_v), pore diameter (d_p), cell length (L_c), wall thickness (d_w) and strut diameter (d_s) are listed in Table 5.1.

Table 5.1 Geometrical parameters of the 3D printed substrates

Substrate	**D (mm)**	**L (mm)**	**S_v (m^2/m^3)**	**d_p (mm)**	**d_s (mm)**	**d_w (mm)**	**L_c (mm)**
D45	25	60	2300	0.95	0.30	-	-
ED	25	60	2000	0.95	0.30	-	-
HC	25	60	2890	-	-	0.20	0.95

5.2.2 Digital Light Processing

The ceramic substrates were manufactured using Al_2O_3 ceramic slurry with optimised rheology and curing characteristics for printing lattice structures. The details on the ceramic slurry preparation can be found in [28]. The printing experiments were conducted on the Admaflex 130 (Admatec Europe BV, Alkmaar, The Netherlands). Admaflex technology is based on Digital Light Processing (DLP) and it applies a "bottom-up" printing approach using a Digital Micromirror Device (DMD) which comprises of an array of mirrors, where each mirror represents a single pixel. The exposed layers are irradiated by DLP irradiation throughout the glass bottom. The printing process is as follows: the platform first descends until the distance between the platform and the slurry layer is equal to one-layer thickness, the light projects the first slice information to the slurry layer. The illuminated suspension is cured for several seconds. When the first layer is cured and adhered to the platform, the platform is then lifted by a distance equal to one-layer thickness to achieve one-layer thickness between the first cured layer and the slurry layer. The second layer is then illuminated, cured and adhered to the first cured layer. This process is repeated until the green body is completely fabricated. The exposure parameters, layer thickness and orientation were chosen based on experience and previous resolution study to achieve the final products of satisfactory accuracy [28]. The lattice structures were printed in horizontal direction (X-Y) in respect of the building axis (Z), with a 45° rotation of the Y-axis, energy density of 42 mJ/cm^2 and layer thickness of 25 µm. The honeycomb was printed in a vertical direction (Z) with energy density of 20.16 mJ/cm^2 and layer thickness of 50 µm. The uncured slurry trapped in the green parts was cleaned by immersing the green parts in an ultrasonic bath filled with dibasic ester (Sigma Aldrich, Gillingham, UK). The manufactured samples were then dried by compressed air stream, debinded and sintered. Although lattices with very thin struts of 0.20 mm can be manufactured with the current technique and ceramic slurry, to guarantee acceptable results in terms of printing and repetability, the minimum strut diameter for lattice structures was determined to be 0.30 mm.

5.2.3 Catalyst preparation and washcoating

Incipient wetness method was used to prepare the catalytic powder for washcoating. An aqueous solution of palladium (II) nitrate hydrate (Sigma Aldrich, Gillingham, UK) and tetraammineplatinum (II) nitrate (Sigma Aldrich, Gillingham, UK) with a weight ratio of 1:1 was prepared to achieve a theoretical PGM loading of 2.5 wt% on Al_2O_3 (Sigma Aldrich, Gillingham, UK). The noble metals salt-water mixture was added dropwise to the Al_2O_3 carrier. The prepared paste was dried overnight in atmospheric conditions, followed by dying in a furnace at 70 °C and subsequent calcination at 600 °C for 4 hours [29].

The washcoating slurry was prepared by mixing 17 wt% of the prepared catalyst powder with deionized water and 5 wt% of dispersant (BYK-180, BYK Chemie, GmbH, Wesel, Germany). The mixture was stirred on a magnetic stirrer, followed by planetary ball milling to achieve a homogeneous distribution of the powder in the solution. 5 wt% of boehmite (Disperal, Sasol Germany GmbH, Hamburg, Germany) was added into the mixture to improve the catalyst adherence to the walls of the AM support. The outside walls of the 3D-printed substrates were wrapped in Teflon tape to limit the coating to the lattice/ honeycomb structure. The AM samples were coated with the identical slurry in the same batch. The substrates were immersed vertically into the catalyst slurry and placed under vacuum for 2 minutes. The procedure was repeated several times until loading of approximately 120 g/ft^3 was achieved. After each dip-coat, the excess slurry was removed with pressurised air and the sample was dried in oven at 120 °C for one hour. Finally, the washcoated samples were calcined at 750 °C for 2 hours [15]. Figure 5.2 shows the washcoated catalysts. Prior to any experiment conditions, the catalysts were thermally conditioned in a furnace at 550 °C for 4 hours.

a) b) c)

Figure 5.2 Washcoated catalysts a) D45 b) ED c) HC

5.2.4 Catalyst characterisation methods

A series of characterisation experiments were conducted after the catalyst powder was prepared in order to assess the performance. X-ray Diffraction (XRD) of the catalyst was performed via AXRD Benchtop Powder Diffraction System (Proto Manufacturing, Michigan, USA) diffractometer using Cu Ka radiation. The intensity of scattered X-rays was measured in a 2θ-range of 20-90°. The diffraction patterns of bare γ-Al_2O_3 support and calcinated bimetallic powder are presented in Figure 5.3. The morphology of the bare and coated samples was analysed using Scanning Electron Microscopy (TM3030 Tabletop SEM, Hitachi High-Technologies, Tokyo, Japan). The SEM images in Figure 5.4 show an example of a) bare lattice and b) the washcoated lattice. The elemental composition of the catalyst powder was identified and quantified in terms of the atomic percentage. The Energy-Dispersive X-ray Spectroscopy (EDS) (JCM-6000, JEOL Ltd., Japan) was employed for this elemental analysis and the results are shown in Figure 5.4c) and d).

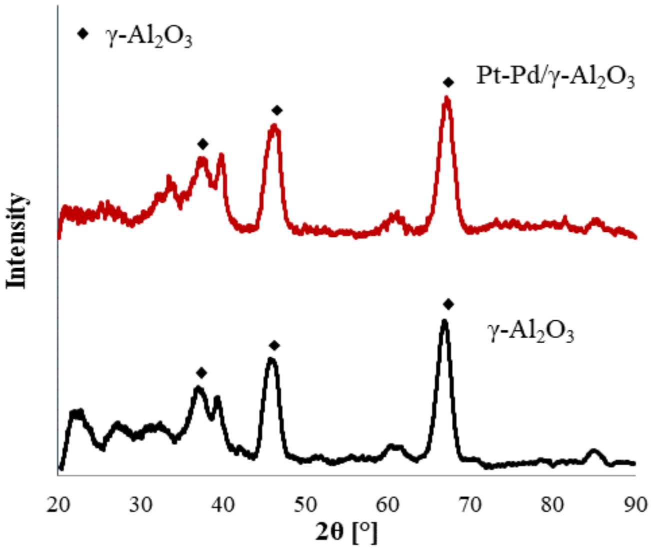

Figure 5.3 XRD of the bare gamma-alumina powder and bimetallic powder sample

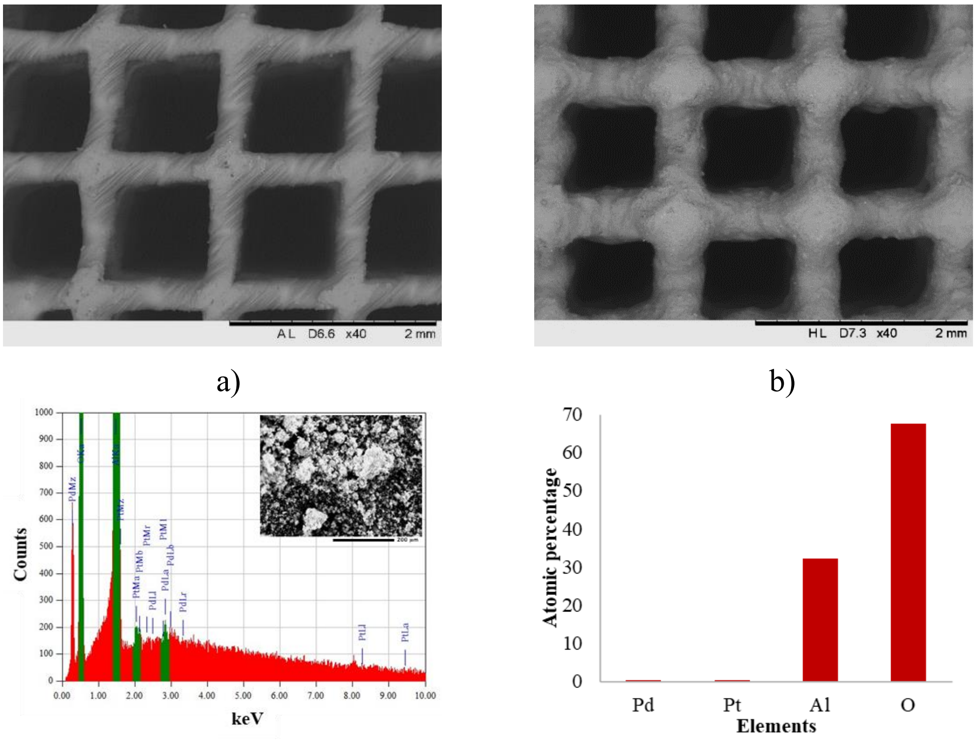

a)

b)

c)

d)

Figure 5.4 SEM images of a) Bare 3D printed sample (D45) b) Coated sample (D45) c) EDX spectrum and d) Summary of the Pt-Pd/γ-Al_2O_3 catalyst

The Brunauer-Emmett-Teller (BET) surface areas of the bare Al_2O_3 support powder and prepared catalytic powder were determined using Micromeritics TriStar II 3020. The samples were degassed for 3 hours at 250 °C before the analysis to remove any volatile adsorbates on the surface.

5.2.5 Engine test procedure

The catalyst washcoated 3D printed substrates were studied in a diesel engine exhaust gas to observe the influence of the substrate geometry on the conversion efficiencies of emissions. A modern common rail single cylinder research diesel engine was used to generate exhaust gas emissions. The engine technical data and specifications are given in Table 5.2.

Table 5.2 Test engine specifications

Engine Specifications	**Data**
Number of Cylinders	1
Bore	84 mm
Connecting Rod Length	160 mm
Displacement Volume	499 cc
Compression Ratio	16.1:1
Maximum Injection Pressure	1500 bar

Standard engine test rig instrumentation to monitor intake air, temperatures (oil, air, inlet manifold and exhaust) and pressures were included in the test rig. The engine was fuelled with ultra-low sulphur diesel provided by Shell Global Solutions, UK. The temperatures at the exhaust manifold, before the catalyst, after the catalyst and at other engine set-up parts were recorded by using K-type thermocouples and a Pico Technology TC-08 thermocouple data logger. The engine condition was kept constant in all tests, to reduce test-to-test variability and ensure steady-state operation. For this purpose, the coefficient of variation of the IMEP for 100 cycles was monitored and kept below 4% during the experiments. The engine was operated at a rotational speed of 1500 rpm with engine load of 2 IMEP to reproduce low-load driving conditions [4]. The detailed testing condition and engine-out emissions repeatability are listed in Table 5.3. The catalyst was placed in a tubular Carbolite Gero furnace with the temperature increase from 100 °C to 400 °C with a heating temperature ramp of 3 °C/min. Gas Hourly Space Velocity (GHSV), defined as the volumetric flow rate of the exhaust gas divided by the external volume of the monolith catalyst, was kept constant at around 33 000 $\pm$ 1000 h^{-1}.

Table 5.3 Engine output emissions concentration

Emissions	**Concentration**
CO (ppm)	271 ± 20
THC (ppm)	305 ± 69
NO (ppm)	215 ± 9
NO_2 (ppm)	61 ± 3
NO_x (ppm)	275 ± 8
N_2O (ppm)	0.68 ± 0.03
CO_2 (%)	4 ± 0.04
H_2O (%)	4.7 ± 0.21

Engine-out exhaust species concentrations were measured at the beginning and at the end of each experiment to monitor the repeatability of the exhaust gas composition during the test. Throughout the experiments, the evolution of the DOC outlet exhaust gas concentration was continuously recorded to calculate the conversion efficiency based on the inlet concentration. An MKS MultiGas 2030 FTIR analyser was used to measure gaseous exhaust emissions. The sampling lines were kept at a temperature of 191 °C to limit any water and hydrocarbon condensation and prevent any reaction between exhaust gas species in the line. A Testo 340 flue gas analyser which is equipped with an oxygen sensor, was used to measure oxygen exhaust content. Light-off experiments were repeated two times to check the repeatability of results. The tests were in good agreement and high repeatability in emissions, and hence in conversion efficiency. To study the influence of hydrogen, pure H_2 from a gas cylinder, purchased from BOC, was introduced upstream of the DOC at a concentration of 1000 ppm. A Bronkhorst digital mass flow controller, EL-Flow was used to precisely measure and control the hydrogen injection. Concentration of hydrogen was measured both upstream and downstream the catalyst by sampling the gas stream using V&F HSense. Figure 5.5 illustrates the schematic diagram of the experimental configuration.

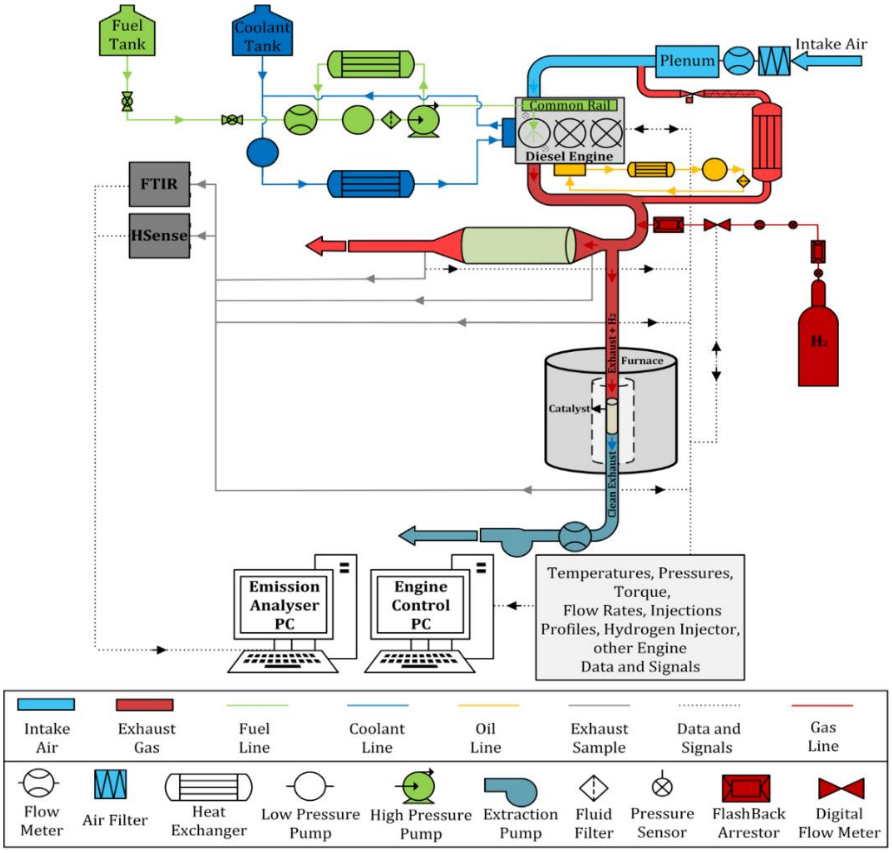

Figure 5.5 Schematic diagram of the experimental setup

5.3 Results and discussion

5.3.1 Catalyst characterisation

XRD patterns of γ-Al_2O_3 support and the bimetallic powder showed very similar profile and almost all the diffraction peaks were attributed to γ-Al_2O_3. Since the XRD peaks for Pt and Pd mainly overlapped with those of γ-Al_2O_3, it was not possible to distinguish any peaks associated with the presence of Pt and Pd. This suggested that the particles were well dispersed and no discernible diffraction signals could be produced [30]. The SEM of the washcoated samples revealed that the inherent surface of the 3D printed substrate disappeared, presenting a complete substrate coverage by the catalytic coating (Figure 5.4b)). EDS showed that the catalyst was composed of Pt, Pd, Al and O. Meanwhile, the atomic percentage of Pt, Pd, Al and O were determined to be 0.1%, 0.1%, 32.2% and 67.6%, respectively. BET analysis revealed the starting Al_2O_3 powder had a BET surface area of 172 m^2/g, whereas after impregnation with Pd and Pt the BET surface area of the catalyst powder slightly decreased to the value of 156 m^2/g, most likely due to the impregnation of the active metals on the support and the high calcination temperature employed at 750 °C [31]. All calcinated washcoated samples had washcoats that were resistant to disintegration during handling. Catalyst substrate comparison in terms of reactivity should involve substrates with the same washcoat amount, the same quantity of active metals, as well as the same available surface area for reactions [11]. In this study, the substrates were coated with identical washcoat, however some variation in coating among the samples was unavoidable due to distinct geometries. For all substrates the washcoat composition and, in particular, the composition and quantity of the active precious metals have been kept identical, since they were coated in the same batch with identical washcoating slurry, thus the reaction behaviour of the catalyst is comparable. The coating method is a key issue for catalytic applications determining catalyst performances and homogeneous coating of 3D printed intricate substrates is often difficult due to the tortuous support geometry [35]. Considering future research, the coating aspect should be further optimised for coating 3D printed structures.

5.3.2 Influence of the substrate structure on the catalyst activity

Additionally, the performance of the prepared catalytic converters in the real engine exhaust versus temperature for CO, THC, NO and ratio of NO_2/NO_x were analysed for the lattices and the reference HC with and without the addition of hydrogen (H_2). Figure 5.6a) illustrates the conversion efficiencies of lattice and honeycomb in terms of CO oxidation. At low temperatures, where the reaction rate is limited by the chemical kinetics of the oxidation reaction, the conversion between the various substrates is relatively comparable. With the increase of the inlet gas temperature, the conversion exponentially increased, and the samples' structure started to have a prominent role in the light-off behaviour. D45 and ED structures had overall higher CO conversion efficiencies as compared to HC. Moreover, all three structures reached 100% conversion with a relatively modest variation between the samples, when the CO conversion became mass transfer limited. The results of the oxidation of the THC are shown in Figure 5.6b). As expected, the THC conversion started after a large amount of CO became oxidised, when more catalytic active sites became available for hydrocarbons to adsorb onto. Nevertheless, all THC oxidation efficiencies were lower than CO and the peak conversion efficiency did not reach 100% in lattices nor in the HC. This phenomenon has been previously ascribed to the presence of certain long-chain hydrocarbons that contribute to the partial conversion of THC due to their lower diffusivity to reach the catalyst active sites, resulting in incomplete conversion [6].

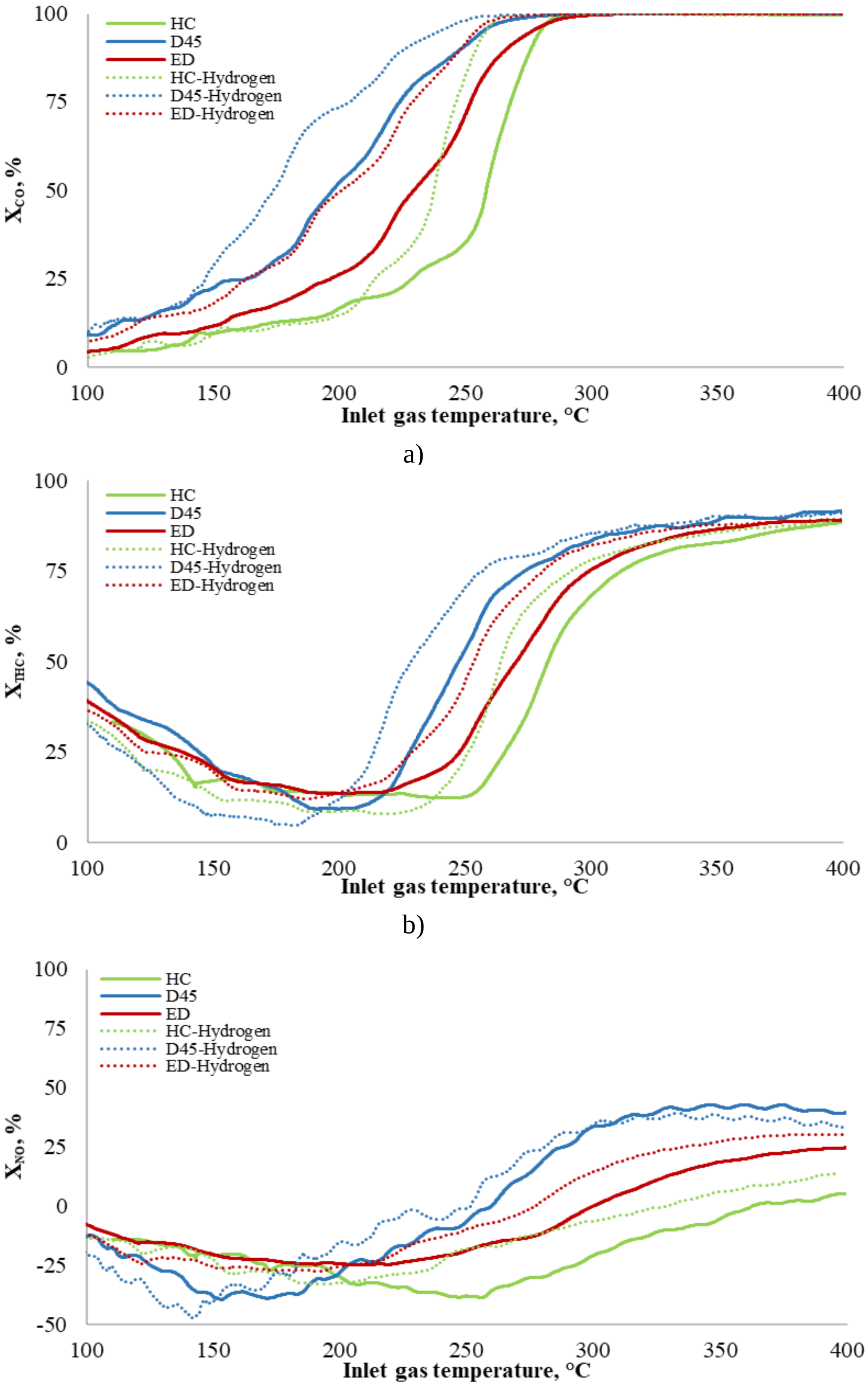

a)

b)

c)

Figure 5.6 Conversion efficiencies for a) CO b) THC c) NO for HC, D45 and ED with and without H_2

In terms of the NO conversion efficiencies (depicted in Figure 5.6c)), D45 reached a maximum of 40% NO conversion, ED 25%, while the conventional HC structure reached only 7%. Conversion curves showed similar light-off trends with the increasing temperature: negligible conversion at low temperatures, then ignition and ultimately, a plateau where the conversion is no longer influenced by the temperature, in line with the literature findings [6]. The NO_2/NO_x yield (Figure 5.7) for both lattice substrates was greater than in the conventional HC at moderate and high temperatures. At low temperatures NO_2 is consumed as an oxidant by hydrocarbons and CO, hence the ratio decreases. As the temperature rises, hydrocarbons begin reacting with molecular oxygen, which results in an increase of NO conversion and a consequent increase in NO_2 concentration for all structures. A steep increase in NO_2/NO_x ratio for the D45 sample at temperatures above 220 °C, implies a rather large selectivity for NO_2 production in this specific structure. However, at high temperatures, the ratio declined, which may be explained by the NO to NO_2 oxidation reaction becoming restricted by the thermodynamic equilibrium [33].

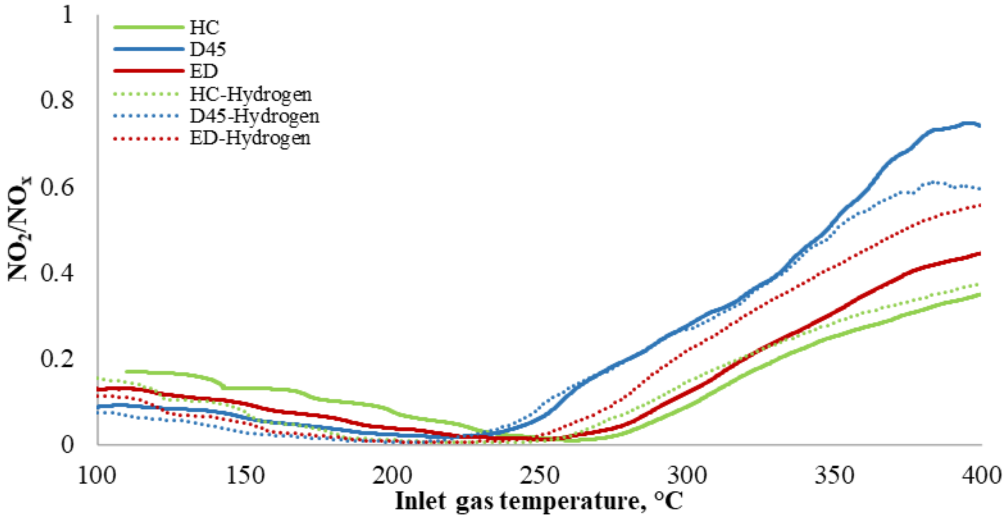

Figure 5.7 NO_2/NO_x ratio for HC, D45 and ED, with and without H_2

In addition, the configurations with the greatest CO and THC conversions were also the ones with the highest NO_2/NO_x ratio illustrating the relations between these exhaust species, in accordance with the literature [34].

5.3.3 Hydrogen effect on the catalyst performance

Table 5.4 presents a comparison of both T_{50} and T_{90} values (temperatures recorded for 50% and 90% conversion levels of CO and THC) for the studied structures, with and without H_2 presence. A promoting effect of H_2 added upstream the catalysts on the CO light-off temperature (T_{50}) can be seen.

Table 5.4 Summary of T_{50} and T_{90} for CO and THC

Catalyst	**CO T_{50}, °C**	**CO T_{90}, °C**	**THC T_{50}, °C**	**THC T_{90}, °C**
HC	252	263	273	399
HC-H_2	233	244	258	390
D45	193	244	242	346
D45-H_2	172	223	226	337
ED	223	259	262	376
ED-H_2	195	241	248	344

A considerable reduction in T_{50} was observed particularly for ED. On the other hand, slightly less H_2 effect was found for D45 and the conventional HC structure. Subsequently, a positive effect on the decrease of T_{90} for CO in all substrates was observed, implying the structures that achieved a faster light-off, also demonstrated complete conversion at lower temperatures. Overall conclusion of conversion efficiency for THC with H_2 (D45>ED>HC) remained consistent. Yet, compared to CO, the gain in THC conversions in H_2 presence was apparent to a lesser extent. The overall reductions of T_{50} for THC conversions were similar for all studied structures. Another important aspect of the DOC aside from CO and THC oxidation is the ability to oxidise NO to NO_2, which may be used for passive continuous regeneration of the downstream DPF or to enhance the fast-SCR reaction [6]. The DOC catalyst is typically designed to boost NO to NO_2 conversion at the temperature range between 300 and 400 °C, which is characteristic of the diesel exhaust stream [35,36].

In the presence of H_2 in the case of D45, a slight impact on the NO conversion was observed only at moderate temperatures, whereas at higher temperatures NO conversion diminished, which reflected on the NO_2 yield (Figure 5.8). However, this structure showed the highest overall NO_2 yield in the moderate to high temperature range, regardless of the H_2 addition, in respect to HC and ED. On the other hand, addition of H_2 seemed to have a positive effect on NO conversion for both HC and ED. Thus far, no significant increase of the maximum NO_2 production was observed for HC. Hydrogen presence was found to positively influence the maximum NO_2 yield in the ED lattice.

Generally, the promotional effects of H_2 on catalyst activities can be explained by the formation of intermediate species that facilitate CO and THC oxidation (e.g. OH and HO_2 radicals), higher availability of active sites for hydrocarbons as CO has been oxidised at lower temperatures reducing the competitive adsorption and exothermic effects of hydrogen and CO oxidation [6,37]. Since hydrogen oxidation is exothermic, the local temperature of the catalysts might be increasing and enhancing the oxidation of other components [38]. The increase of the rate of CO and THC oxidation with H_2 also facilitated the NO adsorption on the active sites [39].

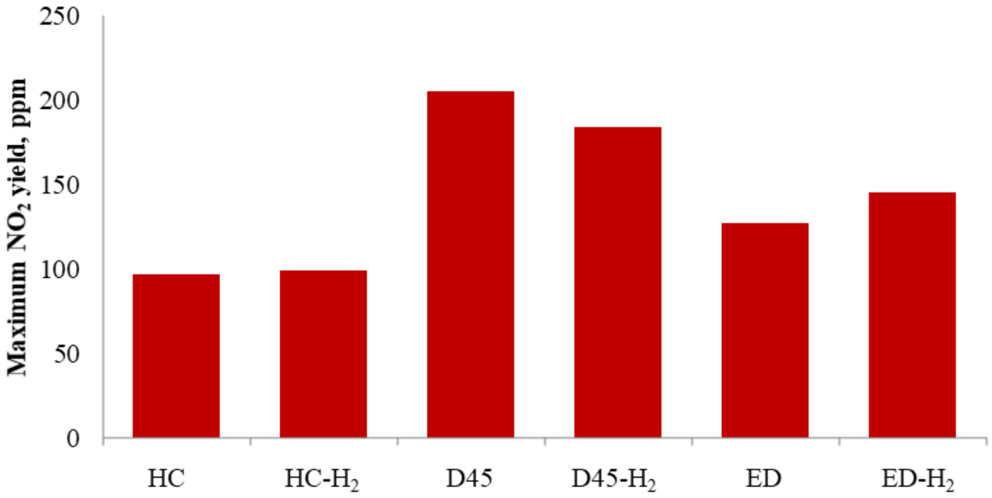

Figure 5.8 Maximum NO_2 yield for various structures with and without H_2 addition

5.3.4 Combined effect of the catalyst structure and hydrogen addition

The differences in conversion efficiencies are attributed merely to the variation of the substrate geometries, since the experimental conditions and the catalyst coating for all tests were equal. Distinct activity of the two lattice catalysts (D45 and ED) could be explained by their unique designs resulting in different gas flow paths inside the structures. It is also evident that the lattice substrates perform better than the standard HC; D45 having approximately 20% and ED 30% less surface area in comparison with HC, in line with findings from [23] which showed that polyhedral cell with four times lower surface area achieve similar light-off behaviour as HC [23]. This implies that the flow regime inside the substrates is more significant than surface area as the surface area is utilised more efficiently in the 3D printed substrates. Overall lower efficiencies are ascribed to the laminar regime in the HC design, whereas flow mixing facilitates conversion increase in 3D printed structures [22,40]. Interestingly, looking at the conversion curves of HC with H_2 in Figure 5.6, generally higher oxidation efficiencies are achieved by ED and D45 even without the H_2 addition for all species. It cannot be discarded that the catalyst surface temperature in lattices was higher than the inlet gas, which further increased the reaction rate, since the ability to interchange flow in both radial and axial directions ultimately raises the possibility of more effective heat utilisation in lattice structures [25]. Lattice structures in combination with hydrogen addition allowed greater contact of the reactant with the catalyst adhered to the structure’s struts, with more efficiently used surface area, which eventually increased the mass transfer. Increased NO_2 yield in the ED lattice may be explained by the unique ED design, where the exhaust flows around lattice struts of narrower angle than in D45, most likely increasing the residence time, which seems to be more influential in enhancing the oxidising of slow chemical reaction of NO to NO_2 with H_2.

In summary, the 3D printed lattice catalysts with similar cell density as the conventional 400 CPSI HC resulted in superior light-off behaviour for all studied species. Both lattice designs overcame the performance of the reference HC catalyst, with H_2 additionally boosting their conversion performance. Clearly, the flow path inside the catalyst structure had a significant influence on the catalyst's activity. Due to the flexibility of the DLP process employed in this study, many other substrate geometries, cell sizes and strut diameters are achievable. The findings for the two distinct 3D printed substrates discussed in this work suggest that an appropriate substrate may be designed based on the application requirements. Furthermore, the structure may be altered to create even more complex designs, such as gradient structures with radial or axial cell density variation, or a combination of the two. In addition, the 3D printing material can be varied as well to further control the thermal response of the substrates.

5.4 Conclusions

The scope of this research was to demonstrate the potential of additively manufactured lattice-based monolithic substrates as catalytic converters. The lattice-based substrates were manufactured using DLP technology and were successfully coated with bimetallic Pt-Pd catalyst supported on γ-Al_2O_3. Furthermore, their light-off behaviour was tested in the exhaust gas environment. In addition, the benefits of hydrogen addition on the lattice performances were explored.

The results support the following conclusions:

- DLP technology was successfully used to manufacture intricate lattice-based substrates
- In case of the lattice-based catalysts, superior catalytic activity was observed for abatement of CO, THC and NO in comparison with 400 CPSI HC, with significant reduction in the light-off temperatures
- In the mass-transfer area, there was no evidence of any significant competition between lattices and honeycomb, even though the lattice substrates had 20-30% lower surface areas
- The addition of hydrogen to all catalyst designs had a positive effect on the CO light-off temperature, however the gain in THC light-off temperature reduction was apparent to a lesser extent
- D45 showed the highest overall NO_2 yield in the moderate to high temperature range, regardless of the hydrogen presence
- Hydrogen addition improved the NO_2 production in the ED lattice, due to the unique structure of ED with increased flow residence time, which seems to be more prominent in enhancing the oxidation of the slow chemical reaction of NO to NO_2 with hydrogen

- The intricate lattice structures in combination with hydrogen addition allowed greater contact of the reactant with the catalyst adhered to the structure's struts due to flow mixing and more efficiently used surface area, shifting the light-off curves of all studied species to lower temperatures

The AM structures described in this paper for DOCs would also be applicable for catalytic converters in other applications, particularly for HEV aftertreatment systems. Moreover, the flexibility of the AM process offers countless possibilities of the substrate design and material of choice. Results of this research proved the importance of 3D printing to design and produce efficient advanced catalytic converters to meet stringent emissions regulations and a way forward to low-emissions vehicles.

Acknowledgements

The research leading to these results has received funding from the Engineering and Physical Sciences Research Council for project FACE - Novel Integrated Fuel Reformer-Aftertreatment System for Clean and Efficient Road Vehicles under grant number EP/P03117X/1. N.K. also thanks to the University of Birmingham for the award of a PhD scholarship.

References

1. Kalghatgi G. Challenges of energy transition needed to meet decarbonisation targets set up to address climate change. J Automot Saf Energy. 2020;11(3):276–86.
2. Olabi AG, Maizak D, Wilberforce T. Review of the regulations and techniques to eliminate toxic emissions from diesel engine cars. Sci Total Environ. 2020;748:141249.
3. Otsuka S, Suehiro Y, Koyama H, Matsuzono Y, Tanner C, Bronfenbrenner D, et al. Development of a Super-Light Substrate for LEV III / Tier3 Emission Regulation. SAE Tech Pap. 2015;(2015-01–1001):2–7.
4. Hamedi MR, Doustdar O, Tsolakis A, Hartland J. Energy-efficient heating strategies of diesel oxidation catalyst for low emissions vehicles. Energy. 2021;230:120819.
5. Theinnoi K, Tsolakis A, Sawatmongkhon B, Chuepeng S. A Study of Hydrogen Addition on Diesel Oxidation Catalyst Activities under the Real Diesel Engine. J Res Appl meachanical Eng. 2013;1(3):1–4.
6. Herreros JM, Gill SS, Lefort I, Tsolakis A, Millington P, Moss E. Enhancing the low temperature oxidation performance over a Pt and a Pt-Pd diesel oxidation catalyst. Appl Catal B Environ. 2014;147:835–41.
7. Avila P, Montes M, Miró EE. Monolithic reactors for environmental applications: A review on preparation technologies. Chem Eng J. 2005;109(1):11–36.
8. Kim JY, Son S. Improving flow efficiency of a catalytic converter using the concept of radially variable cell density - Part I. SAE Tech Pap Ser. 1999;(724).
9. Busse C, Freund H, Schwieger W. Intensification of heat transfer in catalytic reactors by additively manufactured periodic open cellular structures (POCS). Chem Eng Process Process Intensif. 2018;124:199–214.
10. Bach C, Eggenschwiler PD. Ceramic foam catalyst substrates for diesel oxidation catalysts: Pollutant conversion and operational issues. SAE Tech Pap. 2011;20110459.
11. Lucci F, Della Torre A, Montenegro G, Dimopoulos Eggenschwiler P. On the catalytic performance of open cell structures versus honeycombs. Chem Eng J. 2015;264:514–21.
12. Hassanin H, Essa K, Elshaer A, Imbaby M, El-Mongy HH, El-Sayed TA. Micro-fabrication of ceramics: Additive manufacturing and conventional technologies. J Adv Ceram. 2021;10(1):1–27.
13. Santoliquido O, Colombo P, Ortona A. Additive Manufacturing of ceramic components by Digital Light Processing: A comparison between the “bottom-up” and the “top-down” approaches. J Eur Ceram Soc. 2019;39(6):2140–8.
14. Bogdan E, Michorczyk P. 3D Printing in Heterogeneous Catalysis—the State of the Art. Materials. 2020;13(20):1–23.
15. Essa K, Hassanin H, Attallah MM, Adkins NJ, Musker AJ, Roberts GT, et al. Development and testing of an additively manufactured monolithic catalyst bed for HTP thruster applications. Appl Catal A Gen. 2017;542:125–35.
16. Hassanin H, Alkendi Y, Elsayed M, Essa K, Zweiri Y. Controlling the Properties of Additively Manufactured Cellular Structures Using Machine Learning Approaches. Adv Eng Mater. 2020;22(3):1–9.
17. El-Sayed MA, Essa K, Ghazy M, Hassanin H. Design optimization of additively manufactured titanium lattice structures for biomedical implants. Int J Adv Manuf Technol. 2020;110(9–10):2257–68.
18. Hassanin H, El-Sayed MA, Elshaer A, Essa K, Jiang K. Microfabrication of net shape zirconia/alumina nanocomposite micro parts. Nanomaterials. 2018;8(8).

19. Hassanin H, El-Sayed MA, Elshaer A, Essa K, Jiang K. Microfabrication of ceramic nano-composite micro dental parts. Nanomaterials. 2018;7(26).
20. Sabouri A, Yetisen AK, Sadigzade R, Hassanin H, Essa K, Butt H. Three-Dimensional Microstructured Lattices for Oil Sensing. Energy and Fuels. 2017;31(3):2524–9.
21. Santoliquido O, Bianchi G, Dimopoulos Eggenschwiler P, Ortona A. Additive manufacturing of periodic ceramic substrates for automotive catalyst supports. Int J Appl Ceram Technol. 2017;14(6):1164–73.
22. Hajimirzaee S, Doyle AM. 3D printed catalytic converters with enhanced activity for low-temperature methane oxidation in dual-fuel engines. Fuel. 2020;274(1):117848.
23. Papetti V, Dimopoulos Eggenschwiler P, Della Torre A, Lucci F, Ortona A, Montenegro G. Additive Manufactured open cell polyhedral structures as substrates for automotive catalysts. Int J Heat Mass Transf. 2018;126:1035–4.
24. Balzarotti R, Ambrosetti M, Arnesano M, Anglani A, Groppi G, Tronconi E. Periodic open cellular structures (POCS) as enhanced catalyst supports: Optimization of the coating procedure and analysis of mass transport. Appl Catal B Environ. 2021;283.
25. Kovacev N, Li S, Zeraati-Rezaei S, Hemida H, Tsolakis A, Essa K. Effects of the internal structures of monolith ceramic substrates on thermal and hydraulic properties: additive manufacturing, numerical modelling and experimental testing. Int J Adv Manuf Technol. 2020;112:1115–32.
26. Ibrahim HA, Ahmed WH, Abdou S, Blagojevic V. Experimental and numerical investigations of flow through catalytic converters. Int J Heat Mass Transf. 2018;127:546–60.
27. Piqueras P, Ruiz MJ, Herreros JM, Tsolakis A. Influence of the cell geometry on the conversion efficiency of oxidation catalysts under real driving conditions. Energy Convers Manag. 2021;233.
28. Kovacev N, Li S, Essa K. Effect of the preparation techniques of photopolymerizable ceramic slurry and printing parameters on the accuracy of 3D printed lattice structures. J Eur Ceram Soc. 2021;41(15):7734–43.
29. Gremminger A, Pihl J, Casapu M, Grunwaldt JD, Toops TJ, Deutschmann O. PGM based catalysts for exhaust-gas after-treatment under typical diesel, gasoline and gas engine conditions with focus on methane and formaldehyde oxidation. Appl Catal B Environ. 2020;265:118571.
30. Bai Q, Li D, He L, Xiao H, Sui N, Liu M. Solvent-free selective hydrogenation of o-chloronitrobenzene to o-chloroaniline over alumina supported Pt nanoparticles. Prog Nat Sci Mater Int. 2015;25(3):179–84.
31. Karatzas X, Jansson K, Dawody J, Lanza R, Pettersson LJ. Microemulsion and incipient wetness prepared Rh-based catalyst for diesel reforming. Catal Today. 2011;175(1):515–23.
32. Giani L, Cristiani C, Groppi G, Tronconi E. Washcoating method for Pd/γ-Al2O3 deposition on metallic foams. Appl Catal B Environ. 2006;62(1–2):121–31.
33. Resitoglu I., Altinisik K, Keskin A. The Pollutant emissions from diesel-engine vehicles and exhaust aftertreatment systems. Clean Techn Env Policy. 2015;17:15–27.
34. Lefort I, Herreros JM, Tsolakis A. Reduction of low temperature engine pollutants by understanding the exhaust species interactions in a diesel oxidation catalyst. Environ Sci Technol. 2014;48(4):2361–7.
35. Russell A, Epling WS. Diesel oxidation catalysts. Catal Rev - Sci Eng. 2011;53(4):337–423.
36. Jung Y, Pyo YD, Jang J, Kim GC, Cho CP, Yang C. NO, NO2 and N2O emissions over

a SCR using DOC and DPF systems with Pt reduction. Chem Eng J. 2019;369(2):1059–67.

37. Azis MM, Auvray X, Olsson L, Creaser D. Evaluation of H2 effect on NO oxidation over a diesel oxidation catalyst. Appl Catal B Environ. 2015;179(2):542–50.
38. Hoang S, Lu X, Tang W, Wang S, Du S, Nam CY, et al. High performance diesel oxidation catalysts using ultra-low Pt loading on titania nanowire array integrated cordierite honeycombs. Catal Today. 2019;320:2–10.
39. Wang W, Herreros JM, Tsolakis A, York APE. Increased NO2 concentration in the diesel engine exhaust for improved Ag/Al2O3 catalyst NH3-SCR activity. Chem Eng J. 2015;270(2):582–9.
40. Santos H, Costa M. The relative importance of external and internal transport phenomena in three way catalysts. Int J Heat Mass Transf. 2008;51(5–6):1409–22.

CHAPTER 6
ADDITIVE MANUFACTURING OF NOVEL HYBRID MONOLITHIC CERAMIC SUBSTRATES

Authors Contributions:

This chapter of the alternative thesis format is published in Aerospace. I am the first author of this publication. The paper's details and co-authors' contributions are outlined below.

Kovacev N[1], Li S[2], Li W[3], Zeraati Rezaei S[4], Tsolakis A[*], Essa K[**]. Additive manufacturing of novel hybrid monolithic ceramic substrates. Aerospace. 2022; 9(5): 255.

[1] **Nikolina Kovacev:** The main author, designed the interlocks, designed and executed experiments, additive manufacturing, performed all necessary characterisation and data analysis and wrote the manuscript

[2] **Dr Sheng Li:** Proofreading

[3] **Dr Weining Li:** Assistance with SEM

[4] **Dr Soheil Zeraati-Rezaei:** Proofreading

***Prof. Athanasios Tsolakis:** Supervision

****Dr Khamis Essa:** Supervision and proofreading

CHAPTER 6

ADDITIVE MANUFACTURING OF NOVEL HYBRID MONOLITHIC CERAMIC SUBSTRATES

Abstract

Additive Manufacturing (AM) can revolutionise engineering by taking advantage of the unconstrained design and overcoming the limitations of traditional manufacturing capabilities. A promising application of AM is in catalyst substrate manufacturing, aimed at enhancement of the catalytic efficiency and reduction of the volume and weight of the catalytic reactors in the exhaust gas aftertreatment systems. This work addresses the design and fabrication of innovative, hybrid monolithic ceramic substrates through the use of AM technology based on Digital Light Processing (DLP). The designs were based on two individual substrates integrated into a single, dual-substrate monolith by various interlocking systems. These novel dual-substrate monoliths lay the foundation for a potential reduction of the complexity and expense of the aftertreatment system. Several examples of interlocking systems for dual-substrates were designed, manufactured and thermally postprocessed to illustrate the viability and versatility of the DLP manufacturing process. Based on the findings, the sintered parts displayed anisotropic sintering shrinkage of approximately 14% in the X–Y direction and 19% in the Z direction, with a sintered density of 97.88±0.01%. Finally, mechanical tests revealed the mechanical integrity of the designed interlocks. U-lock and Thread configurations were found to sustain more load until complete failure.

Keywords: additive manufacturing; DLP; monolithic substrate; ceramic; hybrid catalyst

6.1 Introduction

Ceramic monolithic substrates find substantial commercial use in the automotive industry as catalyst supports for the purification of noxious exhaust gases in aftertreatment systems [1]. Despite the high surface area and low backpressure of the conventional honeycomb substrates, manufacturing constraints preclude any further improvements in their design for enhancing the catalytic activity. Therefore, compliance with present and forthcoming rigorous vehicle emission legislation poses major difficulties.

It is of interest to reduce the number of individual catalytic systems (e.g., by merging their functions) in the exhaust aftertreatment to reduce the system's volume and weight. For instance, a typical diesel exhaust aftertreatment system can incorporate four separate catalytic systems: diesel particulate filter (DPF), a catalyst for selective catalytic reduction of nitrogen oxides (NO_x) with ammonia (NH_3-SCR), an ammonia slip catalyst (ASC) and a diesel oxidation catalyst (DOC) [2]. Solutions to simplify the state-of-the-art aftertreatment arrangement to decrease the volume and weight of the aftertreatment system, have been suggested in the past. For example, an all-in-one four-way catalytic converter (FWCC) combines oxidation–reduction catalysts to simultaneously remove carbon monoxide, hydrocarbons, particulate matter, and nitrogen oxides. The FWCC is an efficient solution to the limited space capacity in the aftertreatment. However, the complex multi-phase reaction processes where the species interact with each other and compete for active sites affect the catalytic efficiency. On the other hand, dual-catalyst configurations can improve the efficiency of a single component, such as the one proposed by Lefort et al. [3], by placing a DOC catalyst with lower thermal mass to quickly light-off in front, and a DOC catalyst with higher thermal mass in the back to store heat. Moreover, layering of active washcoats on top of one another, or zoning, where the active component concentration in the washcoat changes along the axial length, can have a considerable influence on the catalytic light-off of single components in the aftertreatment. Hazlett et al. [4] showed that Pt-Pd catalysts can be zoned axially along the monolith in varying ratios to increase NO oxidation selectivity by promoting CO oxidation with a larger quantity of Pd at the front, and higher amounts of Pt along the length for NO oxidation. Furthermore, taking advantage of the particular operating temperature range of the individual active materials in SCR can be achieved by layering and zoning Fe/ZSM-5 and Cu/zeolite [4]. The aforementioned layouts do not offer any space savings, but they do have the ability to minimise the precious metal loading and the overall cost. Innovative aftertreatment solutions aimed at the improvement of the performance of the aftertreatment systems, such as exhaust gas fuel reforming, to provide a small concentration of hydrogen (H_2) to the aftertreatment catalyst show great potential [5–7]. Direct hydrogen addition positively affects the performance of various aftertreatment devices, including catalytic converters, DPF and NO_x traps [6,8,9].However, the addition of an on-board catalytic reformer to produce H_2-enriched exhaust gas adds complexity, weight, and volume to the already complex aftertreatment system.

Moreover, in the aerospace sector, additively manufactured monolithic catalysts with high surface areas and low-pressure drops can be employed as monopropellant thrusters. As a result of increased interest in hydrazine-based propellant alternatives, catalysts for high test peroxide (HTP), hydroxylammonium nitrate (HAN) or ammonium dinitramide (ADN) propellant blends have received considerable attention in the last two decades. Within the project Rheform, additively manufactured monolith catalysts with straight channels, cellular structure and polyhedral structure were presented to improve the ADN-based propulsion systems [10]. Moreover, Koopmans et al. [11] compared the performance of the complex additively manufactured monoliths with extruded catalysts with respect to the decomposition of highly concentrated hydrogen peroxide. Decomposition tests revealed that the AM catalysts showed an increase in the temperature transient time compared to the extruded one. Metallic gauzes or screens, ceramic pellets coated with an active catalytic phase or extruded monolithic beds are currently employed in HTP catalyst applications. However, fragmentation, high pressure drop and flooding are common issues in these configurations [12]. Essa et al. [12] have demonstrated additively manufactured high-performance monolithic catalyst beds with complicated geometries for use in hydrogen peroxide monopropellant thruster. The AM catalysts outperformed MnO_x-coated ceria pellets while providing an acceptable pressure drop.

Ceramic additive manufacturing has lately undergone substantial research, introducing brand new possibilities in the design and fabrication of novel monolithic substrates for various applications [13–17]. In recent years, significant scientific efforts have been focused on enhancing the efficiency of the catalyst substrates. Alteration of the substrate design by introducing lattice-based substrates was found to offer advantages in terms of chemical activity over the conventional channel design [18,19]. In light of the opportunities provided by additive manufacturing processes, AM techniques such as material extrusion AM [20,21] and vat photopolymerisation [18] have been successfully utilised to manufacture ceramic catalytic substrates with intricate lattice structures. DLP is one of the additive manufacturing technologies suitable for the fabrication of complex ceramic monolithic substrates with fine features [22]. To create an image, DLP projectors use a digital micromirror device chip (DMD) and a light source, where each image layer is projected onto a layer of photosensitive ceramic slurry, which hardens when exposed to the light source, and the process is repeated until the green body is formed [23]. Upon finalising the green body shaping, the part is removed from the building platform, cleaned from any residual slurry and subjected to debinding and sintering process to obtain the final dense part. Removal of the photopolymerised resin from the interspace of the ceramic particles, known as debinding, is a critical step in the post-treatment. Slow heating rates and appropriate holding temperatures are necessary to avoid delamination, cracks, deformation or collapse caused by thermal stress from the decomposition of the organic components [24]. During the sintering stage at high temperatures, a dense ceramic part is achieved.

In this work, a proof-of-concept is presented to propose a potential solution for the aftertreatment reactor complexity reduction. A procedure to design, additively manufacture and thermally postprocess dual-substrate emission control hybrid supports, that could be separately coated with active material and integrated into a single brick, is proposed. This concept can be applied in catalytic applications where space savings are beneficial. Several interlocking mechanisms are presented to demonstrate the DLP manufacturing process’s feasibility and flexibility.

6.2 Methodology

6.2.1 Interlock designs

The three-dimensional models were designed using CATIA and Ansys SpaceClaim 2020R1 CAD software. The structure of the substrates is based on a unit cell of a diamond lattice [12,18]. The substrates feature a cylindrical core with an interlocking mechanism on the outer surface and a shell substrate with an interlocking mechanism in the cored centre. The CAD designs of the interlocking mechanisms are shown in Figure 6.1.

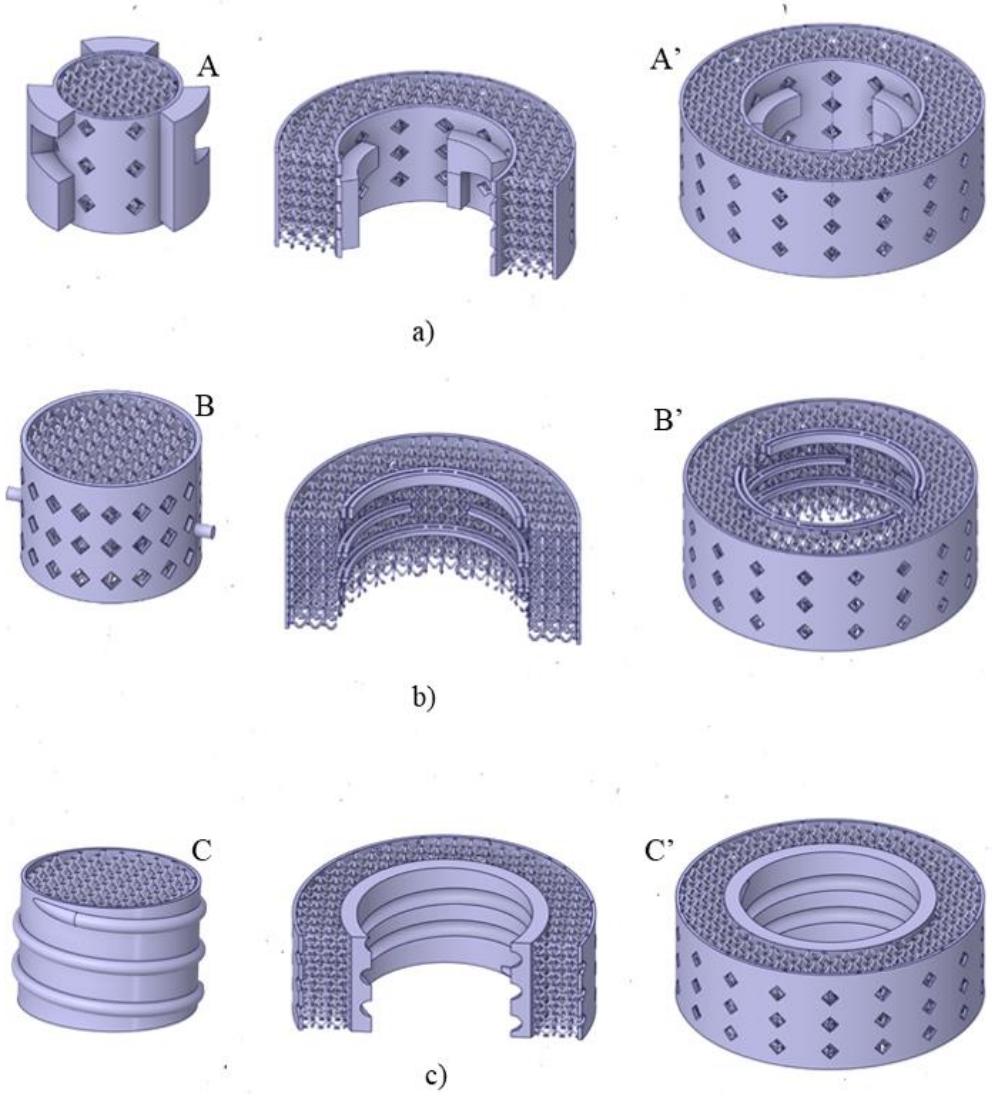

Figure 6.1 CAD models of the fastening designs, iso view of core and shell with cross-sectional shell view for a) U-lock: core (A) and shell (A’) b) Twist-lock: core (B) and shell (B’) c) Thread: core (C) and shell (C’)

6.2.2 Ceramic slurry preparation and characterisation

The ceramic slurry was prepared in-house by first combining the components of the resin: 33.4 wt% of 4-acryloylmorpholine (TCI, Tokyo, Japan), 28 wt% of 1,6-hexanediol diacrylate (TCI, Tokyo, Japan), 18.6 wt% of pentaerythritol tetraacrylate (TCI, Tokyo, Japan) and 20 wt% of dibutyl phthalate (Sigma Aldrich, Gillingham, UK) The chemical structure of the materials used for the preparation of the resin is shown in Figure 6.2.

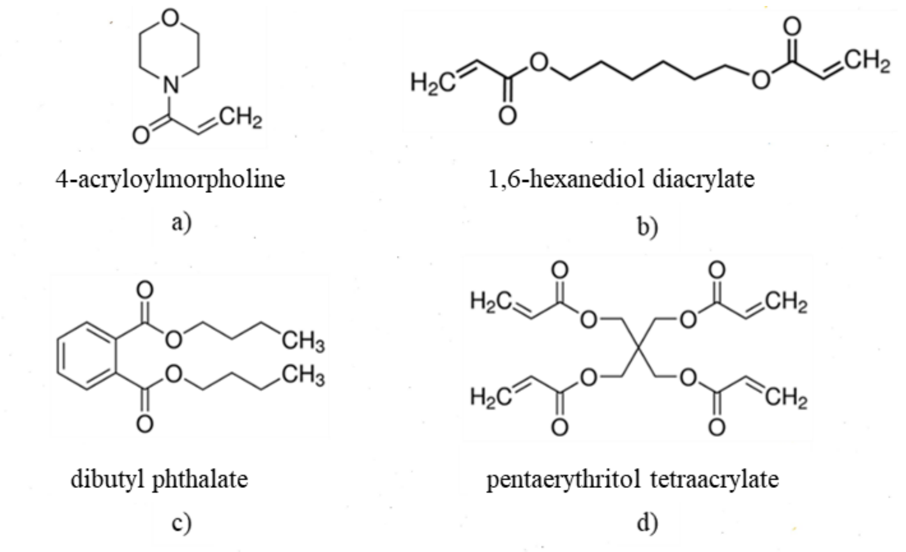

4-acryloylmorpholine

a)

1,6-hexanediol diacrylate

b)

dibutyl phthalate

c)

pentaerythritol tetraacrylate

d)

Figure 6.2 Chemical structure of the resin components a) 4-Acryloylmorpholine b) 1,6-Hexanediol diacrylate c) Dibutyl phthalate d) Pentaerythritol tetraacrylate

The resin components were mixed with an overhead mixer at room temperature for 30 min. Commercially available alumina oxide powder (A16 SG, Almatis GmbH, Ludwigshafen, Germany) was pre-treated with 2 wt% of Disperbyk-145 (BYK Chemie, Wesel, Germany) dispersant according to the procedure described in [22]. Following the pre-treatment, the dispersant pre-treated ceramic powder was incorporated into the resin mixture to achieve 57 vol% solid loading. In the final step, 0.1 wt% (to the reactive resin) of diphenyl (2,4,6-trimethylbenzoyl) phosphine oxide (Sigma Aldrich, Gillingham, UK) was added to initiate the polymerisation reactions and the slurry was thoroughly mixed overnight on a turbula mixer. Before the use on the printer, the slurry was placed under vacuum to remove any air bubbles. The particle size distribution of the pre-treated ceramic powder was evaluated with Sympatec Helos (Sympatec GmbH, Clausthal-Zellerfeld, Germany) using R1 lens. The rheology of the prepared slurry was tested on AR 500 (TA Instruments, New Castle, DE, USA) with a 20 mm parallel plate geometry varying the shear rate from 0.1 to 300 s^{-1} at a constant temperature of 20.0 °C.

6.2.3 Green body shaping via DLP

The parts were printed on Admaflex 130 printer, DLP based additive manufacturing system developed and commercialised by Admatec Europe (Admatec Europe BV, The Netherlands). The prepared .STL files were sliced to a layer thickness of 25 μm using the machine's slicing software. The key parameters of the machine are summarised in Table 6.1.

Table 6.1 Key parameters of the employed DLP printer

Technology	Layer thickness, μm	Printing build volume (X, Y, Z), mm	Individual pixel size, μm	Wavelength, nm
DLP	10-200	96 × 54 ×110	40	405

The main components of the machine (Figure 6.3) are (i) building platform with a build plate, (ii) glass bottom, (iii) light projector, (iv) slurry reservoir, (v) wiper, and (vi) foil rolls. In the first step of the printing process, the slurry is transported on the foil from the reservoir to the building area by the rotating foil system. The building platform then descends until the distance between the platform and the slurry layer is equal to one-layer thickness. The light projects the slice information to the slurry layer and the illuminated slurry is cured for several seconds. The building platform ascends, the excess slurry is transported to the wiper and pumped back into the reservoir. A new slurry layer is recoated, and the platform descends to a distance equal to a one-layer thickness between the first cured layer and the slurry layer, the next layer is then cured and adhered to the previous layer. The process of slurry transport and layer-by-layer curing is repeated until the green part is built.

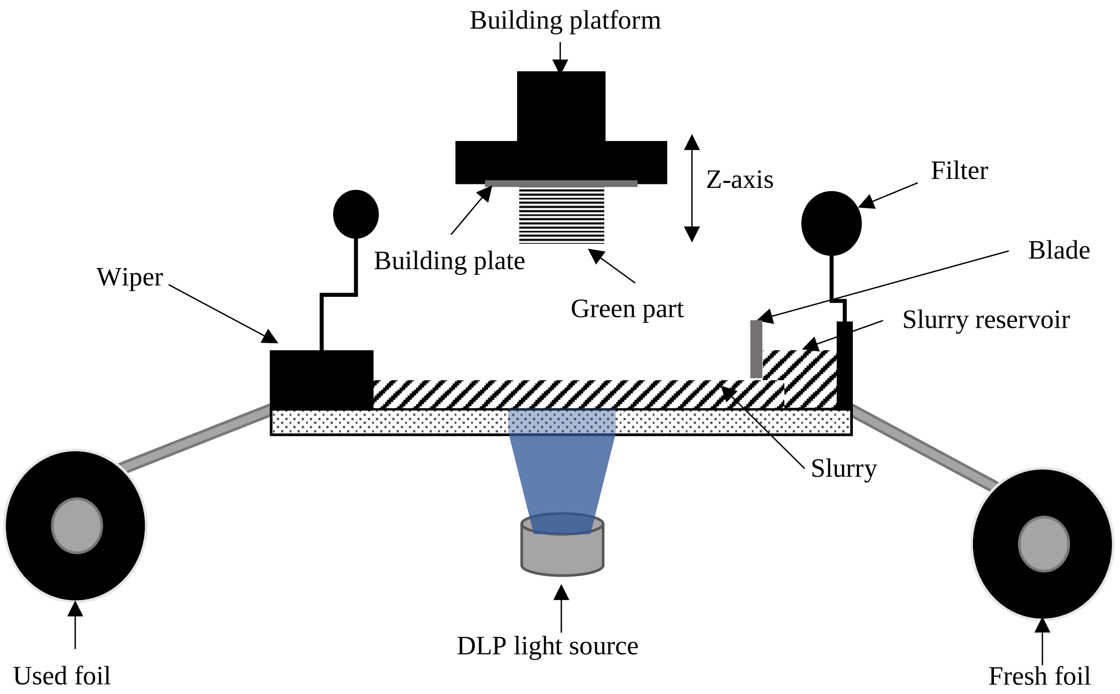

Figure 6.3 Schematic of the Admaflex 130 printer

Given the rigid nature of the cured slurry, direct printing of the part on the base layers resulted in a difficult part extraction. Hence, sacrificial layers were added to the starting CAD models. Furthermore, to ease the detachment of the sacrificial layers from the base, 8 base layers were cured with a light intensity of 27.3 mW/cm^2 and an exposure time of 4 seconds. The intermediate layers were printed by decreasing the light intensity from 27.3 to 14 mW/cm^2 in increments of 3.3-3.4 mW/cm^2 at an exposure time of 4 seconds, followed by decreasing the exposure time at a constant light intensity of 14 mW/cm^2, layer-by-layer, until 3 seconds were reached. The rest of the layers were exposed with an intensity of 14 mW/cm^2 and an exposure time of 3 seconds. After the parts were built, they were extracted from the platform and the sacrificial layers were cut from the green parts. The green parts were then cleaned from the non-polymerised slurry with dibasic ester (Sigma Aldrich, Gillingham, UK), dried in atmospheric conditions and thermally postprocessed via debinding and sintering.

6.2.4 Thermal postprocessing of the green bodies

The debinding program was derived from the Thermogravimetric Analysis (TGA) and Differential Scanning Calorimetry (DSC) of the cured slurry that was carried out on a simultaneous analyser SDT NETZSCH STA in dynamic air (100 mL/min) with a heating rate of 5 °C/min. The debinding process was carried out in a tube furnace (TSH/1S/75/450, Elite Thermal Systems Ltd, UK). After debinding, the specimens were sintered in a chamber furnace (HTF 17/27, Carbolite Gero, United Kingdom) at 1540 °C with a dwell time of 2 hours and a heating and cooling rate of 3 °C/min in air atmosphere. Both thermal processes were carried out under the air atmosphere. The linear shrinkage of the samples was obtained by using measurements of sample dimension in X–Y and Z directions, achieved by using a Vernier caliper, before and after sintering and calculated by the following equation:

$$L_i = \frac{G_i - S_i}{G_i} x\ 100\ \% \qquad \text{Equation 6.1}$$

Where L_i is the linear shrinkage, is the G_i is the dimension of the sample before sintering (green stage) and S_i is the dimension of the sample after sintering. The index *i* represents X–Y or Z direction.

6.2.5 Part characterisation

Structural integrities of the interlocking mechanisms were tested under compression at 0.5 mm/min (Instron 4467 series model, UK) with a rod fixture of 12.7 mm diameter. Displacements and loads were recorded with a 30 kN load cell. A bespoke sample holder with a cylindrical groove was designed to hold the testing specimen and to form a space for the fractured material to fall into. The sample holder was held in place by neodymium disc magnets. Sintered density was estimated using Archimedes' principle with distilled water as the emersion medium and given as percent of the relative density. The equipment used to measure the density of the samples was an Ohaus Adventurer Analytical Balance, with the Archimedes principle measurement complement. This analytical balance allows the direct measurement of the density with a program routine that realises the intermediate calculation. The theoretical density of the Al_2O_3 was taken from the manufacturer's specifications (3.95 g/cm^3). The microstructure of the green and sintered bodies was studied using Scanning Electron Microscopy (SEM) (TM3030 Tabletop SEM, Hitachi High-Technologies, Tokyo, Japan). The fracture surface was examined using SEM (JCM-6000, JEOL Ltd.,Tokyo, Japan).

6.3 Results and discussion

6.3.1 Slurry characterisation

The particle size distribution of the dispersant pre-treated ceramic powder is shown in Figure 6.4a). The mean particle size (d_{50}) was approximately 0.80 µm and 90% (d_{90}) of the particles were smaller than approximately 2.31 µm. The rheology of the prepared slurry expressed by the logarithmic representation of the viscosity curve as a function of shear rate is shown in Figure 6.4b). The viscosity of the prepared slurry decreases with increasing shear rate. The slurry displayed a relatively stable condition under the action of shearing force, and the viscosity of the slurry did not vary considerably from shear rates of 10-300 s^{-1}. Admaflex 130 is specifically designed to print slurries with a broad viscosity range, where a tape casting method with rotating foil is used to spread a fresh slurry layer. The recommended rheology of the suspension for Admaflex technology is a shear thinning behaviour with a dynamic viscosity below 10 Pa·s for shear rates from 10 to 300 s^{-1} [25].

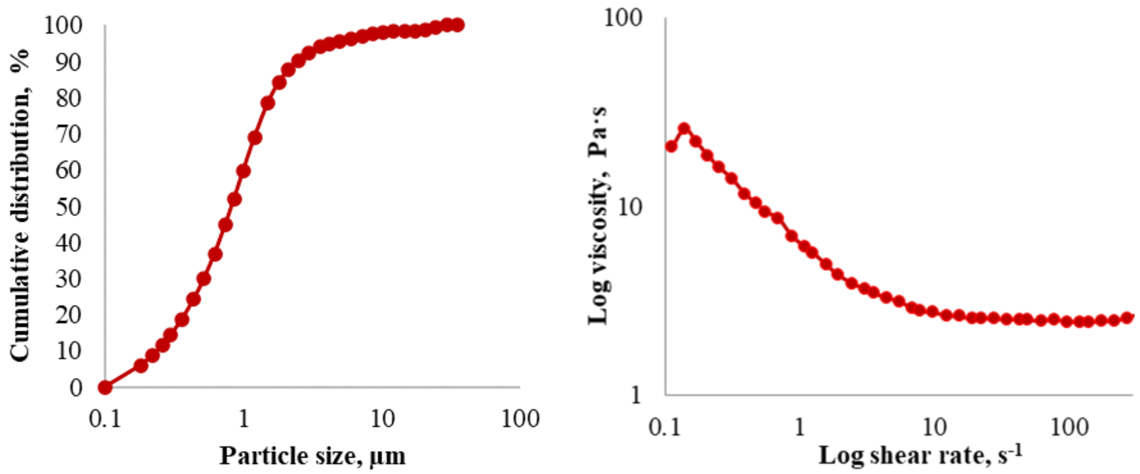

a) b)

Figure 6.4 a) Particle size distribution of the dispersant-treated powder b) Rheology of the prepared slurry

Typical shear rates within the process are up to approximately 200 s^{-1} when using a doctor blade gap of 120 µm and a layer thickness of 25 µm. The viscosity of the prepared slurry was lower than that of the limit value for the Admaflex technology.

6.3.2 Thermal debinding analysis

The TGA-DSC analysis revealed information on the decomposition behaviour of the resin components with the temperature increase. To minimise delamination, cracking, deformation, or collapse induced by thermal stress from polymer breakdown, the debinding process must be evaluated and the heating rate and dwell time adjusted accordingly [26]. The base resin consisted of a mixture of a mono-functional, di-functional, tetra-functional monomer and a plasticiser. 4-acryloylmorpholine is widely used as a reactive monomer in photopolymerisable systems due to its low viscosity and good compatibility with acrylates and oligomers [27].

1,6-hexanediol diacrylate is a low viscosity, di-functional acrylate ester monomer that is often employed as a reactive diluent in photopolymerisable slurry applications [28]. Pentaerythritol tetraacrylate is a tetra-functional monomer that is primarily used to aid in crosslinking for increased final modulus [29]. The function of the dibutyl phthalate as the plasticiser was to increase the flexibility of the part after curing [25].

From the TGA/DSC curve presented in Figure 6.5 it can be observed that the first mass loss of 3.6% begins to occur when the temperature is between 115 and 250 °C. This weight loss of 3.6% is assigned to the evaporation of the adsorbed water and residual cleaning solution. Within the temperature range and employed testing conditions, no peak was observed in the DSC curve [30]. The second rapid mass loss with a peak of 375.9 °C had a mass loss of 8.7%. The final mass loss occurs between 450 °C and 575 °C and is equal to 6.9%. Beyond 575 °C there is a negligible mass loss. According to the DTG curve, the extremum points of mass loss rate appear at 191.2 °C, 375.9 °C and 481.3 °C. The total mass loss is 19.2 wt%. Based on the composition of the prepared, uncured resin the total weight loss is slightly greater than expected, implying total burnout of the binding components. The excess weight loss may be attributed to adsorbed water during storage or the leftover dibasic ester.

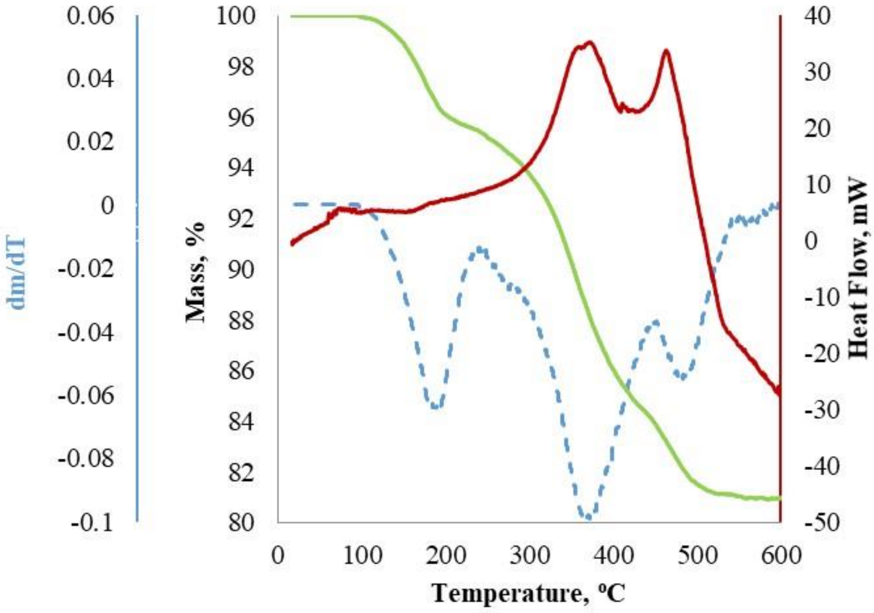

Figure 6.5 DSC/TGA and DTG curves

From the DSC curve, it can be concluded that the thermal debinding reaction is an exothermic process with two major peaks attributed to the oxidative decomposition of polymer chains (372.2 °C) and the thermal decomposition of the crosslinked polymer network (464.1 °C) [31]. The DSC curve also showed a weak peak at 70.8 °C, that may be a result of an artifact caused by the toppling over of the sample in the pan. According to the results of TGA and DSC curves, the parameters of the debinding process are determined. The temperature was first raised from room temperature to 190 °C and then kept for 2 h. After that, the temperature was raised to 375 °C and maintained for 4 h to allow enough time for the decomposition of the organic matter and reduce the effect of thermal stress on the sample. The next step was heating to 480 °C with a dwell time of 2 h. Finally, the temperature was continuously raised to 650 °C to ensure that the resin was completely removed, and then naturally cooled to room temperature. The whole debinding process took a total of 62.5 h without cooling.

6.3.3 Characterisation of the printed and sintered samples

The green parts are shown in Figure 6.6. The parts show sufficient quality after sacrificial layer removal and cleaning, no flaws were determined by visual inspection and the green strength was high enough for handling.

Figure 6.6 Green parts (from left to right U-lock, Thread, Twist-lock)

The layering effect is visible on the surface of the green and sintered parts, which was expected due to the employed additive layering process and over curing. According to the findings of our earlier work, the manufacturability of lattice structures is affected by the cure depth and the size of the exposure area of the sliced layer [22]. The struts of the lattices tend to be very fragile due to their small cross-sectional area, and it is not uncommon to experience complete breakage during the build. As a result, for small exposure areas, larger cure depths were required to establish robust interlayer joints as well as to ensure a continuous build [22]. With the existing slurry formulation, over curing was inevitable. To reduce the layering effect, the literature suggests lowering the slice thickness or the cure time [32,33]. However, the latter can also reduce cure depth, while the thinner slice leads to a longer printing time, reducing the printing efficiency. An example of green and sintered components is presented in Figure 6.7 to illustrate the differences in the part dimensions before and after the thermal-postprocessing stages. As expected, the parts exhibited shrinkage upon sintering at high temperatures. Shrinkages of X−Y and Z directions were approximately 14% and 19%, respectively, with a relatively high difference of 5% between the X–Y and Z directions. This anisotropic dimension shrinkage behaviour of AM parts is related to the layered shaping process [27,34].

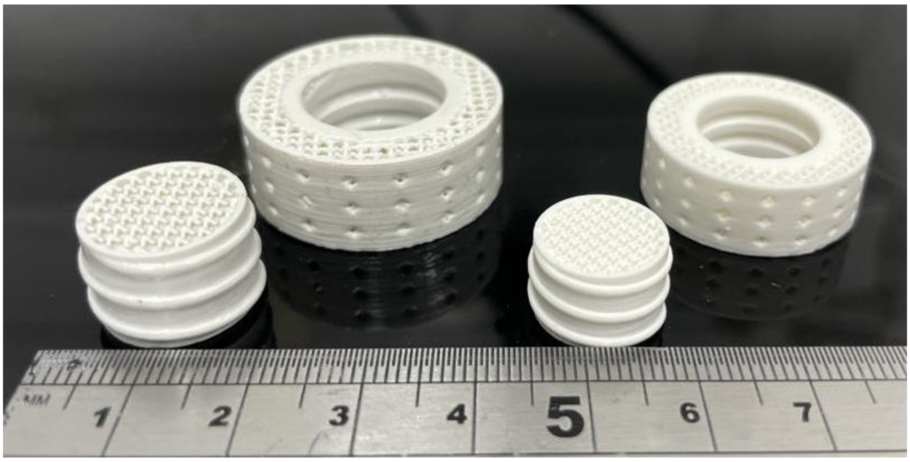

Figure 6.7 Green parts (left) and sintered parts (right)

The anticipated shrinkage was compensated by increasing the starting CAD models by estimated shrinkage factors in X–Y (1.143) and Z (1.205). According to the experimental results, the actual shrinkage factors in X–Y, and Z directions were determined to be 1.143 and 1.235, respectively at the energy dose of 42 mJ/cm^2. Nevertheless, the overall shrinkage of the parts was low due to the high solid phase loading (57 vol%) in the ceramic slurry. In a view of the shrinkage of the actual size, specific values of the ceramic samples in the green stage and the as-sintered stage are shown in Table 6.2.

Table 6.2 Dimensions of the green bodies, sintered bodies and the sintering shrinkage

CAD (mm)			**Green body (mm)**		**Sintered body (mm)**		**Sintering shrinkage (%)**	
Part	**X–Y**	**Z**	**X–Y**	**Z**	**X–Y**	**Z**	**X–Y**	**Z**
A	14.53	10.77	15.02±0.17	10.50±0.23	13.01±0.09	8.52±0.06	13.38	18.86
A’	29.03	10.77	29.16±0.20	10.46±0.18	24.87±0.07	8.40±0.02	14.71	19.69
B	14.53	10.77	14.78±0.08	10.46±0.02	12.78±0.06	8.57±0.21	13.52	18.07
B’	29.03	10.77	29.08±0.14	10.44±0.04	24.81±0.49	8.49±0.11	14.68	18.68
C	14.53	10.77	14.93±0.23	10.44±0.12	12.89±0.10	8.50±0.06	13.66	18.58
C'	29.03	10.77	29.22±0.11	10.58±0.17	24.86±0.07	8.58±0.12	14.92	18.90

The CAD dimensions in the Z direction listed in the Table 6.2. correspond to the parts without the sacrificial layers. The green bodies were up to 3.26% larger than the CAD designs within the X–Y plane. The minor variations in the sample’s heights in the green parts are due to the extraction of the sacrificial layers. Figure 6.8 illustrates the SEM images of the surface of the green and sintered parts: a) shows SEM image of the green body, in which it can be seen that particles are homogeneously distributed in the solidified polymeric resin and b) shows SEM image of the surface after sintering at 1540 °C, where small pores at the grain boundaries are seen, without complete densification.

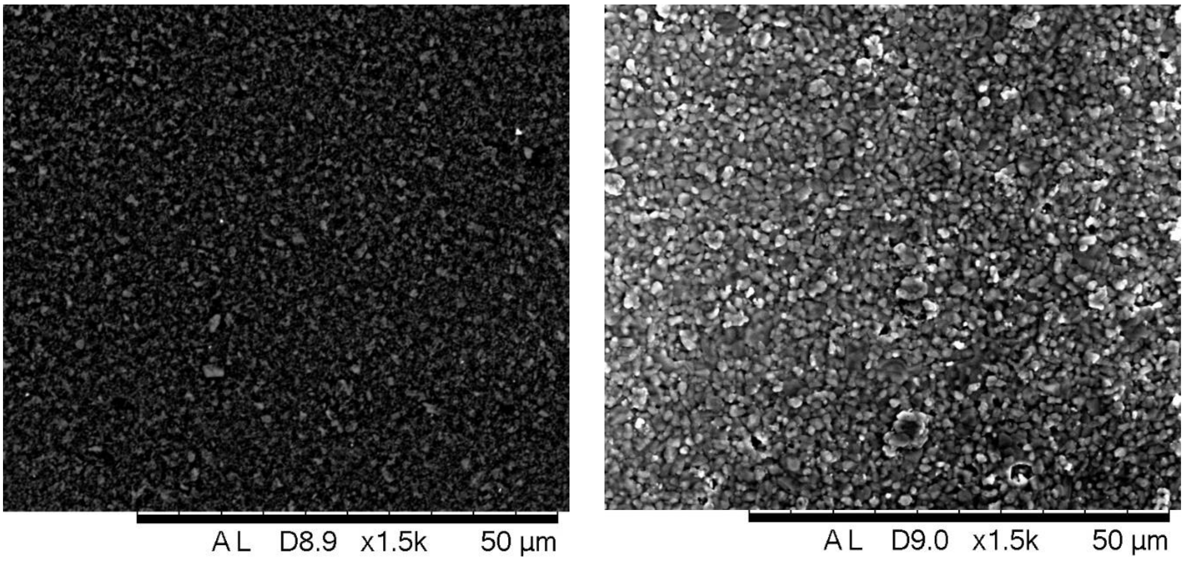

a) b)

Figure 6.8 SEM images of the a) Green surface b) Sintered surface

As the complex features of the parts fabricated in this work may affect the results of density measurements, five cubes were manufactured, debinded and sintered together with the hybrid substrates. The mean density value was determined to be 97.88±0.01%. The resulting density is acceptable for catalytic supports. Achieving higher density would be beneficial for the mechanical strength of the substrates, however, it is not essential for application in catalytic substrates as the residual porosity is advantageous for the adhesion of the washcoat [35].

6.3.4 Mechanical integrity

The results of the mechanical integrity test are presented in Figure 6.9. The deformation behaviour of the parts after the test is shown in Figure 6.10. The samples show similar trends in the force-displacement curves, with several major and minor peaks and finally a force plateau after reaching failure. With external load increasing, multiple peaks were found to appear in the curves of all interlock configurations in this study. At each peak load for the U-lock interlock, a crack formed in the outer shell. The outer shell of the U-lock mechanism experienced greater stresses than the core specimen that spread from the interlocking mechanism to the outer edges of the shell substrate resulting in cracks that run horizontally and perpendicularly as seen in Figure 6.10a).

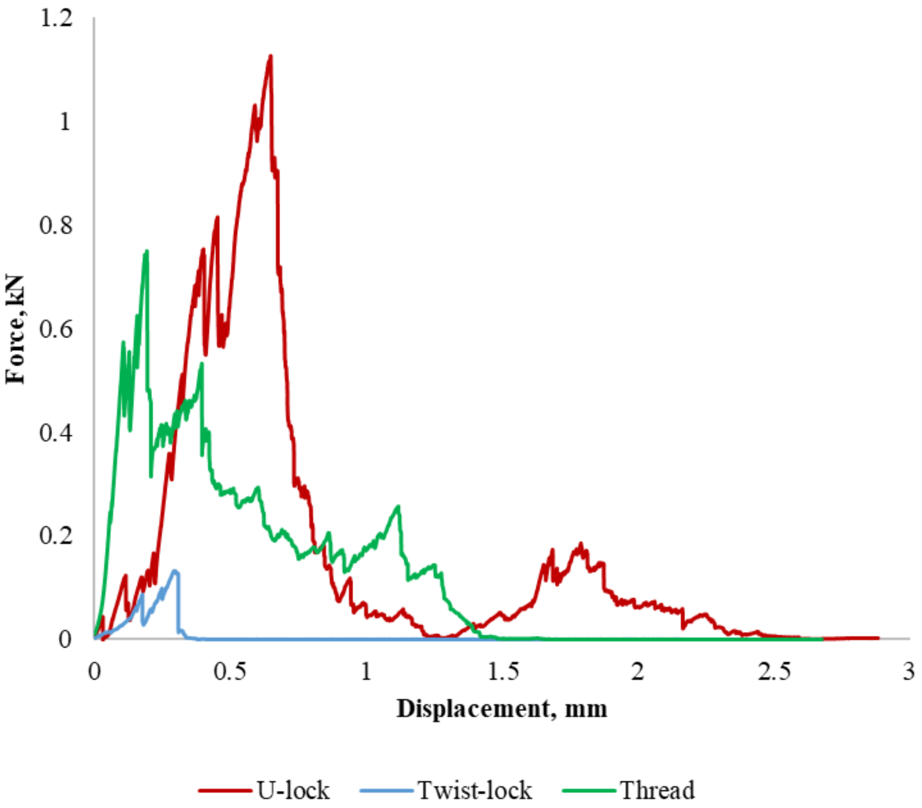

Figure 6.9 Force-displacement relationship for the interlocking mechanisms

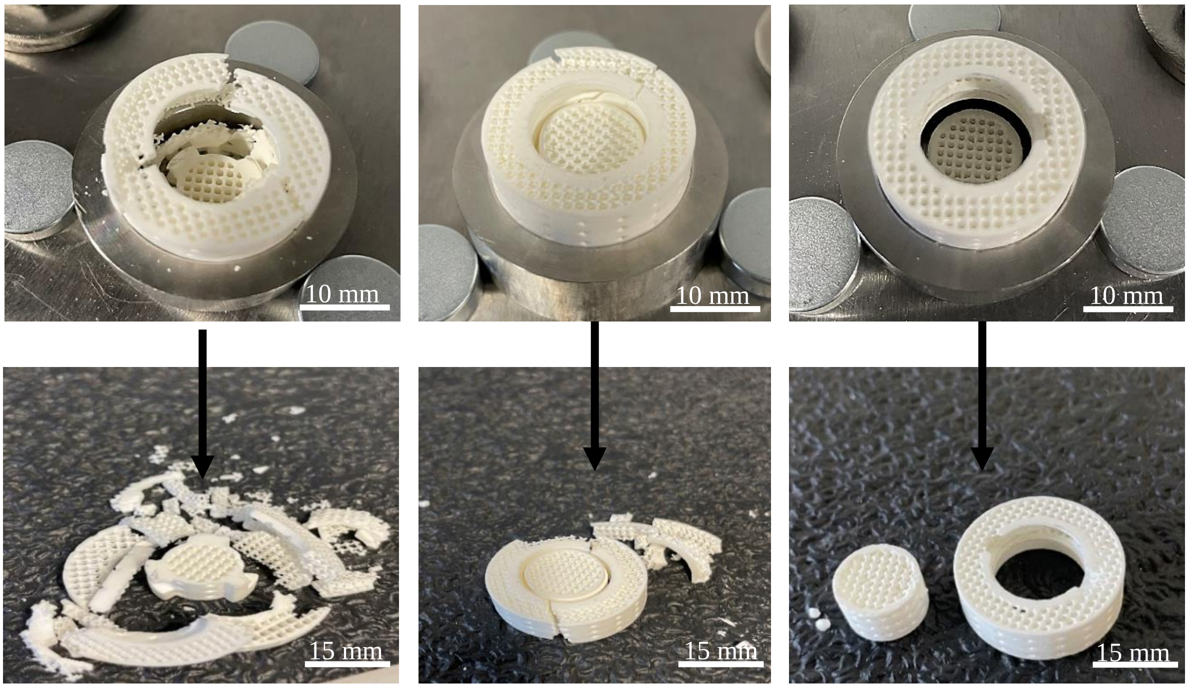

a) b) c)

Figure 6.10 Deformation behaviour of a) U-lock b) Thread c) Twist-lock

The horizontal cracks are anticipated to be a result of the generation of stresses in the outer shell due to the vertical load acting on the core specimen pushing down on the L-shaped protrusions. The shell substrate lost its structural integrity and gradually crumbled and collapsed, leading to catastrophic failure with broken pieces of various shapes and sizes.

The Thread topology force-displacement curve presents various peaks with a gradual decrease of the peak forces with the increase of displacement. The first major peak was lower than the highest peak which was attributed to the settling of the core inside of the shell substrate. As the loading proceeded, the load started to re-direct in a diagonal manner which led to the diagonal fractures of the shell substrate. The major peaks could be attributed to the propagation of diagonal and horizontal cracks in the shell substrate (Figure 6.10b)). The external thread on the core substrate was stronger than the internal thread of the shell substrate. For the Twist-lock specimen, the force-displacement curve presents two force peaks associated with the snapping of the side pins from the surface of the cylindrical core substrate. This is due to the small area of the pins, which did not provide enough resistance to applied force before failure. Once the pins snapped off, the force decreased and plateaued as the core slid out of the outer substrate leaving the interlocking system of the outer shell intact, as seen in Figure 6.10c).

It can be observed that the shape of the force–displacement response is affected by the interlock topology. It is well known that ceramics are sensitive to flaws [17]. Minor flaws introduced during manufacturing and thermal postprocessing of ceramic-printed components can significantly attenuate the strength and toughness of the final parts. SEM micrographs of fractured specimens are shown in Figure 6.11. Interlayer delamination is observed at a number of layer intervals in Figure 6.11a). The delamination originates from the bottom-up layer-by-layer fabrication process and the shrinkage that occurs during the heat treatment process. During loading, the delaminated regions act as stress concentrator and trigger crack propagation [36]. Hence, smaller cracks are seen in Figure 6.11b) which emanate from the delaminated regions. Figure 6.11c) shows a brittle fracture, characteristic of ceramic materials. Both the interlayer and intralayer surfaces are visible in the SEM image. Similar to other AM methods, the DLP manufacturing technique still presents challenges inherent to the layering technique and sintering processes of the printed parts which ultimately influence the mechanical strength of the part [37]. Layer bonding could be improved by systematic optimisation of the printing process parameters in conjunction with heating rate, dwell time and dwell temperatures of the debinding and sintering.

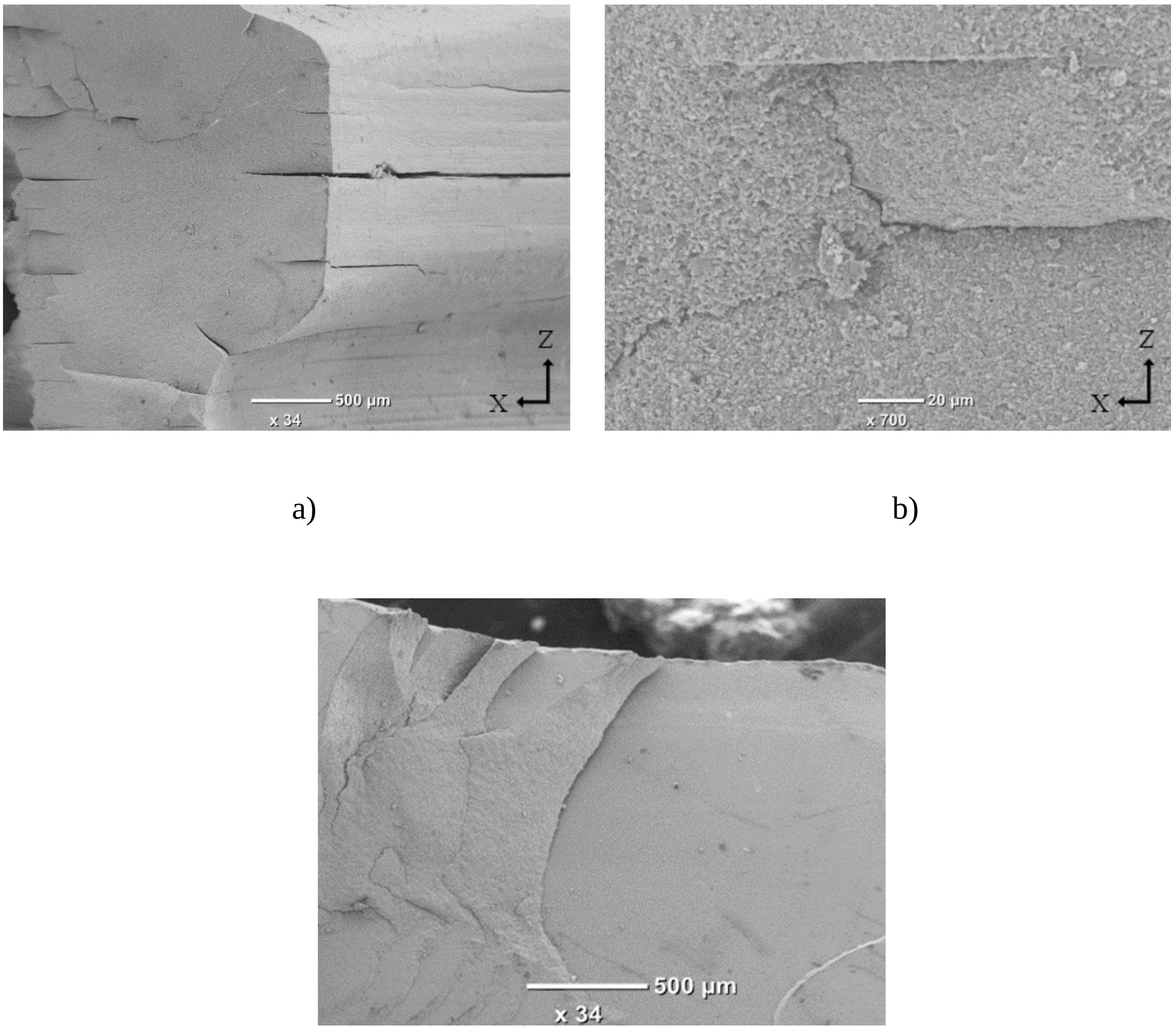

a) b)

c)

Figure 6.11 SEM images of a fracture surface at a) Low magnification and b) High magnification. The legend axis indicates build direction was in the vertical (Z) direction c) Top side of the fracture surface

Employing an additive manufacturing approach for catalyst substrate production can yield improved versatility and allow fabrication of geometries and configurations that traditional manufacturing techniques cannot achieve. The design and manufacturing method employed in this study can be applied to integrate multiple catalytic systems into a single monolithic system. The application and function of the individual substrates in the hybrid concept are highly dependent on the particular application, engine operating procedures, exhaust conditions, etc. For example, the hybrid substrate concept can be applied to reduce the aftertreatment catalyst volume by employing it in advanced aftertreatment solutions, such as exhaust gas reforming, where the core substrate can be catalyst coated to provide reforming and the shell substrate can be coated to provide aftertreatment. The dimensional parameters of the individual substrates can also be altered, for example, to deliver small reformate/H_2 concentrations to the aftertreatment system, a shorter reforming catalyst core can be fitted at the entrance of the longer shell aftertreatment catalyst. In this case, the lattice architecture would aid in directing the flow from the core catalyst to the shell catalyst and provide enhanced interaction of the gas flow with the washcoat. On the other hand, the hybrid substrate approach could be utilised to increase the efficiency of individual components of the aftertreatment, as in the work from Lefort et al. [3], where the core catalyst can provide good light-off performance and the shell substrate can be used to retain heat. In this case, the catalyst loading between the two substrates may be varied, or the substrate design can be modified to include alternative architecture, different strut/wall thickness and/or cell size.

6.4 Conclusions

This study demonstrated the possibility of AM of hybrid monolithic ceramic substrates that could be utilised as catalyst reactors for aftertreatment applications. A novel design approach and an additive manufacturing (AM) technique were proposed to manufacture the dual-substrate monoliths. The DLP manufacturing process enabled the fabrication of highly complex parts with various interlocking mechanisms, which could not be obtained by conventional processing techniques. Photoreactive alumina slurry with suitable rheological behaviour for the employed printer was used as the base material for the parts manufacturing. The green parts were subjected to two thermal treatments- debinding and sintering. Analysis of the DSC/TGA and DTG curves revealed the debinding parameters. The layering effect was observed inherent to the layer-by-layer manufacturing process and high energy dose. The sintered parts displayed anisotropic shrinkage after sintering, with the shrinkage of approximately 14% in the X–Y direction and 19% in the Z direction. The sintered density was 97.88±0.01%, acceptable for catalytic substrate applications. A mechanical testing campaign was performed to study the mechanical integrity of the interlocking configurations. The force-displacement response was found to be affected by the topology of the interlocks in the substrates. U-lock and Thread configurations were found to sustain more load until complete failure. Future work should focus on investigating the feasibility of the proposed integrated substrate in the aftertreatment applications.

Acknowledgements

The research leading to these results has received funding from the Engineering and Physical Sciences Research Council for project FACE - Novel Integrated Fuel Reformer-Aftertreatment System for Clean and Efficient Road Vehicles under grant number EP/P03117X/1. N.K. also thanks the University of Birmingham for the award of a PhD scholarship.

References

1. Baharudin L, Watson MJ. Monolithic substrate support catalyst design considerations for steam methane reforming operation. Rev Chem Eng. 2018;34(4):481–501.
2. Ayodhya AS, Narayanappa KG. An overview of after-treatment systems for diesel engines. Environ Sci Pollut Res. 2018;25(35):35034–47.
3. Lefort I, Tsolakis A. A thermally efficient DOC configuration to improve CO and THC conversion efficiency. SAE Tech Pap. 2013;2.
4. Hazlett MJ, Epling WS. Heterogeneous catalyst design: Zoned and layered catalysts in diesel vehicle aftertreatment monolith reactors. Can J Chem Eng. 2019;97(1):188–206.
5. Megaritis A, Wyszynski ML, Tsolakis A, Cracknell R, Peucheret SM, Xu HM, et al. Exhaust gas fuel reforming for IC Engines using diesel type fuels. SAE Tech Pap Ser. 2010;1:1289–94.
6. Herreros JM, Gill SS, Lefort I, Tsolakis A, Millington P, Moss E. Enhancing the low temperature oxidation performance over a Pt and a Pt-Pd diesel oxidation catalyst. Appl Catal B Environ. 2014;147:835–41.
7. Umar M, Nozari H, Menezes MR, Herreros JM, Lau CS, Tsolakis A. Hydrogen production from bioethanol fuel mixtures via exhaust heat recovery in diesel engines: A promising route towards more energy efficient road vehicles. Int J Hydrogen Energy. 2021;46(46):23603–14.
8. Azis MM, Auvray X, Olsson L, Creaser D. Evaluation of H2 effect on NO oxidation over a diesel oxidation catalyst. Appl Catal B Environ. 2015;179(2):542–50.
9. Theinnoi K, Temwutthikun W, Wongchang T, Sawatmongkhon B. Application of exhaust gas fuel reforming in diesel engines towards the improvement urban air qualities. Energy Procedia. 2018;152:875–82.
10. Negri M. Technology Development for ADN-Based Green Monopropellant Thrusters – an Overview of the Rheform Project. In: Proceedings of the 7th European Conference for Aeronautics and Space Sciences. 2017.
11. Koopmans R, Schuh S, Bartok T, Forschungs- F, Gmbh T, Kaplan-straße V, et al. Performance comparison between extruded and printed ceramic monoliths for catalysts. In: Proceedings of the 7th European Conference for Aeronautic and Space Sciences (EUCASS). 2017.
12. Essa K, Hassanin H, Attallah MM, Adkins NJ, Musker AJ, Roberts GT, et al. Development and testing of an additively manufactured monolithic catalyst bed for HTP thruster applications. Appl Catal A Gen. 2017;542:125–35.
13. Hassanin H, Alkendi Y, Elsayed M, Essa K, Zweiri Y. Controlling the Properties of Additively Manufactured Cellular Structures Using Machine Learning Approaches. Adv Eng Mater. 2020;22(3):1–9.
14. Hassanin H, El-Sayed MA, Elshaer A, Essa K, Jiang K. Microfabrication of net shape zirconia/alumina nanocomposite micro parts. Nanomaterials. 2018;8(8).
15. Sabouri A, Yetisen AK, Sadigzade R, Hassanin H, Essa K, Butt H. Three-Dimensional Microstructured Lattices for Oil Sensing. Energy and Fuels. 2017;31(3):2524–9.
16. El-Sayed MA, Essa K, Ghazy M, Hassanin H. Design optimization of additively manufactured titanium lattice structures for biomedical implants. Int J Adv Manuf Technol. 2020;110(9–10):2257–68.

17. Hassanin H, Essa K, Elshaer A, Imbaby M, El-Mongy HH, El-Sayed TA. Micro-fabrication of ceramics: Additive manufacturing and conventional technologies. J Adv Ceram. 2021;10(1):1–27.

18. Kovacev N, Li S, Zeraati-Rezaei S, Hemida H, Tsolakis A, Essa K. Effects of the internal structures of monolith ceramic substrates on thermal and hydraulic properties: additive manufacturing, numerical modelling and experimental testing. Int J Adv Manuf Technol. 2020;112:1115–32.

19. Papetti V, Dimopoulos Eggenschwiler P, Della Torre A, Lucci F, Ortona A, Montenegro G. Additive Manufactured open cell polyhedral structures as substrates for automotive catalysts. Int J Heat Mass Transf. 2018;126:1035–47.

20. Ferrizz RM, Stuecker JN, Cesarano J, Miller JE. Monolithic supports with unique geometries and enhanced mass transfer. Ind Eng Chem Res. 2005;44(2):302–8.

21. Hajimirzaee S, Doyle AM. 3D printed catalytic converters with enhanced activity for low-temperature methane oxidation in dual-fuel engines. Fuel. 2020;274:117848.

22. Kovacev N, Li S, Essa K. Effect of the preparation techniques of photopolymerizable ceramic slurry and printing parameters on the accuracy of 3D printed lattice structures. J Eur Ceram Soc. 2021;41(15):7734–43.

23. Schweiger J, Bomze D, Schwentenwein M. 3D Printing of Zirconia–What is the Future? Curr Oral Heal Reports. 2019;6(4):339–43.

24. Johansson E, Lidström O, Johansson J, Lyckfeldt O, Adolfsson E. Influence of resin composition on the defect formation in alumina manufactured by stereolithography. Materials (Basel). 2017;10(2).

25. Gonzalez P, Schwarzer E, Scheithauer U, Kooijmans N, Moritz T. Additive manufacturing of functionally graded ceramic materials by stereolithography. J Vis Exp. 2019;2019(143):1–8.

26. Pfaffinger M, Mitteramskogler G, Gmeiner R, Stampfl J. Thermal debinding of ceramic-filled photopolymers. Mater Sci Forum. 2015;825–826:75–81.

27. Sun J, Binner J, Bai J. Effect of surface treatment on the dispersion of nano zirconia particles in non-aqueous suspensions for stereolithography. J Eur Ceram Soc. 2019;39(4):1660–7.

28. Zakeri S, Vippola M, Levänen E. A comprehensive review of the photopolymerization of ceramic resins used in stereolithography. Addit Manuf. 2020;35:101177.

29. He R, Liu W, Wu Z, An D, Huang M, Wu H, et al. Fabrication of complex-shaped zirconia ceramic parts via a DLP- stereolithography-based 3D printing method. Ceram Int. 2018;44(3):3412–6.

30. Borlaf M, Serra-Capdevila A, Colominas C, Graule T. Development of UV-curable ZrO2 slurries for additive manufacturing (LCM-DLP) technology. J Eur Ceram Soc. 2019;39(13):3797–803.

31. Wang L, Liu X, Wang G, Tang W, Li S, Duan W, et al. Partially stabilized zirconia moulds fabricated by stereolithographic additive manufacturing via digital light processing. Mater Sci Eng A. 2020;770:1–8.

32. Kowsari K, Zhang B, Panjwani S, Chen Z, Hingorani H, Akbari S, et al. Photopolymer formulation to minimize feature size, surface roughness, and stair-stepping in digital light processing-based three-dimensional printing. Addit Manuf. 2018;24:627–38.

33. Li X, Zhong H, Zhang J, Duan Y, Bai H, Li J, et al. Dispersion and properties of zirconia suspensions for stereolithography. Int J Appl Ceram Technol. 2019;00:1–9.

34. De Camargo IL, Erbereli R, Taylor H, Fortulan CA. 3Y-TZP DLP additive manufacturing: Solvent-free slurry development and characterization. Mater Res. 2021;24(2):2–9.
35. Santoliquido O, Bianchi G, Dimopoulos Eggenschwiler P, Ortona A. Additive manufacturing of periodic ceramic substrates for automotive catalyst supports. Int J Appl Ceram Technol. 2017;14(6):1164–73.
36. Al-Ketan O, Pelanconi M, Ortona A, Abu Al-Rub RK. Additive manufacturing of architected catalytic ceramic substrates based on triply periodic minimal surfaces. J Am Ceram Soc. 2019;1–18.
37. Osman RB, van der Veen AJ, Huiberts D, Wismeijer D, Alharbi N. 3D-printing zirconia implants; a dream or a reality? An in-vitro study evaluating the dimensional accuracy, surface topography and mechanical properties of printed zirconia implant and discs. J Mech Behav Biomed Mater. 2017;75:521–528.

CHAPTER 7 CONCLUSIONS AND FUTURE WORK

7.1 Conclusions

Monolith catalysts are essential for decreasing exhaust gas emissions. As a result of globalisation and a rise in vehicle use, there is a growing demand for advancements in monolith catalyst design. In accordance with the proposed aim, the research reported in this thesis has focused on the design enhancement of ceramic monolith substrates to overcome some of the limitations of the conventional honeycomb structure of the catalyst substrate for automotive emissions aftertreatment applications. While the conventional ceramic honeycomb catalyst substrate provides a large surface area and a degree of flexibility for heat and mass transfer adaptations, additional emission reduction benefits can be gained by introducing more flexible designs, as outlined in Chapter 2. The use of additive manufacturing techniques for catalyst substrate manufacture allows design and fabrication of unique substrate designs that cannot be achieved by traditional manufacturing methods. The findings of this work are applicable to exhaust aftertreatment systems for both spark and compression ignition engines.

Diamond lattice substrates were proposed as an alternative to the honeycomb design. Computational Fluid Dynamics (CFD) techniques were developed and validated to compare the flow-through resistance and temperature distribution of the lattice substrates with a conventional honeycomb design. The effects that the diamond lattice substrate design parameters had on geometric, hydraulic, and thermal aspects were investigated. The developed models were utilised to predict and evaluate the effect of the design parameters of the lattice structures on geometrical parameters, hydraulic and thermal properties. These are the main findings from the conducted research (Chapter 3):

- DLP additive manufacturing technology enables fabrication of ceramic diamond lattice substrates.
- The numerical simulations revealed that irrespective of the lattice pore size, lower pressure drops were observed in the diamond lattices of varying porosities, when compared to conventional honeycomb in the studied flow rate range, at the expense of a reduced surface area.
- Pressure loss was reduced by 35-48% using a lattice design with the same cell density as the traditional honeycomb substrate.
- When compared to a conventional honeycomb design, diamond lattice substrate designs show reduced axial temperature gradients and uniform temperature distribution in the core area for all studied porosities. The increased heat transfer capabilities were observed due to flow exchange in both the radial and axial directions. This improvement indicated the possibility of more efficient heat utilisation within the lattice substrate.

An alumina photopolymerisable slurry was developed to aid the fabrication of complex and fine-featured lattice structures using DLP technology. To achieve a satisfactory level of dimensional accuracy of the lattice structures, suitable ceramic slurry preparation procedures and the optimum printing process parameters were studied. The effect of the photopolymerisable ceramic slurry preparation techniques on rheology and cure depth and identify the optimal printing parameters for manufacturing tailored lattice structures with fine feature sizes. The following statements summarise the main findings from Chapter 4:

- Pre-treatment of the Al_2O_3 ceramic powder with a dispersant was found to be an important step in the ceramic slurry preparation for DLP. The slurry prepared with the pre-treated powder exhibited appropriate viscosity and curing behaviour for successful processing on the Admaflex 130.

- The calculated critical energy dose for the ceramic slurry prepared with the as-received powder was 5.47 mJ/cm^2 and 9.03 mJ/cm^2 for the ceramic slurry prepared with the pre-treated powder. Indicating an increase in energy required for the photopolymerisation. On the other hand, the depth of penetration D_p was reduced from 136.04 µm to 120.74 µm as a result of the pre-treatment of the powder.
- Lattices with minimum designed diameter size in the X–Y plane of 200 µm were viable for manufacture. The cure depth required for manufacturing was found to be inversely proportional to the diameter size of the strut. Subsequently, light scattering and over curing were inevitable with the current slurry formulation. As a result, the experimental features deviated significantly from the designed models.
- Excess width increased with the increase of the feature size. The broadening parameters were found to be dependent on the layer thickness, energy dose (exposure time and exposure intensity), and the feature size.
- According to the results from DoE and ANOVA, the significant parameters that directly affected the dimensional accuracy were exposure time, exposure power, and their interaction.

Catalytic coating based on Pt-Pd/γ-Al_2O_3 was developed and used to washcoat the additively manufactured substrates. The efficiency of the catalyst coated lattices was evaluated in comparison to a traditional honeycomb catalyst in a real exhaust gas environment. Furthermore, the effect of hydrogen addition on the light-off performance of the lattice-based monolith catalysts was investigated. The main findings of the investigation can be summarised as follows (Chapter 5):

- Superior catalytic activity was observed for the abatement of carbon monoxide, hydrocarbons, and nitrogen oxides for lattice-based catalyst, in comparison with the 400

CPSI honeycomb, with a significant reduction in the light-off temperatures. In the mass-transfer area, there was no evidence of any significant competition between the lattices and honeycomb, even though the lattice substrates had 20-30% lower surface areas than the honeycomb.

- The addition of hydrogen had a positive effect on the carbon monoxide light-off temperature, however, the advance in hydrocarbon light-off temperature reduction was apparent to a lesser extent.
- The diamond-based lattice showed the highest overall NO_2 yield in the moderate to high-temperature range, regardless of the hydrogen presence. Hydrogen addition improved the NO_2 production in the elongated diamond lattice, due to the unique structure of the elongated diamond with increased flow residence time, which was more prominent in enhancing the oxidation of the slow chemical reaction of NO to NO_2 with hydrogen.
- The intricate lattice structures in combination with hydrogen addition allowed greater contact of the reactant with the catalyst adhered to the structure's struts due to flow mixing and more efficiently used surface area, shifting the light-off curves of all studied species to lower temperatures.

Finally, novel hybrid monolith substrates that aim to achieve system complexity reduction were proposed. The hybrid monolith concepts are based on the integration of individual substrates into a modular catalyst substrate via interlocking mechanisms. The main findings of this study were (Chapter 6):

- A proof-of-concept for DLP additive manufacturing of highly complex substrates featuring various interlocking mechanisms to integrate them into a single monolithic substrate for aftertreatment applications was established.

- The green parts were subjected to two thermal treatments- debinding and sintering. Analysis of the DSC/TGA and DTG curves revealed the debinding conditions. The sintered parts displayed anisotropic shrinkage after sintering, with the shrinkage of approximately 14% in the X-Y direction and 19% in the Z direction. The sintered density was 97.88±0.01%, acceptable for catalytic substrate applications.
- Mechanical testing was performed to study the mechanical integrity of the interlocking configurations. The force-displacement response was found to be affected by the topology of the interlocks in the substrates. U-lock and Thread configurations were found to sustain more load until complete failure.

7.2 Future work

This thesis has shown the potential of the ceramic additive manufacturing approach, specifically DLP, to fabricate intricate ceramic substrates for catalytic applications with superior efficiency to the traditional honeycombs. The AM strategy presented enables for greater control and tailoring of cell size, strut diameter, and other geometric patterns to improve the substrate performance. The possibilities of fine-tuning the architecture and catalyst characteristics depending on the application are vast. Based on the work undertaken in this study, further development is recommended in the following directions:

- A detailed study on the influence of the geometrical parameters of the lattice structure on the catalyst performance requires performing full-scale CFD simulations with chemical reaction physics. Topology algorithms could be employed to optimise the structure design in terms of the unit cell, cell size, strut thickness, the shape of the strut cross-section and strut orientation based on input performance objectives.

- The methodology for ceramic slurry preparation and substrate DLP manufacturing of fine and intricate lattice structures, opens the doorways to numerous substrate design concepts where the feature size is not restricted by the manufacturing technique. The conceptual designs of the substrate configurations can be extended to have radial or axial increase/decrease in the cell size and strut/wall thickness where the configuration could be precisely tailored for specific engine exhaust and operating conditions.
- The broadening behaviour in DLP technology should be explored further. The orientation, shape and position of the model on the build plate may have an impact on the dimensional accuracy. The ceramic slurry composition may be evaluated to further understand the influence of the various components (i.e. particle size distribution, solid loading, and resin type) on the broadening behaviour of the DLP printed samples.
- While the slurry washcoating method was successful in producing active and mechanically stable catalyst reactors, there is scope to improve the coating procedure. Given the complexity of the substrate structure and the properties of the sintered substrate material, it was very challenging to achieve a satisfying coating quality. Several dips were necessary to reach the desired catalytic loading with the current washcoating slurry. For future research, optimisation of the washcoat slurry preparation (viscosity, pH, particle size) or implementation of other catalytic washcoating procedures such as spin coating or electrochemical deposition should be investigated. Furthermore, a parametric analysis can be conducted by changing the thickness of the washcoat, BET surface area, washcoat loading or the geometrical parameters of the lattice (strut thickness, cell size, porosity, design).
- The knowledge developed throughout this thesis could be extended into direct DLP forming of high BET surface area ceramic materials with controlled porosity and

sufficient mechanical strength that could yield novel substrates which could reduce time, cost, and labour necessary for their catalytic activation. Moreover, direct 3D printing of active materials on a high surface area ceramic support could allow direct production of catalytically active substrates and reduce the costs and labour requirements.

- Extension of the experimental range of parameters variable for the light-off test i.e. various inlet gas temperatures, flowrates, and different fuel types.
- The hybrid substrate approach should be tested for feasibility. For example, the concept can be applied to optimise aftertreatment system volume by combining for instance, a four-way catalyst. Moreover, as a potential substitute for dual-brick configurations, in which the core catalyst can provide good light-off performance and the shell substrate can be used to retain the heat generated by exothermic reactions. An additional relevant application of the proposed hybrid configuration could be coating the core substrate with a catalyst to provide small reformate/H_2 concentrations to improve the efficiency of the shell substrate coated with active materials to provide aftertreatment.
- Finally, it would be beneficial to establish the commercial feasibility by scaling the DLP process up to the industrial level and to conduct experiments on a full-size lattice-based, fine feature, high surface area catalyst. Current industrial-scale catalysts have been manufactured by material extrusion AM process where the substrate is 3D printed in a several individual pieces and finally assembled catalyst into the can by the stuffing method, where the individual parts are separated by ceramic fibre mat. Ideally, the catalyst substrate could be manufactured in one single brick to preserve integrity. As such, a DLP printer with a larger build volume should be employed.